



HAL
open science

Elaboration of novel sulfate based positive electrode materials for Li-ion batteries

Meiling Sun

► **To cite this version:**

Meiling Sun. Elaboration of novel sulfate based positive electrode materials for Li-ion batteries. Other. Université Pierre et Marie Curie - Paris VI, 2016. English. NNT : 2016PA066686 . tel-01661440

HAL Id: tel-01661440

<https://theses.hal.science/tel-01661440>

Submitted on 12 Dec 2017

HAL is a multi-disciplinary open access archive for the deposit and dissemination of scientific research documents, whether they are published or not. The documents may come from teaching and research institutions in France or abroad, or from public or private research centers.

L'archive ouverte pluridisciplinaire **HAL**, est destinée au dépôt et à la diffusion de documents scientifiques de niveau recherche, publiés ou non, émanant des établissements d'enseignement et de recherche français ou étrangers, des laboratoires publics ou privés.

Université Pierre et Marie Curie

ED 397 – Chimie et physico-chimie des matériaux

Chaire de Chimie du Solide et Energie - Collège de France

Elaboration of novel sulfate based positive electrode materials for Li-ion batteries

By Meiling SUN

PhD thesis in Chemistry

Directed by Jean-Marie TARASCON and Gwenaëlle ROUSSE

To be presented and defended in public on 12 December 2016

In front of the jury :

Dr. Jean-Pierre PEREIRA-RAMOS	Research Director CNRS	Referee
Dr. Valérie PRALONG	Research Director CNRS	Referee
Dr. Domitille GIAUME	Associate Professor	Examiner
Dr. Sophie CASSAIGNON	Associate Professor	Examiner
Prof. Jean-Marie TARASCON	Professor	Director
Dr. Gwenaëlle ROUSSE	Associate Professor	Director

Université Pierre et Marie Curie

ED 397 – Chimie et physico-chimie des matériaux

Chaire de Chimie du Solide et Energie - Collège de France

Elaboration de nouveaux matériaux à base de sulfates pour l'électrode positive des batteries à ions Li

Par Meiling SUN

Thèse de doctorat en Chimie

Dirigée par Jean-Marie TARASCON et Gwenaëlle ROUSSE

Présentée et soutenue publiquement le 12 Décembre 2016

Devant un jury composé de :

Dr. Jean-Pierre PEREIRA-RAMOS	Directeur de Recherche CNRS	Rapporteur
Dr. Valérie PRALONG	Directeur de Recherche CNRS	Rapporteur
Dr. Domitille GIAUME	Maître de Conférences	Examineur
Dr. Sophie CASSAIGNON	Maître de Conférences	Examineur
Prof. Jean-Marie TARASCON	Professeur	Directeur
Dr. Gwenaëlle ROUSSE	Maître de Conférences	Directeur



Table of Contents

General Introduction1

Chapter I. State of the Art5

I.1. Concise Overview of the Main Technologies of Batteries..... 5

- I.1.1. Lead-Acid Batteries 7
- I.1.2. Nickel-Based Technologies 8
- I.1.3. The First Lithium Batteries 8
- I.1.4. Lithium Ion Batteries 9
- I.1.5. Lithium Polymer Batteries 10

I.2. Positive Electrode Materials for Li-ion Batteries 12

- I.2.1. Lithium Transition-Metal Oxides 13
 - I.2.1.1. LiMO_2 ($M = \text{Co, Ni, Mn}$) Layered Compounds 13
 - I.2.1.2. Binary $\text{Li}(M, M')\text{O}_2$ and Ternary $\text{Li}[M, M', M'']\text{O}_2$ 16
 - I.2.1.3. Li-Rich Compounds..... 16
 - I.2.1.4. *Spinel*s..... 18
- I.2.2. Polyanionic Compounds 19
 - I.2.2.1. The NASICON and Anti-NASICON Compounds 19
 - I.2.2.2. Olivine LiMPO_4 ($M = \text{Fe, Mn, Co, Ni}$) Family 23
 - I.2.2.3. Fluorophosphates and Oxyphosphate 25
 - I.2.2.4. Fluorosulfates and Oxysulfate 29
 - I.2.2.1.1 Fluorosulfates 29
 - I.2.2.1.2 Oxysulfates 32

Chapter II. Exploration of LiCuSO_4F & $\text{Li}_2\text{Cu}_2\text{O}(\text{SO}_4)_2$ 35

II.1. Introduction..... 35

II.2. Exploration of Copper-based Fluorosulfate: LiCuSO_4F 35

- II.2.1. Synthesis 35
- II.2.2. Structure Characterization..... 36

II.2.3.	Electrochemical Performance	41
II.2.4.	Density Functional Theory (DFT) Calculations	42
II.2.5.	Conductivity Measurement	46
II.2.6.	Magnetic Property	47
II.3.	Exploration of Copper-based Oxysulfate: $\text{Li}_2\text{Cu}_2\text{O}(\text{SO}_4)_2$.....	49
II.3.1.	Synthesis	49
II.3.2.	Structural Characterization	50
II.3.3.	Thermal Stability Analyses	54
II.3.4.	Bond Valence Energy Landscapes (BVEL).....	55
II.3.5.	Electrochemical Properties	56
I.3.5.1.	“ $\text{Cu}^{3+}/\text{Cu}^{2+}$ ” Redox Activity vs. Li^+/Li^0	56
I.3.5.2.	$\text{Cu}^{2+}/\text{Cu}^+/\text{Cu}^0$ Redox Activity vs. Li^+/Li^0	58
II.3.6.	TEM Investigations.....	61
II.3.7.	DFT Calculations	65
II.3.7.1.	Calculations for “ $\text{Cu}^{3+}/\text{Cu}^{2+}$ ” Oxidation Process.....	65
II.3.7.2.	Calculations for $\text{Cu}^{2+}/\text{Cu}^+/\text{Cu}^0$ Reduction Process	68
II.3.8.	Magnetic Measurement of $\text{Li}_{1.7}\text{Cu}_2\text{O}(\text{SO}_4)_2$	69
II.4.	Conclusions.....	69
Chapter III.	$\text{Fe}_2\text{O}(\text{SO}_4)_2$ - Electrode for Sustainable Li- Based Batteries.....	73
III.1.	Introduction.....	73
III.2.	Exploration of Iron-Based Oxysulfate: $\text{Fe}_2\text{O}(\text{SO}_4)_2$	74
III.2.1.	Synthesis.....	74
III.2.2.	Structure Characterization	76
III.2.3.	Electrochemical Performance.....	82
III.2.4.	Mössbauer Spectroscopy	84
III.2.5.	Chemical Lithiation phase: $\text{Li}_{0.8}\text{Fe}_2\text{O}(\text{SO}_4)_2$	87
III.2.6.	Bond Valence Sum Maps	88
III.2.7.	DFT calculations	89
III.2.8.	Moisture Sensitivity Measurement.....	90
III.3.	Conclusions.....	91

Chapter IV. $A_2VO(SO_4)_2$ (A = Li, Na) as Electrode for Li-ion and Na-ion Batteries95

IV.1. Introduction..... 95

IV.2. Exploration of V-Based Oxysulfate - $Li_2VO(SO_4)_2$ - as Electrode for Li-ion Batteries 96

IV.2.1. Synthesis..... 96

IV.2.2. Structural Characterization..... 97

IV.2.3. Electrochemical Performance..... 101

IV.2.4. Magnetic Property 105

IV.3. Exploration of Vanadium-Based Oxysulfate - $Na_2VO(SO_4)_2$ - as Electrode for Na-ion Batteries..... 106

IV.3.1. Synthesis..... 106

IV.3.2. Structural Characterization..... 106

IV.3.3. Electrochemical Performance..... 108

IV.4. DFT+U Calculations of $A_2VO(SO_4)_2$ (V = Na, Li) 111

IV.5. Conductivity of $Na_2VO(SO_4)_2$ vs. $Li_2VO(SO_4)_2$ 114

IV.5.1. Conductivity Measurement 114

IV.5.2. Bond Valence Energy Landscape..... 115

IV.6. Conclusion..... 116

Conclusions and Perspectives117

Annexes121

A.1. Samples Preparation..... 121

A.1.1 Mechanical-Milling..... 121

A.1.2 Heating Treatment..... 122

A.2. Structural Characterizations 122

A.2.1 Laboratory XRD Measurements 122

A.2.1.1. Facilities..... 123

A.2.1.2.	Air Sensitive Samples	123
A.2.1.3.	In Situ XRD Experiments	123
A.2.1.4.	In Situ High Temperature XRD Measurement	124
A.2.2	Synchrotron XRD Measurements	124
A.2.3	Neutron Powder Diffraction (NPD)	125
A.2.4	TEM Investigation and EDX Analysis	126
A.2.5	Diffraction Data Treatment	126
A.2.5.1.	Refinement of the Structures from XRD and NPD Patterns	126
A.2.5.2.	Crystal Structure Determination	126
A.2.5.3.	Visualization, Drawing and Analyses of the Structures	127
A.2.5.4.	Bond Valence Energy Landscapes	127
A.3.	Electrochemical Characterizations	127
A.3.1	Electrode Preparation	128
A.3.2	Electrochemical Cells	128
A.3.2.1.	Swagelok Cells	128
A.3.2.2.	<i>In Situ</i> Electrochemical Experiments.....	129
A.3.3	Electrochemical Cycling Tests.....	129
A.4.	Other Physical-Chemical Characterizations.....	130
A.4.1	⁵⁷ Fe Mössbauer Spectroscopy	130
A.4.2	Thermogravimetric Analysis.....	131
A.4.3	Conductivity Measurements	131
A.4.4	DFT Calculations	132
A.4.5	Magnetic Measurements	132
Reference	133

General Introduction

Exhaustion of fossil fuels, peculiar climate changes caused by CO₂ emission and explosion of energy demand with ever-increasing global population call more than ever in the request for innovation in energy technologies. In 2015, COP21 also known as the 2015 Paris Climate Conference, for the first time in over 20 years of United Nations’ negotiations, has achieved a legally binding and universal agreement on climate, with the aim of keeping global warming below 2 °C. Thus, energy obviously stands as the main challenge for our planet over the 21st century.

If we are to combat this challenge, that is, to increase the rate of energy production while decrease CO₂ emission, the development of advanced renewable energy becomes a global imperative. There are several renewable energy sources, for instance, wind, solar, tidal, biomass, and geothermal. It is predicted that the penetration of renewables will double to 54% of world electricity output by 2040 with variable renewable technologies such as wind and solar accounting for 42% of generation — up from 11% in 2015, as it is shown in **Figure 1**. To satisfy rising the global demand, 11.4 trillion dollars will be invested in power plants by 2040, among which renewables will make up 60% of the investment [1].

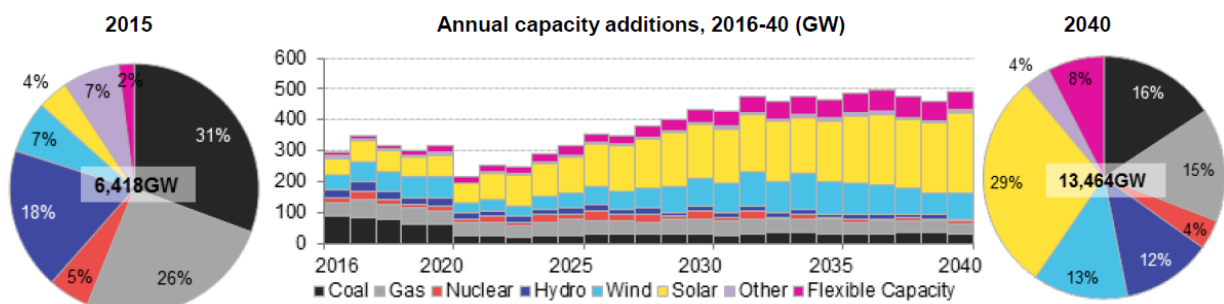


Figure 1: Global installed capacity in 2015 and 2040 and projected capacity additions, by different technologies. The flexible capacity includes power storage, demand responds, and other potential resources (from [1]).

Despite of rich natural resource, the renewable energy sources mentioned above are inherently intermittent and generally dispersed relative to the isolated large-scale facilities that currently supply the vast majority of electrical energy. To make the best use of these energy sources, we need good energy-storage systems. Unfortunately, we currently only have the capacity to store around 1% of the energy consumed worldwide, most of which (98%) through pumped-storage hydroelectricity. Before shifting from a fossil-fuel economy to one based on renewable technologies, there is clearly a pressing need to significantly improve our ability to store energy [2]. One of the best options is making use of chemical and electric energy conversion

through electrochemical devices, such as fuel cells, supercapacitors, and batteries [3]. Batteries, owing to the advantages of wide operation temperature range, flexible choice of chemical system and voltage, variable size and shape, and low cost, have established a starring role in both stationary storage applications (*e.g.* ramp rates control, uninterrupted power supply) and mobile applications (*e.g.* portable electronics, electric and hybrid vehicles).

Among various battery technologies, Li-ion battery is still holding a dominant position when compared to other traditional batteries technologies (*e.g.* lead-acid, nickel-cadmium, nickel-metal hydride) and new technologies (*e.g.* Li-S, Li-air, Al-air, Na/Mg/Ca/Al-ion, and redox-flow systems). The attractiveness of Li-ion battery technology resides in its versatility of a wide coverage of applications requiring dozens of watt-hours (portable electronics), dozens of kilowatt hours (electric vehicles) and tens of megawatt-hours (grid applications), with design capabilities to meet autonomy and power requirements. The electric vehicle (EV) market is particularly deployed recently, as listed in **Figure 2** with a few examples of popular electric cars on the market. However, developing Li-ion batteries to meet different types of society's fluctuating energy needs, as well as bringing environmental benefit, is a formidable challenge especially at the criteria of materials. Electroactive materials with high specific power, energy density, long calendar life, high safety, and low cost are pursued; in addition, environmental sustainable materials which consume less energy and release less CO₂ during production are to be explored (batteries will only begin to have an environmental benefit beyond hundreds of cycles [2]). Thus, this calls for the optimization and revolution of commercial electrode, as well as the creative design of novel materials for Li-ion batteries.



Tesla Model S

Maximum **510** km for one full discharge



Nissan leaf 2017

Maximum **210** km for one full discharge



BMW i3

Maximum **160** km for one full discharge



Renault ZOE 2012

Maximum **210** km for one full discharge



Chevy Spark EV

Maximum **152** km for one full discharge



VW e-Golf

Maximum **134** km for one full discharge



KIA SOUL EV 2015

Maximum **155** km for one full discharge



2016 Ford Focus

Maximum **122** km for one full discharge

Figure 2: Representative electric vehicles available in market or to be launched soon.

The work pertaining to this thesis perfectly agrees with this context, as it targets at designing new polyanionic compounds made from abundant elements which marry rich crystal chemistry and high electrochemical performance via low temperature eco-efficient processes. To achieve this goal, we explored novel sulfate compounds, including a fluorosulfate – LiCuSO_4F , and a new family of oxysulfates with the formulae $\text{Fe}_2\text{O}(\text{SO}_4)_2$, $\text{Li}_2\text{Cu}_2\text{O}(\text{SO}_4)_2$, $\text{Li}_2\text{VO}(\text{SO}_4)_2$. The present manuscript describes the main results obtained through this study.

This thesis is divided into four chapters:

The first chapter begins with giving an insight of the battery research landscape. It introduces the principles of Li-ion battery and the important role the positive electrode plays in the cell; next an overview of the representative families of positive electrode materials is given in terms of the synthesis, structure, and electrochemical performance with a special attention to polyanionic compounds, prior to introducing new fluorosulfates and oxysulfates electrodes for Li-ion batteries which constitute the core of my Ph.D.

In the second chapter, we report the first ordered *triplite* fluorosulfate LiCuSO_4F , and detail its synthesis, solve its structure, and explore its properties. Then we show how such work has been used as scientific platform to discover the copper oxysulfate, $\text{Li}_2\text{CuO}(\text{SO}_4)_2$, a compound that presents attractive electrochemistry, with namely a $\text{Cu}^{3+}/\text{Cu}^{2+}$ redox potential at 4.7 V vs. Li^+/Li^0 .

In chapter III and IV, we further extend our work on oxysulfates to both Fe and V, hence preparing $\text{Fe}_2\text{O}(\text{SO}_4)_2$ and $\text{Li}_2\text{VO}(\text{SO}_4)_2$ phases. For each compound, we report the synthesis, structure, electrochemical performance, and physical properties. Firstly, $\text{Fe}_2\text{O}(\text{SO}_4)_2$, prepared at low temperature from abundant element, delivers a sustained reversible capacity of about 125 mA·h/g at 3.0 V vs. Li^+/Li^0 . In contrast, we show that the capacity of $\text{Li}_2\text{VO}(\text{SO}_4)_2$ is less but its potential is higher. We reveal a redox activity of 4.65 V for the $\text{V}^{5+}/\text{V}^{4+}$ redox couple pertaining to the V=O bonding. This was an impetus to study the Na counterpart — $\text{Na}_2\text{VO}(\text{SO}_4)_2$, which displays a reversible discharge capacity of 60–80 mA·h/g at 4.6 V.

Lastly, we will conclude the thesis by *i*) discovering the advantages and disadvantages of oxysulfate as positive electrode for Li-ion batteries, *ii*) comparing electrochemical performance of various Fe-based sulfate compounds and *iii*) proposing a materials design strategy for future electrode materials development for Li-ion batteries.

Chapter I. State of the Art

To embark on this thesis towards development of positive electrode for next generation of Li-ion battery, the first chapter is targeted at introducing the critical battery technologies and representative families of positive electrode materials in the development of battery. We also show examples of several important polyanionic compounds under intense scrutiny recently, define the challenges of designing next-generation polyanionic compounds, and expose why research is devoted to new fluorosulfates and oxysulfates. Note that the review of the state of the art will not be comprehensively explained here, thus shortages are inevitable.

I.1. Concise Overview of the Main Technologies of Batteries

An electrochemical cell is a device with which electrical energy is converted into chemical energy, or vice versa. There are two types of cells: *electrolytic cells*, in which electric energy is converted into chemical energy (charge), and *galvanic cells*, in which chemical energy is converted into electric energy (discharge). An electrochemical cell is formed by two electrodes, one positive and one negative which have different chemical potentials, separated by an ionically conductive and electronically insulating *electrolyte*, which may be a liquid, a liquid imbibed into a porous matrix, an ionomeric polymer, or a solid. When the electrodes are connected by means of an external circuit, electrochemical reactions take place concomitantly at both sides, with electrons running spontaneously through external circuit and ion transport in the electrolyte to ensure electroneutrality. During discharge an oxidation or anodic reaction occurs at the negative electrode, and a reduction or cathodic reaction occurs at the positive electrode. For rechargeable (secondary) batteries, this process can be reversed during charge* [4-5]. The term “battery” refers to a stack of cells or a single cell. In this electrochemical reactor, the nature of different redox reactions in the electrolyte provides different electrochemical performance. **Figure I.1** shows the schematic operation principle of the electrochemical cell and the energy diagram of an electrochemical cell.

* Even though the negative electrode is in principle an anode during discharge and a cathode during charge, the negative electrode is commonly referred to as an anode in the battery community (*i.e.*, the discharge process is taken as the nominal defining process), and thus the positive electrode is commonly referred to as a cathode.

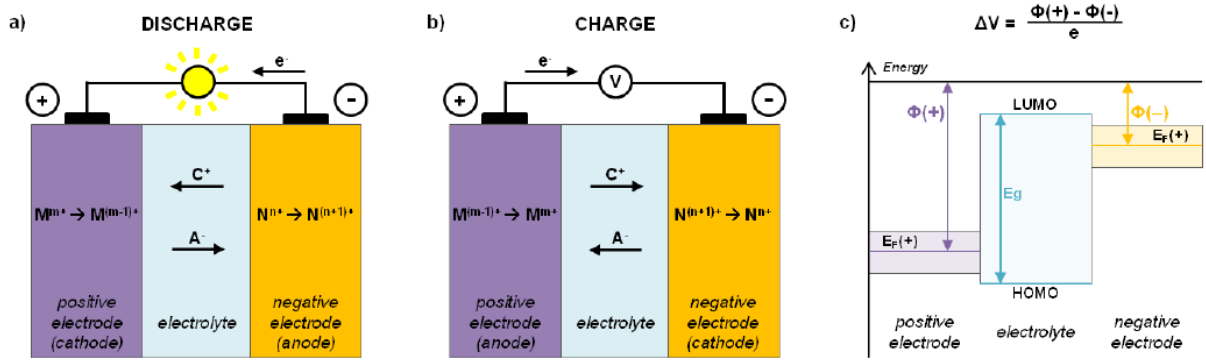


Figure I.1: (a, b) The schematic operation principle of an electrochemical cell on discharge and on charge, respectively. (c) Energy diagram of an electrochemical cell (From [6]).

A historical overview of battery shows us that Li-ion battery technology emerged through the continuous evolution of concepts that previously led to Lead-acid, nickel-cadmium (Ni-Cd), nickel-metal hydride (Ni-MH), Lithium-metal and Li-polymer technologies between 1859 and 1990 (Figure I.2).

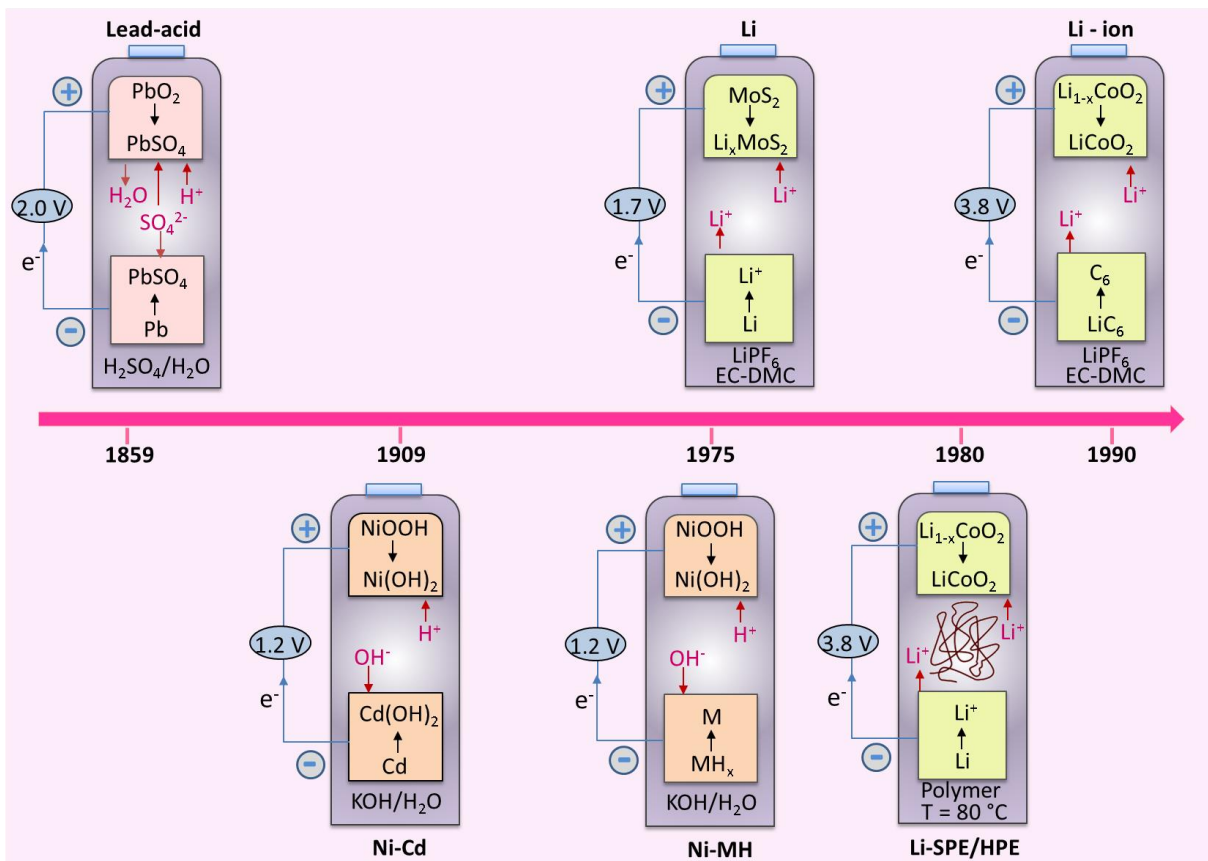


Figure I.2: Battery chemistry evolution over the years until the birth of Li-ion technology (modified from [7]).

The major three criteria to evaluate the performance of a battery includes: the output voltage (expressed in V), the specific capacity (expressed in mA·h/g or A·h/L), the energy density (also known as “specific energy”, it equals to specific capacity multiply by voltage, expressed in W·h/kg or W·h/L) and the electrical power density (also known as “specific power”, expressed in W/kg or W/L). Other characteristics, such as cycle life, safety, cost, volume and shape, as well as sustainability are also pivotal factors that should be taken into account depending on the various aimed applications. For instance, energy density would be the main criterion when choosing a battery for portable or EV/HEV applications. Among all the technologies shown in **Figure I.3**, Li-ion battery is considered to be the most advanced system due to its extremely high volumetric and gravimetric energy density, which is four or even five times than the lead battery (**Figure I.3**).

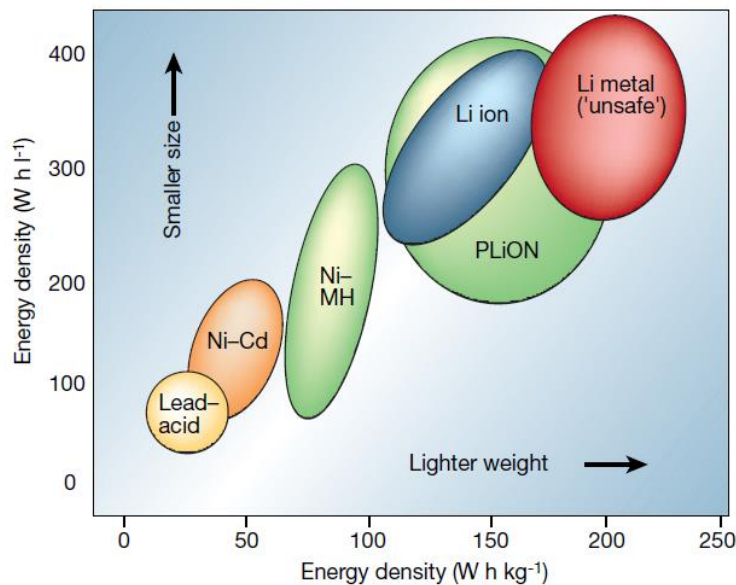


Figure I.3: Comparison of the different battery technologies in terms of volumetric and gravimetric energy density (from [8]).

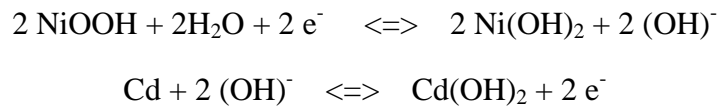
I.1.1. Lead-Acid Batteries

Lead-acid batteries were the first secondary batteries invented by Gaston Planté on 1859 [9], sixty years after the first primary battery proposed by Alessandro Volta [10]. It uses an aqueous electrolyte based on H_2SO_4 which is consumed during discharge due to conversion reactions. These reactions cause the breakage and formation of bonds, $[\text{PbO}_2 \rightarrow \text{PbSO}_4]$ and $[\text{Pb} \rightarrow \text{PbSO}_4]$, at positive and negative electrode, respectively. As the electrolyte also takes part in the reaction, it requires large amount of electrolyte for limiting the concentration change upon discharge to keep acceptable conductivity. The large values of the molar mass of

the species involved in the reactions, and the weight of the current collectors in the lead explain its very low specific energy (25–35 W·h/kg). Although lead also generates environmental contamination problems, the low cost and relative high gravimetric power density makes it attractive for use in automobile SLI (Starting, Lighting and Ignition) systems.

I.1.2. Nickel-Based Technologies

The transition to Nickel-Cadmium (Ni-Cd) accumulators at the beginning 19th century was associated to the one of an electrolyte saturated in potassium hydroxide that does not participate in the electrochemistry of a system. Moreover, this system contains a positive electrode, a layered Ni(OH)₂ which extracts and inserts protons during charge and discharge, respectively. The following reactions take place [11-12]:



By virtue of the toxicity associated with Cd, this technology has evolved with the emergence of Nickel–metal hydride battery (NiMH) on 1980 which relies upon the use of intermetallic alloys with a general formula RM_n (R: rare earth or transition metal; M: transition metal; n = 5, 2 or 1) as the negative electrode, capable of reversibly inserting–extracting 5 H⁺ [13]. Such a NiMH battery delivers an energy density of 80 W·h/kg and has high power rate capability (*i.e.* up to the 2 C rate). They were employed to power hybrid electric vehicles (*e.g.* Toyota Prius, Ford Escape Hybrid) before Li-ion technology appears. Based on this technology, BASF produced a modified microstructure that enables more durable NiMH batteries in 2015, as well as improvement in the cell design which saves considerable weight, leading a gravimetric energy density of ~140 W·h/kg [14].

I.1.3. The First Lithium Batteries

With the merits of being the most electropositive element (*i.e.* -3.04 V versus standard hydrogen electrode), as well as one of the lightest (*i.e.* equivalent weight: 6.94 g/mol; specific gravity: 0.53 g/cm³), Li metal facilitates the design of Li-based storage systems of high energy density. This advantage was first demonstrated in the 1970s with the primary Li cells using Li metal [15]. In 1972, Exxon embarked on a large project which employs TiS₂ as the positive electrode and Li metal as the negative electrode in a lithium-based non-aqueous rechargeable cell [16]. Simultaneously, significant advances in intercalation materials had occurred with the realization at Bell Labs that oxides, besides their early interest for the heavier chalcogenides [17-18], showed the comparable capacity and high voltage. Moreover,

V_6O_{13} eliminated the previously held belief that only low-dimensional materials could result in sufficient ion diffusion, as its framework structure proved to function well [19]. To further enhance the potential, Goodenough proposed Li_xMO_2 ($M = Co, Ni$ or Mn) [20-21], compounds as cathode materials.

The Li-metal battery was marketed in 1985 by Moly-Energy with attractive performances (250 W·h/kg). However, due to the dendritic growth of Li during repetitive cycles which could impale the separator that lead to short circuit, this technology has short-lived. In fact, some of the batteries supplying mobile phones had to be withdrawn by manufacture from the market after explosion in front the ear of their users. To circumvent the safety problem, two strategies were proposed: the Li-ion battery technology which substitute the negative electrode with an insertion compound, and the Lithium-polymer battery technology which replaces liquid electrolyte by a conductive polymeric membrane.

1.1.4. Lithium Ion Batteries

The concept of Lithium ion battery was first demonstrated by Murphy *et al.* [22] and then by Scrosati *et al.* [23], at the end of the 1980s and early 1990s, leading to the “rocking-chair” technology. Substituting lithium metal for Li-ions, the concept resides in that Li^+ ions are rocked back and forth between two intercalation materials (like two “lithium sponges”) during cycles.

Nevertheless, it took almost a decade before the concept of Li-ion could be implemented. To compensate for the increase in potential of the negative electrode by replacing lithium, high-potential insertion compounds are needed for the positive electrode, and emphasis were shifted from the layered-type transition-metal disulphides to layered three-dimensional-type transition-metal oxides [24]. Delays were attributed to the development for the negative electrode (either Li alloys or insertion compounds) and the failure of electrolytes to meet the costs and performance requirements besides safety for a battery technology to succeed. Finally, the discovery of the highly reversible, low-voltage Li intercalation–deintercalation process in carbonaceous material [25] based on previous findings of graphite intercalation compounds (GIC) [26-27], led to the creation of the C/LiCoO₂ rocking-chair cell first commercialized by Sony Corporation in 1991 [28-31], which has evolved over the years. As shown in **Figure I.4**. The negative electrode of Li-ion battery is a graphitic carbon incapable of hosting Li^+ between the layers, whereas the positive electrode is a Li-intercalation compound (*e.g.* LiCoO₂), separated by a non-aqueous electrolyte that transports Li^+ ions between the electrodes. Upon charge, Li ions are extracted from the layered oxide and intercalates into the graphite layers, while on discharge this process is reversed.

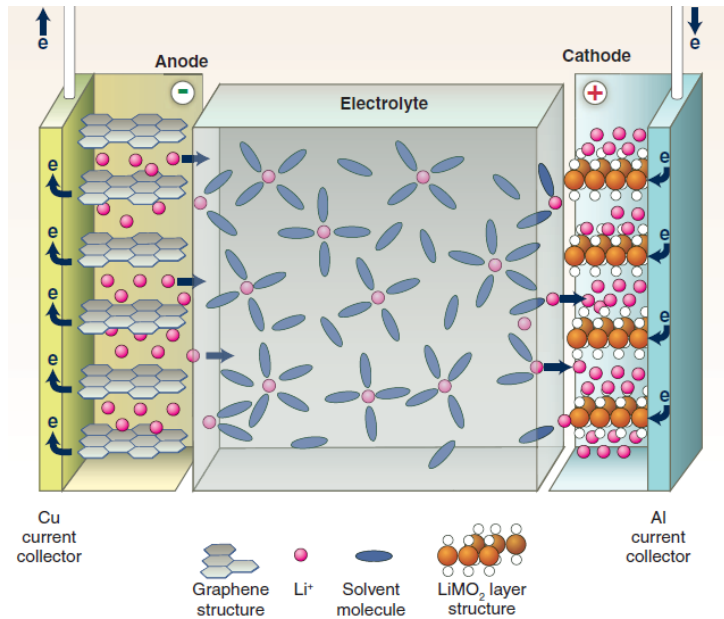


Figure. I.4: Schematic of a Li-ion battery, which uses layered LiCoO_2 and graphite as the positive and negative electrode (from [32]).

Such a Li-ion cell presents a potential exceeding 3.6 V (*i.e.* three times that of alkaline systems) and a gravimetric energy densities as high as 200 W·h/kg (*i.e.* two to three fold those of Ni–Cd batteries). In virtue of such staggering performance, Li-ion batteries are widely used in today’s portable electronic devices. Thanks to the presence of Li in its ionic rather than metallic state, Li-ion cells solve the dendrite problem and are, in principle, inherently safer than Li-metal cells.

I.1.5. Lithium Polymer Batteries

Parallel to the research on Li-ion battery technology, the concept of Lithium Solid-Polymer Electrolyte (Li-SPE) battery (also known as Lithium-metal polymer battery) was firstly introduced by M. Armand on 1979 using a polymer separator (*i.e.* lithium tri-fluoro-sulfonyl imide in poly-ethylene oxide, PEO-LiTFSI) [33–35]. Separator acts both as solvating medium and mechanical separator between two electrodes. Such technology was initially developed by Hydro-Québec in the 1980s, which was taken over by Bolloré 30 years later to the realization of its first battery commercialization (Li-metal anode // Li-salt in PEO // LiFePO_4 cathode). Today, it supplies the “Blue Car” which crosses Paris as part of the urban project “Autolib”. This technology is commercially available for stationary applications which require moderate energy storage and specific power, whereas is hardly transferable to portable devices, owing to the low room temperature conductivities of solid electrolyte as compared to liquid

electrolyte. To compensate for this weak conductivity the electrolyte has to be made in thin film and the cell has to operate at relatively high temperatures (60-90 °C).

Shortly after this, Li hybrid polymer electrolyte (Li-HPE) battery [36-38] emerged with the hope to benefit from the advantages of polymer electrolyte technology without the hazards related to the usage of Li metal. The term “Hybrid” describes three components included in the electrolyte: a polymer matrix swollen with liquid solvent and a salt. Companies such as Valence and Danionics were involved in developing such polymer batteries, but HPE systems never materialized at the industrial scale because Li-metal dendrites was still a safety issue.

Therefore, Bellcore researchers introduced polymeric electrolytes in a liquid Li-ion system and developed the first reliable and practical rechargeable Li-ion HPE battery [38-42], called plastic Li ion (PLiON), which differs considerably from the usual coin-, cylindrical- or prismatic-type cell configurations (**Figure I.5**). Such a thin-film battery technology offers shape versatility, flexibility and lightness. It has been developed commercially since 1999 and has facilitated the trend towards electronic miniaturization. Confusingly called Li-ion polymer batteries, these new cells use a gel-coated, microporous poly-olefin separator bonded to the electrodes (also gel-laden), rather than the (PVDF-HFP)-based membrane used in the plastic Li-ion cells. In spite of several advantages, lithium-polymer battery technology still needs some time to go to the mainstream because of performance issues at room temperature.

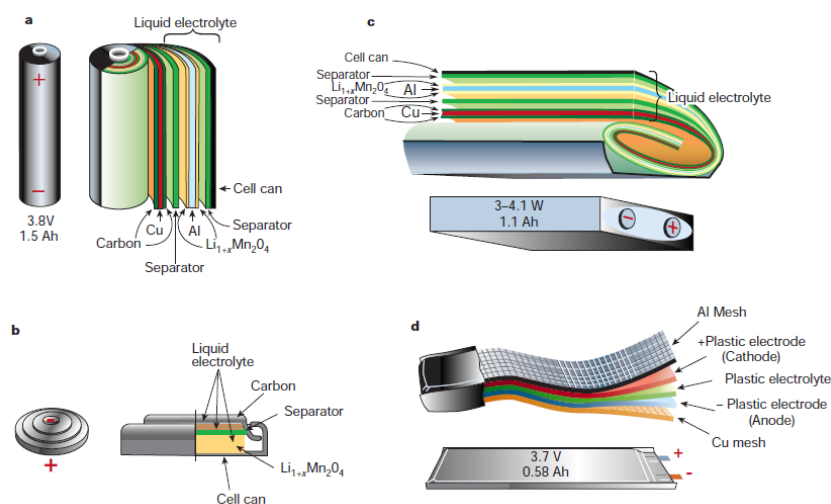


Figure I.5: Schematic drawing showing the shape and components of various Li-ion battery configurations: (a) Cylindrical; (b) Coin; (c) Prismatic; and (d) Thin and flat. Note the unique flexibility of the thin and flat plastic LiION configuration in contrast to the other configurations, the PLiON technology does not contain free electrolyte (From [8]).

Having retraced almost 30 years of scientific venture leading to the development of the rechargeable Li-ion battery, this thesis will focus on Li-ion battery.

I.2. Positive Electrode Materials for Li-ion Batteries

Positive electrodes (also termed “cathodes”) for Li-ion and lithium batteries have been under intense scrutiny since the advent of the Li-ion cell in 1991. Early on, the energy density delivered by Li-ion batteries, based on carbonaceous negative electrode, is mainly controlled by the voltage and capacity of the positive electrode materials; on the other hand, major developments in negative electrode materials with the introduction of nanocomposite Sn/C/Co alloys and Si-C composites also demanded positive electrodes with higher capacity to match. Cost, thermal stability, and cycle life are also closely related to positive electrode material.

Positive electrode materials present a rich and versatile chemistry towards Li. Two main types of cathode materials do exist, those dealing with Li insertion/extraction reactions (*e.g.* LiCoO_2) and those leading to conversion reactions (*i.e.* metal oxides) (**Figure I.6**).

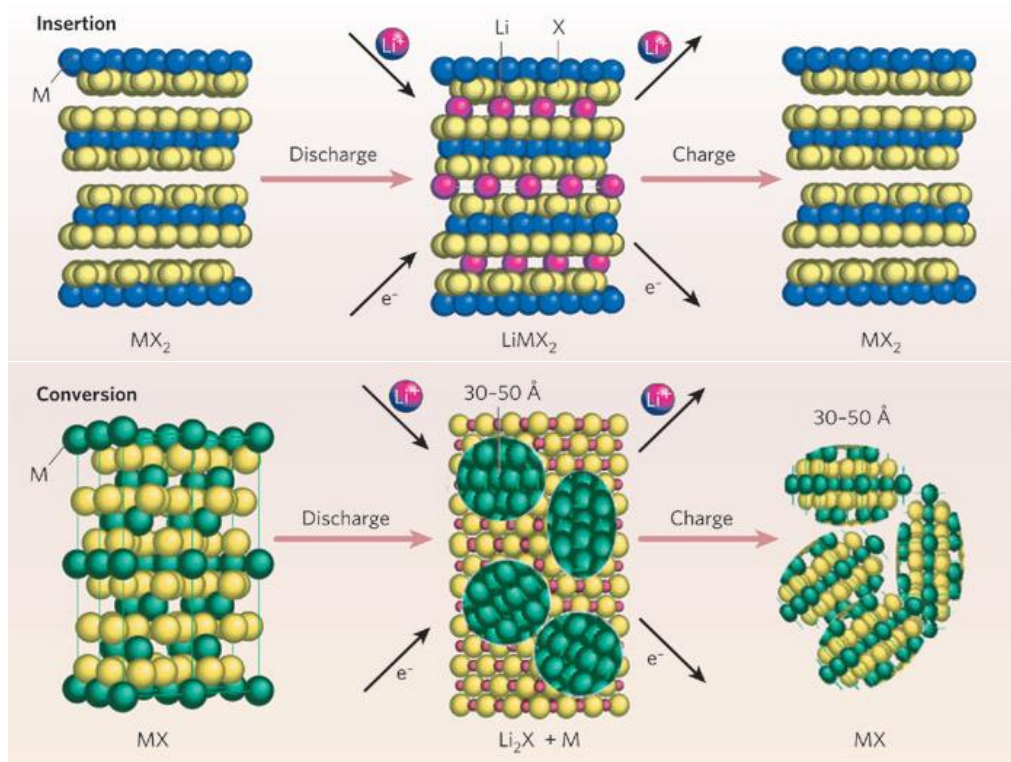


Figure I.6: Schematic representation showing the different reaction mechanisms occurring during discharge for (top) Insertion and (bottom) Conversion reactions (From [7]).

An intercalation cathode is a solid host network, in which guest (here is Li^+) ions can be inserted into and be removed from the host network reversibly. The host network compounds are metal chalcogenides, transition metal oxides, and polyanionic compounds. These intercalation compounds can be divided into several crystal structures, such as *layered*, *spinel*,

olivine, and *tavorite* [20, 43-45]. On the other hand, conversion electrodes undergo changes in crystalline structure that accompanied by the repeated breaking and forming of chemical bonds (i.e. $M_xO_y + 2ye^- + 2yLi^+ \rightleftharpoons xM^0 + yLi_2O$). Compared to intercalation cathode, conversion cathode can transfer multi electrons per reaction which thus provides huge capacity. However this mechanism usually comes with large voltage difference between charge and discharge which results in poor energy efficiency. At this stage, it is beyond the scope of this chapter to provide an exhaustive review of all the positive materials. For that purpose, several reviews are available [7-8, 46-51]. Thus we purposely limit our description to intercalation cathode materials: lithium metal oxides, classic polyanionic compounds - lithium metal phosphates, and title compounds of this thesis - sulfate based compounds.

I.2.1. Lithium Transition-Metal Oxides

I.2.1.1. $LiMO_2$ ($M = Co, Ni, Mn$) Layered Compounds

$LiCoO_2$, firstly reported by Goodenough *et al.* [24], had initialized the commercialization of Li-ion battery in 1991. This compound was synthesized through a conventional solid state reaction and adopts the α - $NaFeO_2$ structure (Figure I.7) with consecutive alternating CoO_2 and Li layers. Both Co and Li atoms are octahedrally coordinated, Co^{3+} resides in the $3a$ site, and Li^+ in the $3b$ site in the $R\bar{3}m$ *ccp* packed O^{2-} lattice. A typical charge/discharge curve for a $Li||Li_xCoO_2$ cell is shown in Figure I.8. The reaction mechanism of Li_xCoO_2 during Li extraction can be summarized as follows (Figure I.7): upon increasing the amount of removed Li, the O3 structure (close-packed oxygen layers with an ABCABC stacking sequence) evolves towards an O1 structure at $x \approx 0.5$ while showing an expansion of the interlayer c axis as a result of electrostatic repulsion of the oxygen layers $x \leq 0.5$ [52-53]. Further delithiation results in the generation of a hybrid host structure that enlists both the O3 and O1 stacking sequences known as the H1-3 structure ($x \approx 0.1-0.2$) [54-55]. Ultimately, a transformation of the O3 $LiCoO_2$ phase into a stable O1 Li_xCoO_2 phase (ABAB stacking sequence) occurs at $x \approx 0.05$ [53, 56]. This stable structure often mixes with the metastable rhombohedral P3 at $x \approx 0$ via differences in chemical or electrochemical processes involved charge compensation from oxygen sites to cobalt sites in the mixed valence state, Co^{4+}/Co^{3+} [56-59]. In the terms of “On” and “Pn” ($n = 1, 2, 3, etc.$), P or O describes the type of alkali coordination (prismatic or octahedral) and the number n indicates the number of sodium layers per unit cell.

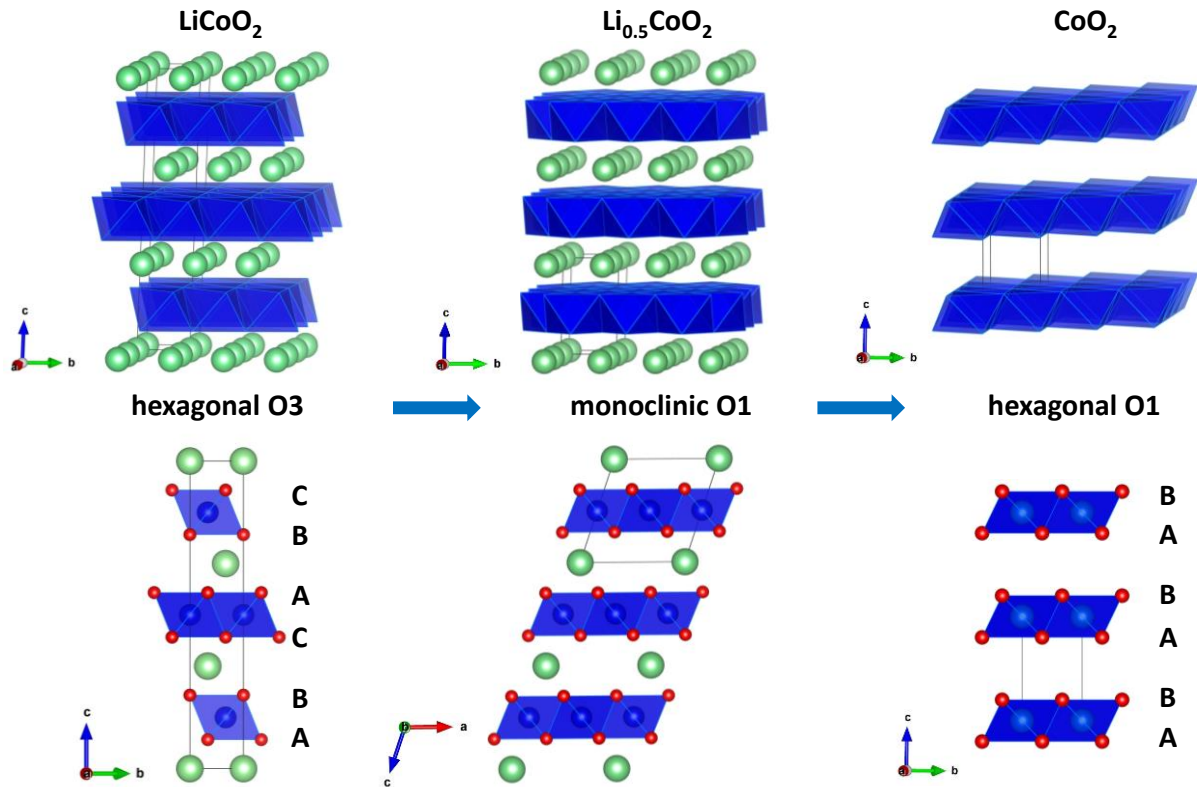


Figure I.7: Schematic diagram of phase transition during delithiation process from O3-LiCoO₂. The CoO₆ octahedrons are shown in blue, oxygen atoms are shown in red, and green spheres represent lithium ions.

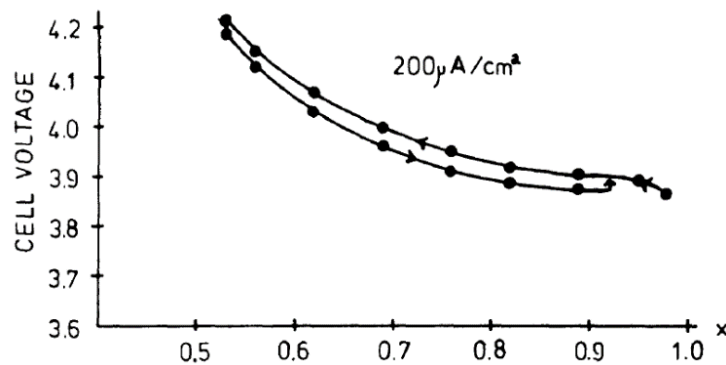


Figure I.8 Typical charge/discharge curve obtained for a Li₂CoO₂||Li cell (from [20]).

LiCoO₂ is an attractive cathode material in terms of its relatively high theoretical specific capacity of 274 mA·h/g, high theoretical volumetric capacity of 1363 mA·h/cm³, and high discharge voltage of 4.2 V vs. Li⁺/Li⁰ [47, 48]. However, only a little over half of the capacity is practically reversible in delithiation/lithiation process. Capacity fading is severe upon extraction of > 0.7 Li due to *i*) the loss of oxygen (resulting from the reduced stability of lithium poor phases) [60], *ii*) the electrolyte decomposition [61-62], and *iii*) the cobalt dissolution [63] in typical electrolytes. Yet, LiCoO₂ has been used as commercial positive

materials for years. Limitation of this material resides in the high cost, low thermal stability, and non-negligible capacity fade at high current rates or during deep cycling.

Following the commercialization of LiCoO_2 , research on alternative layered oxides LiMO_2 ($M = \text{Mn}$ or Ni) was pursued. Isostructural to LiCoO_2 and with a similar theoretical specific capacity (275 mA·h/g), the relatively lower cost and environmentally friendliness (**Table I.1**) drives research on LiNiO_2 [64-66]. LiNiO_2 delivers higher reversible capacity (*i.e.* 200 mA·h/g) [65-66]; However, the spontaneous reduction of Ni^{3+} to Ni^{2+} during synthesis leads the formation of $\text{Li}_{1-z}\text{Ni}_{1+z}\text{O}_2$ compounds, with the $z\text{Ni}^{2+}$ excess being located in the Li Layers, thus blocking the Li diffusion pathways which is detrimental for cell performances [67-71]. Additionally, the stability of LiNiO_2 is lower than the one of LiCoO_2 because Ni^{3+} is more readily reduced [72], the position of the $\text{Ni}^{4+}/\text{Ni}^{3+}$ couple in LiNiO_2 can result in preferential oxidation of the lattice oxide ions and hence release O_2 upon charging of the electrode, with concomitant safety issues. Thus this material could not compete with LiCoO_2 .

Table I.1: Natural abundance, price and indicators of toxicity for cobalt, nickel, iron, manganese, vanadium, and copper elements (figures are taken from [51, 73]).

	Co	Ni	Fe	Mn	V	Cu
Abundance in Earth crust	2.9×10^{-5}	9.9×10^{-5}	6.2×10^{-2}	6.2×10^{-3}	1.36×10^{-4}	6.8×10^{-5}
5 Year Price Rang (USD Ib ⁻¹)	10-25	5-15	0.1-0.25	1-2	10-20	1-5
BGS (British Geological Survey) Relative supply risk index in 2015	8.1	5.7	5.2	5.7	8.6	4.8

With the scope of finding attractive materials from economic and environmental point of view, cathodes based on elements such as Mn or Fe are desirable (**Table I.1**). However, in spite of numerous investigations on the polymorphs of LiFeO_2 , none of them was found to be successful. Layered LiMnO_2 has been deeply investigated. However, the layered LiMnO_2 could not be synthesized via conventional solid state process as the preparation of layered Co or Ni analogues. To bypass this issue reactions have ion exchanged the Na in the thermodynamically stable layered NaMnO_2 for Li to prepare the desired metastable Li-based analogue phase [74-75]. Moreover, the cycling performance of LiMnO_2 was still not satisfactory because *i*) the layered structure tends to transform to *spinel* structure during Li ion extraction [76] and *ii*) Mn leaches out of LiMnO_2 during cycling [77].

I.2.1.2. Binary $\text{Li}(M, M')\text{O}_2$ and Ternary $\text{Li}[M, M', M'']\text{O}_2$

To resolve the problems fascinating to layered oxides, a huge amount of studies have constituted in partially substituted binary or ternary 3d metal layered oxide. Noticeable progresses include $\text{LiMn}_x\text{Ni}_{1-x}\text{O}_2$ (in particular with $x = 0.5$) [33, 78-90], $\text{LiNi}_{1-x-y}\text{Mn}_x\text{Co}_y\text{O}_2$ (in particular with $x = y = 1/3$, named NMC) [91-96], and $\text{LiNi}_{1-x-y}\text{Co}_x\text{Al}_y\text{O}_2$ (in particular the composition $x = 0.15$ & $y = 0.05$, and composition $x = 0.10$ & $y = 0.09$, called NCA) [97-101]. In these compounds, the Co^{3+} helps to increase the electronic conductivity and ensure the layered structure; the small amount of nickel found in the lithium layer contributes to stabilizing the structure without being detrimental for the lithium diffusion, while inert cations (Al^{3+} , Mn^{4+}) prevent the full delithiation and thus the collapse of the structure to enhance both electrode stability at high voltage and its cycling life. Metal substitution in these layered compounds lead to electrode material with high reversible capacities and long storage calendar life. NMC (*ca.* > 200 mA·h/g) and NCA (*ca.* \approx 200 mA·h/g) cathodes, which are relatively widespread commercial use in batteries for EVs/HEVs, for example, NMC has been used on Ford, Volkswagen, Audi, Honda, while NCA has been used on Tesla and Toyota.

I.2.1.3. Li-Rich Compounds

Another promising lithium metal oxide cathode is called Li-rich compounds, whose structure derives from that of parent lamellar LiMO_2 by considering a progressive substitution of excess Li^+ for M^{3+} in the $[\text{MO}_2]$ layers (Figure I.9). Li-rich compound can be viewed as a composite with the formula $[x \text{Li}_2\text{MnO}_3] \cdot [3(1-x) \text{LiMO}_2]$, consisting of layered compounds such as $\text{LiMn}_{0.5}\text{Ni}_{0.5}\text{O}_2$ [102-106] and $\text{LiCo}_{1/3}\text{Ni}_{1/3}\text{Mn}_{1/3}\text{O}_2$ [107-108], with layered *rocksalt* Li_2MnO_3 phase. Li_2MnO_3 (*i.e.* $\text{Li}[\text{Li}_{1/3}\text{Mn}_{2/3}]\text{O}_2$) presents a layered monoclinic, $C2/m$ structure with cation ordering, $1/4$ of the lithium atoms of Li_2MnO_3 lies in the transition metal sheet (Figure I.10).

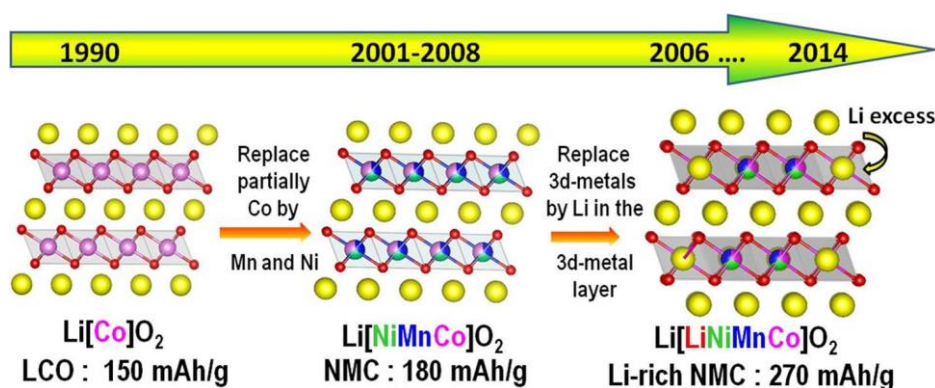


Figure I.9. Chronological evolution of the layered oxide LiCoO_2 chemistry fueled by cationic substitution within the metal layers with partial replacement of Co with Ni and Mn (NMC phase) within the metal layer (purple) and with Li (yellow) to form Li-rich NMC phases (From [109]).

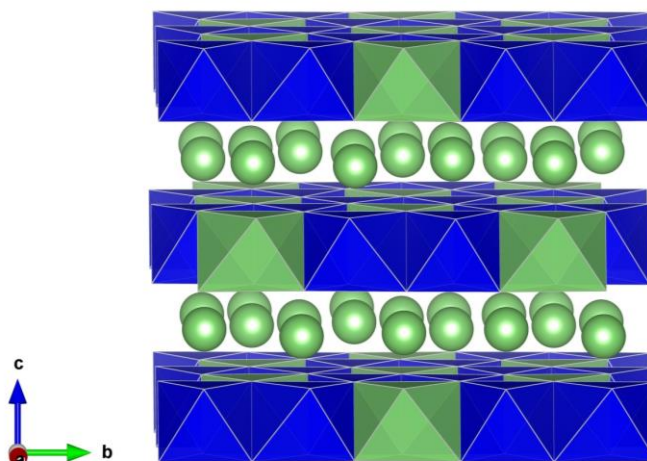


Figure I.10 Structure of Li_2MnO_3 (monoclinic, $C2/m$). MnO_6 and LiO_6 octahedra in the transition metal layer are displayed in blue and green, respectively. Li cations in the lithium layer are shown as green balls.

Lithium-rich layered oxides exhibit high capacities after activation process. For example, $0.3\text{Li}_2\text{MnO}_3 \cdot 0.7\text{LiMn}_{0.5}\text{Ni}_{0.5}\text{O}_2$ can deliver a reversible discharge capacity as high as $287 \text{ mA}\cdot\text{h/g}$ [103]. Its high energy density draws worldwide attention for the next generation of Li-ion batteries. However, numerous ambiguities remain concerning the chemical nature of the compounds, as well as the understanding of the exact oxidation/reduction mechanisms. The capacity of Li-rich compounds exceeds the one calculated considering the exchange of 1 electron per TM, and their voltage decays upon cycling. The scenarios for the origin of the extra capacity and voltage decay had been very controversial. In 2012 Tarascon's group prepared new $\text{Li}_2\text{Ru}_{1-y}\text{Sn}_y\text{O}_3$ phases by replacing 3d element with 4d (Ru and Sn) metals. These phases exhibit similar capacities of $280 \text{ mA}\cdot\text{h/g}$ as Li-rich NMC, but do not present the undesirable potential fading upon cycling [110]. The extra-capacity has been demonstrated as due to cumulative cationic ($M^{n+} \leftrightarrow M^{(n+1)+}$) and anionic ($\text{O}^{2-} \leftrightarrow \text{O}_2^{2-}$) reversible redox processes [110-114], while the voltage decay in Li-rich NMC is mainly nested in ionic radii considerations and size bottleneck issues [115].

The humongous amounts of research within last 25 years dedicated to the layered oxides have witnessed a progression in the materials capacities and passed from $140 \text{ mA}\cdot\text{h/g}$ for LiCoO_2 to $200 \text{ mA}\cdot\text{h/g}$ and $>250 \text{ mA}\cdot\text{h/g}$ for Li-NMC and Li-rich NMC phases respectively through chemical substitution. To sum up, the layered oxides are attractive due to their fully developed synthetic routes, high capacity and ability to facile processing, however they suffer from oxygen evolution at high charging potential and cause serious safety issues.

I.2.1.4. Spinel

In parallel to layered oxides, *spinel* (named after mineral MgAl_2O_4) LiMn_2O_4 has been envisaged and developed in the 1980s and 1990s [21, 43]. In this structure, Li occupies tetrahedral $8a$ sites and Mn is located in octahedral $16d$ sites of space group $\text{Fd}3\text{m}$, with a *ccp* array of oxygen anions (Figure I.11 a). Li^+ can diffuse through vacant tetrahedral and octahedral interstitial sites in the three-dimensional structure. Typical charge/discharge curve of a $\text{Li} \parallel \text{Li}_x\text{Mn}_2\text{O}_4$ cell is shown in Figure I.11 b. With half of the manganese in the oxidation state +3 and the other half in the oxidation state +4. This amphoteric compound can be either oxidized to $\lambda\text{-MnO}_2$ with a potential centered ~ 4.1 V vs. Li^+/Li^0 , or reduced to $\text{Li}_2\text{Mn}_2\text{O}_4$ with a plateau at ~ 3 V vs. Li^+/Li^0 . In Li-ion batteries, only the upper plateau that corresponds to a capacity of 148 mA·h/g can be used highly reversible and at high potential.

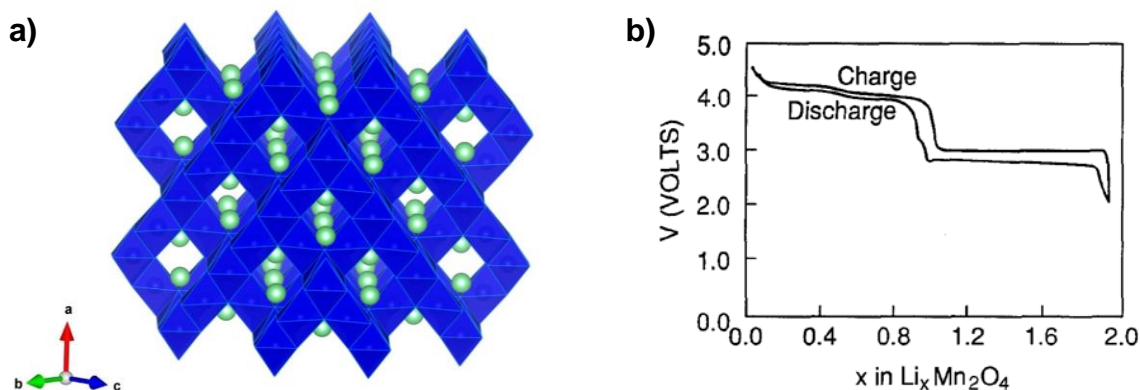


Figure I.11 (a) Structure of the *spinel* LiMn_2O_4 . MnO_6 octahedra are displayed in purple and lithium atoms are represented as green balls. (b) Typical charge/discharge curve of a $\text{Li}_x\text{Mn}_2\text{O}_4 \parallel \text{Li}$ cell (from [116]).

In spite of a slightly lower capacity to that of layered oxides, *Spinel* LiMn_2O_4 presents a high voltage and a good rate capability, which has been considered as a material of choice for high-power applications for long time. However, LiMn_2O_4 cathodes have been plagued by capacity fade, especially at elevated temperatures (> 50 °C). Several mechanisms, such as Mn dissolution in the electrolyte [118]; loss of crystallinity [119]; development of microstrain due to lattice mismatch between two distinct cubic phases formed on cycling [120]; and formation of the $\text{Li}_2[\text{Mn}_2]\text{O}_4$ phase at the surface especially at fast c-rates [121] have all been suggested to be the source of the capacity fade. By using nanoparticles, the rate performance can be greatly improved due to shorter Li^+ diffusion lengths and improved electronic transport [122-125], but this is to the expense of an increase in second reaction.

I.2.2. Polyanionic Compounds

Besides oxides, a class of material called polyanionic compounds, which reunites the strong covalent bonding of tetrahedral polyanion units $(XO_4)^{n-}$ with MO_x (M = transition metal) polyhedra have become a subject of intensive research during the past 20 years. Compared to the layered oxides, the advantage of polyanionic cathode materials resides in:

- Higher thermal stability due to the strong covalently bonded oxygen atoms in MO_x (M = transition metal) polyhedral, by virtue of better safety properties.
- Higher redox potentials than oxides (due to the inductive effect, which will be discussed hereafter) for a given $M^{n+}/M^{(n-1)+}$ redox couple.
- Exhibit a large variety of crystal structures, with great versatility towards cation and anion substitutions for a given structural type.
- The possibility to monitor the potential of a given $M^{n+}/M^{(n-1)+}$ redox couple vs. Li^+/Li^0 in the same structure by just changing the nature of M , or the polyanionic $(XO_4)^{n-}$.

However, it is noteworthy that polyanionic compounds suffer from two main drawbacks: *i*) limited gravimetric capacities because of the weight penalty arising from the heavy polyanionic groups, and *ii*) poor intrinsic electronic conductivities due to the isolation of the various polyhedrons.

Giving an exhaustive list of the various families of polyanionic compounds (M = Fe, Mn, Co, Ni, V, Ti, *etc.*) as electrode materials is out of the aim of this work. The reader is invited to consult various review papers [47-50, 126-128] for a wider outline of the different polyanionic compounds that have already been explored as electrode materials for Li-ion batteries. We rather like to focused on a few representative polyanionic compounds with promising electrochemical performance, namely on sulfated-based ($X = S$) polyanionic compounds which are the subjects of the thesis so as to better put our work in perspective to explore new sulfates, fluorosulfates and oxysulfates.

I.2.2.1. The NASICON and Anti-NASICON Compounds

The NASICON compounds which by no doubt have set up a foundation for the research of polyanionic compounds are introduced first.

NASICON (Sodium (Na) Super (S) Ionic (I) Conductor (CON)) compounds have been the object of immense research effort in the 1970s as solid electrolytes for Na/S batteries, since Hong and Goodenough [129-130] proposed a framework structure with suitable tunnel size

for Na^+ migration in three dimensions of $\text{Na}_{1+x}\text{Zr}_2\text{P}_{3-x}\text{Si}_x\text{O}_{12}$ ($0 \leq x \leq 3$) solid solution [131]. These compounds ($\text{Na}_{1+x}\text{Zr}_2\text{P}_{3-x}\text{Si}_x\text{O}_{12}$) prove that three-dimensional structures can provide high ionic conductivity properties comparable to the ones of layered two-dimensional β'' -alumina ($\text{Na}_2\text{O} \cdot 11\text{Al}_2\text{O}_3$) [132-133]. Subsequently, Goodenough al. [129-130] clearly identified and listed the chemical and structural features responsible for this fast ionic conduction character as follows: *i*) the need to have flexible three-dimensional structures with highly covalent bonds generating large interstitial spaces that may accommodate any changes at a concentration gradient of the alkali metal ions, *ii*) Weak framework-alkali cations interactions, and electrostatic repulsion between neighboring alkali cations must be sufficiently low to enable the rapid spread of alkali cations, and *iii*) three-dimensional network of interconnected conduction pathways.

Structure wise, the NASICON structure is of the general formula $A_aM_2(\text{XO}_4)_3$, where $A = \text{Li}, \text{Na}$, $a \leq 5$, $M =$ transition metal and $X = \text{Mo}, \text{W}, \text{P}, \text{S}, \text{Si}$, etc. They crystallize into two different structures, named NASICON and anti-NASICON (Figure I.12). The basic $M_2(\text{XO}_4)_3$ repeating unit, made of two MO_6 octahedra connected to three XO_4 tetrahedra, has the shape of a “lantern”. In the NASICON structure, these lanterns are stacked parallel to each other, while in the anti-NASICON framework they are alternatively oriented in two different directions, which are almost perpendicular one to another (Figure I.12). The latter anti-NASICON structure is thus less open than the NASICON one, hence less favorable for alkali ion transport. One should note for NASICON and anti-NASICON structure, the interconnection between octahedra and tetrahedra facilitates fast ion conduction, but suffers quite poor intrinsic electronic conductivity: no direct $\cdots\text{M}-\text{O}-\text{M}\cdots$ electronic delocalization is possible as the MO_6 octahedra are isolated from each other and separated by the XO_4 groups.

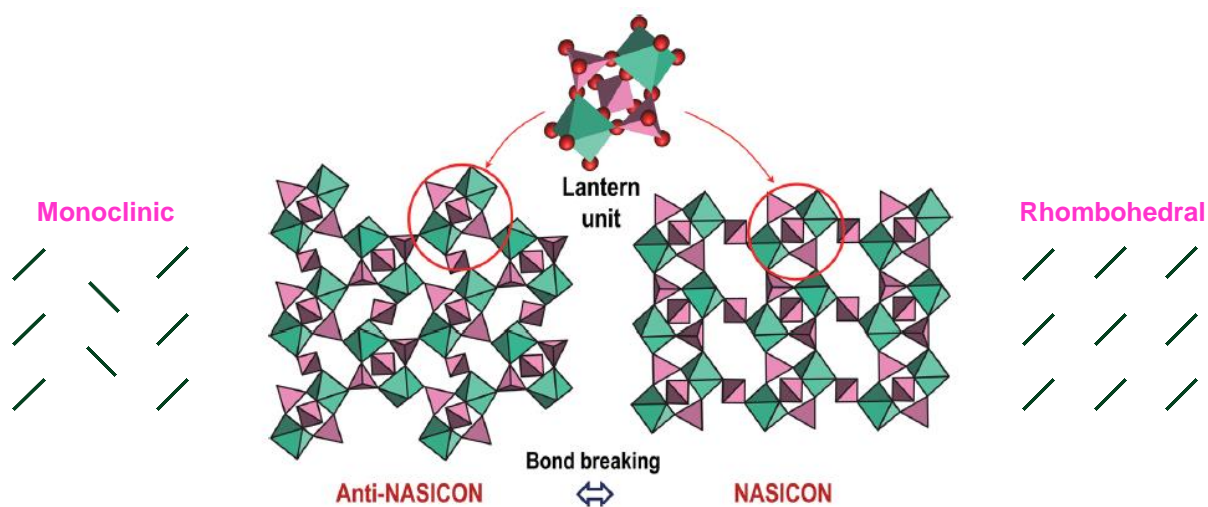


Figure I.12: NASICON (rhombohedral) and anti-NASICON (monoclinic) frameworks of general formula $A_xM_2(\text{XO}_4)_3$ (adapted from [49]).

Besides to be used as solid state electrolyte, the NASICON phases were investigated to be used as positive electrode materials for Li-ion and Na-ion batteries. In 1980s, the groups of Torardi and Delmas were the first to demonstrate the feasibility of reversible alkali (Li and Na) insertion into the NASICON phases $\text{Fe}_2(\text{MoO}_4)_3$ [134-135] and $(\text{Li,Na})\text{Ti}_2(\text{PO}_4)_3$ [136-137], respectively. Goodenough *et al.* immediately extended this study to other NASICON $\text{Li}_x\text{M}_2(\text{XO}_4)_3$ compounds [138-142] by playing on M and X composition. They showed the evolution of different potentials of $M^{n+}/M^{(n-1)+}$ vs. Li^+/Li^0 with varying M metal in phosphates of NASICON structure (Figure I.13 a) [141]; and they envisaged the possibility of tuning and monitoring the properties of these electrodes through polyanion $(\text{XO}_4)^{n-}$ substitutions in Fe-based 3D structures (Figure I.13 b) [142]: the inductive effect engendered by the polyanion has a direct impact on the potential $\text{Fe}^{3+}/\text{Fe}^{2+}$ redox couple vs. Li^+/Li^0 in a given structural type.

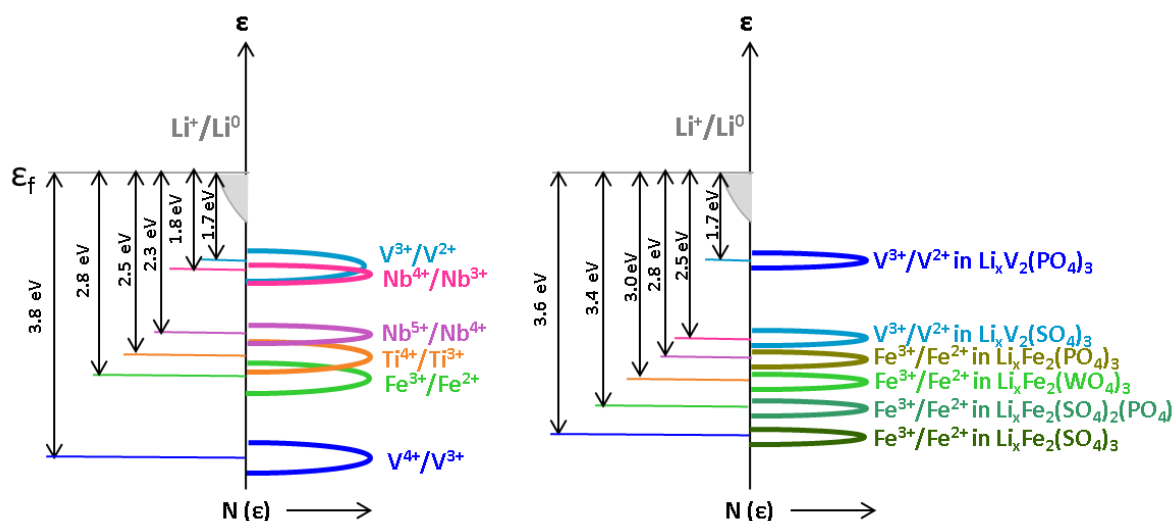


Figure I.13: (a) Relative energies of redox $M^{n+}/M^{(n-1)+}$ couples for different transition metals isostructural in NASICON framework (from [141]). (b) Influence of the nature of the polyanion $(\text{X}_m\text{O}_{3m+1})^{n-}$ on these redox energies (adapted from [142]).

Inductive effect had been used by Goodenough to explain qualitatively the respective positions of the $M^{n+}/M^{(n-1)+}$: the strong covalent bonding within the polyanionic group XO_4 adjacent to the redox center M induces a polarization of the $M\text{--O}$ bond (Figure I.14), which stabilizes the transition metal redox couple (*i.e.* it lowers the redox energy and raises the redox potential) [44, 139, 142]. Thus, the more electronegative X is, the weaker the $M\text{--O}$ bond, and the higher the potential of the $M^{n+}/M^{(n-1)+}$ redox couple.

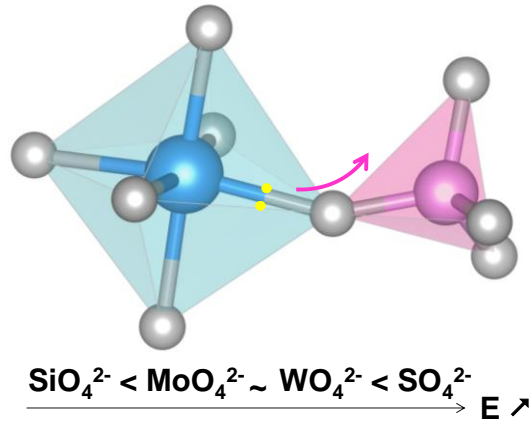


Figure I.14: Schematic representation of the inductive effect.

Therefore NASICON framework demonstrate chemist various possibilities to elaborate electrode materials functioning at controlled operating voltages. The most investigated anti-NASICON composition is $\text{Li}_3\text{V}_2(\text{PO}_4)_3$, the crystal structure of which has been determined by Huang [143-144]. Lithium ions fully occupy three crystallographic sites as $\text{Li}_3\text{Fe}_2(\text{PO}_4)_3$ [145-146] and anisotropic thermal motion factors suggest a favored two-dimensional ion transport. $\text{Li}_3\text{V}_2(\text{PO}_4)_3$ can be electrochemically oxidized at potentials ranging from 3.4 to 4.6 V vs. Li^+/Li^0 [90, 143-144, 147-157], shows a series of four successive phase transitions upon Li extraction toward $\text{Li}_{0.1}\text{V}_2(\text{PO}_4)_3$ with a corresponding high capacity of 197 mA·h/g (**Figure I. 15**) that relies on both $\text{V}^{4+}/\text{V}^{3+}$ and $\text{V}^{5+}/\text{V}^{4+}$ redox couples. (It stands as an example that the valence $n+$ of M^{n+} can help to realize multiple electron transfer so as to improve the capacity of electrode).

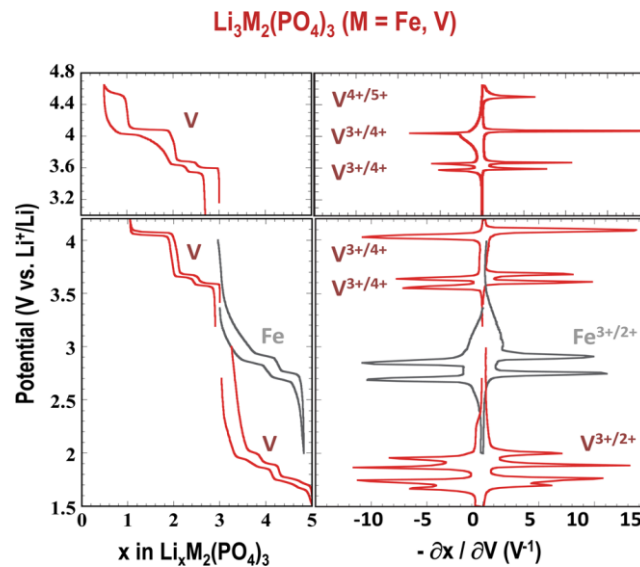


Figure I.15: Galvanostatic Li^+ insertion/extraction and respective redox couples in anti-NASICON $\text{Li}_x\text{M}_2(\text{PO}_4)_3$ (M = Fe, V) compositions (from [49]).

Structurally highly reversible on cycling [151], with excellent power capability data and cycling efficiency after optimized [157], $\text{Li}_3\text{V}_2(\text{PO}_4)_3$ will stand as a promising positive electrode for Li-rechargeable batteries once possible vanadium dissolution in the electrolyte and reactivity with the electrolyte at potentials as high as 4.6 V vs. Li^+/Li^0 have been circumvented. The iron analog $\text{Li}_3\text{Fe}_2(\text{PO}_4)_3$ delivers a reversible capacity of ~ 115 mA·h/g at the rate of C/10 at relatively low voltage at 2.88 and 2.73 V vs. Li^+/Li^0 [144, 158-159]. Therefore this compound cannot be directly used as electrode for commercial Li-ion battery since it cannot be oxidized with the Fe being +3 state in the pristine material.

I.2.2.2. Olivine LiMPO_4 (M = Fe, Mn, Co, Ni) Family

The application of Fe-based compounds as a cathode for lithium batteries includes many advantages in terms of environment (abundance, toxicity) and of thermal stability. However, the iron-based oxides containing O^{2-} as the anion suffer problems for the cathode designer, as in these oxides the $\text{Fe}^{4+}/\text{Fe}^{3+}$ redox energy tends to lie too far below the Fermi energy of a lithium anode and therefore not reachable while the $\text{Fe}^{3+}/\text{Fe}^{2+}$ couple lies too close to it, leading to low potential. In LiFePO_4 the strong covalent bonding within the $(\text{PO}_4)^{3-}$ polyanion actually increases the ionic character of the Fe-O bonding, thus modifies the $\text{Fe}^{3+}/\text{Fe}^{2+}$ couple redox voltage to a suitable level. Since the first report in 1997 by Goodenough *et al.* [44, 160], LiFePO_4 has quickly become one of the most attractive cathode materials in creating an increasing interest for searching for new polyanionic compounds for Li-ion batteries. LiFePO_4 , which is a mineral named *triphylite*, adopts an *olivine* Mg_2SiO_4 crystal structure, built on distorted oxygen hexagonal packing into which Li^+ and Fe^{2+} occupy one-half of the octahedral sites and P occupies 1/8 of the tetrahedral sites (Figure I.16). It crystallizes in an

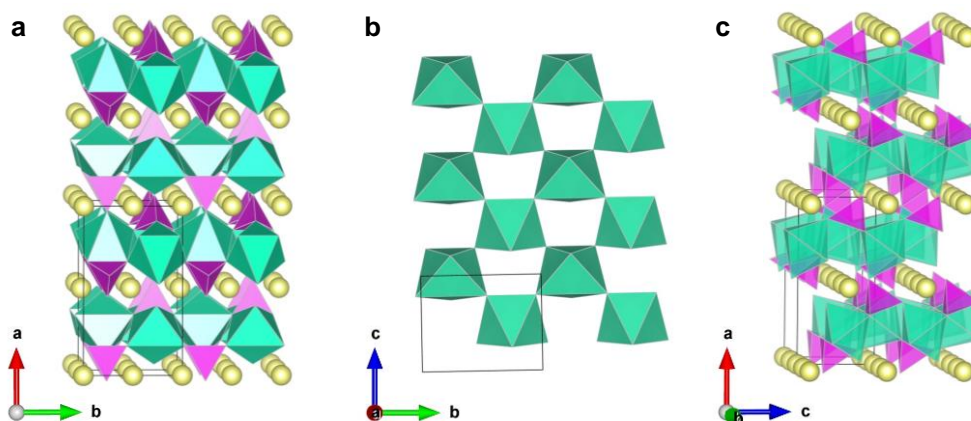


Figure I.16: Representation of crystal structure of LiFePO_4 in the $Pnma$ space group description, viewed along (a) C-axis, (b) A-axis (layer of FeO_6 octahedra perpendicular to the axis), and (c) B-axis (Preferential Li^+ transport). Green octahedra and purple tetrahedra represent the FeO_6 and PO_4 groups, respectively. Lithium atoms are displayed as yellow balls.

orthorhombic unit cell (space group: $Pnma$ or $Pmnb$, depending on the chosen description). FeO_6 octahedra share corners between each other to form layers parallel to the $(ac)Pmnb \equiv (bc)Pnma$ plane, so that electronic delocalization is difficult. Each FeO_6 octahedron shares one edge with a PO_4 tetrahedron and corners with four other PO_4 tetrahedra, thus the average Fe-O distance (2.157 Å) is much longer than what is expected for Fe^{2+} in octahedral coordination. The resulting electrostatic repulsions between the Fe and P cations weaken the $\text{Fe}^{\text{II}}\text{-O}$ bond strength (*i.e.* more ionic). Such an increase in capacity is at the origin the unusually high operating voltage observed for this electrode material (3.45 V vs. Li^+/Li^0) [161]. The lithium atoms sit at the intersection of tunnels, which run along the $aPmnb \equiv bPnma$ and the $cPmnb \equiv cPnma$ axes; conductivity studies have however shown that Li^+ diffusion proceeds preferentially along $[010]_{Pnma}$ [162].

Although LiFePO_4 has a theoretical capacity of only 170 mA·h/g, this compound was long neglected because of the inability to extract more than ~ 0.7 Li (*ca.* ~ 120 mA·h/g) (Figure I.17 a). Such a limitation was overcome by Ravet and Armand [163-164] who showed in 1999 the feasibility to remove all the Li (Figure I.17 b) via a cooling of the particles with a thin film of carbon coating to ensure electronic percolation between the particles. Huang and Yamada [165-166] were the first to show that reducing particle size help to shorten the Li^+ diffusion lengths and improvement of electronic wiring between particles. It is widely accepted a two-phase mechanism were undertaken between the two end members LiFePO_4 and FePO_4 , with a unit-cell volume change ($\Delta V/V$) of 8.5 % [161].

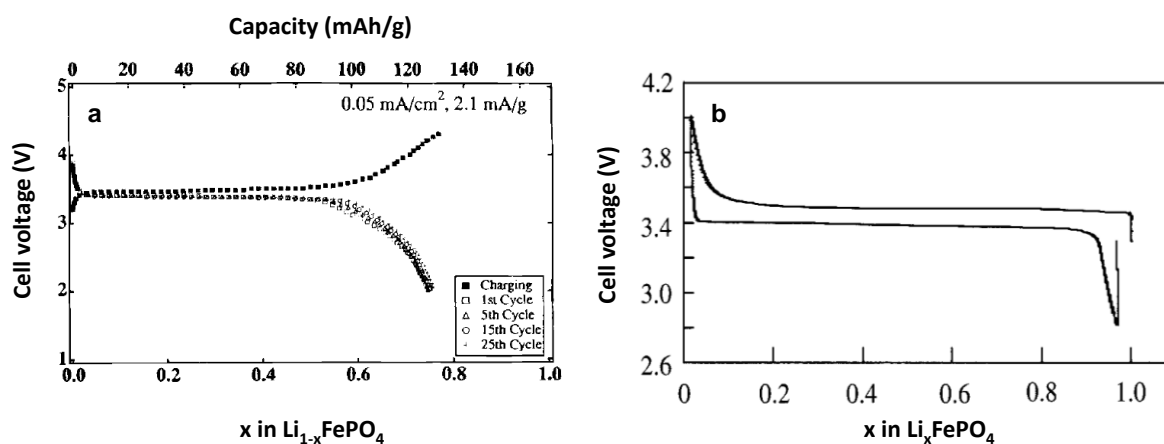


Figure I.17: Galvanostatic curve for a $\text{LiFePO}_4||\text{Li}$ cell (a) without carbon coating in the first report (adapted from [44]), and (b) after carbon coating with cell running at rate of $C/10$ (adapted from [165]).

Synthesis of LiFePO_4 includes a panoply of routes such as solid state synthesis [44, 166-167] (most robust and conventional used in industry), solution-based synthesis (*i.e.* sol-gel process [168-169], solution precipitation [170-171], hydrothermal synthesis [172-174],

organic/microwave-assisted solvothermal synthesis [175-178], templating techniques [179-181], and ionothermal route [182-184]). Through these various routes, samples with impurities, defects, or off-stoichiometry can be obtained with different electrochemical performance.[162, 173, 185-190]. To obtain optimized performance in terms of reversible capacity and kinetic response without sacrificing the volumetric energy density [191], a uniform coating layer with full coverage on LiFePO_4 should be achieved.

Other *triphylite* phases LiMPO_4 ($M = \text{Mn, Co, Ni}$) were also envisaged as possible lithium hosts [44, 192-195]. Among them, the cobalt and nickel analogues present very high operating voltages of 4.8 V and 5.1 V vs. Li^+/Li^0 respectively, which is beyond the stability windows of liquid electrolytes commonly used. LiMnPO_4 displays a higher potential of 4.1 V vs. Li^+/Li^0 compared to LiFePO_4 and below those of LiCoPO_4 and LiNiPO_4 , however, the difficulties with this system are nested in its poor electrical conductivity together with the onset of structural distortions upon oxidation to MnPO_4 which hinder ionic transport resulting in the low capacity as well as poor reversibility [196-198].

Despite of a lower operating voltage than the ones of the layered oxides, the merits based on low cost, abundant resource of elements, cycle stability, safety, environmental compatibility and potential low cost have made LiFePO_4 the “stellar” material for EV applications. However, this situation is challenged as its energy density cannot any longer compete with layered oxides.

I.2.2.3. Fluorophosphates and Oxyphosphate

Given its high electronegativity, fluorine has recently generated great interest and several promising F-containing positive electrodes were proposed. By injecting one electron-withdrawing F^- ion into phosphate, fluorophosphates benefit from both the inductive effect of PO_4^{3-} and the high electronegativity of the F^- ions. One of the first successful fluorophosphate materials was $\text{LiV}^{(3+)}\text{PO}_4\text{F}$. Early research of LiVPO_4F was highly studied by Barker during the period of 2000 to 2007 [156, 199-203]. The crystal structure of LiVPO_4F was not clearly described until 2012 by Croguennec *et al.* [204] As most of the lithium-based $\text{LiM}^{(3+)}\text{PO}_4\text{F}$ compounds, LiVPO_4F is isostructural to the natural minerals *tavorite* LiFePO_4OH [205] and *amblygonite-montebrazite* $\text{LiAlPO}_4(\text{OH})_2\text{F}$ [206], both crystallizing in the same triclinic structure (space group: $P-1$). The crystal structure of LiVPO_4F is built up by VO_4F_2 octahedra which share common fluorine atoms so as to form $\cdots\text{V}\cdots\text{F}\cdots\text{V}\cdots\text{F}\cdots\text{V}\cdots$ infinite chains running along [001] (Figure I.18 a). These chains are connected by corner-sharing phosphate tetrahedra to make a spacious 3D framework: wide “tunnels” are present along all of the [100], [010], and [001] directions so that we have isotopic diffusion of Li^+ .

The extraction/insertion of Li in $\text{LiV}^{(3+)}\text{PO}_4\text{F}$ is highly reversible and associated to two plateaus around 4.2 V and 1.8 V vs. Li^+/Li^0 , which correspond to the $\text{V}^{4+}/\text{V}^{3+}$ and $\text{V}^{3+}/\text{V}^{2+}$ redox couples, respectively (**Figure I.19**). Used as cathode for Li-ion batteries, $\text{LiVPO}_4\text{F}/\text{graphite}$ cell offers a capacity of ~ 140 mA·h/g at moderate rate of C/10 with low polarization and merely 15% of initial capacity fade after 400 cycles. Interestingly, along the same line, they also synthesized $\alpha\text{-LiV}^{(4+)}\text{OPO}_4$ which crystallized in the *tavorite* structure using solid state synthesis. The crystal structure of $\alpha\text{-LiVOPO}_4$ is basically similar to the one of LiVPO_4F , except for two main points: *i*) The lithium ions are distributed over two fully occupied distinct crystallographic sites, Li(1) and Li(1)' at a distance from each other of 3.44 Å, and they lie in two very distorted pentahedral sites (**Figure I.20**) and *ii*) Two independent vanadium sites are encountered in both structures but with very regular V–F distances in LiVPO_4F (1.98 Å) compared with alternate long and short V–O distances in LiVPO_4O (**Figure I.18 b**). $\alpha\text{-LiVOPO}_4$ presents one plateau at 3.95 V on oxidation and a cascade of three plateaus (2.4, 2.2, 2V) upon insertion of 1 Li^+ on reduction which corresponds to the $\text{V}^{5+}/\text{V}^{4+}$ and $\text{V}^{4+}/\text{V}^{3+}$ redox couples, respectively [204].

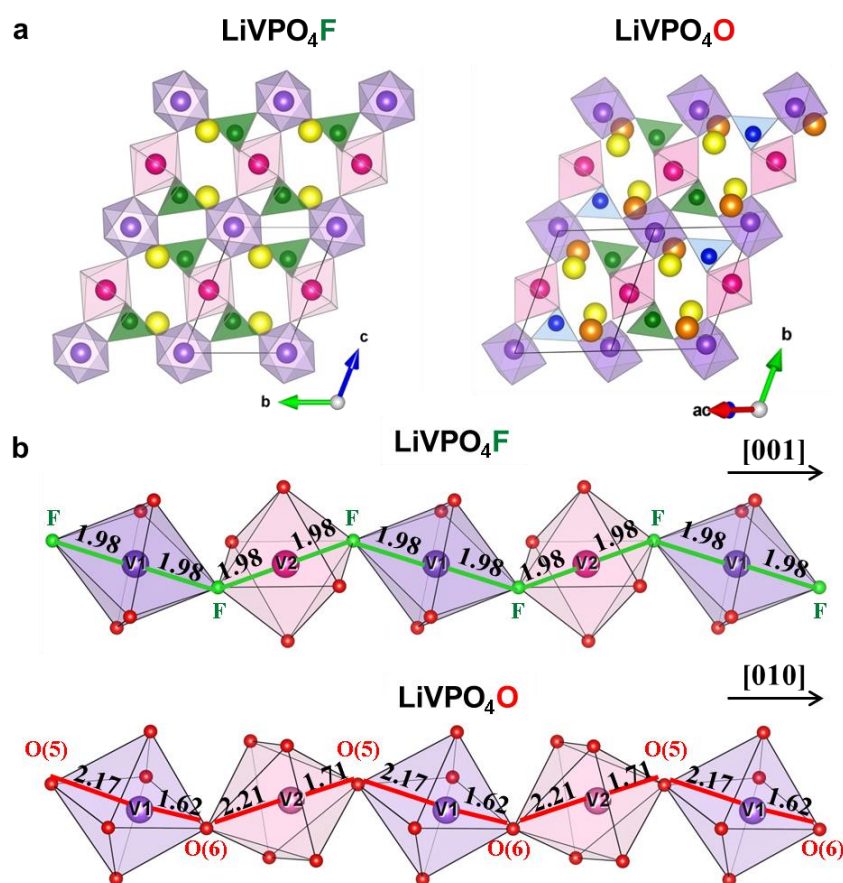


Figure I.18: (a) Representations of the crystal structures of LiVPO_4X ($\text{X} = \text{F}, \text{O}$). (b) Comparison of $[\text{VO}_4\text{X}_2]$ chains in LiVPO_4X ($\text{X} = \text{F}, \text{O}$) (adapted from [204]).

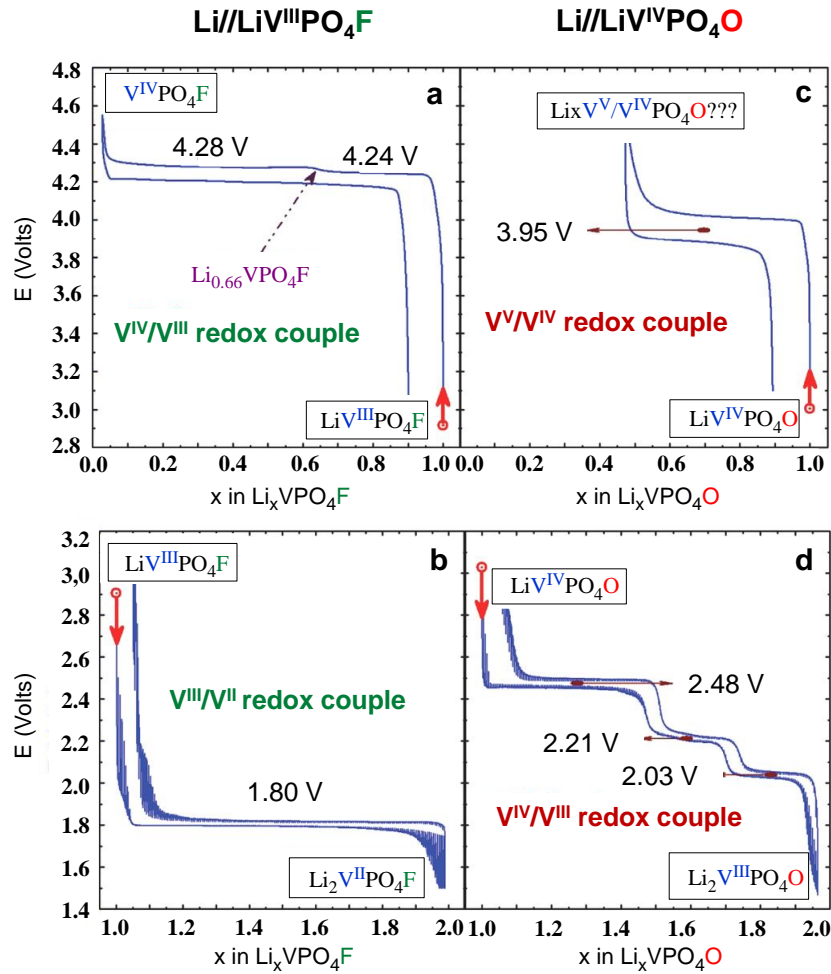


Figure I.19: Voltage–composition plots for $\text{LiVPO}_4\text{X}||\text{Li}$ cells ($\text{X} = \text{F}, \text{O}$) obtained during first cycles at C/50 upon oxidation (a and c) and in GITT mode upon reduction (b and d) (adapted from [204]).

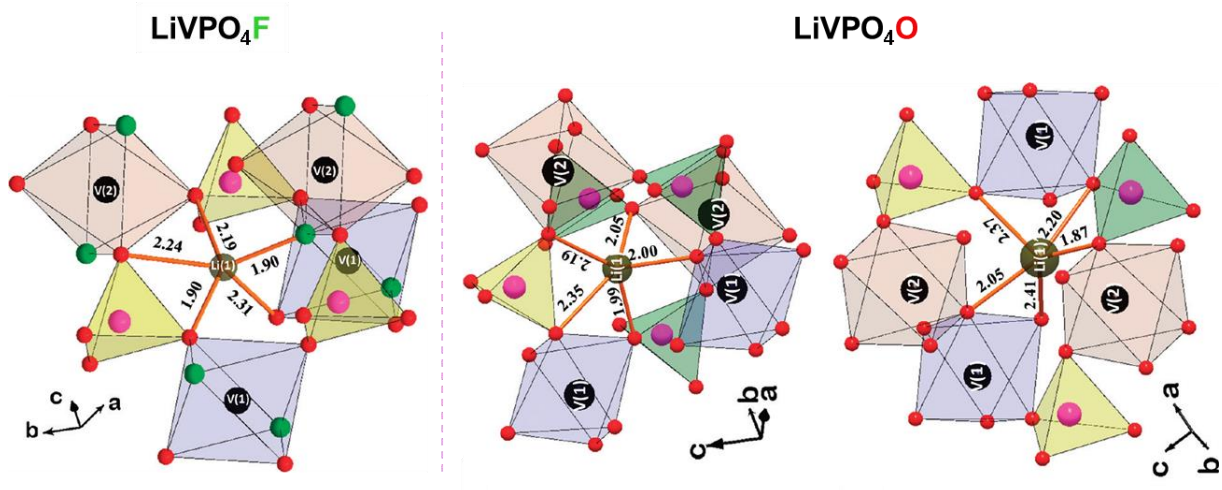


Figure I.20: Environments around (a) $\text{Li}(1)$ crystallographic sites in LiVPO_4F compared to (b) $\text{Li}(1)$ and $\text{Li}(1)'$ crystallographic sites in LiVPO_4O (adapted from [204]).

In spite of the good performance of LiVPO_4F , the low-availability and the high-toxicity of vanadium (**Table I.1**) prevents commercialization of LiVPO_4F in Li-ion batteries market, hence the research for attentive Fe-based polyanionic compound such as LiFePO_4F , was undertaken. The synthesis and the electrochemical properties of $\text{LiFe}^{(3+)}\text{PO}_4\text{F}$ were firstly reported on 2010 by Tarascon's group [184, 207-208] and independently by Nazar's group [209-210]. The lithium extraction from LiFePO_4F is obviously not feasible as the redox potential of $\text{Fe}^{4+}/\text{Fe}^{3+}$ locates above 4.7 V which beyond the electrochemical stability window of the electrolyte. In contrast LiFePO_4F can reversibly insert nearly 1 Li^+ at 2.8 V vs. Li^+/Li^0 leading to a capacity of 145 $\text{mA}\cdot\text{h}/\text{g}$. (**Figure I.21**). This discharge process was described as a two-phase mechanism, leading to the phase $\text{Li}_2\text{FePO}_4\text{F}$, which conserves the *tavorite* framework with a volume expansion of $\sim 8\%$ [209].

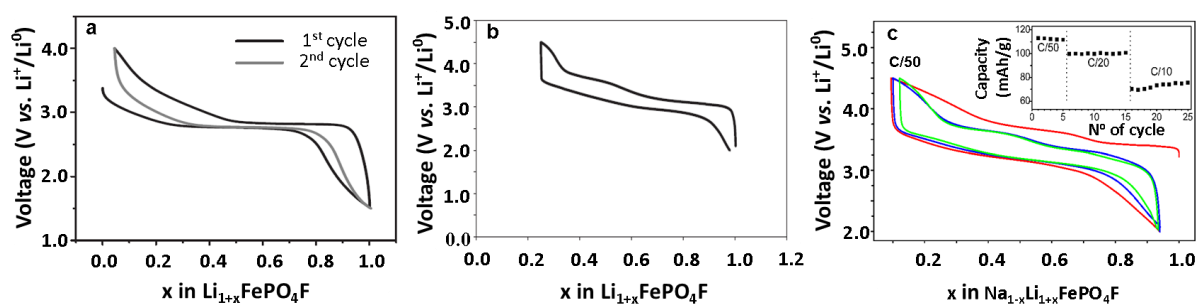


Figure I.21: Lithium insertion-extraction curves of (a) A $\text{LiFe}^{3+}\text{PO}_4\text{F}||\text{Li}$ cell (adapted from [209]), (b) A Layered $\text{Li}_2\text{Fe}^{2+}\text{PO}_4\text{F}||\text{Li}$ cell (adapted from [211]), and (c) a 3D (*Pnma* group) $\text{Li}_2\text{Fe}^{2+}\text{PO}_4\text{F}||\text{Li}$ cell (adapted from [212]).

Interestingly, Nazar [211] and Delmas [212] et. al. independently succeed in preparing $\text{Li}_2\text{Fe}^{(2+)}\text{PO}_4\text{F}$ cathode that can directly operate on the $\text{Fe}^{2+}/\text{Fe}^{3+}$ couple by using both electrochemical and chemical ion exchange using respectively either layered $\text{Na}_2\text{Fe}^{(2+)}\text{PO}_4\text{F}$ that based on face-sharing FeO_4F_2 octahedra or 3D $\text{NaLiFePO}_4\text{F}$ (space group: *Pnma*) that is built of edge-sharing FeO_4F_2 octahedra. Both the obtained $\text{Li}_2\text{FePO}_4\text{F}$ polymorphs exhibit similar electrochemical behavior. They deliver reversible capacity (100-110 $\text{mA}\cdot\text{h}/\text{g}$) in the solid-solution regime at 3.4 V.

It is worth mentioning that the $\text{Fe}^{3+}/\text{Fe}^{2+}$ redox potential observed for $\text{LiFe}^{(3+)}\text{PO}_4\text{F}$ (2.8 V vs. Li^+/Li^0) and $\text{Li}_2\text{Fe}^{(2+)}\text{PO}_4\text{F}$ polymorphs (3.4 V vs. Li^+/Li^0) are very different. Moreover, the potential of LiFePO_4F is much lower than the one of the *olivine* LiFePO_4 (3.45 V vs. Li^+/Li^0) which contains no fluorine. Therefore, this observation illustrates that incorporation of more electronegativity element fluorine into a given composition does not always systematically enhance the potential of the redox center. In fact, besides the nature of the neighboring atoms of the redox center, other structural factors (*e.g.* the connectivity between atoms, the nature of

the bonding) experimentally affect the position of redox potential. Arroyo *et al.* performed first-principle calculations on F-based materials and have shown that their electrochemical behavior strongly depended on the particular crystallographic site occupied by F as well as the stability of the M-F bonds [213]. Recently Rouse [50] has suggested polymorphs which are denser and preferentially built of edge or face-sharing octahedra are usually the more ionic and gain higher potential, and this can explain different $\text{Fe}^{3+}/\text{Fe}^{2+}$ redox potentials of $\text{Li}_2\text{Fe}^{(2+)}\text{PO}_4\text{F}$ polymorphs as illustrated above.

I.2.2.4. Fluorosulfates and Oxysulfate

I.2.2.1.1 Fluorosulfates

Driven by the need to increase the redox potential of Fe-based polyanionic compound, Tarascon's group decided in 2010 to replace $(\text{PO}_4)^{3-}$ by a more electronegative polyanion $(\text{SO}_4)^{2-}$ while preserving F^- as another high electronegative element. Thus the LiFeSO_4F was targeted and prepared for the first time via ionothermal synthesis.

Two kinds of $\text{LiFe}^{2+}\text{SO}_4\text{F}$ polymorphs crystallized in either *tavorite* or *triplite* structure (Figure I.22) were obtained. From the structural point of view, the *triplite* structure significantly differs from the *tavorite* one, as seen in Figure I.22. The main differences regards the 3d-metal and lithium atoms, which sit in well-defined crystallographic sites in the *tavorite* structures, while they are statistically distributed on two octahedral sites (denoted M_1 and M_2) in the *triplite* structure; Moreover, the fluorine atoms are arranged in a *trans* configuration (*tavorite*), rather than a *cis* one (*triplite*) within the strongly distorted FeO_4F_2

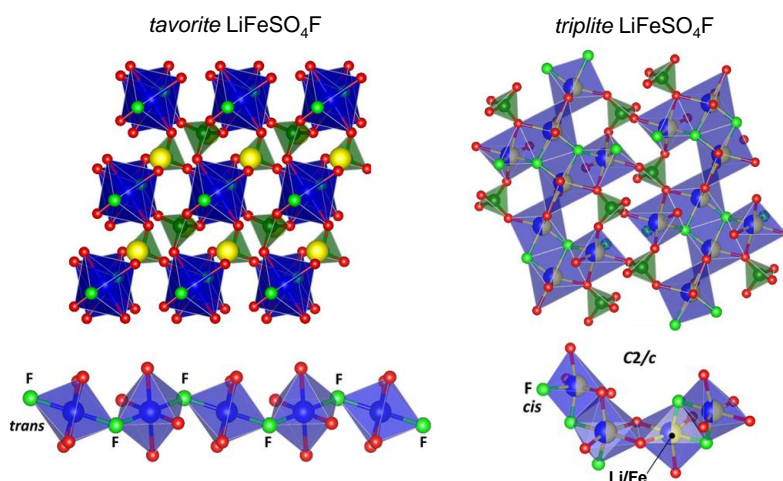


Figure I.22: Comparison of the *tavorite* and the *triplite* structures of LiFeSO_4F polymorphs (adapted from [50]). FeO_4F_2 octahedra are shown in blue, and SO_4 tetrahedra in green. Lithium atoms are displayed as yellow balls.

octahedral. Lastly dealing with FeO_4F_2 octahedra, they are only interconnected through corners in the *tavorite* structures, whereas in the *triplite* they share edges to form chains

running along the [101] and [010] directions of the monoclinic unit cell (space group: $C2/c$). Regarding the electrochemical performances (**Figure I.23**), the ordered (*tavorite*) and disordered (*triplite*) LiFeSO_4F polymorphs display a redox potential of 3.6 V (*tavorite*) and 3.9 V (*triplite*) vs. Li^+/Li^0 respectively [45, 214]. The potential of *tavorite* LiFeSO_4F is 0.8 V greater than the one of the isostructural fluorophosphate LiFePO_4F , as expected. Nearly 0.9 lithium ions per formula unit (*i.e.* 135 mA·h/g) can be reversibly extracted from *tavorite* LiFeSO_4F with good capacity retention; while nearly 0.75 Li^+ ions per formula unit (*i.e.* 113 mA·h/g) can be reversibly removed from the *triplite* LiFeSO_4F [45, 214]. The redox process of both polymorphs follows a biphasic mechanism and leads to the delithiated FeSO_4F phase (in the *tavorite* phase, the FeSO_4F conserves the *tavorite* framework and dihedral angle between adjacent FeO_4F_2 octahedra deviates from zero when Li is inserted [215], **Figure I.23 a**), resulting in a volume change of 8% in *tavorite* LiFeSO_4F compared to merely 0.5% in *triplite* LiFeSO_4F . Despite this low global volume change capacity retention of the *triplite* was worse than that of the *tavorite* polymorph [50] as well as the larger discharge/charge polarization. The reasons for such finding are rooted due to the statistical distribution of Li and Fe over both sites, in the absence of clear channels for Li diffusion which results in a slower Li^+ diffusion.

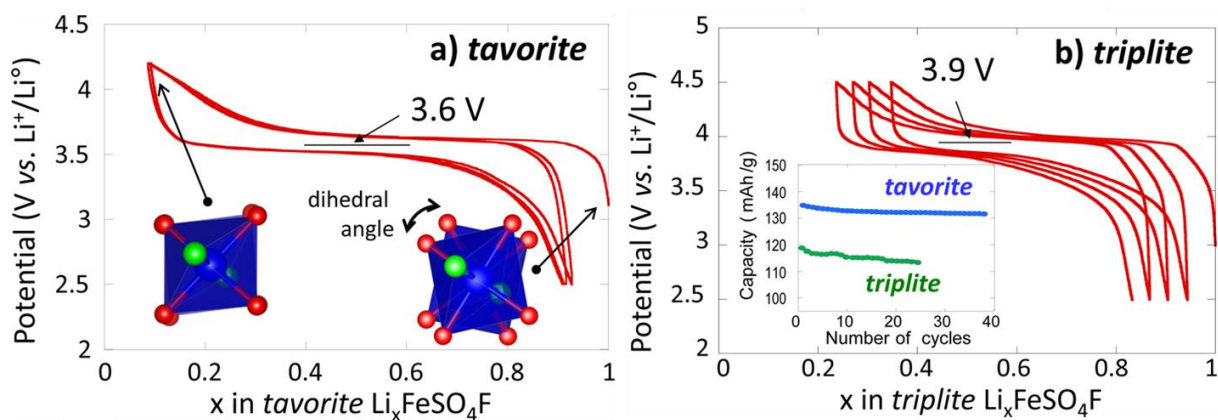


Figure I.23: Voltage versus composition curve for (a) *Tavorite* $\text{LiFeSO}_4\text{F}||\text{Li}$ cells and (b) *Triplite* $\text{LiFeSO}_4\text{F}||\text{Li}$ cells. For the *tavorite* polymorph, the dihedral angle between adjacent FeO_4F_2 octahedra (colored in blue) deviates from zero when Li is inserted. The inset in b shows the capacity retention upon cycling for *tavorite* and *triplite* LiFeSO_4F (from [50]).

This 3.9 V redox potential of *triplite* LiFeSO_4F is the highest potential ever reported up to now for the $\text{Fe}^{3+}/\text{Fe}^{2+}$ redox couple in any inorganic compound. The energy density for *tavorite* LiFeSO_4F (~480 mA·h/g) and *triplite* LiFeSO_4F (440 mA·h/g) is comparable to LiFePO_4 (~470 mA·h/g). Thus the practical interest of such phases for battery applications provided the synthesis conditions can be better mastered to ensure greater reproducibility. In

terms of synthesis, *tavorite* LiFeSO_4F was firstly synthesized by Tarascon group through ionothermal route [45, 184, 216]. The fact that this phase decomposes at temperature beyond 375°C and is soluble in water makes it quite difficult to use ceramic methods, which was reported earlier for synthesizing the first *tavorite* fluorosulfate - LiMgSO_4F [217], or through low-temperature solution chemistry in aqueous media. One of the determinant factors for the success of the synthesis was the use of *szomolnokite* $\text{FeSO}_4\cdot\text{H}_2\text{O}$ and lithium fluoride as the precursors to make use of the topotactic reaction [50]. Indeed this topotactic reaction had been successfully generalized to the syntheses of other 3d-metal fluorosulfates LiMSO_4F ($\text{M} = \text{Co}, \text{Ni}, \text{Zn}, \text{Mn}$) [218], among which LiCoSO_4F and LiNiSO_4F displays *tavorite* structure [45, 218], while LiMnSO_4F adopts *triplite* structure [219], and LiZnSO_4F shows *sillimanite* structure [220-221]. None of them has shown more attracting electrochemically performance than LiFeSO_4F polymorphs. To bypass using ionic liquid which is quite expensive, alternative eco-efficient approaches were developed to synthesize *tavorite* LiFeSO_4F , which includes polymer approach [222-223] or a solid state reaction [224] in sealed bombs. Generally the reaction kinetics is faster when solution rather than solid-state reaction processes were used. DFT calculations suggests formation of *triplite* is entropically driven by Li/Fe site mixing [225], therefore solid-state routes [226-227] and later through spark plasma sintering (SPS) [214], mechanical ball-milling [214] and ultra-rapid microwave synthesis [228] that capable of promoting disorder had been explored and shown effective to synthesize the *triplite* LiFeSO_4F . Meanwhile, attempts to prepare pure *triplite* polymorphs of LiCoSO_4F or LiNiSO_4F have failed [221].

Besides the delicacy complexity in obtaining pure LiFeSO_4F phases, moisture sensitivity is another big issue that should be considered to process fluorosulfates for large-scale applications. Water sources along the synthesis and processing of LiFeSO_4F electrodes should be maximally eliminated. A detailed report on the influence of relative humidity on the structure and electrochemical performance of LiFeSO_4F electrodes for Li-ion batteries was recently published by Tarascon's group [229]. This study clearly demonstrated *tavorite* LiFeSO_4F is extremely moisture sensitive, which can fully evolve into $\text{FeSO}_4\cdot n\text{H}_2\text{O}$ ($n = 1, 4, 7$) and LiF in a highly humid environment ($>65\%$ RH at 25°C) (**Figure I.24 a**). H_2O molecules released during $\text{FeSO}_4\cdot n\text{H}_2\text{O}$ ($n = 4, 7$) dehydration will induce LiPF_6 decomposition and HF formation [230-231], and the corrosive species will further attack the electrode and lead to metal dissolution and performance degradation. Moreover, moisture has been shown to trigger the $(\text{Li})\text{FeSO}_4\text{OH}$ phase to have a huge impact on the electrochemical behavior of *tavorite* LiFeSO_4F (**Figure I.24 b**) [229], which has been confirmed by other reporters [232-233]. A similar behavior was also shown for *triplite* LiFeSO_4F but with a lower degradation rate [229].

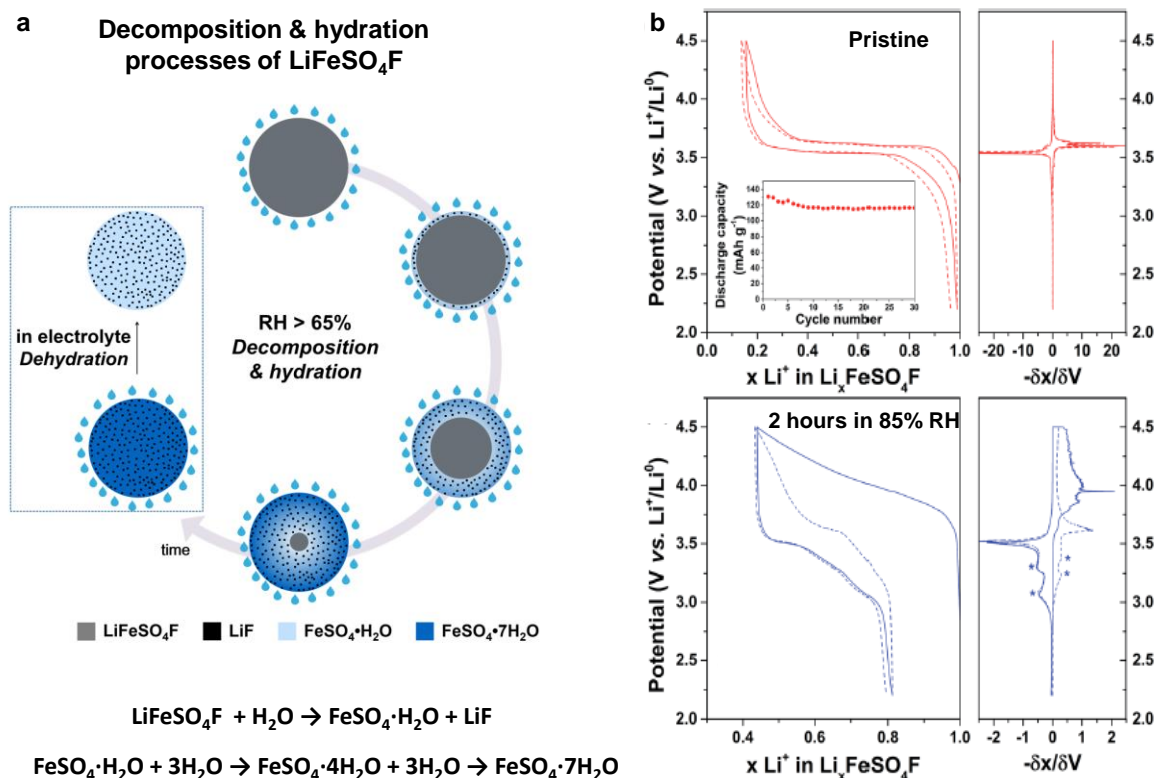


Figure I.24: (a) Schematic illustration of the decomposition & hydration processes of LiFeSO_4F in a humid environment ($\text{RH} > 65\%$), and the dehydration reactions to generate $\text{FeSO}_4 \cdot 7\text{H}_2\text{O}$ in the electrolyte (on bottom). (b) Effect of moisture on the electrochemical behaviors of the *tavorite* LiFeSO_4F electrode in 85% RH at 25 °C for 0 hour (red curve) and 2 hours (blue curve), with their corresponding differential capacity curves on the right (adapted from [229]).

I.2.2.1.2 Oxyulfates

Although Li-ion batteries are still using LiPF_6 salts there is a continuous push to find alternatives to lower the amount of fluorine because of safety hazards (toxic gases). Thus there is a sore need to design high-voltage F-free derivatives as environmentally benign electrode. For such a reason our group has explored the hydroxysulfates [234-235].

Oxygen has abundant source in nature, which can be viewed as “free” and “green” element. Other than fluorine, oxygen is the second anion owning high electronegativity to play on the M-O bond, which, once been injected into the polyanionic compounds, may bring some benefits on increasing the voltage for Li-ion batteries. Due to the dead weight of polyanions, to improve the capacity becomes a bottleneck for polyanionic compound to achieve competent energy density as layered oxides. Moreover, Li-rich compounds have shown high energy density arising from anionic ($\text{O}^{2-} \leftrightarrow \text{O}_2^{2-}$) reversible redox processes. Is it possible to make use of capacity from anionic redox of oxygen in polyanionic compounds?

Although phosphates are less prone to polymorphism, both sulfate and phosphate crystal chemistries bear some resemblances, such as the fluorine-based compounds $\text{Li}_2\text{FePO}_4\text{F}$ [211]/ LiFeSO_4F and hydroxide-based ones $\text{Li}_2\text{FePO}_4\text{OH}$ [236]/ LiFeSO_4OH [234, 237]. Additionally, 3d-transition metal oxyphosphates and oxysilicates capable of reversibly inserting Li^+ ions are known to form as recently demonstrated by the existence of LiVOPO_4 [238-239] and $\text{Li}_2\text{VOSiO}_4$ [240]. Thus a legitimate course of inquiry was, could an iron-based oxysulfate insertion compound be stabilized?

In contrast to the numerous reports on oxyphosphates (*i.e.* LiVOPO_4 , $\text{Li}_4\text{VO}(\text{PO}_4)_2$) as positive electrode for Li-ion batteries, the amount of work done on exploration of oxysulfates counterpart, is very slim. Twenty years ago Gaubicher *et al.* revealed an equilibrium redox potential of 2.84 V *vs.* Li^+/Li^0 for the intercalation of Li^+ in $\beta\text{-VOSO}_4$ [241]. Among the most common 3d- metal salts of Fe, Co, Mn, V, Cu, only VOSO_4 [242-244] and Cu_2OSO_4 [245-246] are known compounds, however no electrochemically active Li-based oxysulfates were reported.

This was an impetus for our group to explore the 3d-M oxysulfate as possible electrode for Li-ion batteries. Through this thesis a novel family of oxysulfate, with formulae $\text{Li}_2\text{Cu}_2\text{O}(\text{SO}_4)_2$, $\text{Li}_2\text{VO}(\text{SO}_4)_2$, $\text{Fe}_2\text{O}(\text{SO}_4)_2$ were isolated in terms of their synthesis, structure determination, electrochemical characterizations, and some physical properties.

The rest of this thesis will describe how such new phases were made prior to present their structure, electrochemical and physical properties. Among them the new phase $\text{Li}_2\text{Cu}_2\text{O}(\text{SO}_4)_2$ turns out to be the most interesting as it presents the highest voltage of $\text{Cu}^{3+}/\text{Cu}^{2+}$ redox potential (4.7 V *vs.* Li^+/Li^0) so far reported. This phase together with LiCuSO_4F will be the subject of chapter II.

Chapter II. Exploration of LiCuSO_4F & $\text{Li}_2\text{Cu}_2\text{O}(\text{SO}_4)_2$

II.1. Introduction

Sulfate-based compounds generally display higher potentials than phases with other polyanionic groups (phosphate, borate, silicate, *etc.*), thanks to the inductive effect of the polyanions $(\text{XO}_4)^{n-}$ [49, 142]. Among the family of electrochemically active compounds termed as 3d-metal fluorosulfates (formula $\text{Li}_x\text{MSO}_4\text{F}$, $M = \text{Fe, Co, Ni, Mn}$), the *triplite* LiFeSO_4F phase was shown to display the highest potential (3.9 V vs. Li^+/Li^0) ever reported so far for any Fe-based inorganic compounds [219, 226]. The origin of its high voltage has been correlated to the high ionic character of the Fe-O bonds, and to structural features inherent to mineral *triplite*, with *i*) the presence of two crystallographic sites M1 and M2 which are statistically occupied by two metals, here Li and Fe and *ii*) the strong distortion of the resulting MO_4F_2 octahedra, with fluorine atoms sitting in *cis* configuration [225, 247].

Another way to modify the redox potential of polyanionic compounds is provided by changing the nature of the 3d-metal and recent Density Functional Theory (DFT) calculations have indicated that potentials as high as 5.1 V should be achievable for *tavorite* LiCuSO_4F [248]. Combining with the friendly environmental character of Cu (Table I.1), this was an impetus to further explore the Cu-based fluorosulfate chemistry which was so far counting a sole member, the *tavorite* NaCuSO_4F phase which has been shown to be electrochemically inactive [249].

When exploring the synthesis process of LiCuSO_4F , we came across a new phase of formula $\text{Li}_2\text{Cu}_2\text{O}(\text{SO}_4)_2$. By controlling synthesis condition, each of these two compounds could be isolated as pure phase. Herein we present the synthesis, structure, electrochemical performance with some physical properties for them respectively. DFT calculations have also been used to confirm the phase stabilities and to understand their electrochemical performance.

II.2. Exploration of Copper-based Fluorosulfate: LiCuSO_4F

II.2.1. Synthesis

CuSO_4 (Sigma Aldrich, 99–100.5%) and LiF (Sigma Aldrich, 300 mesh) were used as Cu and Li-based precursors for the targeted phase with the former being dried at 260 °C under vacuum for 24 h to ensure its pureness. Stoichiometric amounts of powders were thoroughly

ball milled in a SPEX-8000M mixer-miller, pressed into a pellet and annealed at 400°C – 415°C in an alumina boat for 8 – 10 hours under argon flow. The recovered yellowish pellet, once scrapped to remove a thin green film (**Figure II.1**) and ground, displays sharp reflections on the X-ray diffraction (XRD) patterns, reminiscent of a new phase proved to be LiCuSO_4F that will be described in the following section. The green shell of the pellet in contrast shows a totally different XRD pattern (proved to be $\text{Li}_2\text{Cu}_2\text{O}(\text{SO}_4)_2$, to be described in the following section). We found the amount of the greenish phase to increase with temperature and annealing time, hence the need to cautiously define the annealing protocol. The best protocol to obtain LiCuSO_4F with minimum amount of impurities consists in annealing time of 8 hours at $\sim 415^\circ\text{C}$ under an argon flow.

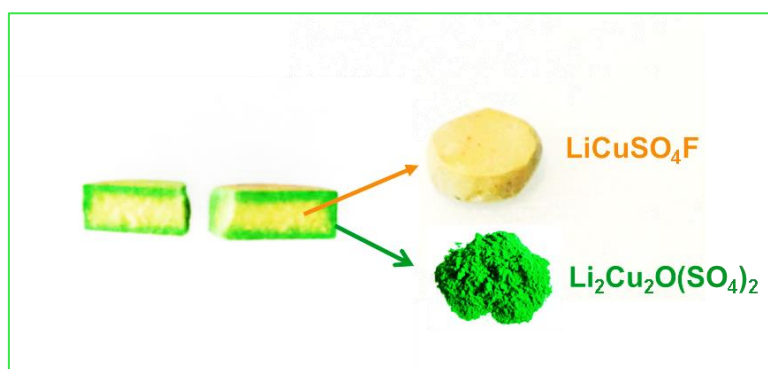


Figure II.1: The photo of the pellet directly synthesized at 415°C for 10 hours, showing a filmy green shell of $\text{Li}_2\text{Cu}_2\text{O}(\text{SO}_4)_2$ and a yellowish core phase of LiCuSO_4F .

II.2.2. Structure Characterization

The structure of LiCuSO_4F was solved from X-ray powder diffraction coupled with neutron powder diffraction. The finely ground yellowish powder was loaded in a 0.7 mm diameter capillary and the sample was measured in transmission mode ($\lambda = 0.41374 \text{ \AA}$) on the 11-BM beamline at Argonne National Lab. The XRD pattern of the as-prepared powder shows the presence of many sharp peaks coexisting with tiny attributed to CuSO_4 and $\text{Li}_2\text{Cu}_2\text{O}(\text{SO}_4)_2$ [250]. As the latter are well-defined compounds, they were treated with the Rietveld method and all remaining peaks were attributed to LiCuSO_4F . Thus, the main phase could be indexed using the Dicvol program [251] in a *C*-centered monoclinic unit cell, with lattice parameters $a = 12.83164(12) \text{ \AA}$, $b = 6.13124(6) \text{ \AA}$, $c = 10.01640(11) \text{ \AA}$ and $\beta = 117.3549(7)^\circ$, *i.e.* structural characteristics of *triplite*. The corresponding volume ($V = 699.918(12) \text{ \AA}^3$) is suitable to accommodate eight formulae per unit cell.

This unit cell and space group was confirmed by Electron Diffraction (ED) patterns and Energy Dispersive X-ray (EDX) spectra* obtained for the sample. All ED patterns (**Figure II.2**) can be indexed on a C -centered monoclinic unit cell with the lattice parameters $a \approx 12.8 \text{ \AA}$, $b \approx 6.1 \text{ \AA}$, $c \approx 10.0 \text{ \AA}$, $\beta \approx 117^\circ$, in good agreement with the results of X-ray powder diffraction. The presence of the $00l$, $l \neq 2n$ reflections in the $[100]$ and $[110]$ ED patterns seemingly violates the $h0l: l = 2n$ reflection condition imposed by the $C2/c$ space group derived from powder XRD. However, this reflection condition is affected by multiple diffraction that was confirmed by vanishing the $00l$, $l \neq 2n$ reflections upon tilting the crystal around the c^* reciprocal lattice axis.

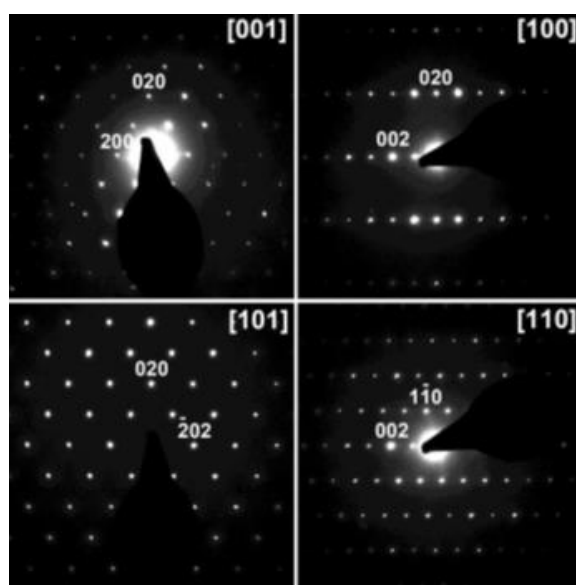


Figure II.2: Main Electron diffraction patterns of LiCuSO_4F .

The structure was then solved *ab initio* in the $C2/c$ space group using the FOX program [252], with SO_4 groups taken as rigid tetrahedra with a S-O distance of 1.49 \AA . The initial structural model found was then fully refined without any distance or angle restraints, and further confirmed by a Rietveld refinement conducted with the FullProf program [253] against high resolution neutron powder diffraction data recorded on the same powder at High-Resolution Powder Diffractometer for Thermal Neutrons (HRPT), SINQ (PSI, Switzerland) with a wavelength of 1.495 \AA (**Figure II.3**). In agreement with the nominal composition, Cu to S and Cu to F atomic ratios of 1 were confirmed by EDX analysis (**Figure II.4**) and atomic emission analysis (lead to a formula $\text{Li}_{0.98}\text{Cu}_{1.03}\text{SO}_4\text{F}_{1.02}$).

* ED patterns and EDX analysis were obtained cooperated with Dr. Artem M. Abakumov and Dr. Gustaaf Van Tendeloo (University of Antwerp, Antwerp, Belgium) with a *Tecnai Osiris* electron microscope equipped with a Super-X EDX detector.

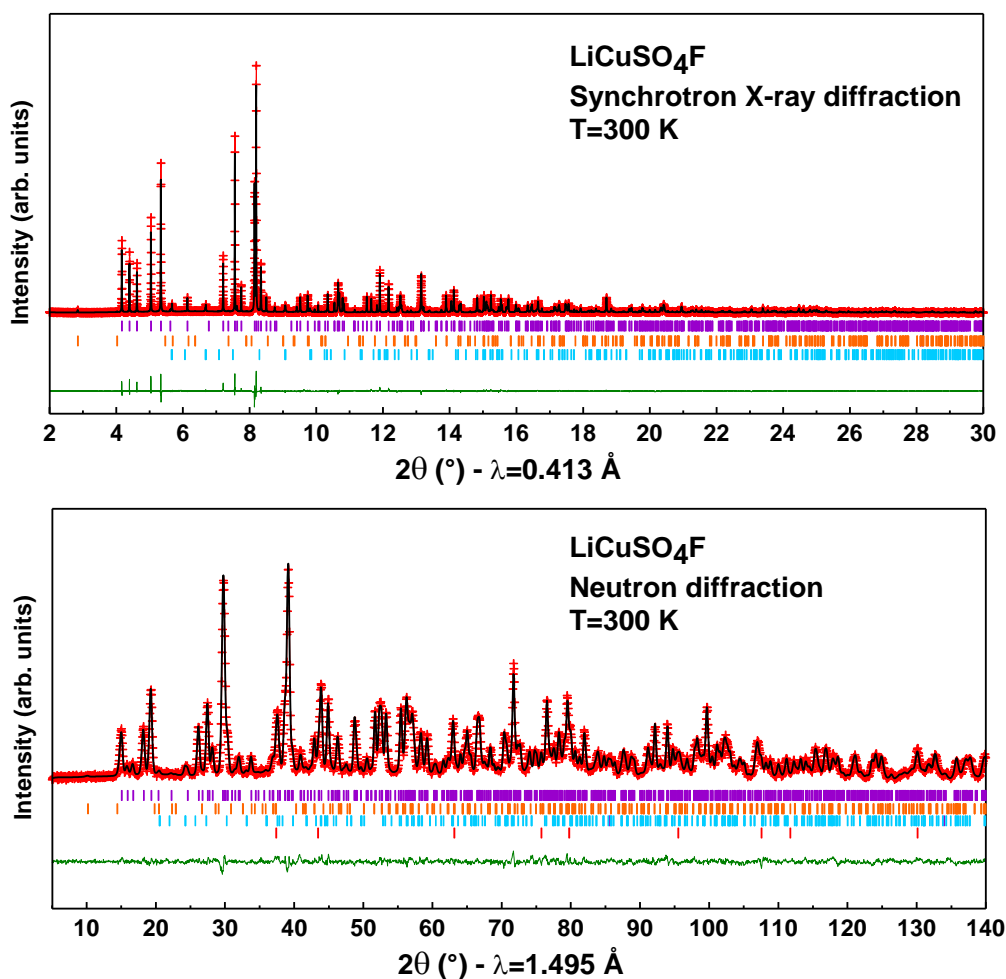


Figure II.3: Rietveld refinement of synchrotron and neutron diffraction patterns of LiCuSO_4F ($T = 300 \text{ K}$). The red crosses, black continuous line and bottom green line represent the observed, calculated, and difference patterns, respectively. Vertical tick bars mark the Bragg reflections (from top to bottom): purple: LiCuSO_4F (95%); orange: $\text{Li}_2\text{Cu}_2\text{O}(\text{SO}_4)_2$ (1%); blue: CuSO_4 (3%); red: LiF (1%, only observed from neutron diffraction).

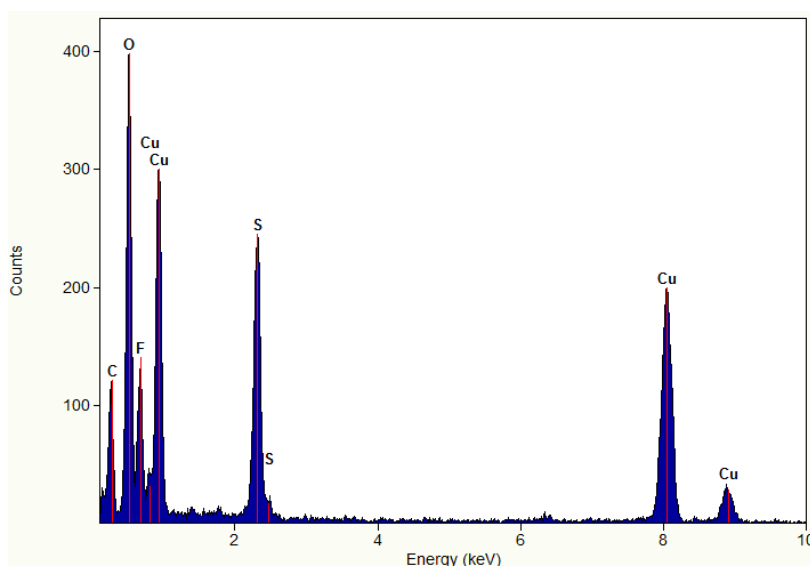


Figure II.4: EDX spectrum of LiCuSO_4F . The Cu:S atomic ratio was found to be equal to 1.08(7):0.92(7), in good agreement with the LiCuSO_4F formula.

The refined structural parameters for LiCuSO_4F are shown in **Table II.1**, with the structure of it presented in **Figure II.5** which can be described in several ways. Firstly, if we consider metal-ligands at distances below 2.5 Å, Cu is coordinated by three oxygen and two fluorine atoms, to form CuO_3F_2 square-based pyramid which are linked via F-F edges, leading to $\text{Cu}_2\text{O}_6\text{F}_2$ dimers (**Figure II.5 a**). These $\text{Cu}_2\text{O}_6\text{F}_2$ entities are connected through SO_4 tetrahedra so as to form layers stacked along [001] (**Figure II.5 b**). However it is worth noting that one of the two Cu-F bonds is rather long (2.34 Å) as compared to the other (1.88 Å), therefore a more adequate description of the structure is to consider only four ligands for copper (O1, O2, O3, F) at distances ranging between 1.88 and 1.98 Å, see **Figure II.5 c**, which gives almost square planar coordination as commonly observed for this Jahn-Teller $3d^9$ cation. CuO_3F squares are then connected to SO_4 tetrahedral groups so as to form ladders running along [001]. Lastly, a sixth oxygen atom coordinates Cu at 2.62 Å; the resulting CuO_4F_2 elongated octahedra share O-O and F-F edges to form 1D chains (**Figure II.5 e**). The lithium environment is easier to describe unambiguously as it adopts a similar coordination with distorted LiO_4F_2 octahedra sharing alternatively F-F and O-O bonds (**Figure II.5 f**). Therefore, one-dimensional pathways for Li conduction may occur along [010] in LiCuSO_4F .

Table II.1 Structural parameters for LiCuSO_4F deduced from the Rietveld refinement of the neutron diffraction patterns at 300 K.

LiCuSO_4F, Space Group: $C2/c$						
$a = 12.83164(12)$ Å, $b = 6.13124(6)$ Å, $c = 10.01640(11)$ Å and $\beta = 117.3549(7)^\circ$,						
$V = 699.918(12)$ Å ³ , Density = 3.522 g/cm ³ , $Z = 8$						
Atom	Wyckoff site	x	y	z	Occupancy	$B(\text{Å}^2)$
Cu	$8f$	0.35806(15)	0.1008(3)	0.16503(19)	1	0.63(3)
F	$8f$	0.4750(2)	0.0947(5)	0.1009(3)	1	0.95(4)
S	$8f$	0.1701(4)	0.0902(8)	0.2948(4)	1	0.71(7)
O1	$8f$	0.2883(2)	0.1260(4)	0.3039(3)	1	0.96(5)
O2	$8f$	0.1422(2)	0.2843(3)	0.3601(3)	1	0.56(4)
O3	$8f$	0.3212(2)	0.4080(4)	0.1042(3)	1	0.95(4)
O4	$8f$	0.0851(2)	0.0510(4)	0.1403(3)	1	1.23(5)
Li	$8f$	0.0448(8)	0.2574(15)	0.4936(10)	1	1.31(14)

Reliability parameters: $\chi^2 = 2.36$; Bragg R-factor = 3.24%

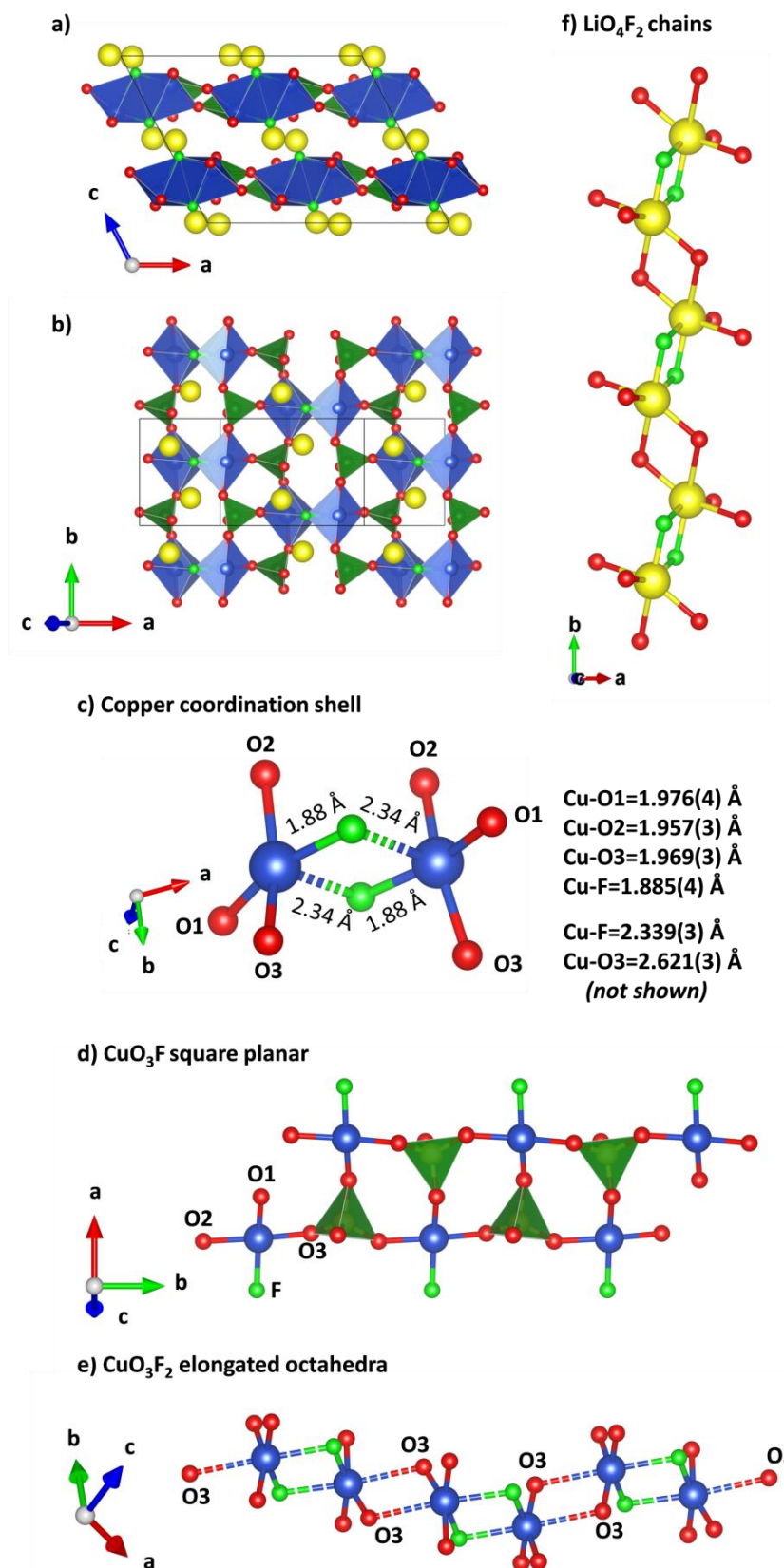


Figure II.5: (a) Structure of LiCuSO_4F along the $[010]$ direction. (b) View of one layer made of $\text{Cu}_2\text{O}_6\text{F}_2$ dimers and SO_4 tetrahedra. (c) Cu coordination in $\text{Cu}_2\text{O}_6\text{F}_2$. (d) CuO_3F square planes. (e) CuO_3F_2 elongated octahedral.

(f) Chains of edge-sharing LiO_4F_2 octahedra. Cu is blue, O is red, F is light green, Li is yellow, and SO_4 tetrahedra are dark green.

At this stage the structure of LiCuSO_4F presents clear similarities with the *triplite* structure reported for LiFeSO_4F [226], LiMnSO_4F [219] and minerals $(\text{Mn}, \text{Fe}, \text{Mg}, \text{Ca})\text{PO}_4\text{F}$ [254-255]. However, all previously reported structures presented a statistical cationic distribution over the two M1 and M2 crystallographic sites (**Figure II.6 b**); in the present case, M1 is occupied by Cu and M2 by Li only (**Figure II.6 a**), making LiCuSO_4F the first experimental realization of a fully ordered *triplite*.

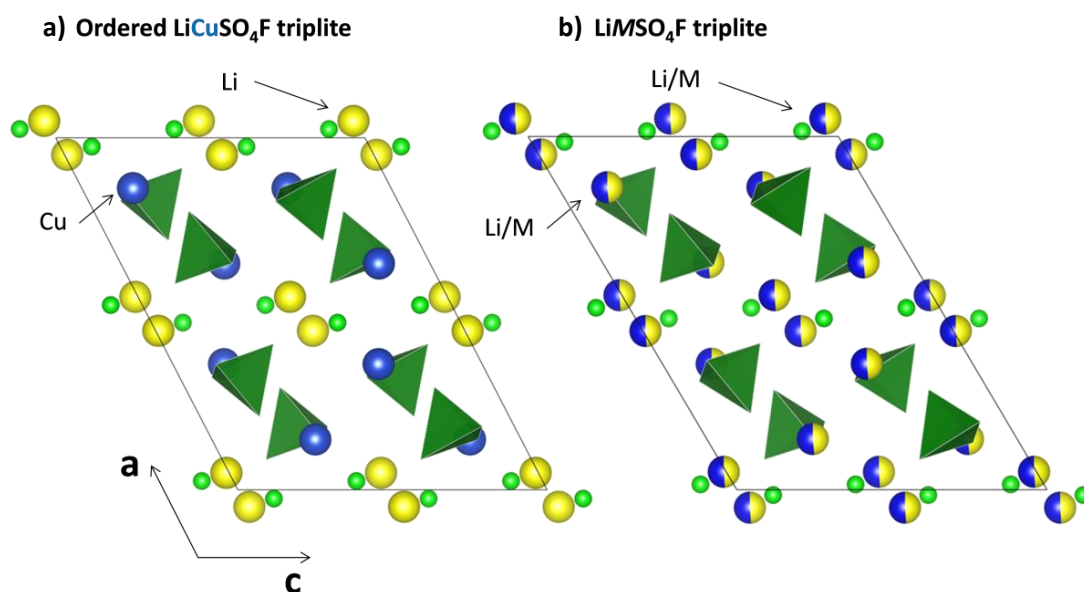


Figure II.6: (a) Structure of LiCuSO_4F compared to (b) *Triplite* structure reported for LiFeSO_4F , LiMnSO_4F and $(\text{Mn}, \text{Fe}, \text{Mg}, \text{Ca})_2\text{PO}_4\text{F}$ minerals. M is blue, Li is yellow, F is light green, and SO_4 tetrahedra are dark green.

II.2.3. Electrochemical Performance

This new phase was tested for its electrochemical activity towards Li by assembling $\text{LiCuSO}_4\text{F}||\text{Li}$ Swagelok-type cells using a 1M LiPF_6 solution in *LP100* electrolyte (1:1:3 EC:PC:DMC ratio by weight) in an argon dry box. The cells were charged to either 4.9 V or 5.2 V (**Figure II.7 a**) at different rates (**Figure II.7 b**) via a VMP system (Biologic S.A., Claix, France) operating in galvanostatic mode, but no sign of redox activity could be detected in the voltage composition curves. This means that no Li can be removed from this structure till 5.2 V, the cutoff voltage at which we found the electrolyte to copiously decompose.

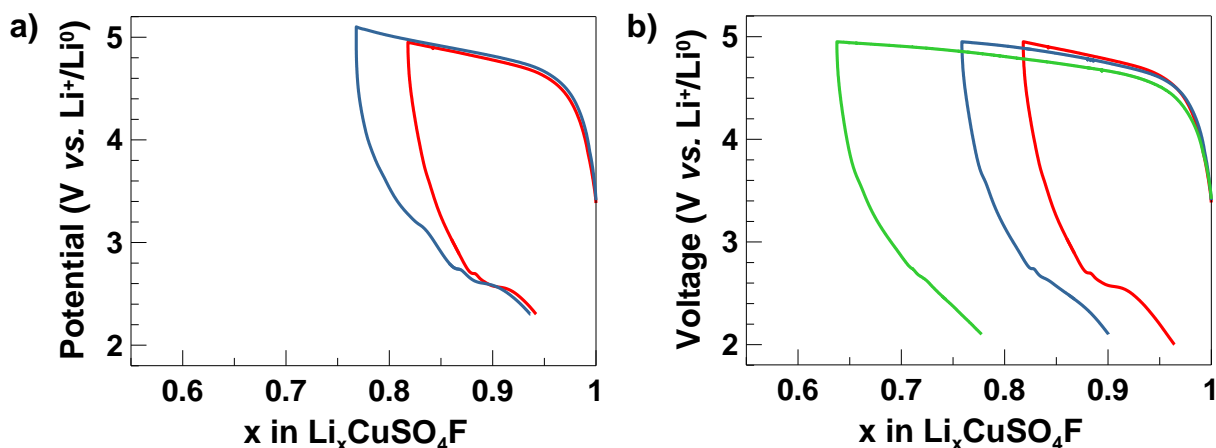


Figure II.7: Typical voltage–composition curve of $\text{LiCuSO}_4\text{F}||\text{Li}$ cells started on oxidation with (a) Different oxidation potential limit of 4.9 V (red) and 5.2 V (blue) at the same rate of C/15, and (b) Different cycle rates of C/15 (red), C/20 (blue) and C/30 (green).

II.2.4. Density Functional Theory (DFT) Calculations

Owing to its different structure from previous ordered LiMSO_4F ($M = \text{Mg}, \text{Mn}, \text{Co}, \text{Fe}, \text{Ni}$) phases, DFT calculations* have been used to evaluate the competitive formation of disordered or ordered *triplite* phase. Two perfectly ordered Li-Cu distributions in which Cu ions in which Cu ions exclusively lies on the M1 sites (noted Cu_{M1} as experimentally found) and on the M2 sites (Cu_{M2} , hypothetical structure) were first considered. Then, 9 different partial disordered Li-Cu orders (noted Cu_{M1M2}) were investigated, following the methodology described in ref. [256] (**Figure II.8**). After full structural relaxations, the perfectly ordered distributions Cu_{M1} and Cu_{M2} are found as two different polymorphs with equivalent energies, the latter being only 10 meV/FU higher than the former. This is rationalized in terms of local Cu environments which are very similar in both phases with evidence of the Jahn-Teller distortion expected. Interestingly, the 9 Cu_{M1M2} partially disordered phases, having a lower degree of Jahn-Teller distortion (**Figure II.9**), lie 60 meV to 200 meV/FU higher energy than the perfectly ordered Cu_{M1} and Cu_{M2} distributions. The fact that the energy difference between all these structures is far above the room temperature thermal energy (~ 25 meV) clearly indicates that configurational entropy associated to cation intermixing is not sufficient to stabilize the disordered polymorphs, suggesting that enthalpy governs the phase stability.

* DFT calculations were performed in cooperation with M. Saubanère and M. L. Doublet (Institut Charles Gerhardt and University of Montpellier).

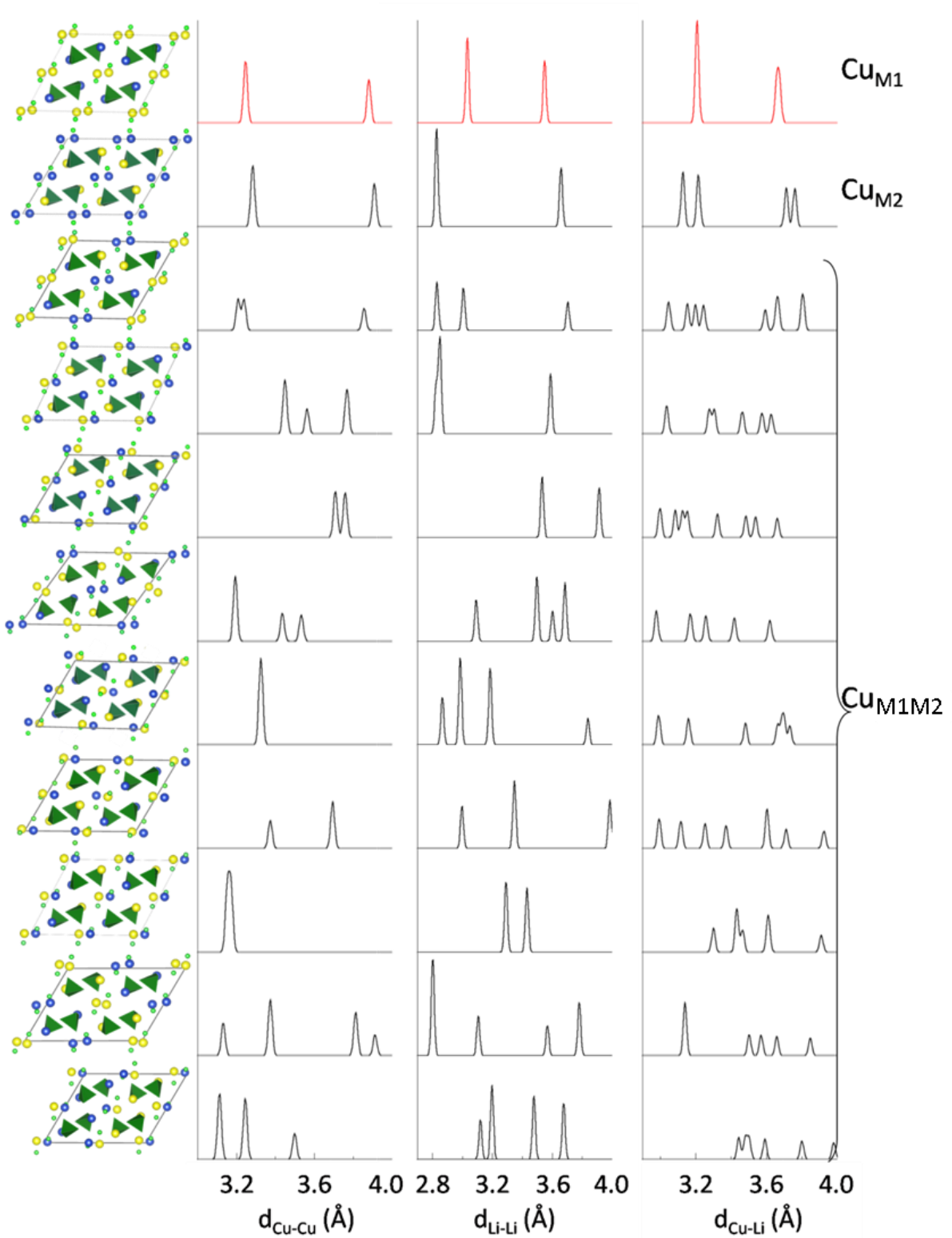


Figure II.8: (Left) Li-Cu orders considered, blue (yellow) spheres refer to Cu (Li) atoms, small green spheres refer to F and dark green tetrahedral to SO_4 tetrahedra, and oxygen atoms are not shown. The top phase corresponds to the Cu_{M1} order, followed by the Cu_{M2} order. Phases are ranked as a function of their energies, the top (down) one corresponding to the most (less) stable. (Right) Finger-print analysis [256] of Cu-Cu, Li-Li and Cu-Li distances, showing the effect of cation distribution.

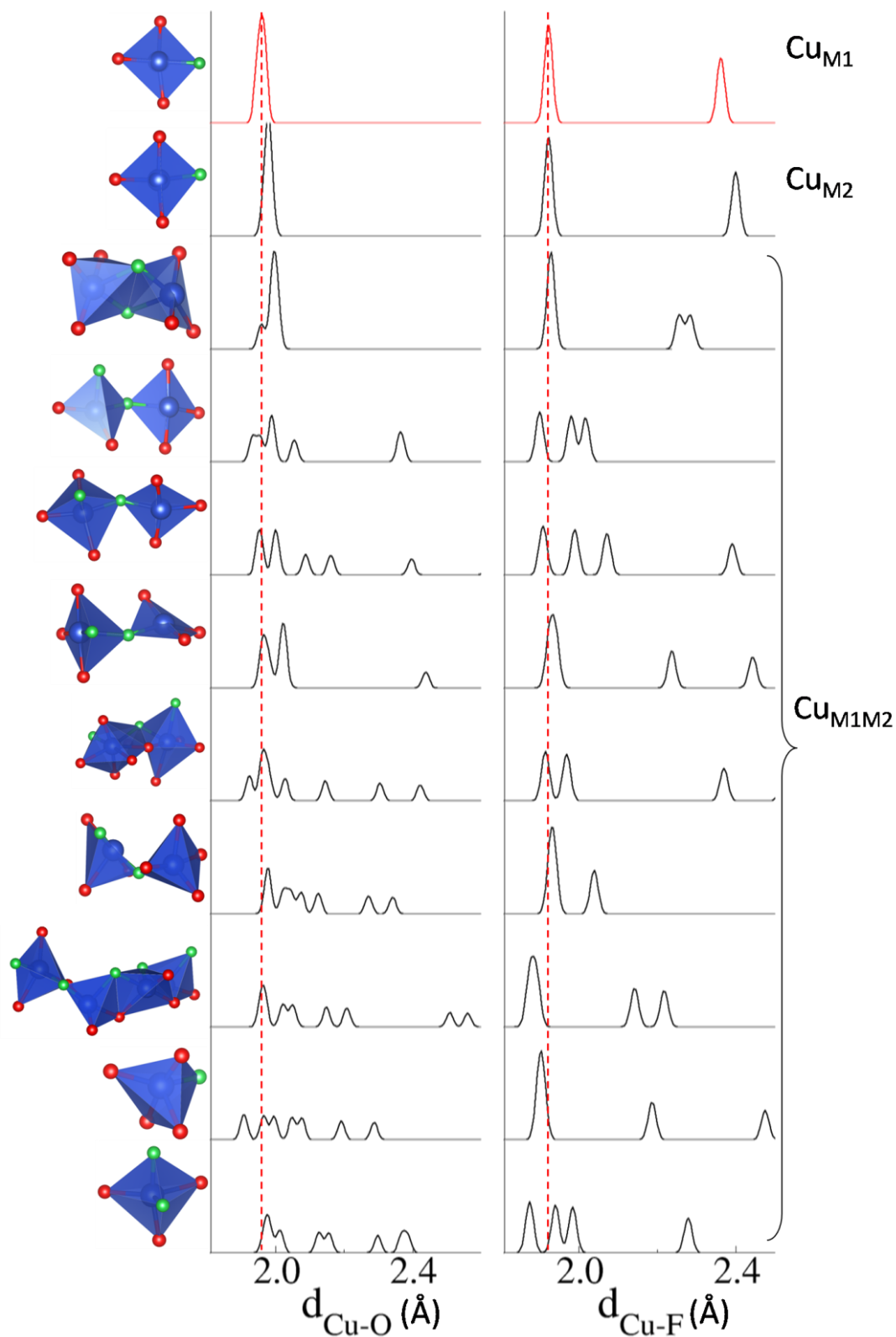


Figure II.9: (Left) Cu Local environment with a cutoff distance of 2.3 Å, blue sphere refers to Cu, red sphere to oxygen and green sphere to F. The top phase corresponds to the Cu_{M1} order, followed by the Cu_{M2} order. Phases are ranked as a function of their energies, the top (down) one corresponding to the most (less) stable. (Right) Finger-print analysis of Cu-O and Cu-F distances, showing the effect of Cu-Li distribution on local distortion of the Cu environment.

Figure II.10 a displays the electrostatic energy computed with a point charge model (using the DFT Bader charges) versus DFT energies for each Cu-Li order. Surprisingly, the higher the electrostatic energy, the lower the corresponding DFT energy is, indicating that the Cu local environment overrules the cation-cation electrostatic energy. For the sake of completion, we have also tested the stability of *tavorite* LiCuSO_4F using the *tavorite* LiFeSO_4F structure as the starting structure and substitute Fe for Cu. The *tavorite* polymorph is found 76 meV higher versus experimental ordered *triplite*.

To further understand the electrochemical behavior we perform the $T = 0\text{K}$ phase stability diagram of $\text{Li}_x\text{CuSO}_4\text{F}$ considering the different Li-Cu orders test-cases and the *tavorite* structure within DFT+U ($U = 4\text{ eV}$ for Cu) (**Figure II.10 b**). It shows the stabilization of the $\text{Li}_{0.5}\text{CuSO}_4\text{F}$ as an intermediate composition obtained by the delithiation of the experimental Li-Cu ordered phase. It is worth noting that all delithiations from different Li-Cu orders in the *triplite* lead to phase much higher in energy. The electrochemical potentials computed for the first delithiation process of LiCuSO_4F : $\text{LiCuSO}_4\text{F} - 0.5\text{Li} \rightarrow \text{Li}_{0.5}\text{CuSO}_4\text{F}$ is found to be 5.15 V. During the second delithiation process $\text{Li}_{0.5}\text{CuSO}_4\text{F} - \text{Li}_{0.5} \rightarrow \text{CuSO}_4\text{F}$ a phase transition may appear as the CuSO_4F phases derived from the *tavorite* appears to be 63 meV more stable than CuSO_4F derived from the experimental ordered *triplite*, the potential of this reaction is found to be 5.4 V.

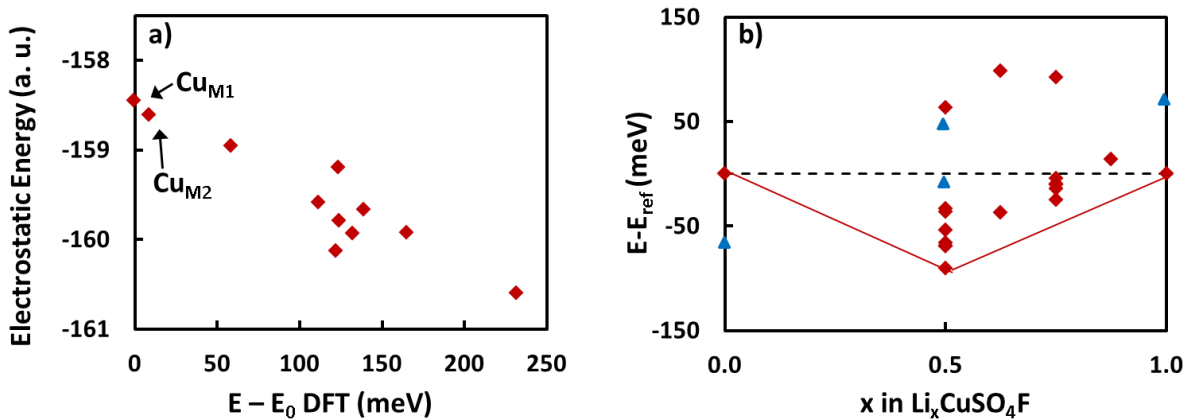


Figure II.10: (a) Electrostatic energy of the different Li-Cu order test-cases considered for the *triplite* structure computed with a point charge model using the DFT+U bader charges as a function of the DFT + U energy relative to the energy of the experimental Li-Cu ordered and disordered phases. (b) $T = 0\text{K}$ phase stability diagram of $\text{Li}_x\text{CuSO}_4\text{F}$ as a function of x from DFT + U calculations ($U_{\text{eff}} = 4\text{ eV}$ for Cu). The red diamonds refer to single $\text{Li}_x\text{CuSO}_4\text{F}$ phases obtained from Li removal from the relaxed experimental ordered *triplite* LiCuSO_4F structure, and the blue triangle corresponds to the phase obtained by substituting Fe by Cu in the *tavorite* LiFeSO_4F as in Ref [248].

To focus on the redox mechanism, we plotted the atom-projected density of states (**Figure II.11 a**) of the LiCuSO_4F structure. Interestingly, the DOS reveals a dominant contribution of the oxygen electronic levels at the Fermi level, suggesting an oxidation process mostly driven by the oxygen and negligible modification of the Cu^{2+} environment upon Li-removal. This is confirmed by the DOS in the partially delithiated phase $\text{Li}_{0.5}\text{CuSO}_4\text{F}$ where states the upper Fermi Level are primarily of oxygen type (**Figure II.11 b**). Combining the electrochemical test and DFT calculations, the removal of 0.5 Li^+ from the LiCuSO_4F phase should be achievable and reversible at 5.15 V provided that electrolytes, stable against oxidation up to such high voltages, could be developed in the future.

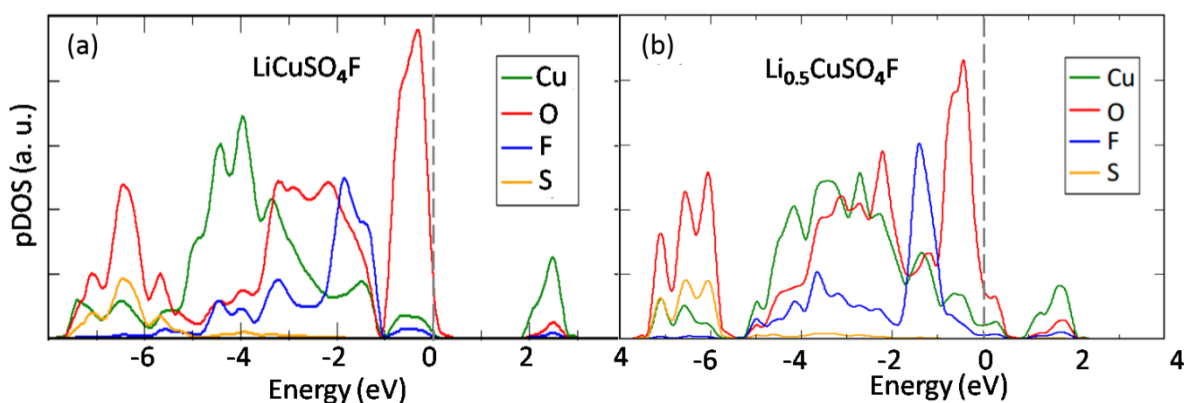


Figure II.11: Atom-projected density of states for (a) LiCuSO_4F and (b) $\text{Li}_{0.5}\text{CuSO}_4\text{F}$ as obtained by DFT+U calculation ($U_{\text{eff}} = 4 \text{ eV}$ for Cu).

II.2.5. Conductivity Measurement

To understand the poor electrochemical performance of LiCuSO_4F , we decided to measure its transport properties. Conductivities (a.c. and d.c.) were measured on a sintered LiCuSO_4F pellet (synthesized directly at 415°C , $\varnothing 10 \text{ mm}$, compactness 89%) between ionically blocking gold electrodes. The measurement was done under argon at various stabilized temperatures ranging from 100 to 300°C in a frequency range of 30 MHz to 0.1 Hz and with an excitation voltage of 100 mV . **Figure II.12** shows the evolution of the a.c. conductivity of LiCuSO_4F . An activation energy of 1.11 eV was obtained by fitting the a.c. data with an Arrhenius law and a room temperature a.c. conductivity of $1.5 \times 10^{-15} \text{ S}\cdot\text{cm}^{-1}$ was extrapolated. The low frequency tail of the impedance spectra suggests an ionic component to the overall conductivity.

To further grasp insights on this ionic vs. electronic competition, d.c. conductivity measurements were done by applying polarization voltages. An activation energy of $E_a = 0.9 \text{ eV}$ was found with conductivities values slightly higher than the a.c. ones which cumulate

both electronic and ionic contribution, hence indicating that the electronic conductivity is dominating. Interestingly, a similar behavior had been found for LiFePO_4 which was explained via a polaronic model (*e.g.* hopping of localized electrons) and was confirmed by ab-initio calculations [257]. Lastly, For meaningful comparison we measured the conductivity of *triplite* LiFeSO_4F (sintered at 250°C for 1h $\varnothing 10$ mm, compactness 70%) under similar experimental protocols and found E_a for a.c. and d.c. of LiFeSO_4F are 0.79 eV and 0.78 eV respectively. The strong electronic contribution to the overall conductivity displayed by these insulating-like polyanionic compounds calls for further investigations of their transport properties.

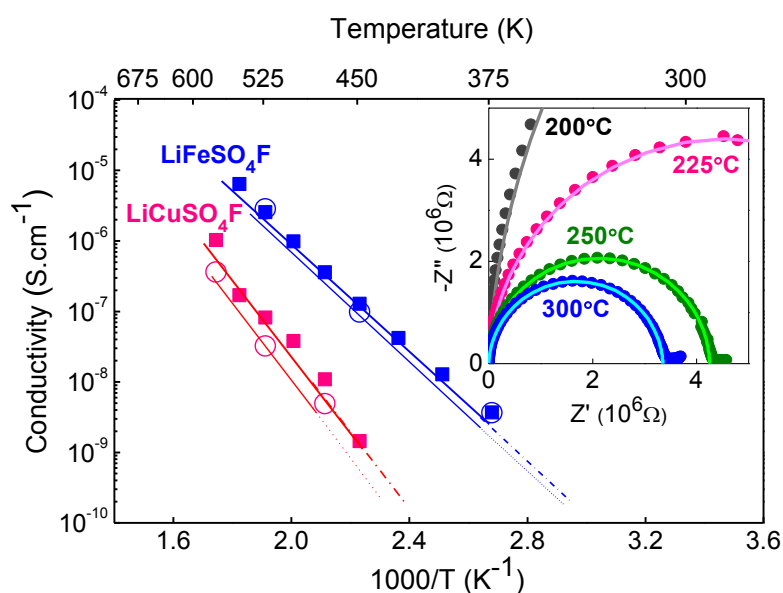


Figure II.12: Transport properties of LiFeSO_4F (blue) and LiCuSO_4F (pink), the filled squares and open circles refer to a.c. and d.c. measurements, respectively; the inset shows impedance spectra (filled circles) and the fit of each spectra (continuous line) of LiCuSO_4F in argon at various temperatures.

II.2.6. Magnetic Property

The temperature dependence of magnetization was measured using a SQUID (XL, Quantum Design), under both zero-field cooled (ZFC) and field cooled (FC) conditions under 1 kOe between 50 K and 300 K. The magnetic susceptibility of LiCuSO_4F (**Figure II.13**) shows a typical Curie-Weiss paramagnetic behavior. This region was fitted to the Curie-Weiss equation $\chi_{\text{cw}} = C/(T - \theta) + \chi_0$. An effective magnetic moment of $\mu_{\text{eff}} = 1.98 \mu\text{B}$ per Cu and $\theta = -55$ K are deduced. This value nearly agrees with the theoretical $\mu_{\text{eff}} = 1.73 \mu\text{B}$ that is expected for Cu^{2+} [258]. Numerous publications reported values of μ_{eff} varying from (1.8 - 2.1 μB) for Cu^{2+} pertaining to different compounds [258]. The negative Curie-Weiss temperature indicates strong antiferromagnetic correlations. Neutron powder diffraction experiments were

performed on D20 diffractometer at the Institut Laue-Langevin (ILL, Grenoble, France) with a wavelength of 2.4 \AA in the low temperature range 2 K to 200 K. No new peaks were observed on the diffraction patterns (**Figure II.14**), suggesting no long-range antiferromagnetic order.

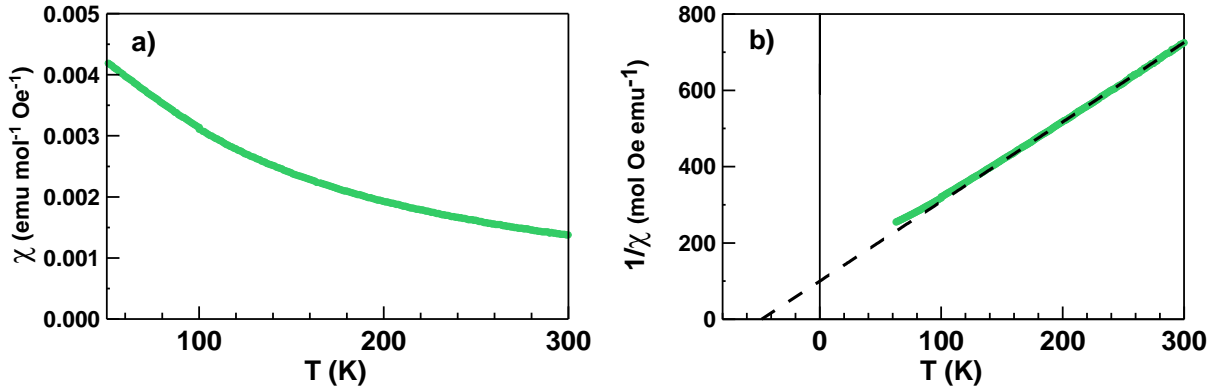


Figure II.13: (a) Temperature dependence of the magnetic susceptibility of LiCuSO_4F , measured under field-cooling conditions with a field of 1 kOe between 300 K and 2 K. The fit of the Curie–Weiss law is shown in (b) The inverse magnetic susceptibility ($1/\chi$) as a function of temperature as well as the Curie–Weiss fit as indicated by the black dotted line.

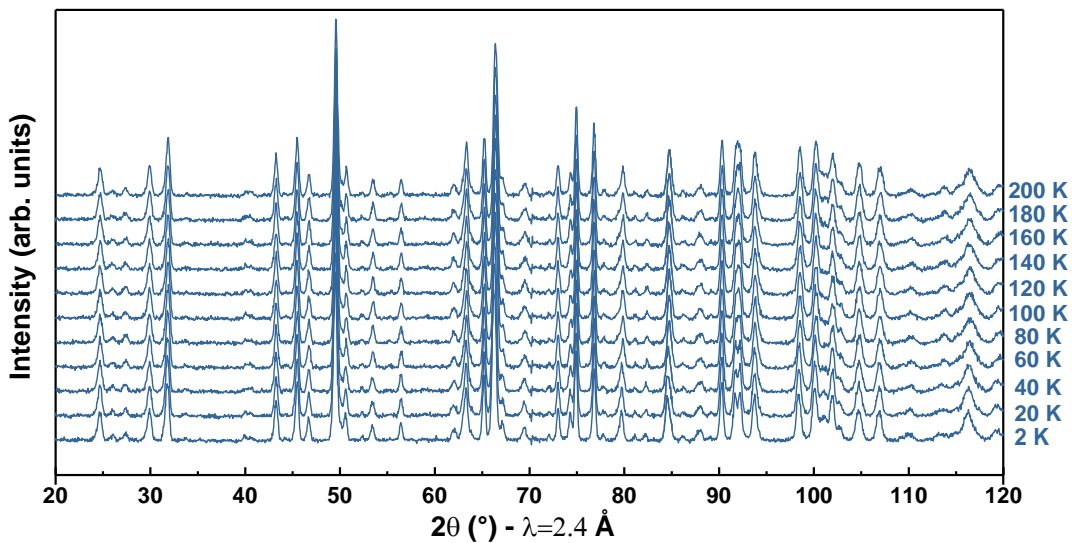


Figure II.14: Temperature dependence of neutron powder diffraction patterns collected between 2 K to 200 K (From bottom to top).

II.3. Exploration of Copper-based Oxysulfate: $\text{Li}_2\text{Cu}_2\text{O}(\text{SO}_4)_2$

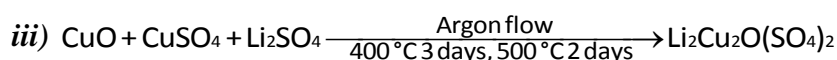
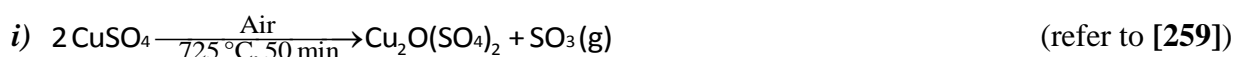
II.3.1. Synthesis

As previously explained, $\text{Li}_2\text{Cu}_2\text{O}(\text{SO}_4)_2$ was first spotted as a green powder during the synthesis of LiCuSO_4F (see § II.2.1). This green powder obtained from scrapping the surface of the pellet was shown to display a completely different XRD diffraction pattern, which triggers our interest to further explore its growth mechanism, composition and structure. Preserving the protocol defined for preparing LiCuSO_4F but by only extending the annealing time from 8 – 10 hours to 4 days, a complete emerald green pellet was obtained (**Figure II.15**), which proves to be $\text{Li}_2\text{Cu}_2\text{O}(\text{SO}_4)_2$ in the following section.



Figure II.15: The photo of pellet synthesized and the resulting ground powder of $\text{Li}_2\text{Cu}_2\text{O}(\text{SO}_4)_2$.

Subsequently, other routes consisting in the use of non-fluorinated precursors had also been successfully explored to prepare $\text{Li}_2\text{Cu}_2\text{O}(\text{SO}_4)_2$:



In each route two or three components among Li_2SO_4 (Alfa Aesar, 99.7%), Li_2O (Alfa Aesar, 99.5%), CuSO_4 (Alfa Aesar, Reagent grade), and CuO (Alfa Aesar, 99.9%) were used as precursors for the targeted phase. The powders were thoroughly ball milled in an argon-filled ball-mill jar with a stainless-steel ball/powder weight ratio of 20, pressed into a pellet and

annealed under argon flow for 4 – 5 days at 400°C – 500°C (specific annealing time and temperature is written in each reaction above) to produce a well crystallized sample with sharp reflections on the XRD powder pattern reminiscent of a new $\text{Li}_2\text{Cu}_2\text{O}(\text{SO}_4)_2$ phase as described next. The recovered powders prepared through route *i* contains minute amounts of Li_2SO_4 , however routes *ii* and *iii* were found to display an X-ray diffraction pattern with no sign of impurity phases.

II.3.2. Structural Characterization

The X-ray diffraction (XRD) pattern of $\text{Li}_2\text{Cu}_2\text{O}(\text{SO}_4)_2$ was recorded in Bragg-Brentano geometry with a Bruker D8 Advance diffractometer. The pattern contains several peaks whose width and shape indicating a highly crystallized sample as the peak width corresponds to the instrumental one (absence of sample broadening). All diffraction peaks can be indexed using the Dicvol program [251] in a tetragonal unit cell, with lattice parameters $a = 8.32586(2)$ Å and $c = 5.091351(17)$ Å. The corresponding volume ($V = 352.933(2)$ Å³) is suitable to accommodate two formulae per unit cell. This unit cell was confirmed by Transmission Electron Microscopy (TEM) investigation. EDX analysis revealed a Cu:S atomic ratio of 50(1):49(1) (Figure II.16), which agrees well with the $\text{Li}_2\text{Cu}_2\text{O}(\text{SO}_4)_2$ formula which was independently confirmed by atomic absorption analysis as the ratio of Li to Cu and S was found to nicely match the nominal composition. ED patterns and EDX spectra were obtained with a *Tecnai G2* electron microscope operated at 200 kV.

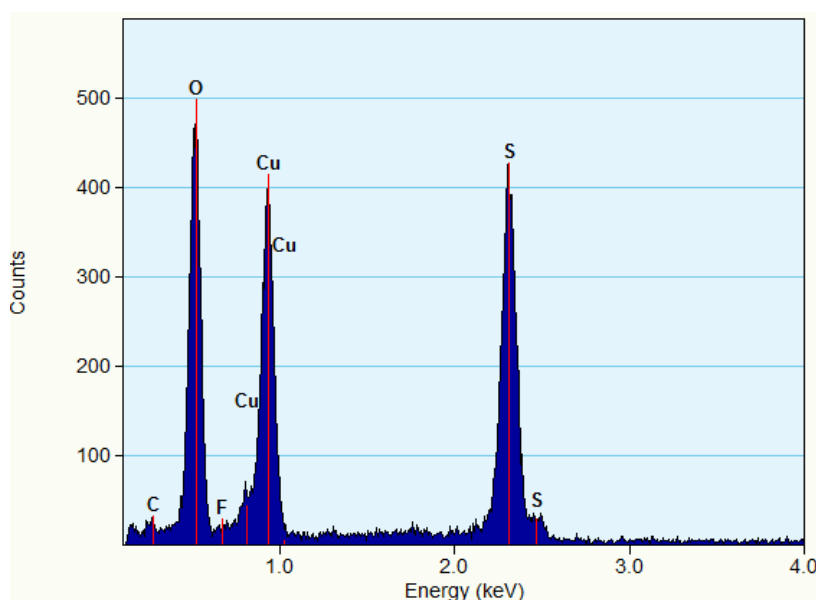


Figure II.16: EDX spectrum of $\text{Li}_2\text{Cu}_2\text{O}(\text{SO}_4)_2$.

All obtained ED patterns can be indexed on a primitive tetragonal unit cell with approximate lattice parameters $a \approx 8.3 \text{ \AA}$, $c \approx 5.1 \text{ \AA}$ (**Figure II.17**), thus confirming at first sight the unit cell found by XRD. However, inspection of the [001] ED pattern shows that the angle between the a^* and b^* reciprocal lattice axes slightly deviates from 90° ; this may reveal a small monoclinic distortion or result from a damage caused by the electron beam (the latter is supported by synchrotron X-ray diffraction experiments). Indeed, the material demonstrates very high sensitivity to the electron beam irradiation, which makes high resolution TEM imaging virtually impossible. The only reflection condition was found to be $00l$: $l = 2n$. This reflection condition is not visible due to multiple diffraction, however it was confirmed by vanishing the $00l$, $l \neq 2n$ reflections upon tilting the crystal around the c^* reciprocal lattice axis. The possible space groups are $P4_2/m$, $P4_2$, or assuming a possible monoclinic distortion, $P2_1/m$, $P2_1$.

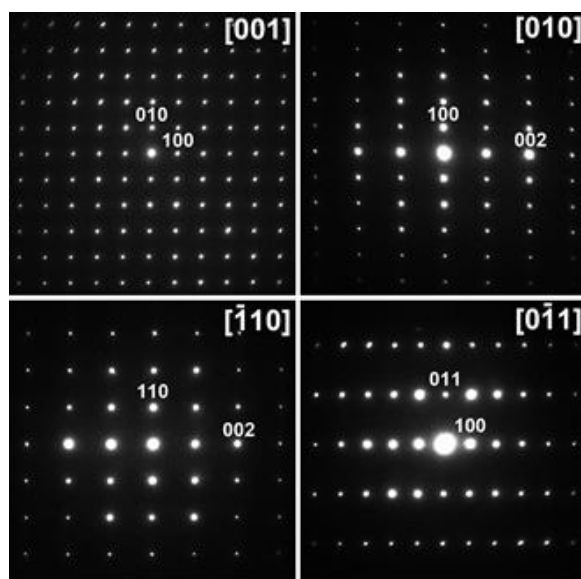


Figure II.17: Electron diffraction patterns of $\text{Li}_2\text{Cu}_2\text{O}(\text{SO}_4)_2$ along different crystallographic directions.

Investigation of a possible monoclinic distortion was performed using high resolution synchrotron X-ray diffraction. The finely ground powder was loaded in a 0.5 mm diameter capillary and the sample was measured in transmission mode ($\lambda = 0.41374 \text{ \AA}$) on the 11-BM beamline at Argonne National Lab. (**Figure II.18 a**). Structural determination was undertaken from the synchrotron data using direct methods with the EXPO software [260]. Absolutely no splitting of the reflections was observed, so the determination was conducted in the $P4_2/m$ space group, and lead to a pertinent atomic distribution of Cu, S and O in the unit cell. As lithium atoms are weakly scattered by X-rays due to their small number of electrons, we used neutron powder diffraction to locate them. The sample was put in a cylindrical vanadium container and measured on the HRPT neutron diffractometer at SINQ-PSI (Villigen,

Switzerland) with a wavelength of 1.4928 \AA [261]. The partial “ $\text{Cu}_2\text{O}(\text{SO}_4)_2$ ” model deduced from XRD was implemented into the neutron diffraction pattern and difference Fourier maps were calculated to locate Li atoms using the GFourier program available in the FullProf suite of program [253]. Negative peaks (the neutron scattering length of Li is negative: $b_{\text{Li}} = -1.90 \text{ fm}$) can be seen in the $y = 1/2$ section of the Fourier map (**Figure II.18 b**, right), revealing two lithium positions Li1 and Li2 corresponding to the $2d$ and $2f$ Wyckoff sites, respectively. The final structural model was obtained by a combined Rietveld refinement [262] of the neutron and Synchrotron XRD patterns conducted with the FullProf program [253], and the result is shown in **Figure II.18**. The structural information and atomic positions within the tetragonal $P4_2/m$ unit cell are compiled in **Table II.2**.

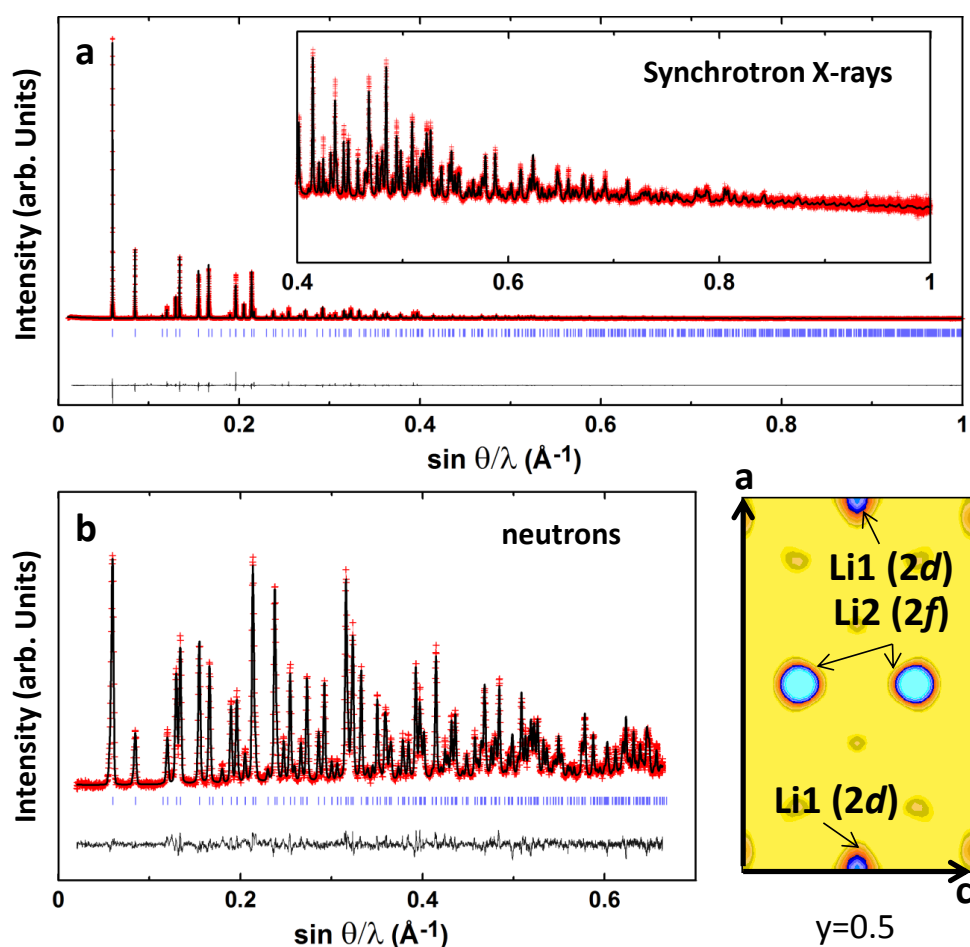


Figure II.18: Rietveld refinement of (a) Synchrotron and (b) Neutron diffraction patterns of $\text{Li}_2\text{Cu}_2\text{O}(\text{SO}_4)_2$. The x-axis plots $\sin(\theta)/\lambda$ which allows a direct comparison between the two patterns even if recorded at different wavelengths. The red crosses, black continuous line and bottom dark grey line represent the observed, calculated, and difference patterns, respectively. Vertical blue tick bars are the Bragg positions. The inset in (a) is an enlargement at high angle. The right part of (b) is a cut of the difference Fourier map at $y = 1/2$. Blue domains correspond to negative values and reveal Li positions.

Table II.2: Structural parameters for $\text{Li}_2\text{Cu}_2\text{O}(\text{SO}_4)_2$, deduced from the combined Rietveld refinement of the Synchrotron XRD and neutron diffraction patterns. A bond valence sum analysis (BVS) for each atom is also reported.

$\text{Li}_2\text{Cu}_2\text{O}(\text{SO}_4)_2$, Space Group: $P4_2/m$						
$a = 8.32586(2) \text{ \AA}$, $c = 5.091351(17) \text{ \AA}$, $V = 352.933(2) \text{ \AA}^3$, Density = 3.285 g/cm^3 , $Z = 2$						
Atom	Wyckoff site	x	y	z	$B(\text{\AA}^2)$	BVS
Li1	$2d$	0	0.5	0.5	2.0(3)	0.916(2)
Li2	$2f$	0.5	0.5	0.25	0.62(19)	1.255(4)
Cu	$4j$	0.16033(9)	0.06497(9)	0	0.482(11)	2.030(4)
S	$4j$	0.31730(18)	0.22610(17)	0.5	0.60(2)	6.036(21)
O1	$8k$	0.3305(3)	0.1237(2)	0.7367(4)	1.32(4)	2.019(9)
O2	$4j$	0.1679(3)	0.3132(3)	0.5	0.85(5)	2.007(13)
O2	$4j$	0.4577(3)	0.3368(4)	0.5	0.75(5)	2.069(13)
O4	$2e$	0	0	0.25	0.46(7)	2.073(2)

Reliability parameters: $\chi^2 = 3.02$;
 Neutrons: Bragg R-factor = 4.16%, Rf-factor = 2.38%;
 Synchrotron: Bragg R-factor = 5.39%, Rf-factor = 4.57%

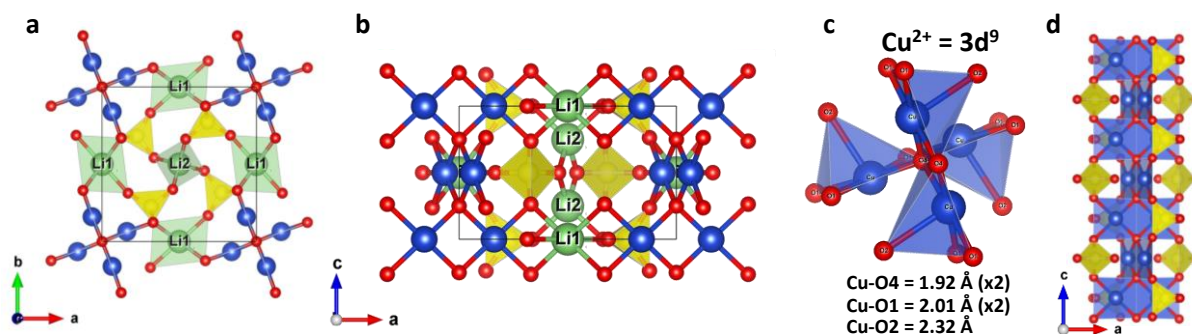


Figure II.19: Structure of $\text{Li}_2\text{Cu}_2\text{O}(\text{SO}_4)_2$: (a) and (b) General view of the unit cell content along $[001]$ and $[010]$, respectively. (c) Cu coordination and Cu-O bond lengths. (d) The chains of edge-shared square CuO_4 running along $[001]$. Li is green, Cu is blue, O is red, S is yellow.

The four Cu and S atoms are placed on the Wyckoff site $4j$, while oxygen is distributed among four sites. O1, O2 and O3 define the SO_4 tetrahedra while O4 is on the $2e$ position. **Figure II.19** presents the structure of $\text{Li}_2\text{Cu}_2\text{O}(\text{SO}_4)_2$. Cu is surrounded by four oxygen atoms forming an almost perfect square planar environment (two Cu-O distances at 1.92 and two at 2.01 \AA). A fifth oxygen (O2) is found at a longer distance of 2.32 \AA to form a square-based CuO_5 pyramid. As a square planar environment is commonly expected for Jahn-Teller Cu^{2+}

ions (electronic configuration d^9), the structure is from here on described as such. The CuO_4 squares are linked through edges to form Cu_2O_6 dimers, and are repeated with a 90° rotation under the effect of the 4_2 screw axis. This gives rise to infinite chains running along $[001]$. O4, the only oxygen not being part of SO_4 tetrahedra, constitutes the link of the chain. The SO_4 groups are positioned around the chains, with two ligands pointing towards Li2 giving rise to tetrahedral coordination. Li1 atoms are located in an octahedral environment, built on four oxygens linked to Cu ($4 \times \text{O1}$) and two oxygens from a sulfate group ($2 \times \text{O2}$). In order to confirm the refined structure, a bond valence sum analysis was performed using the Zachariasen formula $V_i = \sum_j s_{ij} = \sum \exp\{(d_0 - d_{ij})/0.37\}$ with the d_0 parameters characterizing cation-anion pairs taken from reference [263]. Results are indicated in **Table II.2** and the obtained valence sums are in perfect agreement with oxidation states of +1, +2, +6 and -2 for Li, Cu, S, and O respectively.

II.3.3. Thermal Stability Analyses

The thermal stability of $\text{Li}_2\text{Cu}_2\text{O}(\text{SO}_4)_2$ was determined by thermogravimetric analysis (TGA) coupled with mass spectrometry. The TGA profiles collected by heating the compound with the rate of $5^\circ\text{C}/\text{min}$ either in air or argon indicate a decomposition temperature of 580°C (**Figure II.20 a**), above which SO and SO_2 were released. This decomposition temperature was confirmed by *in operando* high temperature XRD measurements (**Figure II.20, inset**) which reveals CuO as the main decomposition product (**Figure II.20 b**).

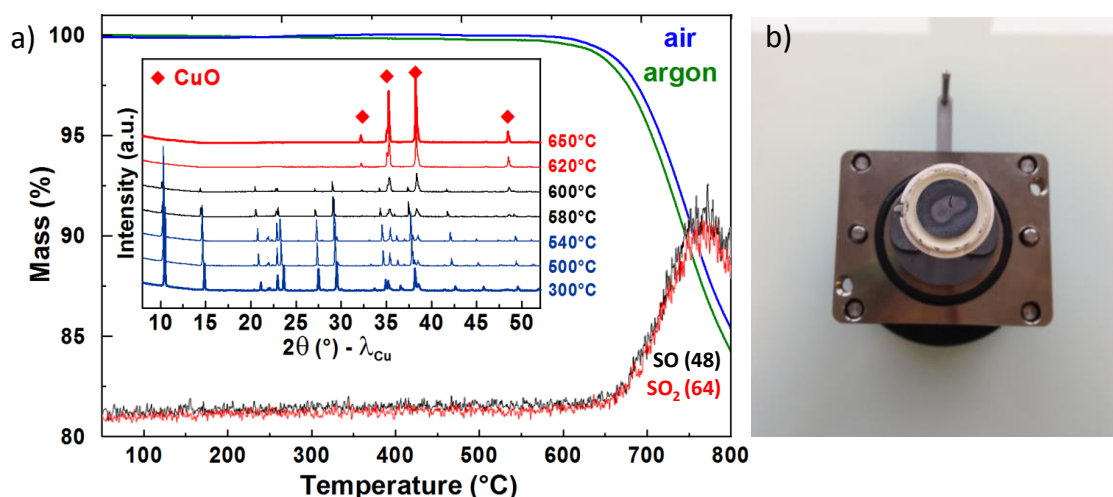


Figure II.20: (a) Thermal stability of $\text{Li}_2\text{Cu}_2\text{O}(\text{SO}_4)_2$. TGA under air (blue line) and argon (green line) between room temperature and 800°C , coupled with mass spectrometry revealing SO and SO_2 gas formation above 600°C (black and red lines). The inset shows the XRD powder patterns of $\text{Li}_2\text{Cu}_2\text{O}(\text{SO}_4)_2$ recorded in air between 300°C and 650°C . Note the appearance of CuO from 580°C which becomes single phase above 600°C (red diamond symbols). (b) Photo of CuO (black) product obtained from *in situ* high temperature XRD measurements after cooling down.

II.3.4. Bond Valence Energy Landscapes (BVEL)

A prerequisite for Li-based materials to be used as electrodes in Li-ion batteries is the existence of Li-diffusion paths within the structure. To get more information on how Li ions can travel inside the framework, we generated Bond Valence Energy Landscapes (BVEL) using the BondStr program available in the FullProf suite by using the soft bond valence sum parameters developed by S. Adams [264]. BVEL are obtained from soft-BVS parameters by transforming the valence into energy units, using a Morse-type potential for the attractive part and a screened Coulomb potential for the repulsive part [265]. The probing ion, in our case Li^+ for $\text{Li}_2\text{Cu}_2\text{O}(\text{SO}_4)_2$, is placed in all points of the unit cell and its interaction energy, using the above mentioned potential, is calculated up to a common distance of 10 Å. The minimal energies leading to an infinitely connected surface for Li in $\text{Li}_2\text{Cu}_2\text{O}(\text{SO}_4)_2$ is denoted as “activation energy”.

Figure II.21 shows the generated BVEL for Li^+ conduction in the “ $\text{Li}_x\text{Cu}_2\text{O}(\text{SO}_4)_2$ ” framework. A surface level corresponding to the value of 1.8 eV above the minimum was chosen to plot the BVEL. This corresponds to 0.2 eV above the activation energy for Li transport. It does not come as a surprise that the highlighted Li^+ conduction paths meet the Li1 and Li2 positions we determined from neutron powder diffraction, but it also reveals that Li conduction can occur through a three dimensional pathway as shapes around the helical Cu-O chains. This was an impetus to further study the electrochemical properties of this phase as discussed next.

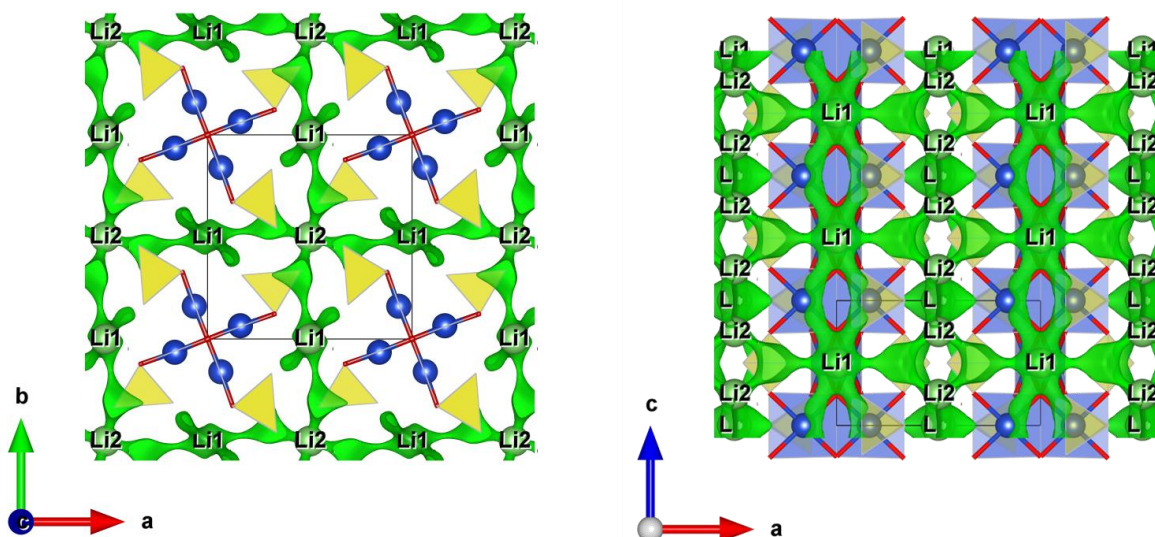


Figure II.21: Bond valence energy landscape deduced for $\text{Li}_2\text{Cu}_2\text{O}(\text{SO}_4)_2$. The green domains correspond to the migration paths for Li in the structure, obtained using an iso-surface value of 1.8 eV over the minimum energy.

II.3.5. Electrochemical Properties

The electrochemical properties of $\text{Li}_2\text{Cu}_2\text{O}(\text{SO}_4)_2$ versus Li were tested either in oxidation or reduction using Swagelok cells which cycled in a temperature controlled environment ($T=25 \pm 0.5^\circ\text{C}$) using a VMP system operating in galvanostatic mode. The working electrode of about 6 to 8 mg of active material was made by ball milling powders of $\text{Li}_2\text{Cu}_2\text{O}(\text{SO}_4)_2$ with 20% in mass of carbon SP for 15 minutes. The positive electrode was separated from the Li metal disc negative electrode by a glass fiber sheet saturated with *LP100* electrolyte. If not otherwise specified in the figure captions, cells were cycled at C/25.

I.3.5.1. “ $\text{Cu}^{3+}/\text{Cu}^{2+}$ ” Redox Activity vs. Li^+/Li^0

Upon initial oxidation, the potential of the $\text{Li}_2\text{Cu}_2\text{O}(\text{SO}_4)_2$ cell rapidly increases to 4.5 V and then progressively reaches a plateau located at 4.75 V with the concomitant release of nearly 0.5 Li. Upon discharge, ~ 0.3 out of the 0.5 Li can be reinserted. This leads to a sustainable reversible capacity of 0.3 Li per formula unit centered at 4.7 V vs. Li^+/Li^0 which corresponds to *ca.* 20 mA·h/g (**Figure II.22 a**). Such large irreversibility between the first cycle and the subsequent ones is most likely due to electrolyte decomposition. We find that the irreversible component of the $\text{Li}_2\text{Cu}_2\text{O}(\text{SO}_4)_2/\text{Carbon}$ electrode capacity is dependent on grain size, with the minimum irreversibility achieved when a hand-ground rather than ball milled composite was used as positive electrode (**Figure II.22 b**).

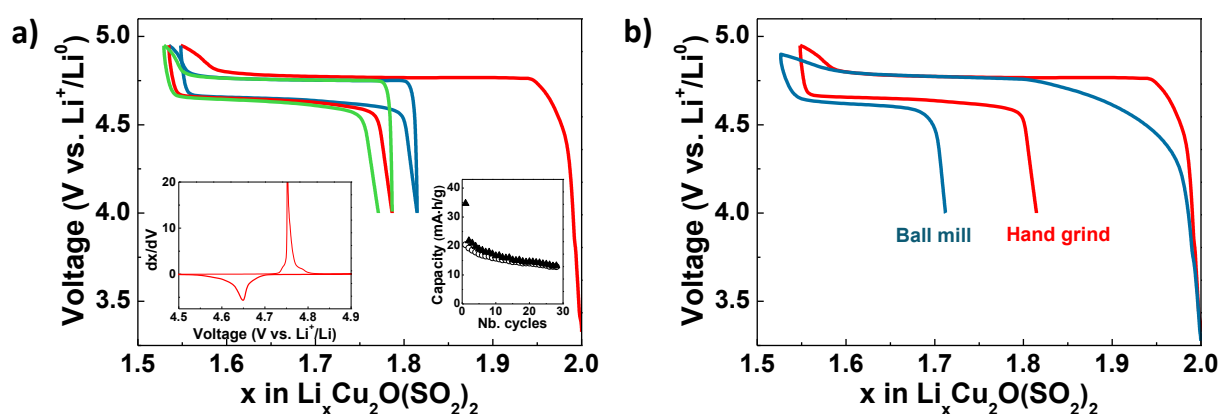


Figure II.22: Typical voltage–composition curves of $\text{Li}_2\text{Cu}_2\text{O}(\text{SO}_4)_2||\text{Li}$ cells (a) Started on oxidation at C/25. The first, second and third cycles are shown in red, blue and green, respectively. Capacity retention on charge and discharge are presented in filled triangles and open circles (right insert). The derivative curves for the second cycle are also reported (left insert). (b) Whose cathodes are prepared by hand grinding (red) and ball-milled (blue) for 5 mins, both of which were cycled at C/25.

Attempts to remove more Li by increasing the charge cutoff voltage led to a second oxidation (~ 5.1 V) pseudo-plateau. Its origin is mainly due to copious electrolyte decomposition since almost no extra reversible capacity was found on the subsequent discharge. Moreover, the persistence of the 4.7 V process with similar amplitude whether a 4.8 or 5.2 V charging cutoff voltage was used indicates that the material remains stable at high voltage (**Figure II.23**). This suggests that more Li might be extracted from this compound if electrolytes highly resistant against oxidation could be found.

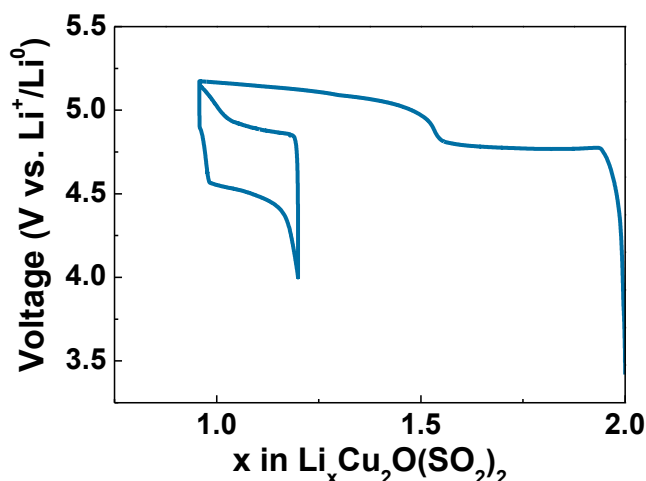


Figure II.23: Voltage–composition curves of a $\text{Li}_2\text{Cu}_2\text{O}(\text{SO}_4)_2||\text{Li}$ cell cycled up to 5.2 V.

The Li extraction-insertion mechanism in $\text{Li}_2\text{Cu}_2\text{O}(\text{SO}_4)_2$ was further examined by *in situ* X-ray diffraction (**Figure II.24**). During cell charging, no noticeable changes are observed in the X-ray powder pattern until the voltage reaches the plateau at 4.75 V; this supports the notion that the initial measured capacity is mainly due to electrolyte decomposition. Once the plateau is reached, a new set of XRD peaks appear (at a lower angle than those of the pristine phase) and they grow upon further delithiation at the expense of the pristine phase prior to become single phase when the voltage departs from 4.75 V. The oxidized material of composition $\sim \text{Li}_{1.7}\text{Cu}_2\text{O}(\text{SO}_4)_2$, as deduced from both coulometric titration and estimate of the irreversible capacity, is single phase. It crystallizes in a monoclinic structure with lattice parameters $a = 8.64 \text{ \AA}$, $b = 8.59 \text{ \AA}$, $c = 4.92 \text{ \AA}$ and $\beta = 93.9^\circ$. The latter corresponds to a monoclinic distortion of the pristine cell with, however, a volume 3% greater than the di-lithiated phase (364.3 \AA^3 vs. 352.9 \AA^3). Unfortunately, absorption by the Beryllium window combined with the broadening of peaks caused by the electrochemical process prevented us from more precise and definite structural determination. The XRD pattern taken at the end of the subsequent discharge superimposes neatly with the pristine one. This is indicative of a fully reversible Li-driven “ $\text{Cu}^{3+}/\text{Cu}^{2+}$ ” redox process in $\text{Li}_2\text{Cu}_2\text{O}(\text{SO}_4)_2$.

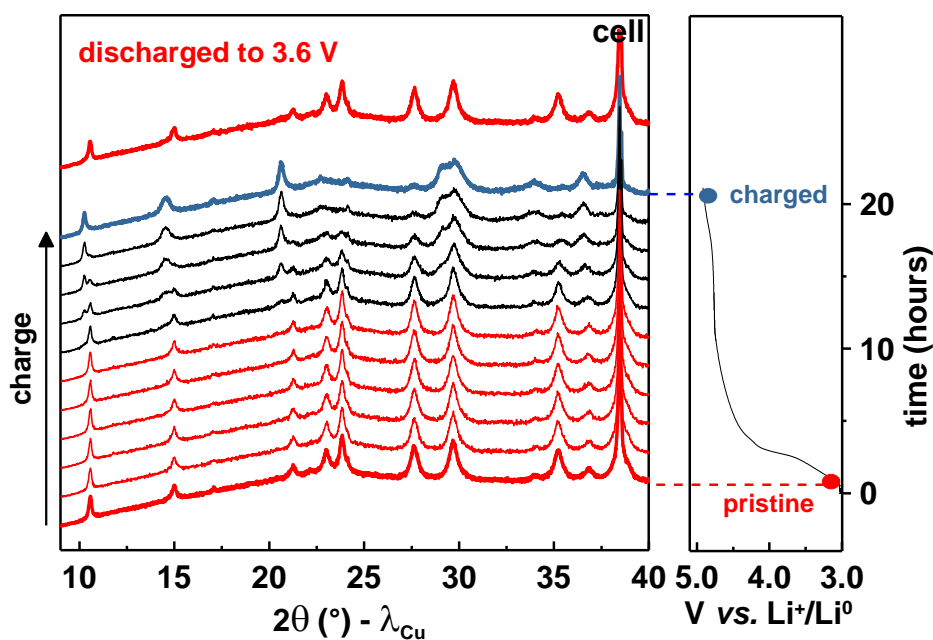


Figure II.24: Behavior of a $\text{Li}_2\text{Cu}_2\text{O}(\text{SO}_4)_2\|\text{Li}$ *in situ* cell on charge at C/25. Left: *in situ* XRD patterns recorded behind a Be window while the cell is charged to 5 V (right curve). The red patterns correspond to the pristine phase, the blue one is the pattern of the fully oxidized $\text{Li}_{1.7}\text{Cu}_2\text{O}(\text{SO}_4)_2$, while the black ones correspond to biphasic domains. The pattern on top was recorded at 3.6 V at the subsequent discharge, and indicates the good reversibility of the process.

I.3.5.2. $\text{Cu}^{2+}/\text{Cu}^+/\text{Cu}^0$ Redox Activity vs. Li^+/Li^0

To further explore the electrochemical activity of this compound towards Li, a second $\text{Li}_2\text{Cu}_2\text{O}(\text{SO}_4)_2\|\text{Li}$ cell was initially started on reduction. The cell voltage rapidly drops to 2.3 V and decreases continuously and smoothly to 2.1 V with the concomitant uptake of ~ 2 Li^+ (**Figure II.25**). Then it shows faster voltage decay down to 1.8 V corresponding to the uptake of an extra 0.4 Li^+ . The 2.4 inserted Li^+ can be fully removed when the cell is charged back to 4.6 V (**Figure II.25**, red curve), and presents a voltage profile quite dissimilar from the discharge curve of classical intercalation compounds: it enlists first a pseudo plateau around 3.3 V followed by a second one above 4 V. All taken together, the reduction process exhibits a single redox peak on discharge as opposed to two on oxidation parted by nearly 1 V, suggesting different reacting paths. This difference is highlighted by the large shift of the reduction peaks between the first (solid line) and second (dashed line) derivative curves (**Figure II.25**, bottom). Once this “electrode formation stage”, which progresses through the 3rd cycle, is over, the charge discharge curves superimposed leading to a sustained capacity of 200 mA·h/g upon cycling (**Figure II.25**, bottom left inset). By limiting the charge cutoff voltage to 3.9 V the overall cell capacity was found to decrease to 150 mA·h/g with the maintenance of a good capacity retention (**Figure II.25**, bottom right inset).

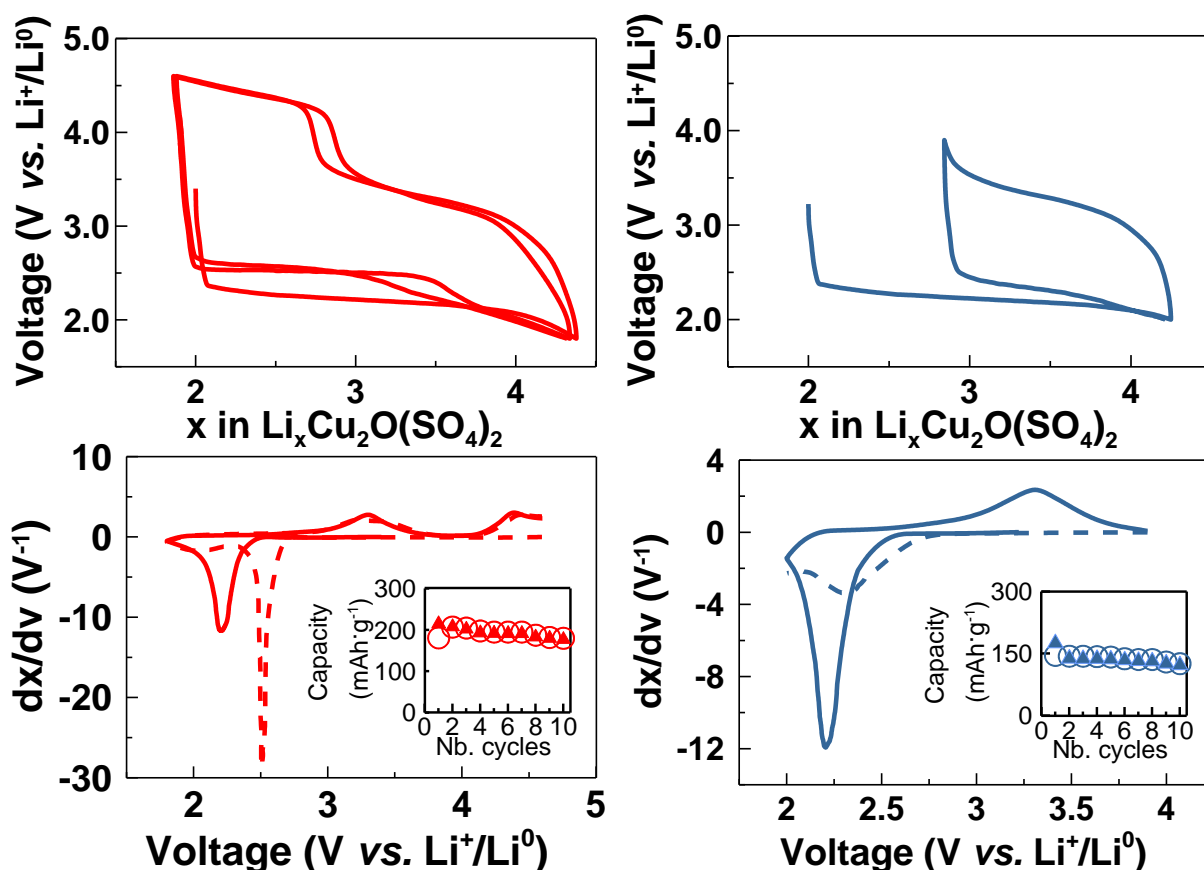


Figure II.25: Typical voltage–composition curves of $\text{Li}_2\text{Cu}_2\text{O}(\text{SO}_4)_2\|\text{Li}$ cells started on reduction, cycled between electrochemical window of either 1.8 V–4.6 V at C/25 (red curves, left) or 2 V–3.9 V at C/15 (blue curves, right). The bottom panel represents for each the derivative dx/dV curve for each (plain line = first cycle, dotted line = second cycle). In each case the corresponding capacity retentions are reported in inset (open circles = capacity on charge, triangles = capacity on discharge).

Another interesting feature of the discharge curve is nested in the amount of Li-uptake (2.4 Li per formula unit) which is greater than expected (2 Li per formula unit) from the full reduction of Cu^{2+} to Cu^+ . This suggests that a tiny fraction of Cu^+ might be reduced to metallic Cu, indicating the feasibility of extruding copper from the lattice via either displacement reactions, as already reported for Cu-based compounds [266], or conversion reactions in various oxides which usually proceed at lower voltages [267–268]. While the former preserves the framework of the structure, the latter enlists a complete structural reorganization.

To explore this last possibility, we cycled a $\text{Li}_2\text{Cu}_2\text{O}(\text{SO}_4)_2\|\text{Li}$ cell down to 0.5 V (**Figure II.26**). Decreasing the voltage from 1.8 to 0.5 V leads to an extra uptake of 1.9 Li^+ , leading to an overall uptake of 4.3 Li^+ per unit formula out of which most of them can be removed on oxidation till 4.6 V. The charge voltage trace is here different from that collected when the cell is only discharged to 1.8 V with the complete cycling voltage profile looking alike those

collected for materials enlisting conversion reaction processes. Overall, whatever the cycling conditions, these results highlight the complexity of the reacting mechanism of $\text{Li}_2\text{Cu}_2\text{O}(\text{SO}_4)_2$ against Li below 3 V.

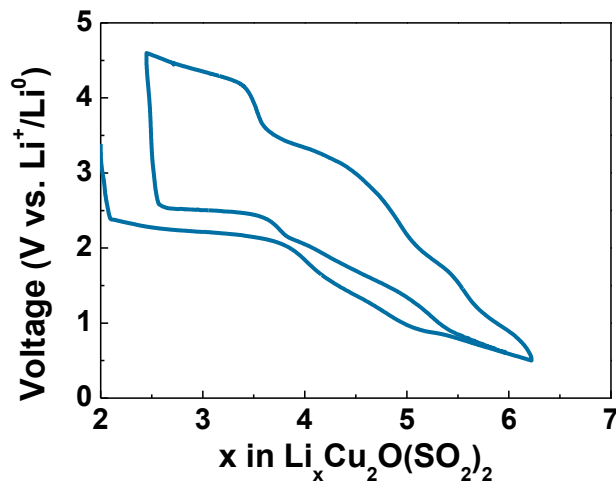


Figure II.26: Voltage versus composition curve of a $\text{Li}_2\text{Cu}_2\text{O}(\text{SO}_4)_2||\text{Li}$ cell cycled down to 0.5V at C/40.

To gain further insights into the mechanism of this process, *in situ* X-ray diffraction was performed (**Figure II.27**). A progressive intensity loss without peak-broadening was observed

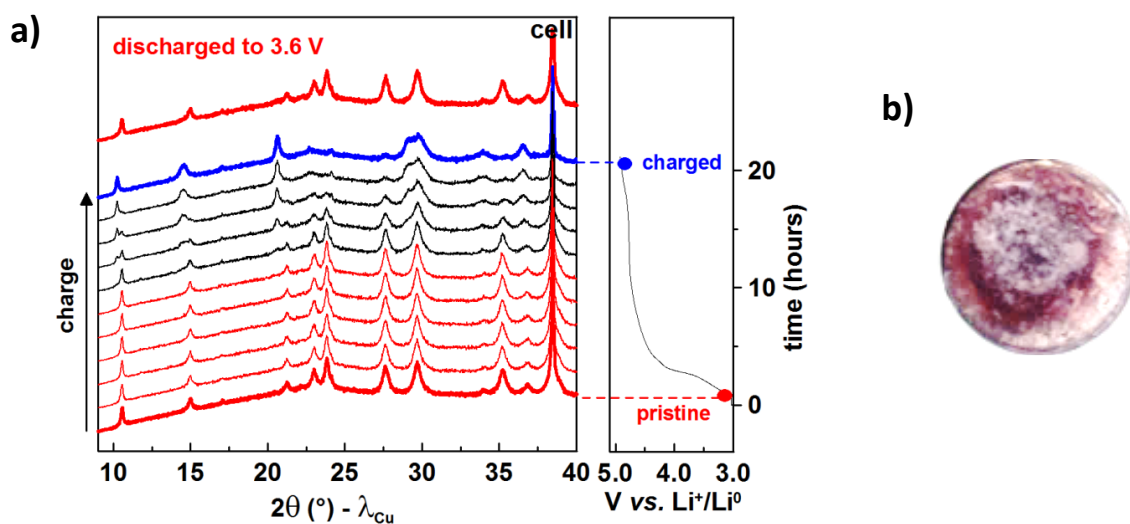


Figure II.27: Behavior of a $\text{Li}_2\text{Cu}_2\text{O}(\text{SO}_4)_2||\text{Li}$ cell on discharge cycled at C/30. **(a)** *In situ* XRD patterns recorded while the cell is being discharged to 2 V (right curve). The pattern on top was recorded at the end of discharge on the Li side and shows Bragg peaks consistent with Cu metal. **(b)** The image of the Li negative electrode at the end of discharge.

so that the XRD patterns become featureless for x approaching 4, and remain as such on subsequent cycles without any evidence of Bragg peaks corresponding to Cu metal (even

when the cell voltage was lowered to 0.5 V). This result does not preclude the formation of Cu, which could precipitate out of the matrix in a nanoscale form not detectable by XRD. We observed evidence for the ejection of some copper by taking an XRD pattern (**Figure II.27 a, top**) and an image (**Figure II.27 b**) of a Li-disc recovered from a cell at the end of the first discharge process: the Cu Bragg peaks and some red particles are clearly present. This suggests the formation of some Cu^+ ions during the electrode lithiation, which are dragged through the negative electrode by the electrical field and reduced into copper metal.

II.3.6. TEM Investigations

To shed more light on the electrochemical behavior of $\text{Li}_2\text{Cu}_2\text{O}(\text{SO}_4)_2$, we conduct TEM investigations of the electrodes recovered from cells that were charged to 4.95 V (**Figure II.28**) and discharged to 1.8 V and 0.5 V (**Figure II.29**), respectively.

After been charged to 4.95 V or discharged to 1.8 V/0.5 V, the positive electrode was obtained from a $\text{Li}_2\text{Cu}_2\text{O}(\text{SO}_4)_2/\text{Li}$ cell, washed with Dimethyl Carbonate (DMC) three times in an Ar-filled glove box, and dried under vacuum in its antechamber. The crystals of each sample were prepared in the glove box by crushing them in a mortar in anhydrous hexane and depositing drops of suspension onto holey carbon grids, before been transported to the microscope column. The whole process was excluding contact with air completely. High Angle Annular Dark Field - Scanning Transmission Electron Microscopy (HAADF-STEM) and Images and Energy Dispersive X-ray (EDX) compositional maps were obtained with a Tecnai Osiris electron microscope equipped with a Super-X EDX detector and operated at 200 kV.

The sample charged to 4.95 V consists of a mixture of amorphous and crystalline material. The ED patterns from the crystalline materials can be indexed on a primitive tetragonal unit cell with approximate lattice parameters $a \approx 8.3\text{\AA}$, $c \approx 5.1\text{\AA}$ (**Figure II.28 a**), *i.e.* identical to those of the pristine $\text{Li}_2\text{Cu}_2\text{O}(\text{SO}_4)_2$. EDX spectra from these crystals are also virtually identical to those of the $\text{Li}_2\text{CuO}(\text{SO}_4)_2$ material (**Figure II.28 b**).

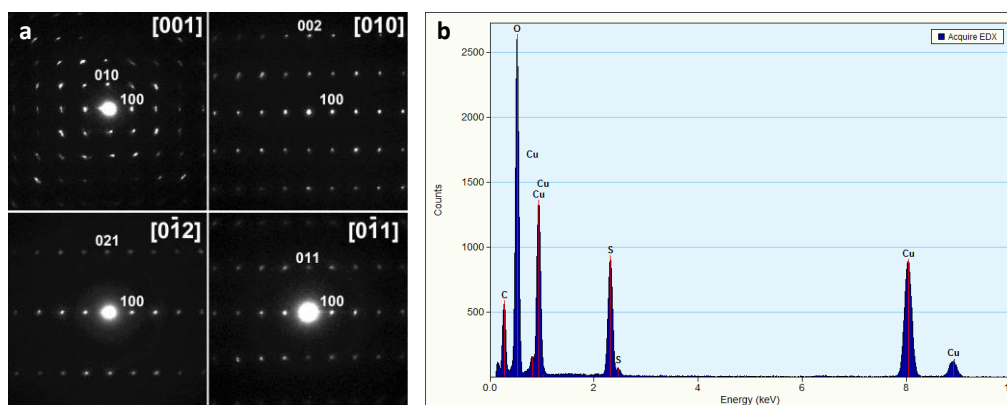


Figure II.28: (a) ED patterns and (b) EDX spectra of the crystalline phase in the $\text{Li}_2\text{CuO}(\text{SO}_4)_2$ sample charged to 4.95V.

Because the charged sample sensitivity to electron beam irradiation we could not work neither on the HAADF-STEM nor Annular Bright Field (ABF)-STEM modes to visualize atomic repartition. Turning to the reduced samples down to 1.8 V and 0.5 V EDX mapping was feasible (**Figure II.29**). Both samples demonstrate the presence of nanoparticles with sizes in the range of 5 – 20 nm. Such particles are more rounded and more numerous in the sample discharged to 0.5 V. EDX compositional mapping indicates that nanoparticles in the 1.8 V sample are oxidized, being most probably a copper oxide, while they are solely copper in the 0.5 V sample.

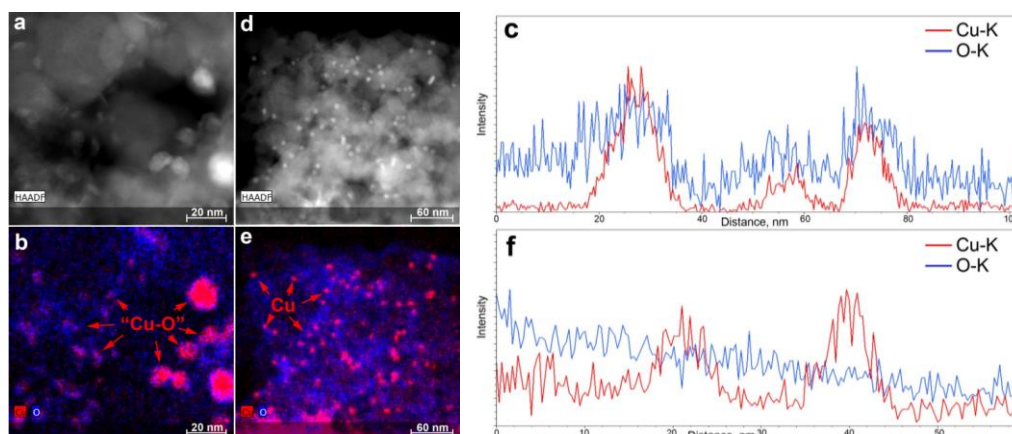


Figure II.29: HAADF-STEM images (a, d) show numerous nanoparticles, which are enriched with Cu, according to the EDX compositional maps (b, e). The intensity profiles of the Cu-K and O-K lines demonstrate that in the sample discharged to 1.8 V, the O-K signal varies concomitantly with the Cu-K signal (c) indicating that the particles are copper oxide (likely Cu_2O). In the sample discharged to 0.5 V (f) the O-K signal does not depend on the presence/absence of the nanoparticles, indicating that they are metallic Cu.

To determine the outcome of CuO_x and Cu nanoparticles formed during the discharge process to 1.8 V upon subsequent charging, two cells were discharged to 1.8 V and charged to 3.8 V

and 4.6 V, respectively. Independent of the charging voltages, ED patterns display only diffraction rings attributed to graphitic carbon, indicative of the formation of an amorphous material (**Figure II.30** a, b). Moreover, HAADF-STEM images do not reveal the presence of either Cu or CuO_x oxide nanoparticles as supported by EDX compositional maps that show relatively homogeneous distributions of Cu, S and O (**Figure II.30** c).

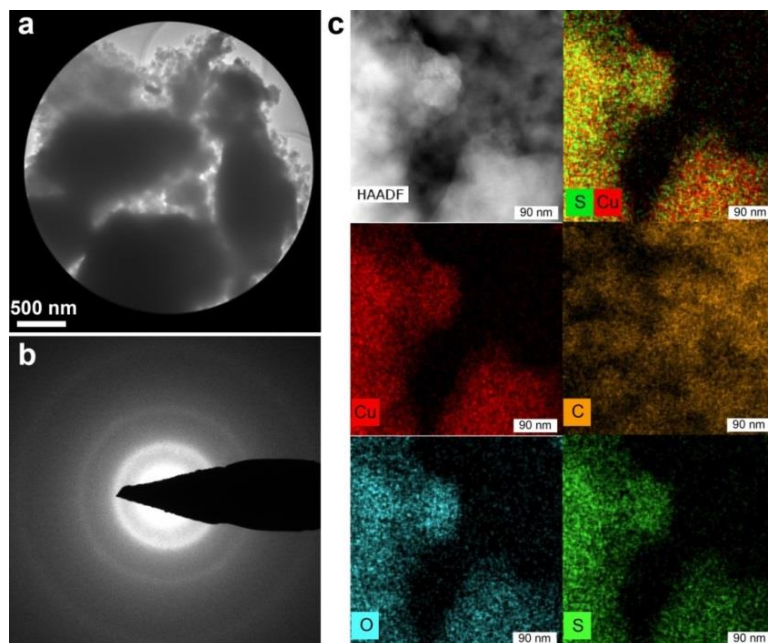


Figure II.30: (a) TEM image. (b) Corresponding electron diffraction pattern, (c) Typical HAADF-STEM image and compositional EDX maps of the $\text{Li}_2\text{Cu}_2\text{O}(\text{SO}_4)_2$ samples recharged to 3.8 V. The diffraction rings are attributed to graphitic carbon. No segregation of Cu in the form of nanoparticles is observed.

However, for the 3.8 V sample, small Cu-rich regions are occasionally noted (**Figure II.31**) with Cu segregation occurring in the form of alternating Cu- CuO_x lamellas. Although such a specific texture could bear some textural/structural hints on how the electrode is oxidized, we have not further explored these features as their appearance is sporadic. Unlike the oxidation of $\text{Li}_2\text{Cu}_2\text{O}(\text{SO}_4)_2$, which basically obeys a classical deinsertion-insertion process, its reduction is more complex due to intriguing features such as *i*) the non-symmetric voltage trace between charge and discharge, *ii*) non-superimposable voltage profiles between the first and second discharges, *iii*) the ability to insert an amount of Li greater than allowed from solely the reduction of Cu^{2+} to Cu^+ (2 per formula unit), with this amount increasing drastically to 5 Li as the voltage is lowered to 0.5 V, and *iv*) the appearance of Cu-O and Cu nanoparticles as the discharge cutoff voltage is lowered. Only a few reaction mechanisms can account for such large amounts of Li uptake.

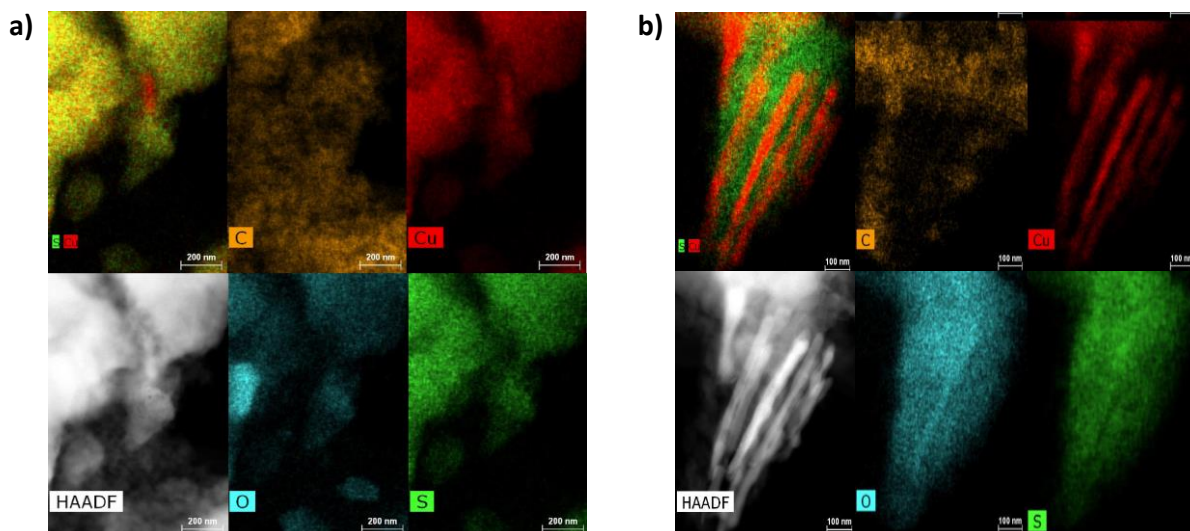
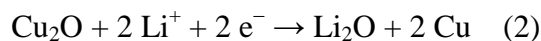
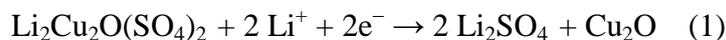


Figure II.31: (a) HAADF-STEM image and compositional EDX maps of the $\text{Li}_2\text{Cu}_2\text{O}(\text{SO}_4)_2$ samples recharged to 3.8 V (after being initially discharged to 1.8 V), showing local Cu segregation. (b) HAADF-STEM image and compositional EDX maps of the $\text{Li}_2\text{Cu}_2\text{O}(\text{SO}_4)_2$ samples recharged to 3.8 V (after being initially discharged to 1.8 V), highlighting the Cu lamellas are formed in this area. The central lamella appears to be oxidized.

The first mechanism, mainly specific to Cu-based compounds, is a Li-driven displacement reaction leading to the growth and disappearance of metallic Cu. In the presence of Cu^{2+} , the displacement reaction will enlist a two-electron process ($\text{Cu}^{2+} \rightarrow \text{Cu}^+ \rightarrow \text{Cu}^0$), that is the uptake of 2 Li (4 per unit formula) to fully extrude metallic copper from the matrix. The likelihood of such a process occurring here is at first sight improbable as it cannot account for the appearance of CuO in as observed by electron microscopy.

An alternative and more likely explanation which integrates all the experimental facts is nested in the feasibility of our compound to entails a conversion reaction which can be described by the following reactions which occur sequentially:



We believe that $\text{Li}_2\text{Cu}_2\text{O}(\text{SO}_4)_2$ reacts against Li via a process involving uptake of Li by the host structure which induces the reduction of Cu^{2+} and Cu^+ . Since Cu^+ usually prefers a different oxygen coordination (square planar or elongated octahedron for Cu^{2+} vs. dumbbell O- Cu^+ -O as in Cu_2O [269] or Cu_4O_3 [270]), such structural hindrance might result in a progressive decomposition of the parent phase into CuO_x (reaction 1), leading to an amorphous composite. The Cu oxide then transforms, via reaction 2 which is well documented in the literature, into metallic Cu whose amount increases as the discharge potential is lowered to 0.5 V. This is consistent with the discharge voltage curve which

departs from the 2.1 V plateau when 2 Li have reacted as well as with the major formation of CuO_x with slight amount of Cu metal in the 1.8 V discharged sample and of solely Cu in the 0.5 V discharged one (**Figure II.28**). Upon the subsequent charge, the two reactions proceed in opposite direction. This reversibility is again consistent with the fact that CuO and Cu nanoparticles are disappearing when the cell is recharged to 3.8 and 4.5 V, respectively as deduced by microscopy. Although, at the moment it is premature to speculate in greater details about the way CuO_x is re-injected into the “Li-Cu-S-O” amorphous phase: we should just recall that the CuO crystal structure shows nearly equivalent edge-shared CuO_4 square-planes as those occurring in $\text{Li}_2\text{Cu}_2\text{O}(\text{SO}_4)_2$.

II.3.7. DFT Calculations

II.3.7.1. Calculations for “ $\text{Cu}^{3+}/\text{Cu}^{2+}$ ” Oxidation Process

As an alternative approach to rationalize the electrochemical behavior upon oxidation, we turned to theoretical calculations. Orbital analysis and density functional calculations (DFT) were performed to access a microscopic picture of the electrochemical behavior of this phase. The phase stability diagram obtained for the $\text{Li}_x\text{Cu}_2\text{O}(\text{SO}_4)_2$ system is shown in **Figure II.32**. It reveals that the complete Cu^{2+} to Cu^{3+} oxidation (*i.e.* removal of 2 Li) would occur at 5.20 V as shown in green path. However, this is strongly thermodynamically disfavored over partial oxidation processes associated with the formation of intermediate phases at $x = 1.75$, 1.5 and even 1 following the blue path.

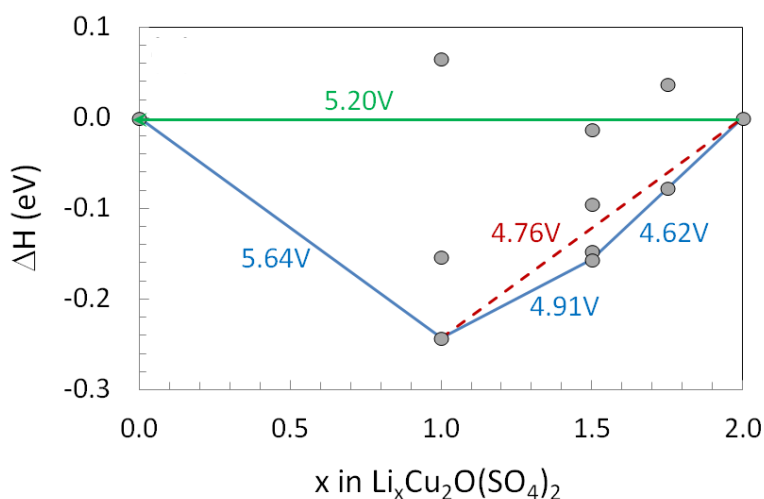


Figure II.32: Phase stability diagram for the $\text{Li}_x\text{Cu}_2\text{O}(\text{SO}_4)_2$ ($0 \leq x \leq 2$) system computed from DFT+U. The black circles correspond to the formation energy (ΔH in eV) of $\text{Li}_x\text{Cu}_2\text{O}(\text{SO}_4)_2$ single phases. The most probable reaction mechanism (thermodynamically favored) is illustrated by the convex hull of these phase diagrams (blue lines) while competitive reactions are indicated in dotted red lines

The density of states (DOS) of the $\text{Li}_2\text{Cu}_2\text{O}(\text{SO}_4)_2$ phase shows that the band involved in the oxidation process is mainly of oxygen character (**Figure II.33**), suggesting an anionic rather than a cationic redox activity upon lithium removal.

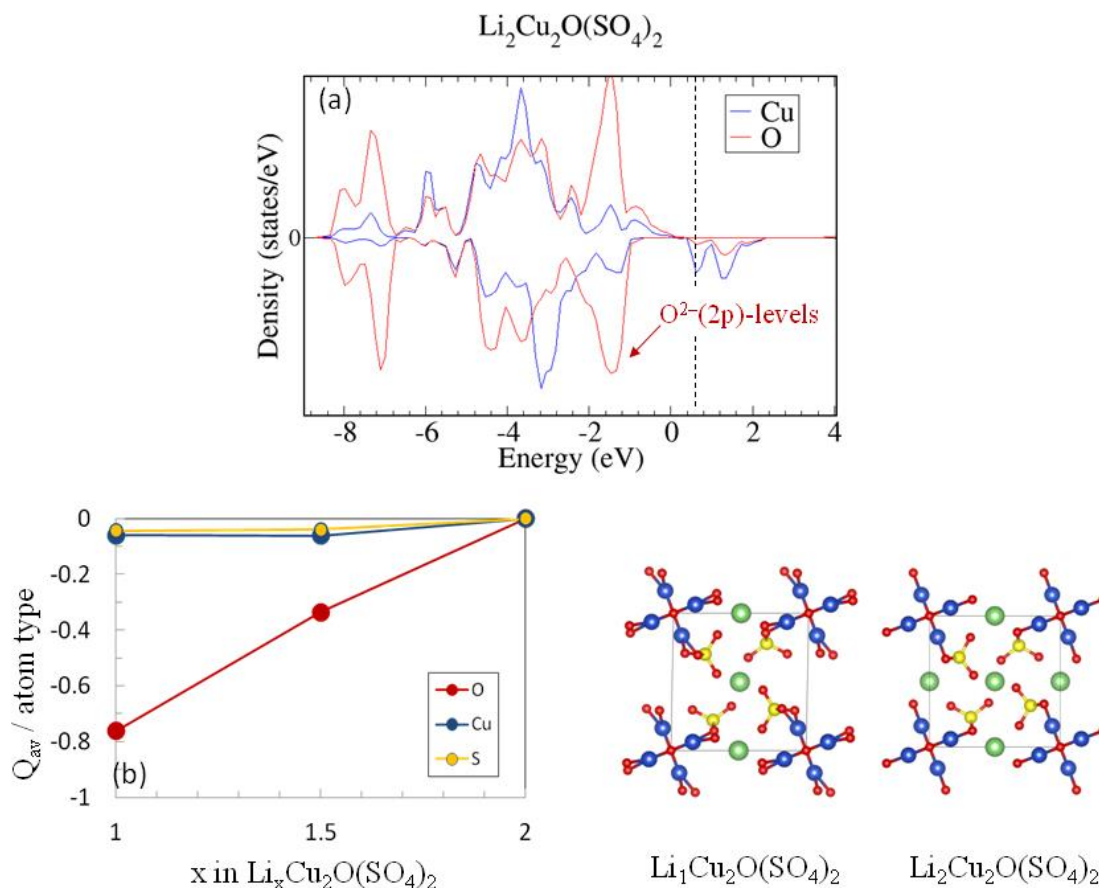


Figure II.33: (Top) Cu- and O-projected densities of states (DOS) for the $\text{Li}_2\text{Cu}_2\text{O}(\text{SO}_4)_2$ phase where the dotted line represents to Fermi level. (Bottom) Average Bader charge per atom type Q_{av} (in electron) computed for the $\text{Li}_x\text{Cu}_2\text{O}(\text{SO}_4)_2$ phase showing that more than 75% of the charge transfer upon oxidation is supported by the oxygens. The total charge transfer from $x = 2$ to $x = 1.5$ and from $x = 2$ to $x = 1$ is assumed to be 0.5 and 1.0, respectively. The crystal structures of the $\text{Li}_2\text{Cu}_2\text{O}(\text{SO}_4)_2$ and $\text{Li}_1\text{Cu}_2\text{O}(\text{SO}_4)_2$ are displayed on the bottom right part of the figure.

A deeper analysis of the electronic levels lying just below the Fermi level confirms the strong hybridization of the Cu (3d) orbitals with the O (2p) orbitals of the oxygen atoms bridging the CuO_4 square-planes. These oxo-ligands (O^{2-}) – being much less electronegative than those belonging to sulfate (SO_4) $^{2-}$ groups – can take part to the redox process (**Figure II.34**). Upon Li removal from the $\text{Li}_2\text{Cu}_2\text{O}(\text{SO}_4)_2$ phase, holes are then created on these bridging oxo-ligands so that the oxidation process corresponds to the formation of “ $\text{Cu}^{2+}\text{--O}^-$ ” species rather than $\text{Cu}^{3+}\text{--O}^{2-}$. This is corroborated by atomic charge analysis on Cu, S and O showing that more than 75% of the removed charge (hole) is located on the oxygen (**Figure II.33**). According to the phase stability diagram of **Figure II.32**, oxidation of the $\text{Li}_2\text{Cu}_2\text{O}(\text{SO}_4)_2$

electrode should proceed in two steps through the extraction of 0.5 Li each. The average voltages obtained for the $x = 2$ to $x = 1.5$ (4.62 V) and $x = 1.5$ to $x = 1$ (4.91 V) processes compare well with experiments (**Figure II.32**) although slightly underestimated. The intermediate $\text{Li}_{1.5}\text{Cu}_2\text{O}(\text{SO}_4)_2$ and $\text{Li}_1\text{Cu}_2\text{O}(\text{SO}_4)_2$ phases show slightly distorted CuO_4 square-planes and a $\text{Cu}-(\text{O}_2)-\text{Cu}$ angle deviating from 90° which is consistent with the monoclinic distortion experimentally observed and with the loss of the 4_2 screw axis (**Figure II.33**). Note that the full oxidation from $\text{Li}_1\text{Cu}_2\text{O}(\text{SO}_4)_2$ to $\text{Cu}_2\text{O}(\text{SO}_4)_2$ is associated with quite a high potential (5.64 V), likely unachievable with current electrolytes. We note that the $\text{Cu}_2\text{O}(\text{SO}_4)_2$ structure is however very close to that of the starting $\text{Li}_2\text{Cu}_2\text{O}(\text{SO}_4)_2$ phase with nearly no volume contraction and a perfectly planar CuO_4 configuration.

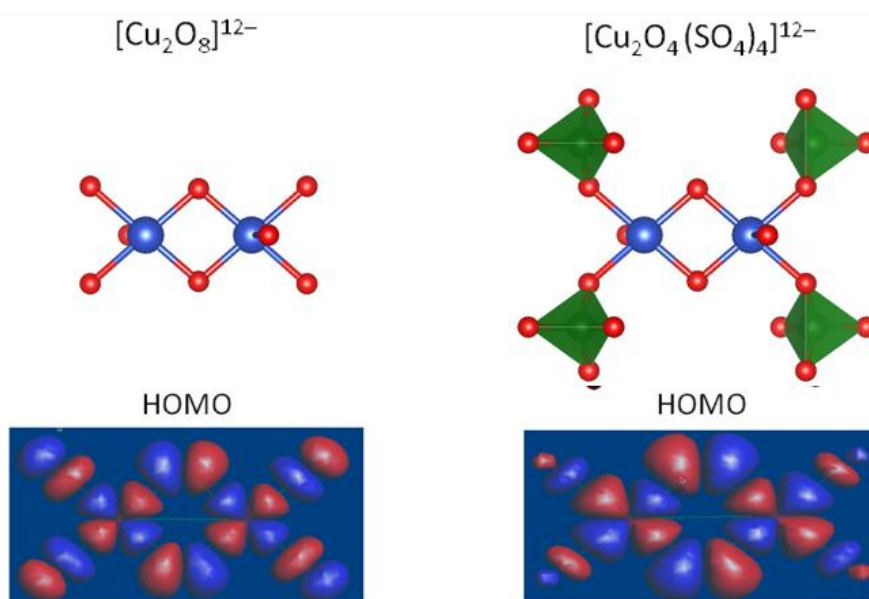


Figure II.34: Illustration of the local electronic levels involved in the redox band of the $\text{Li}_2\text{Cu}_2\text{O}(\text{SO}_4)_2$ system, *i.e.* the Highest Occupied Molecular Orbital (HOMO) projected on a dimer of edge-shared CuO_5 square-based pyramids (**left**) and on a dimer of edge-shared $\text{CuO}_3(\text{SO}_4)_2$ square-based pyramids (**right**). This picture shows that the addition of $(\text{SO}_4)^{2-}$ to the external oxygen atoms the dimer decreases the contribution of their $\text{O}(2p)$ -orbitals to the HOMO due to the inductive effect. In contrast, the bridging oxygen atoms show a higher contribution to the HOMO with strong $\text{Cu}(3d)-\text{O}(2p)$ overlap, therefore acting as actor ligands in the redox activity of the system.

II.3.7.2. Calculations for $\text{Cu}^{2+}/\text{Cu}^+/\text{Cu}^0$ Reduction Process

To confirm the mechanism of electrochemical process upon reduction, a DFT+U phase stability diagram was computed for the $\text{Li}_x\text{Cu}_2\text{O}(\text{SO}_4)_2$ system ($2 \leq x \leq 6$) assuming different electrochemical reactions, namely insertion (black circles), displacement (black triangles) and conversion reactions (blue and red squares). It is given in **Figure II.35** where the reference energy (green horizontal line) corresponds to the reaction enthalpy of the direct conversion of $\text{Li}_2\text{Cu}_2\text{O}(\text{SO}_4)_2$ into $2\text{Cu}^0 + \text{Li}_2\text{O} + 2\text{Li}_2\text{SO}_4$ with the exchange of 4Li. Displacement and insertion (electrodes, namely $\{\text{Li}_{2+x}\text{Cu}_{2-x/2}\text{O}(\text{SO}_4)_2 + x/2\text{Cu}^0\}$ and $\text{Li}_{2+x}\text{Cu}_2\text{O}(\text{SO}_4)_2$, respectively) are found much higher in energy than the conversion electrodes whatever is the lithium content. Reactions (1) and (2) are clearly the thermodynamically favored mechanism (blue squares) which supports our mechanistic hypothesis. We note however, that a second mechanism (red squares) involving the formation of an intermediate $\{\text{CuO} + \text{Cu}^0 + 2\text{Li}_2\text{SO}_4\}$ electrode could compete with reaction (1). Although thermodynamically less favored than reactions (1) + (2) this mechanism is consistent with the appearance of CuO particles in the discharge samples and could be kinetically activated by the formation of a CuO phase which is closely related to the initial $\text{Li}_2\text{Cu}_2\text{O}(\text{SO}_4)_2$ phase.

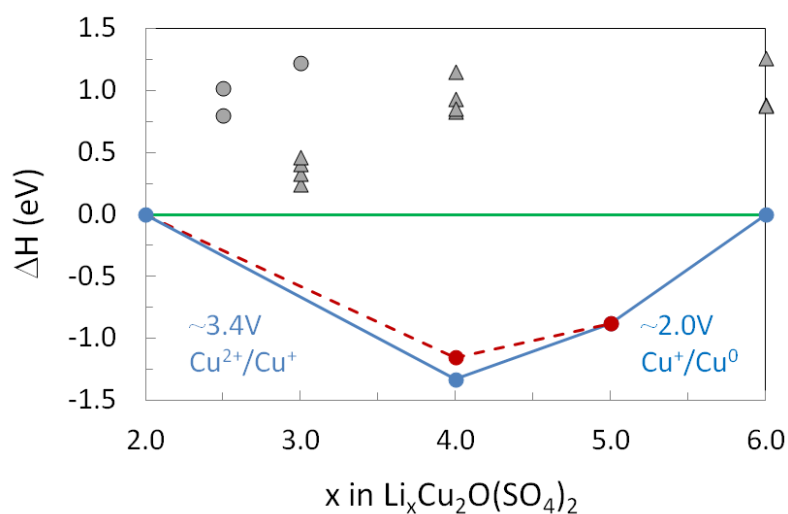


Figure II.35: Phase stability diagrams for the $\text{Li}_x\text{Cu}_2\text{O}(\text{SO}_4)_2$ ($2 \leq x \leq 6$) system computed from DFT+U. The black circles and triangles illustrate the formation energy of $\text{Li}_x\text{Cu}_2\text{O}(\text{SO}_4)_2$ single phases or $\text{Li}_x\text{Cu}_{2-x/2}\text{O}(\text{SO}_4)_2 + x/2\text{Cu}^0$ with respect to a reference energy illustrated by a green line (ΔH in eV). For $2 \leq x \leq 6$, the full conversion reaction is $\text{Li}_2\text{Cu}_2\text{O}(\text{SO}_4)_2 + 4\text{Li} \rightarrow \text{Li}_2\text{O} + 2\text{Cu}^0 + 2\text{Li}_2\text{SO}_4$. The most thermodynamically favored reaction mechanism is illustrated in blue line while competitive reactions are indicated in dotted red lines. The average voltages vs. Li are indicated for each process.

II.3.8. Magnetic Measurement of $\text{Li}_{1.7}\text{Cu}_2\text{O}(\text{SO}_4)_2$

In light of the colossal amount of work previously done on the high T_c cuprates “ $\text{YBa}_2\text{Cu}_3\text{O}_7$ and others” containing Cu in its Cu^{+2} and Cu^{+3} oxidation states it was tempting to check for superconductivity in $\text{Li}_2\text{Cu}_2\text{O}(\text{SO}_4)_2$ which in its oxidized state also contains a fraction of Cu^{3+} . However, as deduced from low field (20 Oe) magnetic measurements, no sign of superconductivity was found for the oxidized sample $\text{Li}_{1.7}\text{Cu}_2\text{O}(\text{SO}_4)_2$ phase down to 2 K (Figure II.36).

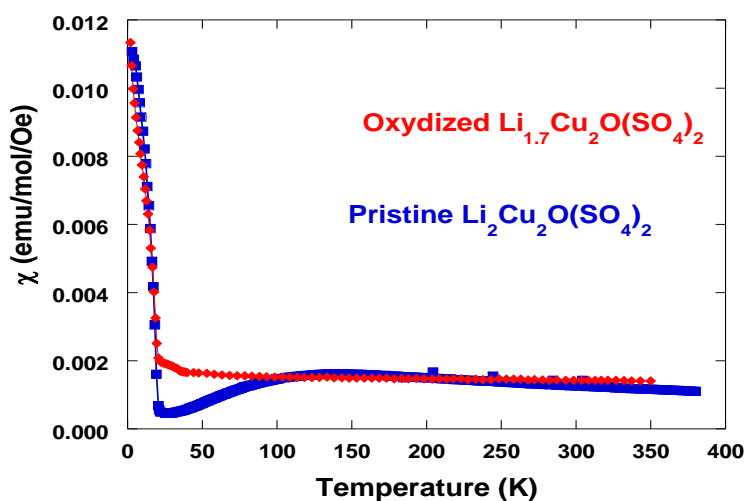


Figure II.36: Comparison of the magnetic susceptibility of the charged $\text{Li}_{1.7}\text{Cu}_2\text{O}(\text{SO}_4)_2$ phase (20 Oe) compared with that of the pristine $\text{Li}_2\text{Cu}_2\text{O}(\text{SO}_4)_2$ material. The upturn below 20K is likely due to the minute amounts of Cu_2OSO_4 impurity in the sample.

II.4. Conclusions

In this chapter, we explored copper-based fluorosulfate and oxysulfate: LiCuSO_4F and $\text{Li}_2\text{Cu}_2\text{O}(\text{SO}_4)_2$, which were newly synthesized through a low temperature solid state process. These two phases were shown to have different structures but also different electrochemical performance.

Structural-wise, LiCuSO_4F crystallizes in a fully ordered *triplite* structure, instead of a *tavorite* structure as previously predicted from high-throughput calculations [248]. From DFT calculations, we could demonstrate that ordered *triplite* LiCuSO_4F polymorphs are more stable than either “*tavorite*” or “disordered *triplite*” polymorphs. The Li/Cu intermixing over the M1 and M2 sites was shown to minimize the Jahn-Teller distortion around the Cu^{2+} cations, which prevents Cu-orbital stabilization and leads to less stable distributions despite more favorable electrostatic energies. This indicates that enthalpy governs the formation of an

ordered LiCuSO_4F *triplite* and contrasts with the entropy-driven formation of LiFeSO_4F disordered *triplite* in which all Fe-Li distributions are energetically equivalent (so as the local Fe environment) [225].

LiCuSO_4F was found to be electrochemically inactive, while DFT calculations predicted a reversible electrochemical activity of *triplite* LiCuSO_4F towards Li^+/Li^0 at 5.15 V. Kinetic issues associated to the poor Li ionic conductivity in LiCuSO_4F is certainly one of the main reasons while we could also blame the lack of suitable electrolytes to explore such high voltage materials. Whatever, it results that the attractiveness of this new phase is limited application-wise.

Turning to $\text{Li}_2\text{Cu}_2\text{O}(\text{SO}_4)_2$, which can easily synthesized through different combination of precursors, it crystallizes in a tetragonal unit cell which contains infinite edge-sharing CuO_4 chains. Interestingly, these chains were shown to be connected by an oxygen (noted as O4, refer to **Figure II.19**) that does not belong to SO_4 tetrahedra. Within this phase, the Cu-Cu interaction topologies are of great interest. They are triangular forming then a frustrated 1D $S = 1/2$ system which is of great interest for the battery community.

Otherwise, $\text{Li}_2\text{Cu}_2\text{O}(\text{SO}_4)_2$ displays amphoteric nature of electrochemical reactivity towards Li: the compound can either be oxidized or reduced enlisting respectively the “ $\text{Cu}^{3+}/\text{Cu}^{2+}$ ” and $\text{Cu}^{2+}/\text{Cu}^+$ redox couples. On charge, Cu^{2+} is oxidized to Cu^{3+} at 4.7 V vs. Li/Li^0 , one of the highest ever reported potential for such couple in any Cu-based inorganic compound. In fact, compared to LiCuSO_4F , the inductive effect of the sulfate group in $\text{Li}_2\text{Cu}_2\text{O}(\text{SO}_4)_2$ is mitigated by the presence of the oxo-group and the absence of highly electronegative F^- , resulting in the voltage to be lower than 5.15 V computed for *triplite* LiCuSO_4F and 5.09 V for *tavorite* LiCuSO_4F [248]. Moreover, the strong hybridization of the metallic 3d-orbitals with the oxo-ligand’s 2p-orbitals is responsible for Cu(3d)/O(2p) band overlap, which is shown to promote anionic redox activity through the creation of holes on the bridging oxygen of the CuO_4 square planes. In short Cu^{3+} can be viewed as Cu^{2+} hole, in analogy to what was found for the high T_c cuprates having Cu^{2+} in square planar environments. It is also worth mentioning that for this Cu-based oxysulfate, it is the oxygen not belonging to SO_4^{2-} (O4) that provides the anionic activity. This finding suggests that oxysulfate could be fertile ground to expand the family of materials showing anionic network redox activity beyond the Li-rich lamellar oxides [110].

The practical advantage offered by such a high potential is however counterbalanced by the limited capacity. Removing only 0.3 Li from the Li1 and Li2 positions destabilizes the structure, which undergoes a monoclinic distortion as observed at the end of charging (4.8 V). Moreover, Li acts as a screening agent between chains: when Li is removed the electrostatic

repulsion between adjacent SO_4 tetrahedra is increased, which is why the volume of the unit cell increases upon (partial) delithiation.

In summary, the finding of LiCuSO_4F has broadened the rich crystal-chemistry of sulfate-/phosphate-based polyanionic electrodes which were found to adopt either the *tavorite* or disordered *triplite* structures, and contribute further in the understanding technically important polyanionic electrodes. By substituting F^- with O^{2-} , we show that the more environmental friendly $\text{Li}_2\text{Cu}_2\text{O}(\text{SO}_4)_2$ displays capacities of 20 mA·h/g and 200 mA·h/g at high (~ 4.7 V) and low (~ 2.5 V) average voltage. While the high-potential process entails a classical biphasic reversible insertion de-insertion reaction, the low-potential process proceeds via a complex displacement-conversion reaction.

Overall, we hope this work will propel a more intense search for Cu-based polyanionic compounds capable of supporting the anion redox activity-driven $\text{Cu}^{3+}/\text{Cu}^{2+}$ couple, a transition metal that has been unduly disregarded. Additionally, $\text{Li}_2\text{Cu}_2\text{O}(\text{SO}_4)_2$ could provide a basis for better understanding $S = 1/2$ frustrated magnetic chains, and may be of interest for the discovery of new superconductors.

Chapter III. $\text{Fe}_2\text{O}(\text{SO}_4)_2$ - Electrode for Sustainable Li-Based Batteries

III.1. Introduction

In the previous chapter, we have demonstrated through our work on $\text{Li}_2\text{Cu}_2\text{O}(\text{SO}_4)_2$ that oxysulfates stand as a fertile ground to design non-fluorinated polyanionic compound with promising electrochemical performance. This was an impetus to explore the iron-based oxysulfate as described next.

Looking back to the iron-based sulfates, $\text{Li}_2\text{Fe}(\text{SO}_4)_2$ displays an $\text{Fe}^{3+}/\text{Fe}^{2+}$ redox potential of 3.83 V vs. Li^+/Li^0 [271-272]. It shows polymorphism with a monoclinic and an orthorhombic form [273-274], both of which are electrochemically active, similar to many of the other recently discovered Li-insertion sulfate compounds such as LiFeSO_4F [45, 219, 226] and $\text{Li}_x\text{FeSO}_4\text{OH}$ [234-235, 237]. Polymorphism also exists in Li-free sulfate compounds as exemplified by $\text{Fe}_2(\text{SO}_4)_3$ presenting either a rhombohedral or a monoclinic form [139-140], with the latter being difficult to isolate and showing poor electrochemical performance vs. Li.

Although phosphates are less prone to polymorphism, both sulfate and phosphate crystal chemistries bear some structural resemblances, such as the fluorine-based compounds $\text{Li}_2\text{FePO}_4\text{F}$ [275]/ LiFeSO_4F and hydroxide-based ones $\text{Li}_2\text{FePO}_4\text{OH}$ [236]/ LiFeSO_4OH . Additionally, 3d-transition metal oxyphosphates and oxysilicates capable of reversibly inserting Li^+ ions are known to form as demonstrated by the existence of LiVOPO_4 [238-239] and $\text{Li}_2\text{VOSiO}_4$ [276]. Thus a legitimate course of inquiry was, could an iron-based oxysulfate insertion compound be stabilized?

An iron oxysulfate is expected to present many appealing aspects. Fundamentally, it stands as a case example to further prove the beneficial inductive effect of sulfate groups, beyond the sustainability and safety appeal of iron. Structure-wise, oxo anion which does not belong to $(\text{SO}_4)^{2-}$ might limit the moisture sensitivity of sulfates. Application-wise, an oxysulfate benefits from a lighter molecular weight and hence a greater theoretical capacity than $\text{Fe}_2(\text{SO}_4)_3$. Thus, the reason why we embarked on the synthesis and exploration of $\text{Fe}_2\text{O}(\text{SO}_4)_2$.

The literature is rich of thermal analysis studies dealing with thermal decomposition behavior in various iron (2+) sulfate hydrates and hydroxides [277-283]. Among these, one previous report [281] indicates the formation of the hydroxysulfate FeSO_4OH occasionally coexisting with another phase, referred to as the oxysulfate " $\text{Fe}_2\text{O}(\text{SO}_4)_2$ ". The respective quantities of

both phases are dictated by the temperature treatment, the gas used to conduct the reaction and the control of water pressure throughout the reaction. Although the formation of $\text{Fe}_2\text{O}(\text{SO}_4)_2$ can simply be viewed as the result of a condensation/dehydration reaction, several attempts to isolate $\text{Fe}_2\text{O}(\text{SO}_4)_2$ as a pure phase have failed with its structure being still unknown [280, 282]. Moreover, suspicions remain regarding this “supposed” compound since different sets of interplanar spacing were reported through the years. This was an impetus to check the real existence of this compound, solve its structure and determine its electrochemical activity vs. Li.

III.2. Exploration of Iron-Based Oxysulfate: $\text{Fe}_2\text{O}(\text{SO}_4)_2$

III.2.1. Synthesis

Based on the previous research, we decided to begin the synthesis with dehydration of FeSO_4OH . The hydroxysulfate precursor was initially prepared from $\text{FeSO}_4 \cdot 7\text{H}_2\text{O}$ as described by M. Anji et al [237]. The commercial heptahydrate Fe(II) sulfate ($\text{FeSO}_4 \cdot 7\text{H}_2\text{O}$, Alfa Aesar, 99%) was first purified to remove traces of Fe^{3+} impurity phases by dissolving the powder in distilled water in the presence of a small amount of ascorbic acid and subsequent precipitation with absolute ethanol before being dried under vacuum at 60 °C. The purified powder was ground in an agate mortar to a fine powder, transferred to an alumina boat, and heated in air at 280 °C for 4 c 7 days.

To narrow down the thermal conditions, we surveyed the effect of temperature on the thermal stability of FeSO_4OH . The thermogravimetric analysis profile was collected by heating FeSO_4OH with a rate of 5°C/min in the air (**Figure III.1 a**), indicating a first phase transformation rang of 435 – 545 °C. Based on the TGA result, the FeSO_4OH powder was parted in several batches and placed in different alumina crucibles, which were all placed in a chamber furnace whose temperature was progressively increased to 440 °C and then maintained at this temperature for one day prior to being increased in 5°C steps to 550 °C. A crucible was removed from the oven at each step and X-rayed to monitor the evolution of the phase’s formation. The XRD evolution as a function of temperature is shown in **Figure III.1 b**. The hydroxysulfate remains the dominant phase up to 445 °C, although a small amount of rhombohedral $\text{Fe}_2(\text{SO}_4)_3$ is also present at this temperature. Above 450 °C a new phase – presumably $\text{Fe}_2\text{O}(\text{SO}_4)_2$ – appears, coexisting with $\text{Fe}_2(\text{SO}_4)_3$. The two phases coexistence persists up to 475 °C, after which hematite Fe_2O_3 begins to form via decomposition of first $\text{Fe}_2(\text{SO}_4)_3$, shortly followed by decomposition of $\text{Fe}_2\text{O}(\text{SO}_4)_2$. This survey suggests that the temperature ranges over which this new phase forms is very narrow.

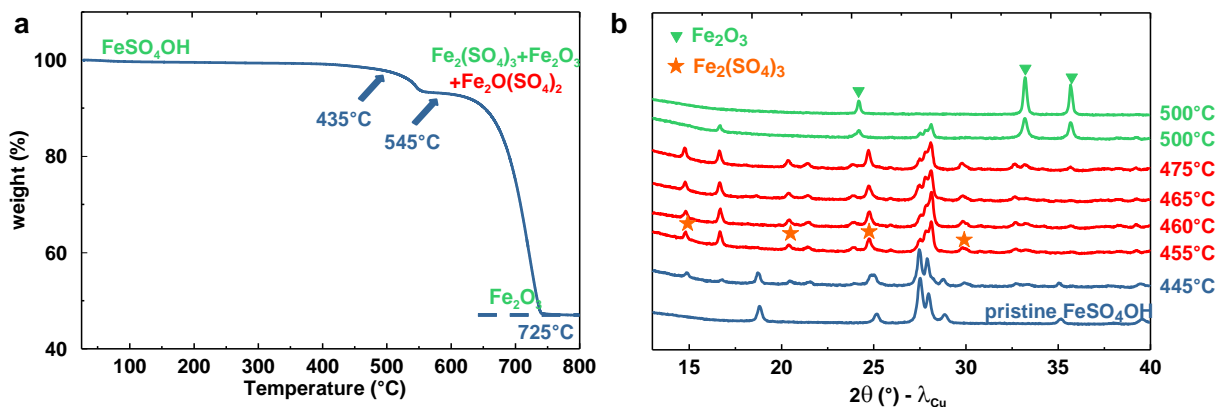


Figure III.1: (a) TGA of FeSO_4OH heated under air with the heating rate of $5\text{ }^\circ\text{C}/\text{min}$. (b) X-ray diffraction pattern of FeSO_4OH heated in air at different temperatures for 72 hours. Note the appearance of a definite phase that co-exists with $\text{Fe}_2(\text{SO}_4)_3$ (shown as orange stars) in the narrow range $455\text{ }^\circ\text{C} - 475\text{ }^\circ\text{C}$. At higher temperatures, this biphasic powder decomposes into hematite Fe_2O_3 (shown as green triangles).

Our best $\text{Fe}_2\text{O}(\text{SO}_4)_2$ sample, containing minimum traces of Fe_2O_3 and $\text{Fe}_2(\text{SO}_4)_3$, was obtained by annealing FeSO_4OH pellets in a chamber furnace in air at $465\text{ }^\circ\text{C}$ for 4 days. Due to the solubility difference between $\text{Fe}_2(\text{SO}_4)_3$ (completely soluble) and $\text{Fe}_2\text{O}(\text{SO}_4)_2$ (insoluble) in water, we washed the as-prepared powder with water three times and rinsed with ethanol to produce yellow samples containing only a minimum amount of Fe_2O_3 (**Figure III.2 a**) (less than 10%, as determined by Mossbauer spectroscopy and Rietveld refinements, see the next section).

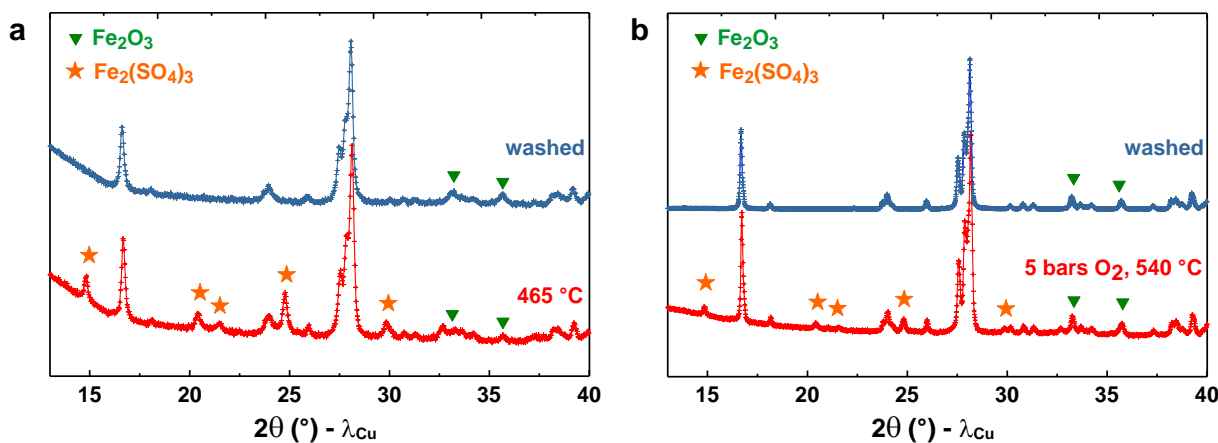


Figure III.2: X-ray diffraction pattern of the $\text{Fe}_2(\text{SO}_4)_3$ (shown as orange stars) and $\text{Fe}_2\text{O}(\text{SO}_4)_2$ biphasic powder (a) Resulting from the heating of FeSO_4OH at $465\text{ }^\circ\text{C}$, and (b) Obtained from synthesis in 5 bar of O_2 at $540\text{ }^\circ\text{C}$ by using $\text{FeSO}_4\cdot\text{H}_2\text{O}$ as precursor. In both cases $\text{Fe}_2(\text{SO}_4)_3$ was removed after washing with water and ethanol (top blue pattern compared to bottom red pattern). The blue pattern in b is highly crystallized an $\text{Fe}_2\text{O}(\text{SO}_4)_2$ samples which remains as an almost pure phase.

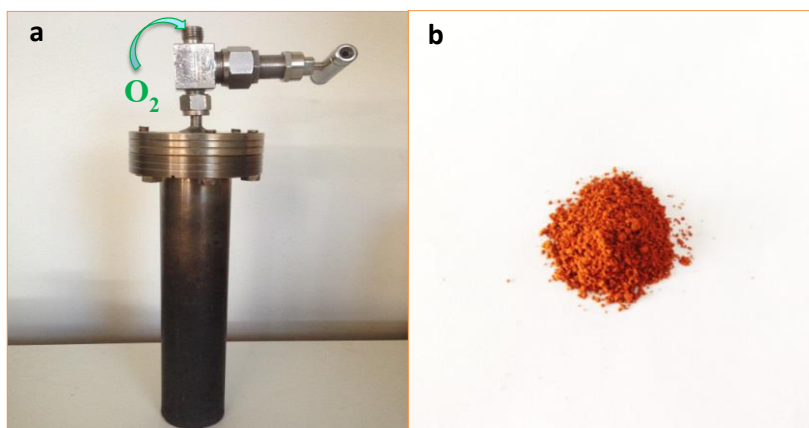


Figure III.3: (a) Experimental vessel used to synthesize $\text{Fe}_2\text{O}(\text{SO}_4)_2$ under pressure. (b) Photo of $\text{Fe}_2\text{O}(\text{SO}_4)_2$ powder synthesized.

To shorten the synthetic time, we explored the synthesis under controlled pressure environment. Specifically, various amounts of $\text{FeSO}_4 \cdot \text{H}_2\text{O}$ contained in a 50 cm^3 vacuum vessel were filled with O_2 , with pressures ranging from 1 to 7 bars (**Figure III.3 a**). The vessel was placed in a vertical tubular furnace and heated at temperatures ranging from $450 \text{ }^\circ\text{C}$ to $600 \text{ }^\circ\text{C}$ for durations between 1 and 4 days. The cleanest sample, which contained 90 wt.% $\text{Fe}_2\text{O}(\text{SO}_4)_2$ with approximately 5 wt.% $\text{Fe}_2(\text{SO}_4)_3$ and 5 wt.% of Fe_2O_3 (**Figure III.2 b**), was obtained using 1 g of $\text{FeSO}_4 \cdot \text{H}_2\text{O}$ with an O_2 backfill pressure of 5 bars by heating for one day at $540 \text{ }^\circ\text{C}$. As before, the sample was washed with water to remove $\text{Fe}_2(\text{SO}_4)_3$ to obtain nearly single-phase $\text{Fe}_2\text{O}(\text{SO}_4)_2$, showing yellowish brown color (**Figure III.3 b**). This sample, being more crystalline than samples prepared in air as a result of the higher synthesis temperature, was used to solve the structure. In contrast, owing to its simplicity, the previous synthetic path, which occurs at lower temperatures and does not rely on the use of stainless-steel pressure vessels, was preferred for preparing large amounts (10 to 50 grams) of materials for making electrodes for electrochemical testing.

III.2.2. Structure Characterization

The powder XRD pattern of $\text{Fe}_2\text{O}(\text{SO}_4)_2$ was collected using a Bruker D8 diffractometer with a Cu-K_α radiation source. It presents many peaks (**Figure III.2**) including a tiny one at $d = 6.42 \text{ \AA}$, with strong overlap among the triplet of reflections visible around $2\theta = 28^\circ$ ($d = 3.2 \text{ \AA}$), which indicates that the crystallographic unit cell might be large and/or of low symmetry. In such cases, automatic indexing programs (Dicvol [284], Treor [285], and others) commonly used to determine possible unit cells give many possibilities, and it is a challenge to find the correct cell.

To figure out the structure, firstly we studied the $\text{Fe}_2\text{O}(\text{SO}_4)_2$ sample by TEM. The TEM image shows that the sample consists of highly agglomerated nanocrystals with sizes ranging from about 20 nm to 100 nm (**Figure III.4 a**). The ring electron diffraction pattern taken from an agglomerate (**Figure III.4 b**) demonstrates the intensity distribution reminiscent to that on the XRD pattern of the $\text{Fe}_2\text{O}(\text{SO}_4)_2$ sample (**Figure III.4 c**) indicating that neither vacuum in the TEM column nor the electron beam irradiation alter the crystal structure substantially. EDX analysis of the nanocrystals indicates the presence of Fe, S and O. The reciprocal lattice of $\text{Fe}_2\text{O}(\text{SO}_4)_2$ has been reconstructed by taking a series of Selected Area Electron Diffraction (SAED) patterns while rotating the crystallite around a selected reciprocal lattice row. All obtained SAED patterns can be indexed in an *I*-centered monoclinic cell with the approximate lattice parameters $a \approx 9.5 \text{ \AA}$, $b \approx 6.1 \text{ \AA}$, $c \approx 9.8 \text{ \AA}$, $\beta \approx 97^\circ$. The SAED patterns along the main zone axes are shown in **Figure III.5**. No extra reflection conditions besides those imposed by the *I*-centering were observed in the ED patterns, suggesting the space group *I2/m* or its acentric subgroups.

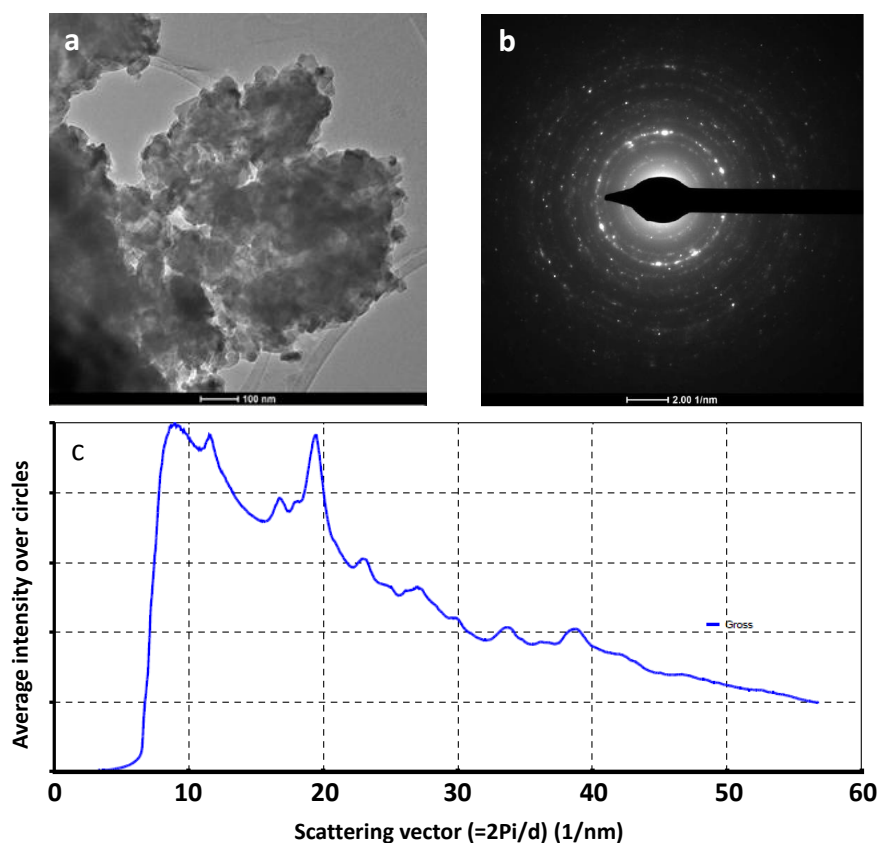


Figure III.4: (a) Low magnification TEM image and (b) Ring ED pattern of the of $\text{Fe}_2\text{O}(\text{SO}_4)_2$ nanocrystals and (c) the corresponding integrated intensity profile. Note the close resemblance of the ED profile and the XRD pattern (see **Figure III.2**).

This monoclinic cell was then further tested against the 11-BM synchrotron X-ray diffraction pattern in a 0.5 mm diameter capillary in transmission mode ($\lambda = 0.41374 \text{ \AA}$). We found that unit cell parameters of $a = 9.71082(8) \text{ \AA}$, $b = 6.35288(3) \text{ \AA}$, $c = 9.92501(6) \text{ \AA}$, $\beta = 98.2851(5)^\circ$ ($V = 605.901(7) \text{ \AA}^3$, $Z = 4$) with space group $I2/m$ could perfectly index all peaks, except for the reflections attributed to hematite Fe_2O_3 . Note that we did not transform the structure to the standard $C2/m$ setting as this would lead to an β angle significantly different from 90° . The crystal structure of $\text{Fe}_2\text{O}(\text{SO}_4)_2$ was solved directly using the EXPO software [286], which revealed the positions of the Fe, S and O atoms, with the obtained structural model which is consistent with the expected chemical formulae $\text{Fe}_2\text{O}(\text{SO}_4)_2$. The structure was then refined by the Rietveld method [287] using the FullProf suite [288] against the synchrotron pattern (Figure III.5 b), with Fe_2O_3 as a secondary phase.

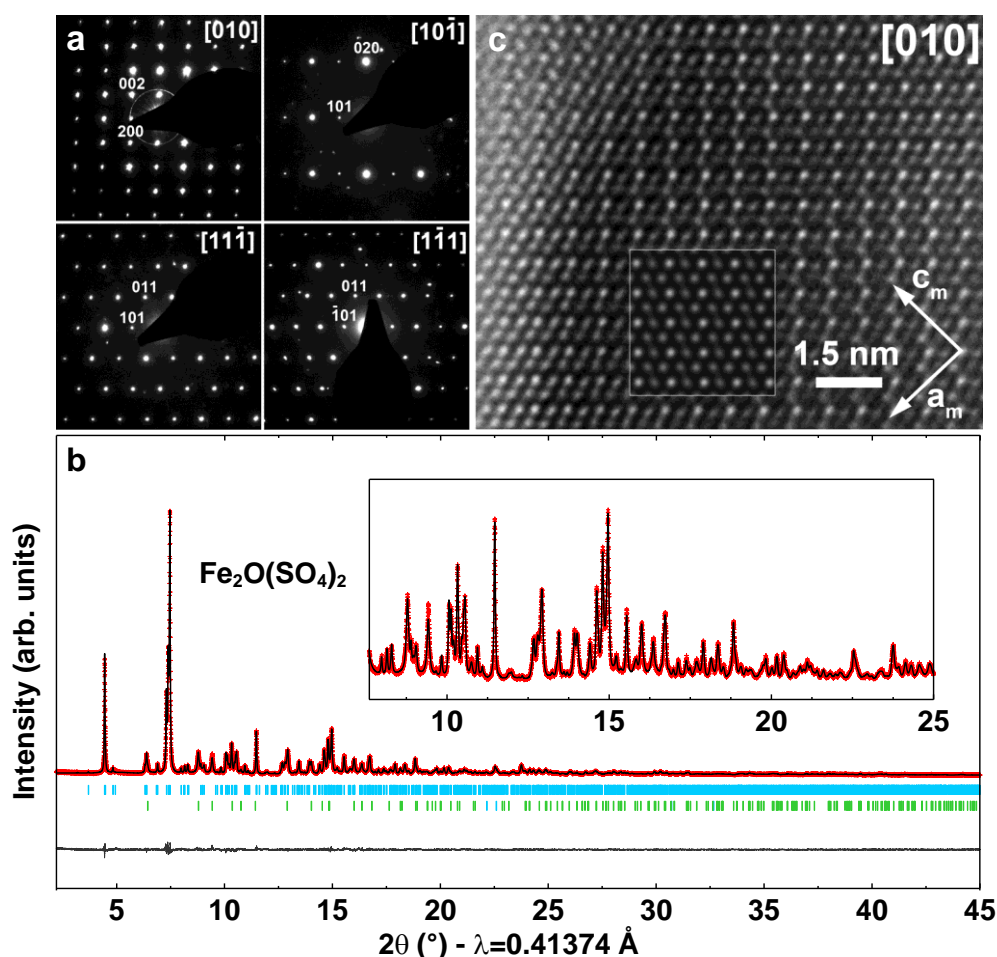


Figure III.5: (a) Main SAED patterns of $\text{Fe}_2\text{O}(\text{SO}_4)_2$ indexed on a monoclinic $I2/m$ unit cell. (b) Rietveld refinement of $\text{Fe}_2\text{O}(\text{SO}_4)_2$ against high resolution X-ray synchrotron powder data ($\lambda = 0.41374 \text{ \AA}$, $R_{\text{Bragg}} = 2.93\%$, $\chi^2 = 0.93$). The red crosses, black continuous line and bottom dark grey line represent the observed, calculated, and difference patterns, respectively. Vertical tick bars are the Bragg positions (blue: $\text{Fe}_2\text{O}(\text{SO}_4)_2$; green: Fe_2O_3). The inset is an enlargement at high angle. (c) [010] HRTEM image of $\text{Fe}_2\text{O}(\text{SO}_4)_2$.

Noting that the peak width was wider than the instrumental broadening, we refined isotropic size parameters (inducing a FWHM varying as $Y/\cos\theta$), and strain parameters. As the isotropic strain varies as $X\tan\theta$, it can be decoupled from the size parameter Y . The average crystallite size was refined to 616(5) Å. Anisotropic strain parameters, whose S_{hkl} values using Stephens notation [289] are reported in **Table III.1**, indicate some fluctuations of lattice parameters, especially along [100]. The final atomic parameters are reported in **Table III.1**, together with the results of a bond valence sum analysis (BVS) done using the Zachariasen formula with the d_0 parameters characterizing cation-anion pairs taken from reference [290].

Table III.1: Structural parameters for $\text{Fe}_2\text{O}(\text{SO}_4)_2$, deduced from the Rietveld refinement of the Synchrotron XRD pattern. A bond valence sum (BVS) analysis for each atom is also reported.

$\text{Fe}_2\text{O}(\text{SO}_4)_2$, Space Group: $I 2/m$						
$a = 9.71082(8) \text{ \AA}$, $b = 6.35288(3) \text{ \AA}$, $c = 9.92501(6) \text{ \AA}$, $\beta = 98.2851(5)^\circ$, $V = 605.901(7) \text{ \AA}^3$						
Density = 3.506 g/cm ³ , Z = 2						
Atom	Wyckoff site	x	y	z	B(Å ²)	BVS
Fe1	4i	0.80645(14)	0	0.44500(14)	0.53(3)	3.171(19)
Fe2	4i	0.55208(14)	0	0.64497(14)	0.54(3)	3.150(17)
S1	4i	0.8940(2)	0	0.7633(2)	0.71(4)	6.056(36)
S2	4i	0.3330(2)	0	0.8699(2)	0.41(4)	6.161(39)
O1	8j	0.3219(4)	-0.1868(5)	0.9492(4)	0.46(7)	2.187(17)
O2	4i	0.7453(5)	0	0.7557(4)	1.18(13)	2.143(24)
O3	4i	0.2178(6)	0	0.7526(4)	0.82(10)	2.033(20)
O4	4i	0.9404(6)	0	0.6208(5)	0.99(11)	1.826(20)
O5	8j	0.5481(4)	0.3165(5)	0.6609(3)	0.33(7)	2.073(15)
O6	4i	0.6282(6)	0	0.4727(5)	1.06(13)	2.082(19)
O7	4i	0.4708(6)	0	0.8196(5)	1.69(13)	1.934(25)

Reliability parameters: $\chi^2 = 0.93$, Bragg R-factor = 2.73%, Rf-factor = 3.24%

Although prolonged electron beam irradiation gradually leads to the sample's amorphization, the stability of the structure under electron beam is sufficient for high resolution TEM (HRTEM) imaging. The [010] HRTEM image in **Figure III.5 c** demonstrates a perfectly ordered $\text{Fe}_2\text{O}(\text{SO}_4)_2$ crystal structure. The simulated HRTEM image (insert in **Figure III.5 c**, defocus $d = 6.0$ nm, thickness $t = 6.4$ nm) reproduces the experimental contrast fairly well, confirming the correctness of the refined structure.

Figure III.6 and **Figure III.7** present the refined $\text{Fe}_2\text{O}(\text{SO}_4)_2$ structure. Iron atoms are distributed on two crystallographic sites, being octahedrally coordinated with oxygen. These octahedra are linked two by two through edges so as to form Fe_2O_{10} dimers, which are connected through one oxygen (denoted O6 in **Table III.1**) to form infinite chains running along [100]. These chains, located at $[0 \frac{1}{2} 0]$ and $[0 0 \frac{1}{2}]$, are connected to each other through regular SO_4 tetrahedral groups.

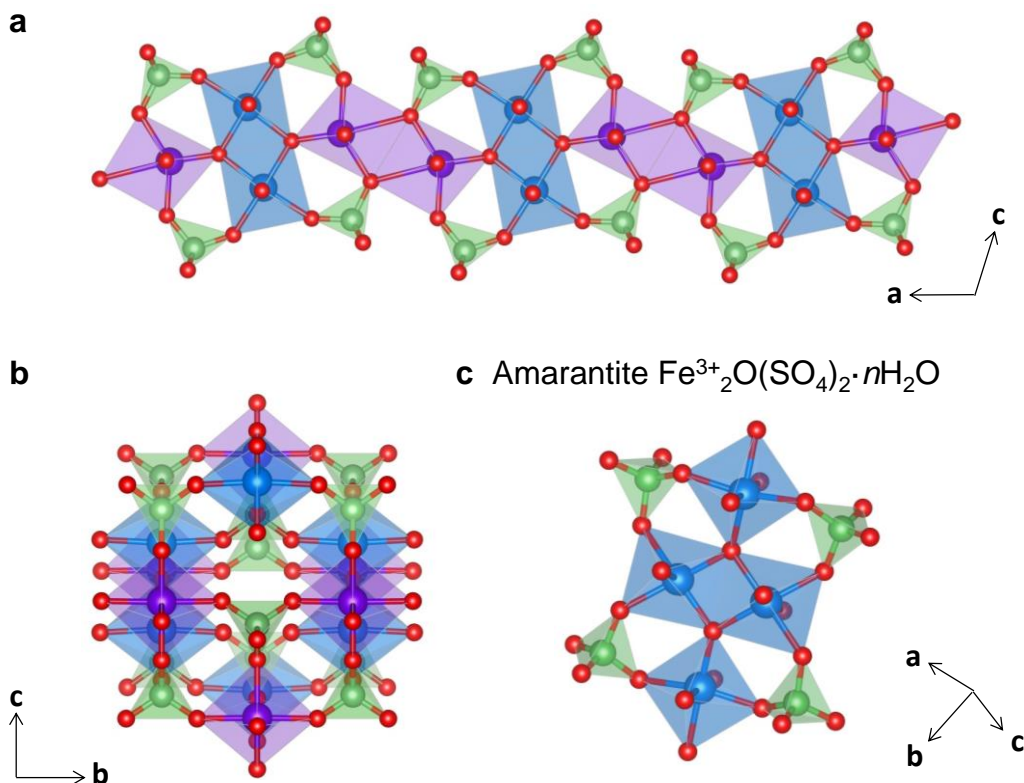


Figure III.6: Structure of $\text{Fe}_2\text{O}(\text{SO}_4)_2$ built upon (a) Chains of edge- and corner-sharing FeO_6 octahedra running along the [100] direction (b) View perpendicular to the chains which are linked via SO_4 tetrahedra. Fe is shown as purple and blue balls for Fe1 and Fe2, respectively; O is yellow, S is green. (c) Structure of $\text{Fe}_2\text{O}(\text{SO}_4)_2 \cdot n\text{H}_2\text{O}$ minerals belonging to the *amarantite* family, drawn with the same color code.

A closer look at the structure of $\text{Fe}_2\text{O}(\text{SO}_4)_2$ indicates that O6 is the only oxygen atom which is not a part of SO_4 tetrahedra. O6 is 3-fold coordinated by one Fe1 and two Fe2 atoms (**Figure III.7 a**). While Fe2 sits at the center of a nearly regular octahedron ($d_{\text{Fe}_2\text{-O}} \approx 1.96 - 2.03 \text{ \AA}$), Fe1 clearly appears to be off-centered in its octahedron, with one very short (1.79 \AA) and one very long (2.63 \AA) Fe2-O distances, whereas the distances to four other oxygen atoms are between 1.94 and 2.02 \AA . This rather uncommon coordination for Fe^{3+} is achieved in order to satisfy the bond valence sum of the O6 oxygen. To check this further, we examined a model with Fe1 at the center of its coordination octahedron at position $(0.8432, 0, 0.43702)$, *i.e.* shifted by 0.37 \AA from the refined position $(0.80645(14), 0, 0.44500(14))$. The resulting

refinement using this hypothetical structural model clearly worsens as can be seen from **Figure III.7 b**, and the bond valence sum of O6 is reduced to 1.5. It is worth noting that such small Fe-O distances (1.79 Å) have been reported in other iron – based phosphate and oxyphosphate compounds, such as $\text{Fe}_4(\text{P}_2\text{O}_7)_3$ [291] and $\text{Fe}_4(\text{PO}_4)_2\text{O}$ [292]. Similarly, distorted FeO_6 octahedra have also been observed in ferrite perovskites $(\text{Pb,Bi})_{1-x}\text{Fe}_{1+x}\text{O}_{3-y}$ but here the driving force for the off-centering of Fe is attributed to the presence of stereochemically active lone-pair elements bismuth or lead [293-294].

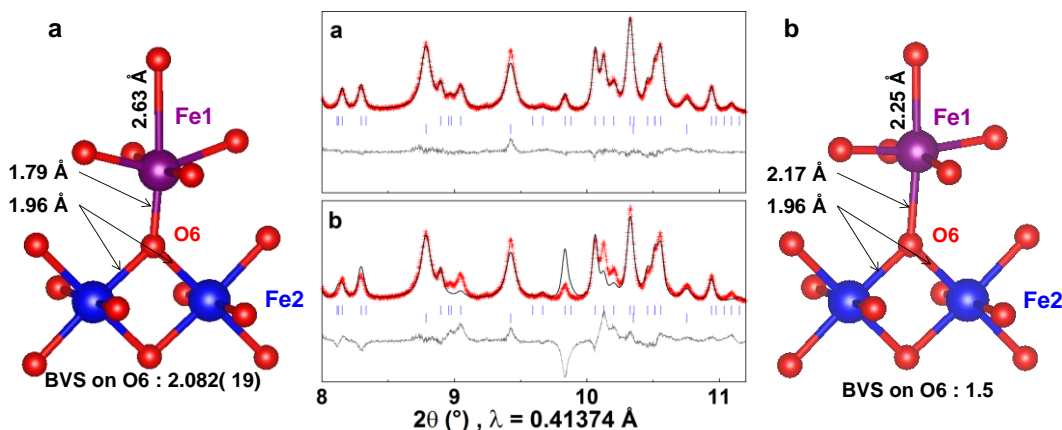


Figure III.7: (a) Local arrangement of $\text{Fe}_2\text{O}(\text{SO}_4)_2$ with the off-centering of Fe1 (purple) in its O_6 octahedron. The bond valence sum (BVS) deduced for O6, the oxygen that bridges the three FeO_6 octahedra and is not part of a SO_4 tetrahedron, is displayed. (b) Virtual arrangement with Fe1 placed in the middle of its octahedron and resulting BVS on O6. The middle panel shows the influence on the position of Fe1 on the quality of the refinement of synchrotron powder X-ray diffraction data (11BM, $\lambda = 0.41374$ Å).

it is worth noting that the structure of $\text{Fe}_2\text{O}(\text{SO}_4)_2$ presents similarities with the structures presented in the *amarantite* group [295-297], which enlist three minerals that differ only by their water content: *hohmannite* $\text{Fe}^{3+}_2\text{O}(\text{SO}_4)_2 \cdot 8\text{H}_2\text{O}$, *amarantite* $\text{Fe}^{3+}_2\text{O}(\text{SO}_4)_2 \cdot 7\text{H}_2\text{O}$, and *metahohmannite* $\text{Fe}^{3+}_2\text{O}(\text{SO}_4)_2 \cdot 3\text{H}_2\text{O}$. These three hydrated iron sulfates are all built upon the same unit made of four FeO_6 octahedra, with two of them linked by an edge and the two others connected through vertices as shown in **Figure III.6 c**. The same units are present in $\text{Fe}_2\text{O}(\text{SO}_4)_2$ but they are condensed so as to form chains. In spite of such a structural resemblance, we did not observe a transformation from $\text{Fe}_2\text{O}(\text{SO}_4)_2$ to any *amarantite* related mineral when the sample was washed with water. This does not come as a surprise as *hohmannite* is known to be an unstable mineral that transforms into the less hydrated forms *amarantite* and *metahohmannite*. Obviously, in light of these remarks, an obvious extension of this work is to prepare these minerals so as to provide an alternative eco-efficient process for the preparation of pure $\text{Fe}_2\text{O}(\text{SO}_4)_2$. We have begun initiating this approach but in preliminary trials have encountered difficulties obtaining the aforementioned hydrates as pure phases.

III.2.3. Electrochemical Performance

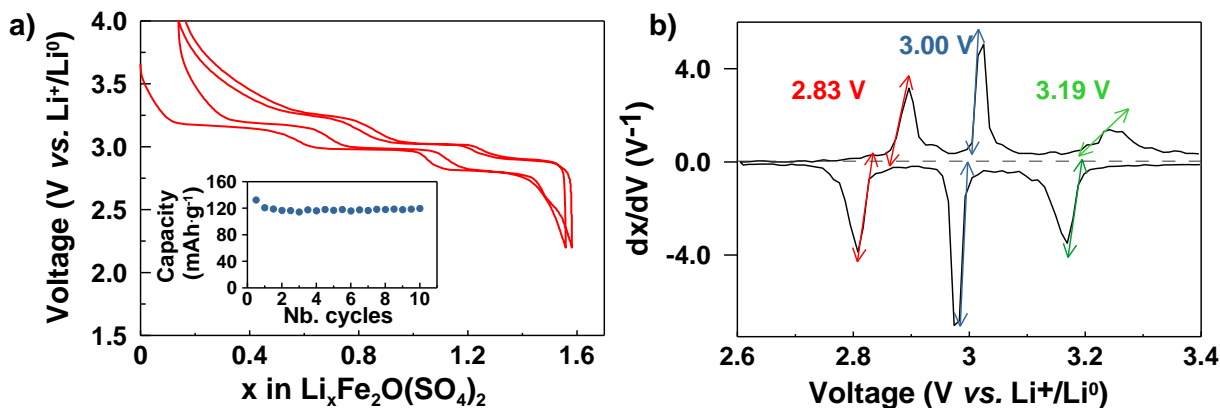


Figure III.8: (a) Typical voltage–composition curve for a $\text{Fe}_2\text{O}(\text{SO}_4)_2||\text{Li}$ cell cycled at the rate of C/40. The capacity retention is shown as inset. (b) Derivative curve dx/dV of the first cycle.

The electrochemical performance of $\text{Fe}_2\text{O}(\text{SO}_4)_2$ vs. Li was evaluated with Swagelok-type cell using a lithium metal disc as negative electrode, and a Whatman GF/D borosilicate glass fiber sheet saturated with 1M LiPF_6 in ethylene carbonate and dimethyl carbonate (1:1 w/w) as the electrolyte. The electrode was prepared by ball milling $\text{Fe}_2\text{O}(\text{SO}_4)_2$ with 20 wt.% carbon black (SP) for 15 min. The voltage-composition trace for a $\text{Fe}_2\text{O}(\text{SO}_4)_2||\text{Li}$ cell cycled in galvanostatic mode between 2.2 V and 4.0 V at a rate of C/40 is shown in **Figure III. 8 a**. The cell shows electrochemical activity with the ability to reversibly insert 1.6 Li per Fe atom with good capacity retention upon cycling (see inset). This leads to a sustained reversible capacity of about 120-125 mA·h/g. More precisely the voltage-composition trace presents a staircase variation with the presence of three well defined plateaus occurring respectively at ≈ 3.2 , 3.0 and 2.8 V on discharge. Although less pronounced, similar plateaus occur during the subsequent charge sweep and remain upon further cycling. Plotting the derivative dx/dV curves (**Figure III.8 b**), which contain a series of 3 sets of redox peaks, highlights the reversibility of these features. The first set of peaks centered at 2.8 V with a hysteresis of 30 mV and the second set at 3 V without hysteresis are reminiscent of first order phase transitions, that is involving two distinct phases. The third set at 3.2 V also seems to indicate a first order phase transition, but with slow kinetics on oxidation as compared to the reduction.

To understand the mechanism of the Li insertion/extraction process, *in situ* XRD measurements (**Figure III.9**) were conducted using a home-made cell with an X-ray-transparent beryllium window. XRD patterns (λ_{Cu}) were collected every hour for a cell cycled at C/30, *i.e.*, with every change in lithium stoichiometry of 0.067. During the reduction sweep of the $\text{Li}/\text{Fe}_2\text{O}(\text{SO}_4)_2$ cell, we observe a gradual modification of the group of peaks at $2\theta \approx$

28° , which at the end of discharge are well separated. The pattern at the end of charge resembles the pattern of the pristine compound, indicating a reversible charging process.

To analyze the data, we selected the patterns recorded at inflexion points between two plateaus in the voltage profile curve because they are usually reminiscent of single phase materials. Patterns of single phases $\text{Li}_x\text{Fe}(\text{SO}_4)_2$ with $x \approx 0.5$, $x \approx 1$ and $x \approx 1.5-1.6$ (patterns shown in color in **Figure III.9**) were then refined starting with the structural model of the pristine phase but leaving the lattice parameters as variables. Compared to a Le Bail fit, this semi-Rietveld method has the advantage of avoiding confusion between overlapping (hkl) reflections as intensities of peaks are imposed by the structural model. The refinements are shown in **Figure III.10** together with the resulting lattice parameters and unit cell volumes. The overall volume change $\Delta V/V$ is 10% for $\text{Li}_{1.6}\text{Fe}_2\text{O}(\text{SO}_4)_2$ as compared to 7% for LiFePO_4 , the most praised material for EV applications. Moreover, note the sudden decrease of the a-axis parameter towards the end of the discharge process to 2.5 V. This decrease in the a-axis could be indicative of the total suppression of Fe-off centering beyond threshold Li content, as considered in the discussion section.

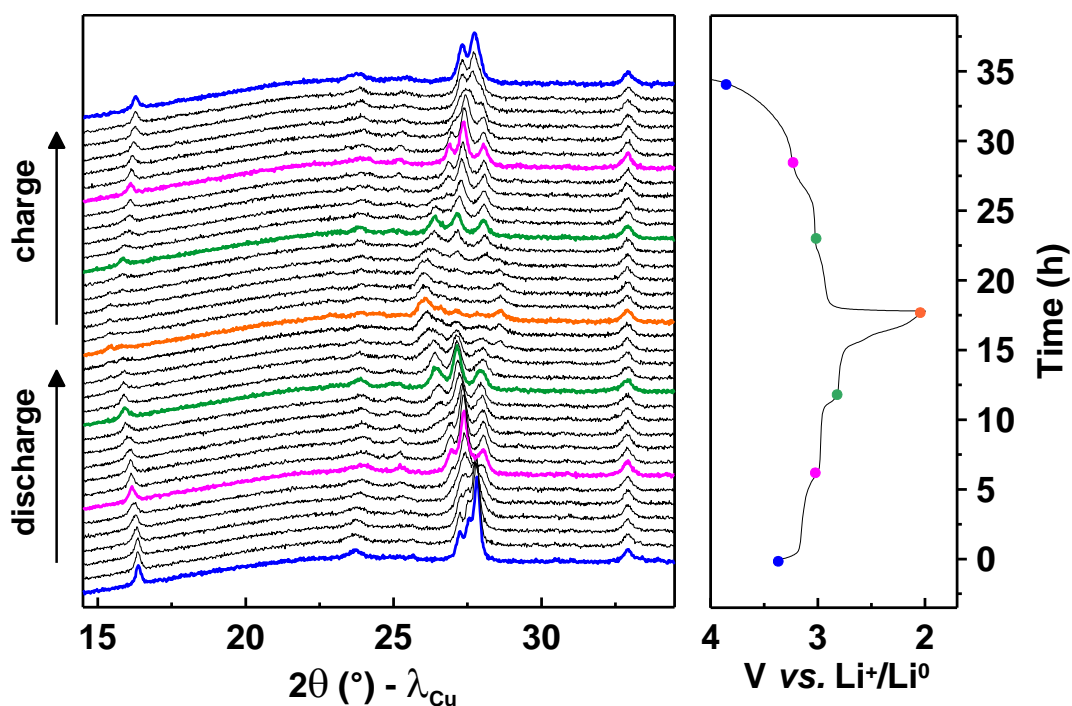


Figure III.9: X-ray diffraction patterns recorded *in situ* on the first discharge and subsequent charge. Patterns highlighted in color refer to single phase compounds whereas the one shown in black correspond to a mixture of phases (biphasic process). The corresponding voltage vs. time curve is shown on the right. Note the good reversibility of the process.

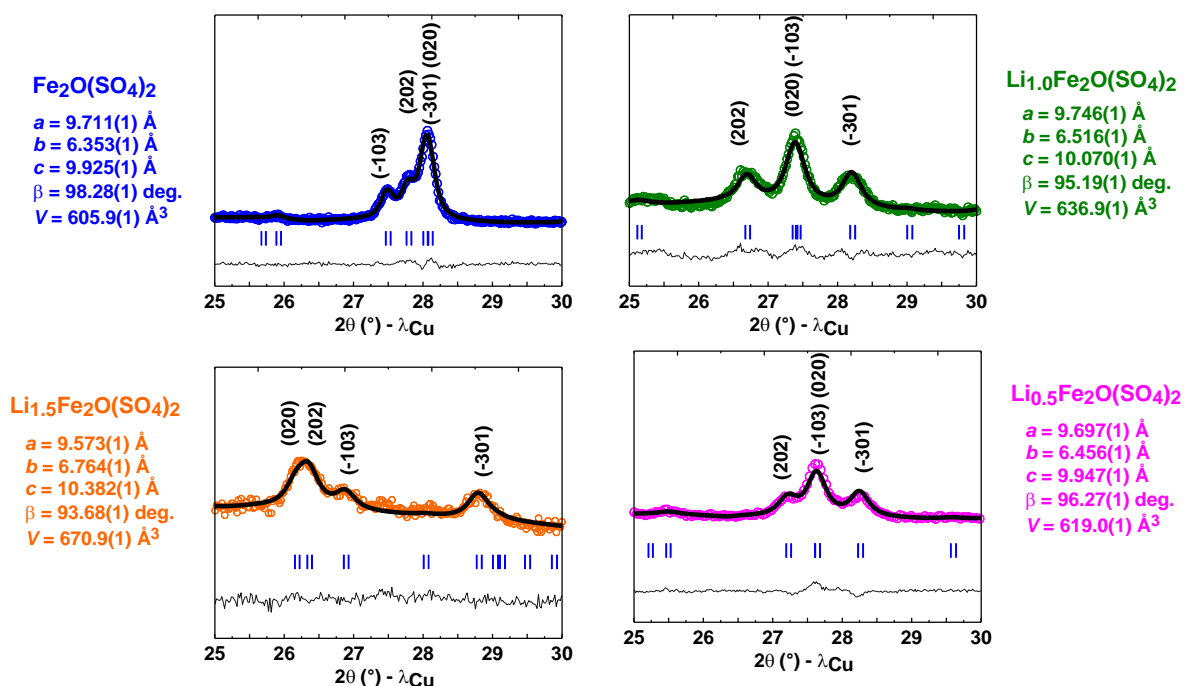


Figure III.10: Portion of the semi-Rietveld refinement of three X-ray diffraction patterns collected for pristine $\text{Fe}_2\text{O}(\text{SO}_4)_2$ and at different states of discharge, i.e. $\text{Li}_x\text{Fe}_2\text{O}(\text{SO}_4)_2$ with $x \approx 0.5$, $x \approx 1$ and $x \approx 1.5-1.6$ which are the patterns corresponding to single phase compounds. For each composition, lattice parameters and unit cell volumes are indicated.

III.2.4. Mössbauer Spectroscopy

Mössbauer spectroscopy* was performed to probe the oxidation state and the environment of the iron in the $\text{Fe}_2\text{O}(\text{SO}_4)_2$ powder synthesized (**Figure III.11 c**). The room temperature Mössbauer spectroscopy consists of absorption peaks with average isomer shifts of ~ 0.4 mm/s, characteristic of high spin octahedrally coordinated Fe^{3+} cations. Three doublets (*i.e.* 3 iron environments) are used to fit the data; the two main components, in equal amount, present similar isomer shifts (IS = 0.43 and 0.44 mm/s) but different quadrupole splittings (QS) = 0.72 and 0.43 mm/s respectively, attributed to the crystallographic sites Fe1 (brown) and Fe2 (red) on the basis that distorted Fe environments lead to larger QS. The minor doublet (6%, pink) is likely due to residual Fe_2O_3 . No trace of $\text{Fe}_2(\text{SO}_4)_3$ can be detected in the Mössbauer spectra, which agrees with XRD result.

* The Mössbauer spectroscopy experiments were conducted in collaboration with Dr. Moulay Tahar Sougrati at the Institut Charles Gerhardt (UMR 5253), Université de Montpellier 2, Montpellier, France.

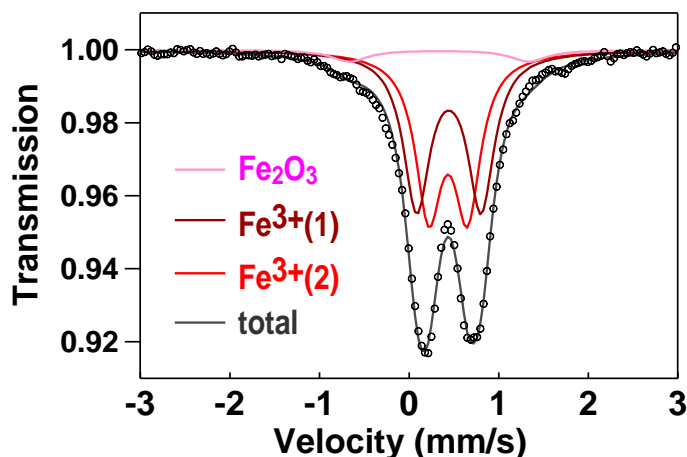


Figure III.11: Mössbauer spectra of $\text{Fe}_2\text{O}(\text{SO}_4)_2$. The brown and red contributions correspond to the two crystallographically distinct Fe^{3+} atoms in the structure; the pink doublet comes from $\sim 6\%$ Fe_2O_3 impurity.

Moreover, we also performed *in situ* Mössbauer experiments to probe local perturbations in the Fe environments during cycling, by using an electrochemical cell cycled at the rate of C/50 operating in transmission mode. The obtained spectra summarized in **Figure III.12** indicate a drastic modification of the Mössbauer spectra with increasing Li content. In comparison with the pristine material which could be fitted with two doublets, now four doublets denoted (d1, d2), and (d3, d4) are needed for Fe^{3+} and Fe^{2+} , respectively to fit the partially lithiated samples successfully. The Mössbauer study indicates that the insertion process entails 3 steps, which confirms our aforementioned *in situ* X-ray diffraction data.

During the 1st plateau at ~ 3.2 V vs. Li^+/Li , both Fe1 and Fe2 of the pristine phase are partially reduced to form two Fe^{2+} sites (denoted d3 and d4, blue and green). Interestingly the remaining Fe^{3+} presents large QS (contribution d2, 1.4-1.6 mm/s, shown in brown). This partial reduction results in the formation of a new phase that can be written as $\text{Li}_x(\text{Fe}^{3+})_{2-x}(\text{Fe}^{2+})_x\text{O}(\text{SO}_4)_2$ with $x \sim 0.5-0.6$. On further discharge through the second plateau the amount of Fe^{2+} increases while the remaining Fe^{3+} presents a higher value of QS (1.99 mm/s), indicative of a strongly distorted environment. At the end of discharge, doublets corresponding to Fe^{3+} are strongly reduced in exchange for a large Fe^{2+} contribution (d4, in green). **Figure III. 12** also shows the variation of the total amounts of Fe^{3+} and Fe^{2+} . It is worth mentioning that during the first discharge, in agreement with the electrochemical curve, 78% of Fe^{3+} is reduced, with nearly the same amount being oxidized on the following charge, hence confirming the reversibility of the lithiation-delithiation process as suggested from electrochemical data.

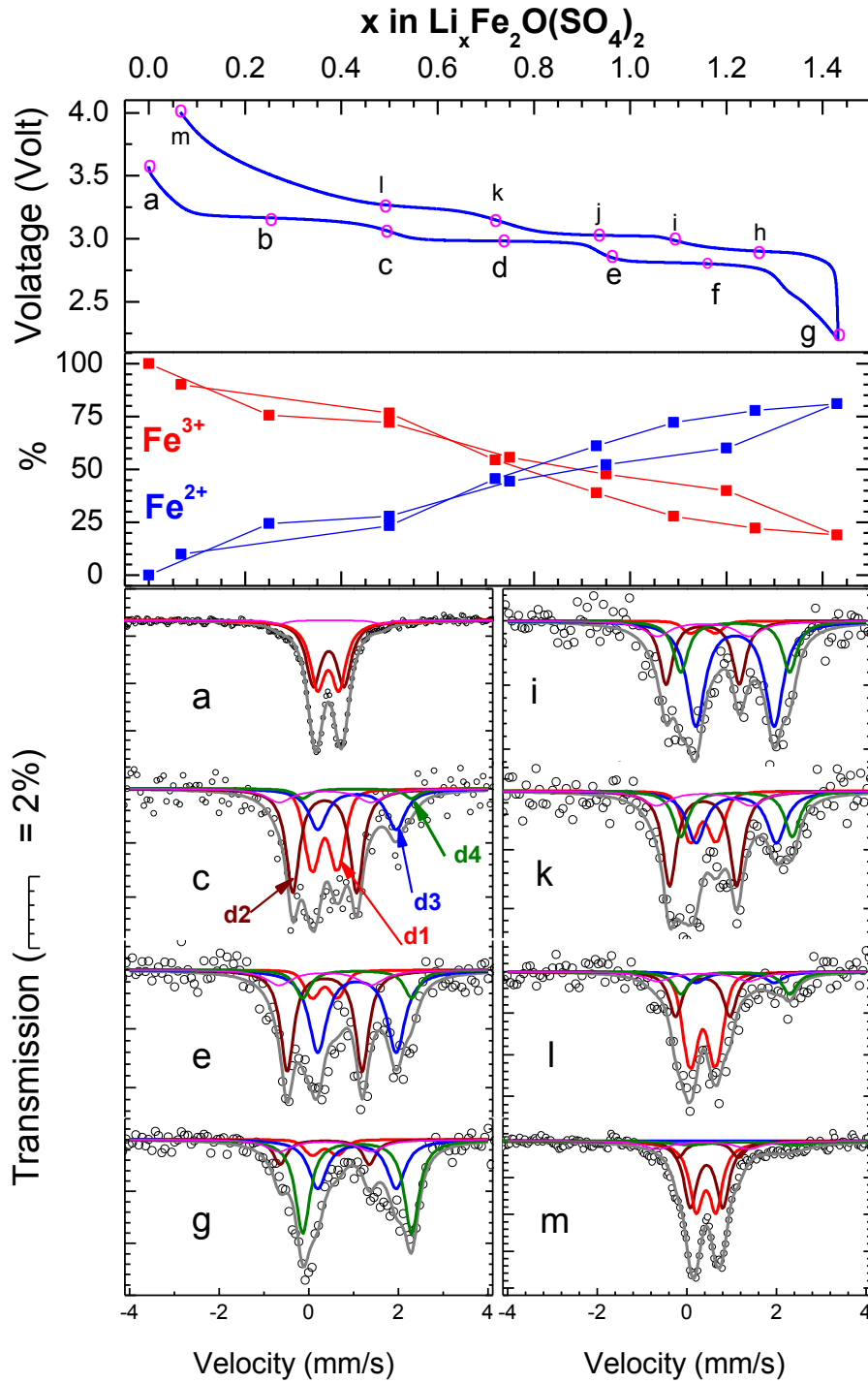


Figure III.12: Mössbauer spectra evolution of $\text{Li}_x\text{Fe}_2\text{O}(\text{SO}_4)_2$ ($0 \leq x < 2$) during the first discharge and subsequent charge. The red (d1) and brown (d2) contributions are from Fe^{3+} , whereas the blue (d3) and green (d4) present characteristics of Fe^{2+} . The pink contribution comes from 6% Fe_2O_3 impurity. The total amount of Fe^{2+} and Fe^{3+} is given in the graph in the middle.

III.2.5. Chemical Lithiation phase: $\text{Li}_{0.8}\text{Fe}_2\text{O}(\text{SO}_4)_2$

At this stage a legitimate question regards our inability to electrochemically drive the full lithiation of $\text{Fe}_2\text{O}(\text{SO}_4)_2$ (e.g. reaching a $\text{Li}_2\text{Fe}_2\text{O}(\text{SO}_4)_2$ phase with no remaining Fe^{3+}). Several trials to synthesize $\text{Li}_2\text{Fe}_2\text{O}(\text{SO}_4)_2$ through solid state methods by imitating $\text{Li}_2\text{Cu}_2\text{O}(\text{SO}_4)_2$ have failed. To address this issue, we first tried to mimic the electrochemical reaction using a mild reducing agent of LiI in acetonitrile (5 times in excess). From the lattice parameters ($a = 9.708(3)$ Å, $b = 6.487(2)$ Å, $c = 10.058(3)$ Å and $\beta = 95.04(1)^\circ$) of the obtained “ $\text{Li}_x\text{Fe}_2(\text{SO}_4)_2$ ” after two days of reaction at room temperature (**Figure III.13**), we could indirectly deduce a Li content of 0.8 per formula unit in agreement with atomic absorption measurement and consistent with the limited reducing power of the Γ/I_3^- couple (~ 2.7 V vs. Li^+/Li^0), which compares well with the *in situ* XRD experiment pattern. To increase the amount of incorporated Li ions we tried stronger reducing agents such as n-BuLi (~ 1.2 V vs. Li^+/Li^0); in this case we observed the production of an amorphous compound, confirming the difficulty of achieving complete lithiation [$\text{Li}_2\text{Fe}_2\text{O}(\text{SO}_4)_2$].

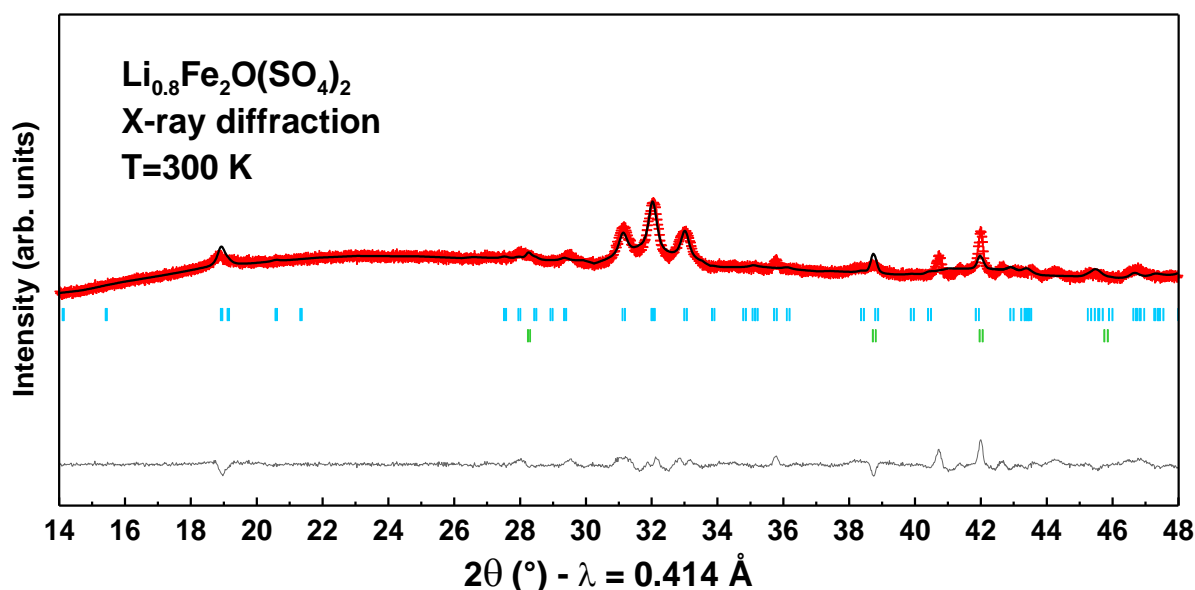


Figure III.13: Semi-Rietveld refinement of the X-ray diffraction pattern collected for lithiated phase $\text{Li}_x\text{Fe}_2\text{O}(\text{SO}_4)_2$ prepared by reductive reaction with LiI in acetonitrile.

III.2.6. Bond Valence Sum Maps

The complete reduction of Fe^{3+} into Fe^{2+} would imply an insertion of two lithium ions per formula unit, but experimentally we could not exceed an insertion of 1.6 Li per formula unit. To gain insight on this issue we created bond valence maps to assess the possible Li positions in the structure (**Figure III.14**). For this analysis we considered $\text{Li}_{1.6}\text{Fe}_2\text{O}(\text{SO}_4)_2$ with the previously determined cell lattice parameters ($a = 9.573(1) \text{ \AA}$, $b = 6.764(1) \text{ \AA}$, $c = 10.382(1) \text{ \AA}$ and $\beta = 93.68(1)^\circ$), but with atomic positions kept as those of the pristine $\text{Fe}_2\text{O}(\text{SO}_4)_2$. The cell content was then discretized through a grid of $50 \times 50 \times 50$, a Li is placed on each not and its bond valence sum was calculated.

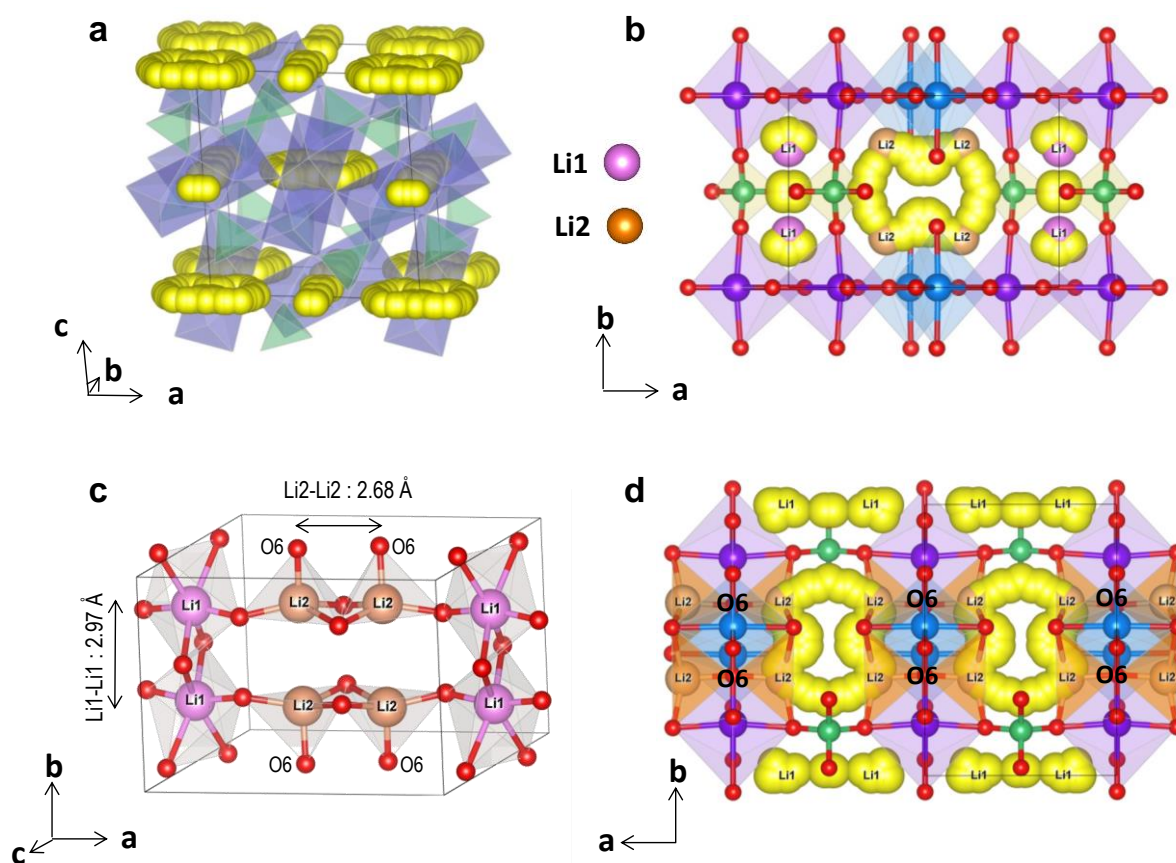


Figure III.14: Bond valence sum maps with (a) a general view of the unit cell with yellow balls corresponding to the positions at which Li would have a BVS sum close to 1, (b) The positions of the for Li1 (4h) and Li2 (8j) sites with neighboring FeO_6 octahedra and SO_4 tetrahedra. (c) Coordination of the most probable Li1 and Li2 positions for lithium and the resulted Li-Li distances. (d) Li(2)-O4 tetrahedra (orange), in which O6 may be associated with the suppression of Fe2 off-centering (purple) in the charge process.

Figure III.14 shows positions within the cell corresponding to a bond valence calculation of +1, which are positions suitable for Li. All possible positions are found at $z \approx 0$ (and $z \approx 1/2$ due to the *I*-cell centered unit cell). Among these, two representative positions for lithium; Li1 (1/2, 0.22, 0) and Li2 (0.14, 0.76, 0) which correspond respectively to the 4*h* and 8*j* Wyckoff positions (**Figure III.14 b**) can be considered. Li1 is 6-coordinated with oxygen while Li2 is located in a distorted tetrahedral site as highlighted in **Figure III.14 c**. The tetrahedral Li environment involves the creation of a Li2-O6 bond that may be associated with the suppression of Fe2 off-centering at the end of discharge (**Figure III.14 d**). Moreover, it is worth noting that the distance between Li1 and Li2 is only 2.7 Å, suggesting that electrostatic repulsions could be the origin of our inability to fully lithiate $\text{Fe}_2\text{O}(\text{SO}_4)_2$.

III.2.7. DFT calculations

To gain further insights into the lithiation mechanism, DFT+U calculations have been operated for $\text{Fe}_2\text{O}(\text{SO}_4)_2$. The cohesive energies (eV) for the $\text{Li}_x\text{Fe}_2\text{O}(\text{SO}_4)_2$ phases ($x = 0, 1$ and 2) and the average voltages for the direct and partial $\text{Fe}_2\text{O}(\text{SO}_4)_2 + x\text{Li} \rightarrow \text{Li}_x\text{Fe}_2\text{O}(\text{SO}_4)_2$ electrochemical reactions were computed. Partial lithiation ($x = 1$) was considered with a Li-site filling of the 4*h* (Li1) or half the 8*j* Wyckoff positions (Li2) of the pristine structure (**Table III.2**). The average value of redox potential of ~3.0 V was confirmed by assuming partial (0.5 Li/Fe) and full lithiation (1 Li/Fe). The 8*j* Wyckoff positions (Li2), as deduced from the accessible surface area of the non lithiated starting material, has lower Cohesive energies compared to the 4*h* Wyckoff position (Li1), thus was considered to be the most probable Li site occupation (**Figure III.15** and **Table III.2**). This result further confirms our bond valence sum calculation (see §III.2.6).

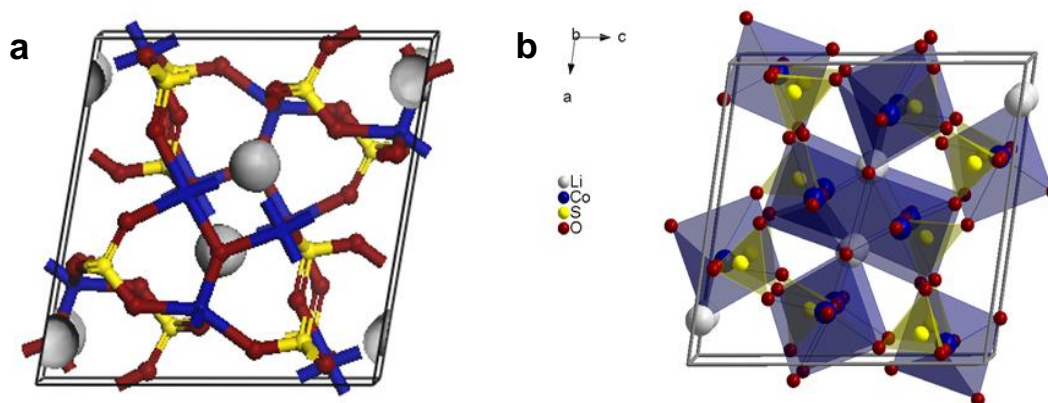


Figure III.15: (a) Accessible surface area (or Connolly surface) represented as grey volumes in the non lithiated $\text{Fe}_2\text{O}(\text{SO}_4)_2$ phase and estimated with a Connolly radius of 1.0 Å for the Li^+ cations. (b) $\text{Li}_2\text{Fe}_2\text{O}(\text{SO}_4)_2$ relaxed structures from DFT+U calculations using the initial Li positions, as obtained from the Connolly surfaces.

Table III.2: Cohesive energies (eV) for the $\text{Li}_x\text{Fe}_2\text{O}(\text{SO}_4)_2$ phases ($x = 0, 1$ and 2), and the average voltages (Volt) computed for the direct and partial $\text{Fe}_2\text{O}(\text{SO}_4)_2 + x\text{Li} \rightarrow \text{Li}_x\text{Fe}_2\text{O}(\text{SO}_4)_2$ electrochemical reactions from DFT+U calculations.

		Cohesive Energies per formula units (eV)				Average Voltage V (Volt)		
		0	1 (4h)	1 (8j)	2 (8j)	0 \rightarrow 1 (8j)	1 \rightarrow 2 (8j)	0 \rightarrow 2(8j)
$\text{Li}_x\text{Fe}_2\text{O}(\text{SO}_4)_2$	4	-41.3023	-43.6425	-43.8224	-46.1721	3.1473	2.8064	2.9768
	5	-41.0263	-43.4219	-43.5799	-46.0094	3.2143	2.9660	3.0901

III.2.8. Moisture Sensitivity Measurement

As we discussed in § I.2.2.4, the structural and electrochemical behaviors of LiFeSO_4F is strongly dependent upon the room temperature relative humidity (RH). A moisture sensitivity measurement* of $\text{Fe}_2\text{O}(\text{SO}_4)_2$ was done (**Figure III.16**). $\text{Fe}_2\text{O}(\text{SO}_4)_2$ powders were left for various amounts of time (*i.e.* 2h, 8h, 24h) in desiccators containing KCl saturated solutions with autogenous equilibrium RH of 85%, respectively at 25 °C as determined by a hygrometer within an accuracy of $\pm 1\%$. No changes have been noticed on the XRD patterns, indicating $\text{Fe}_2\text{O}(\text{SO}_4)_2$ is not moisture sensitive, in agreement with our final step of synthesis which we used water to get rid of $\text{Fe}_2(\text{SO}_4)_3$ impurity.

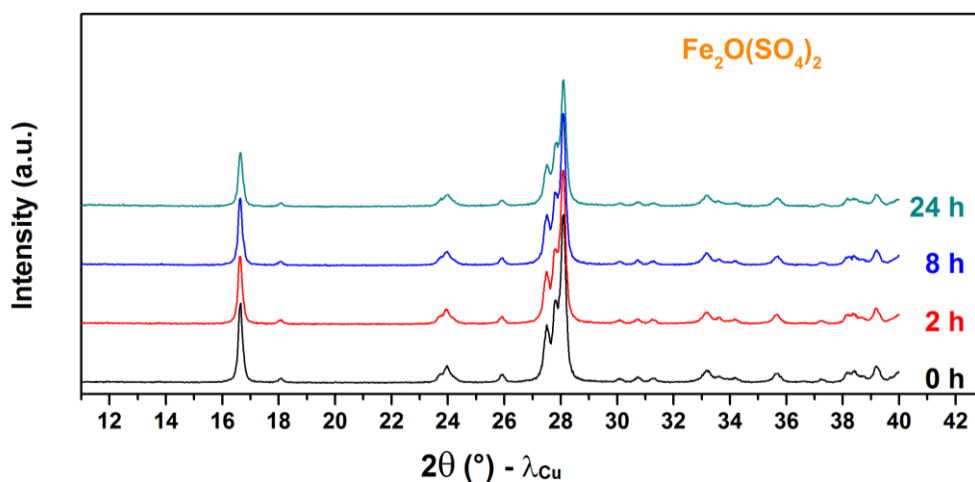


Figure III.16: Moisture sensitivity test of $\text{Fe}_2\text{O}(\text{SO}_4)_2$. Powders were placed in a desiccator with 85% RH for 2 hours (red), 8 hours (blue), and 24 hours (dark cyan) and compared with pristine ones (black).

* This experiment is operated in cooperation with PhD student Zhang LT (Collège de France, Paris, France) who studies moisture effect for sulfates.

As reported by Zhang [229], Apart from the $\text{Fe}_2\text{O}(\text{SO}_4)_2$, other Fe-based sulfates such as hydroxysulfates (LiFeSO₄OH-layered, FeSO₄OH-*tavorite*) and Li₂Fe(SO₄)₂ (layered, orthorhombic), and Na₂Fe₂(SO₄)₃ were all shown to react with water with different degrees of severity depending upon their structure and state of division. The moisture sensitivity is inherent to sulfate-based electrodes, which due to the fact that the oxygen atoms in both (SO₄)²⁻ and H₂O have comparable Lewis basicity (~0.17 v.u.), which is for instance not the case for phosphates (~0.25 v.u.). The insolubility of the oxysulfate $\text{Fe}_2\text{O}(\text{SO}_4)_2$ may result from the presence of an oxygen atom that does not belong to any sulfate group, which therefore presents a different Lewis basicity and limits its moisture sensitivity.

III.3. Conclusions

We have reported the existence of the Li-free Fe-oxysulfate with a formula $\text{Fe}_2\text{O}(\text{SO}_4)_2$, and reported its crystal structure, which has the peculiarity of containing FeO₆ octahedra with half of Fe off-centering. Aside from this peculiar aspect which permits the oxygen O6 not linked to a sulfate group to fulfill the bond valence sum, previous reports have addressed the thermal decomposition of FeSO₄·H₂O in oxygen poor or rich atmospheres, with the latter supposedly leading to single phase $\text{Fe}_2\text{O}(\text{SO}_4)_2$ at 540°C. Caution must be exercised that none of those reported X-ray diffraction data are similar to the pattern of the $\text{Fe}_2\text{O}(\text{SO}_4)_2$ phase characterized herein. Structurally, their published data for $\text{Fe}_2\text{O}(\text{SO}_4)_2$ examined is in fact a mixture of most rhombohedral Fe₂(SO₄)₃ with the oxysulfate $\text{Fe}_2\text{O}(\text{SO}_4)_2$ as minority phase (**Figure III.17**), although the peaks of Fe₂(SO₄)₃ are slightly shifted from their expected positions presumably due to angle offsets and/or sample height errors. This is most likely the reason the authors stated “The results obtained in characterizing $\text{Fe}_2\text{O}(\text{SO}_4)_2$ prove that in its structural, chemical and morphological properties $\text{Fe}_2\text{O}(\text{SO}_4)_2$ is quite similar to Fe₂(SO₄)₃”.

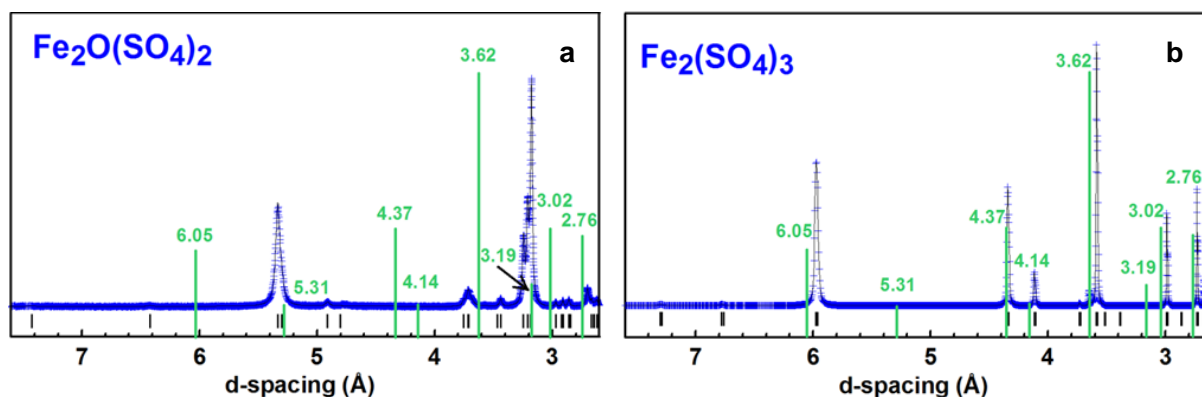


Figure III.17: Comparison of XRD pattern of the previously reported “ $\text{Fe}_2\text{O}(\text{SO}_4)_2$ ” [282] (shown as vertical green bars whose height represent relative intensities, and numbers indicate the reported d-spacing in Å) with (a) $\text{Fe}_2\text{O}(\text{SO}_4)_2$ reported in this paper and (b) Rhombohedra Fe₂(SO₄)₃.

This contradicts our finding as we obtained high purity $\text{Fe}_2\text{O}(\text{SO}_4)_2$ by washing away $\text{Fe}_2(\text{SO}_4)_3$, direct evidence that the phases have distinct chemical properties. Indeed, we took advantage of this difference to easily prepare large amounts of $\text{Fe}_2\text{O}(\text{SO}_4)_2$ electrodes. It nevertheless remains that the earlier reported phase differs from $\text{Fe}_2\text{O}(\text{SO}_4)_2$ and we believe that such a difference is nested in the synthesis conditions. We found that controlling the equilibrium between the $\text{Fe}_2(\text{SO}_4)_3$, Fe_2O_3 , and $\text{Fe}_2\text{O}(\text{SO}_4)_2$ phases is quite tricky. Slight changes in temperature, annealing time or partial pressure of the oxidative O_2 - H_2O gas mixture can result in multiphase samples with different $\text{Fe}_2\text{O}(\text{SO}_4)_2$ contents. This difficulty explains why few oxysulfates including a 3d metal different from iron have so far been reported [259, 298-300]. This is also consistent with a previous report [292] stating that structures having O^{2-} anions coexisting with highly stable polyanions $(\text{XO}_4)^{n-}$ are quite unusual and become more rare as the charge of X increases in going from Si, P and S, hence explaining the large number of oxysilicates reported as compared to oxyphosphates or oxysulfates. Within such types of oxo-based structures, of which $\text{Fe}_2\text{O}(\text{SO}_4)_2$ serves as an excellent example, oxygen atoms that are not part of the $(\text{SO}_4)^{2-}$ polyanion but bonded specifically to Fe atoms (such as O6 herein) are relatively labile, explaining why the purely polyanionic $\text{Fe}_2(\text{SO}_4)_3$ phase is always the phase competing with $\text{Fe}_2\text{O}(\text{SO}_4)_2$.

We have shown the electrochemical behavior of anhydrous iron oxysulfate towards Li, which entails a complex Li-insertion-deinsertion process as indicated by the staircase profile of the voltage-composition curve. Interestingly, aside from a shift in the potential, the voltage composition curve nearly resembles that recently reported during the insertion of Li into LiVOPO_4 [301], which also contains three successive plateaus associated with phase transformations as vanadium is reduced from 4+ to 3+ (*i.e.* to Li_2VOPO_4). The authors found a decrease of the vanadium off centering from the octahedral VO_6 center (*e.g.*, progressive disappearance of the vanadyl-type bonds) as V is reduced from 4 and 3, respectively. Since Fe is off-centered in our pristine material, it could well be that a decrease in Fe off-center displacements takes place as Fe^{3+} is reduced to Fe^{2+} , even though the analogy between the V^{4+} -O and Fe^{3+} -O bonding is not straightforward.

Lastly, performance-wise, this $\text{Fe}_2\text{O}(\text{SO}_4)_2$ phase, which can be synthesized simply from abundant elements via a process enlisting a relatively low temperature step followed by a washing in water, presents an interest for Li metal polymer batteries. It displays a reversible capacity of 125 mA·h/g, similar to $\text{Fe}_2(\text{SO}_4)_3$ while not being sensitive to moisture, a serious asset for electrode processing. In contrast, its voltage is lower owing to the lower inductive effect provided by the smaller number of $(\text{SO}_4)^{2-}$ groups per Fe in $\text{Fe}_2\text{O}(\text{SO}_4)_2$ than for $\text{Fe}_2(\text{SO}_4)_3$. This new phase shows a lower capacity and potential than LiFePO_4 , but to its advantage requires neither nano-sizing nor nanocoating for proper function. Improvements

and extensions of the present work are immediately apparent and include a broadening of the oxysulfate family by preparing the other 3d transition M based oxysulfates (M = Mn, Co, V), respectively. Overall, this work provides a solution for stabilizing sulfate-based materials against moisture solubility while offering a new material design path in our quest for new electrode materials.

Chapter IV. $A_2VO(SO_4)_2$ ($A = Li, Na$) as Electrode for Li-ion and Na-ion Batteries

IV.1. Introduction

In chapters II and III, we presented the electrochemical properties of Copper- and Iron- based oxysulfate. The $Li_2Cu_2O(SO_4)_2$ phase shows a Cu^{3+}/Cu^{2+} redox activity at nearly 4.7 V vs. Li^+/Li^0 with a limited reversible capacity of 20 mA·h/g (*i.e.* ~0.3 Li/formula). Turning to $Fe_2O(SO_4)_2$, it delivers a greater capacity of ~125 mA·h/g (*i.e.* ~0.8 Li/Fe) but at lower voltage; 3.0 V vs. Li^+/Li^0 compared to $LiFePO_4$ (3.45 V). It is therefore worth mentioning that this Li-free compound can solely be used with lithiated anode materials. In our quest towards Li-based oxysulfates with higher energy densities, we explored the Li-based Mn and Co-based oxysulfates analogues, which are expected from DFT+U calculations to have voltages approaching ~3.55 V and ~4.05 V vs. Li^+/Li^0 , respectively. However, many trials to synthesize $Li_2Mn_2O(SO_4)_2$ and $Li_2Co_2O(SO_4)_2$ by solid state synthesis have failed. Whatever precursors and experimental conditions we tried, the product seems tend to form $Li_2Mn_2(SO_4)_2$ and $Li_2Co_2(SO_4)_2$ instead of oxysulfate. This again remind us that oxysulfates are quite rare and less prone to form than oxysilicates and oxyphosphates, as indicated from reference [292].

Under such circumstances we search for 3d-metal based oxysulfates already existing among the various minerals. In addition to $Cu_2O(SO_4)_2$ (*dolerophanite*) and $Fe_2O(SO_4)_2 \cdot nH_2O$ ($n = 4, 7, 8$, corresponding to *Metahohmannite*, *Amarantite*, *Hohmannite*), we become aware of $VOSO_4$ which exists under two polymorphs (α -form: tetragonal, β -form: orthorhombic, *Pauflerite*). Their synthesis, structure and magnetic properties have already been reported [243, 302].

Vanadium exists in a variety of stable valence states, and is considered to be one of the most prone 3d-metals to undergo a multi-electron transfer process ($V^{3+} \leftrightarrow V^{4+} \leftrightarrow V^{5+}$), as shown in a high-throughput first principles analysis report enlisting phosphate-based cathodes [303] and been exemplified by vanadium oxyphosphates such as $V^{5+}OPO_4$ and $LiV^{4+}OPO_4$ [239]. These phases, have recently attracted great interest of researchers as they offer high capacities. Among the 8 polymorphs of $VOPO_4$ which are differ in the connection and arrangement of VO_6 octahedral and PO_4 tetrahedral units [304-311], ϵ - $VOPO_4$ displays potentials of 4 and 2.5 V for the V^{5+}/V^{4+} and V^{4+}/V^{3+} redox couples, respectively, with an overall capacity approaching 200 mA·h/g over 50 cycles [311]. Efforts had also been paid to the Li-based

counterparts, three polymorphs $LiVOPO_4$ (triclinic [α], orthorhombic [β], and tetragonal [α_1]) were found to present one plateau at ~ 4 V on oxidation [204, 312-314] and the ability to insert 1 Li^+ on reduction [239, 315-316] which corresponds to the V^{5+}/V^{4+} and V^{4+}/V^{3+} redox couples, respectively. Although different mechanism of Li^+ insertion were proposed for samples from different synthesis routes [239, 315], α - $LiVOPO_4$ was reported to achieve a high capacity of 240 mA·h/g (*i.e.* 1.65 Li^+/V) for up to 20 cycles [316]. In parallel, another vanadyl phosphate with a formula $Li_4VO(PO_4)_2$ showing a layered structure was reported to exhibit a reversible capacity of 60 mA·h/g at 4.1 V vs. Li^+/Li^0 (V^{5+}/V^{4+} redox couple) [317], which can electrochemically insert one Li^+ to form the $Li_5VO(PO_4)_2$ phase [318].

As already reported, the substitution of PO_4^{3-} with a more electronegative SO_4^{2-} polyanion (*e.g.* $LiFePO_4F - LiFeSO_4F$) leads to electrode materials showing higher redox potentials, hence the desire to implement this strategy with vanadium-based compounds [142]. Surprisingly, the electrochemistry of V-based oxysulfates has barely been explored at a few exceptions. Previous studies have revealed an equilibrium redox potential of 2.84 V vs. Li^+/Li^0 corresponding to V^{4+}/V^{3+} couple for the Li^+ intercalation of β - $VOSO_4$ [241]. It is higher than the one of $VOPO_4$ polymorphs which are generally located below 2.5 V. At this stage, a legitimate question regards the feasibility of synthesizing Li-based vanadium (4+) oxysulfates that can present V^{5+}/V^{4+} and V^{4+}/V^{3+} redox activities.

Herein we report the synthesis, structure, ionic conductivity and electrochemical performances of a new $Li_2VO(SO_4)_2$ compound which shows a redox potential of 4.7 V for the V^{4+}/V^{5+} redox couple. Moreover, for sake of completion of this study and due to the existence of a reported $Na_2VO(SO_4)_2$ compound [319] having the analogous formula, we decided to explore the structural relation between the two phases together with the electrochemical properties of the Na-based phase so far not been reported.

IV.2. Exploration of V-Based Oxysulfate - $Li_2VO(SO_4)_2$ - as Electrode for Li-ion Batteries

IV.2.1. Synthesis

A ceramic process has been used to prepare the targeted $Li_2VO(SO_4)_2$ phase. $VOSO_4 \cdot xH_2O$ (Alfa Aesar, 99.9% metal basis) and Li_2SO_4 (Alfa Aesar, 99.7%) were used as V- and Li-based precursors for the targeted $Li_2VO(SO_4)_2$ phase. $VOSO_4 \cdot xH_2O$ (Alfa Aesar, 99.9% metal basis) was firstly dehydrated in argon at 260 °C to prepare α - $VOSO_4$ as illustrated in literature [243]. Then stoichiometric amounts of Li_2SO_4 and $VOSO_4$ were thoroughly ball milled,

pressed into a pellet and annealed under Ar for 12 hours at 400 – 415°C to produce a well-crystallized sample with sharp reflections on the XRD powder pattern reminiscent of a new phase according to the following reaction:



IV.2.2. Structural Characterization

To determine the structure of $Li_2VO(SO_4)_2$, we examined the powder synthesized above using synchrotron X-ray and neutron powder diffraction. For synchrotron XRD, the finely ground aquamarine powder was loaded in a 0.7 mm diameter capillary and the sample was measured in transmission mode ($\lambda = 0.41417 \text{ \AA}$). For neutrons, the sample (from the exact same batch) was put in a cylindrical vanadium container and measured on the HRPT high resolution neutron diffractometer ($\lambda = 1.4934 \text{ \AA}$).

Due to the close resemblance between the neutron and XRD patterns obtained for $Li_2VO(SO_4)_2$ with the ones reported for $Li_4VO(PO_4)_2$ [317] and arsenate $Li_4VO(AsO_4)_2$ [320], we first refined the patterns using their structural models, $P 4/n$ and $P 4/n c c$ respectively, both being tetragonal. However our trials to refine $Li_2VO(SO_4)_2$ starting from these analogs led to un-satisfactory refinements, as shown in **Figure IV.1**.

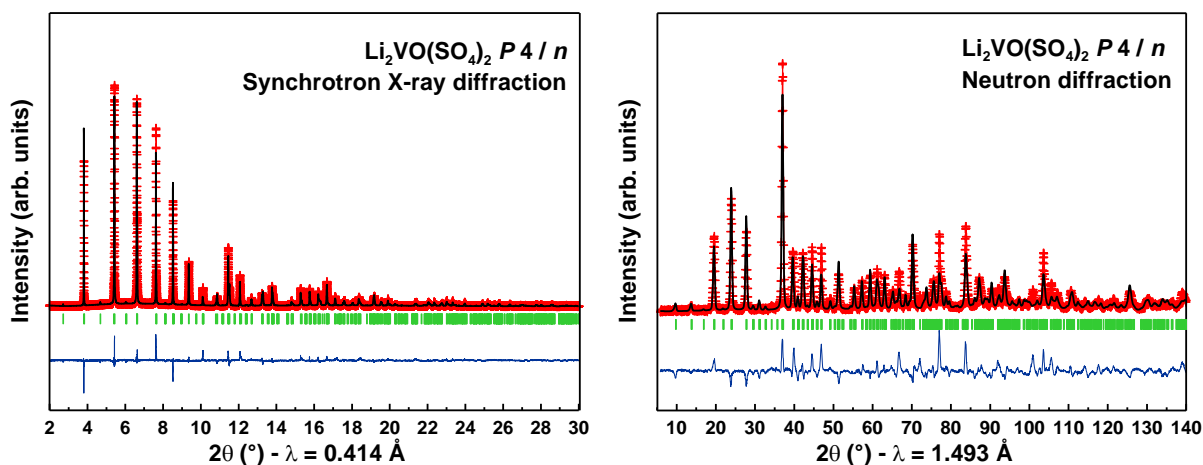


Figure IV.1: Unsatisfactory Rietveld refinement of synchrotron and neutron diffraction patterns obtained for $Li_2VO(SO_4)_2$ ($T = 300 \text{ K}$) using the structure model of $Li_4VO(PO_4)_2$ (space group: $P 4/n$).

Therefore we solved the structure of $Li_2VO(SO_4)_2$ from the beginning. First, we used Dicvol program [251] to index the synchrotron X-ray diffraction peaks, suggesting a tetragonal unit cell with lattice parameters $a = 8.81158(4) \text{ \AA}$ and $c = 8.75256(6) \text{ \AA}$. The corresponding volume ($V = 679.584(6) \text{ \AA}^3$) is suitable to accommodate four formulae per unit cell, and this unit cell is metrically similar to the one reported for the phosphate and arsenate compounds

mentioned above. However, the observed (hkl) reflections indicate a body-centered unit cell, which is further confirmed by electron diffraction (**Figure IV.2**). At this stage, we performed explorations through combining neutron/X-ray powder diffraction in different space groups using FOX software [252]. SO_4 groups were treated as rigid tetrahedra with S-O distances of 1.49 Å. The best structural model was obtained in space group $I4cm$ that we confirmed by performing a combined Rietveld refinement of the neutron and synchrotron XRD patterns with the FullProf program [253], the result is shown in **Figure IV.3**. For the latter, the peak shapes were described using Thomson-Cox-Hastings profile functions; all atoms and their isotropic temperature factors were freely refined, except for vanadium which is placed at (0, 0, 0) to fix the floating z-origin. Final atomic positions are reported in **Table IV.1**.

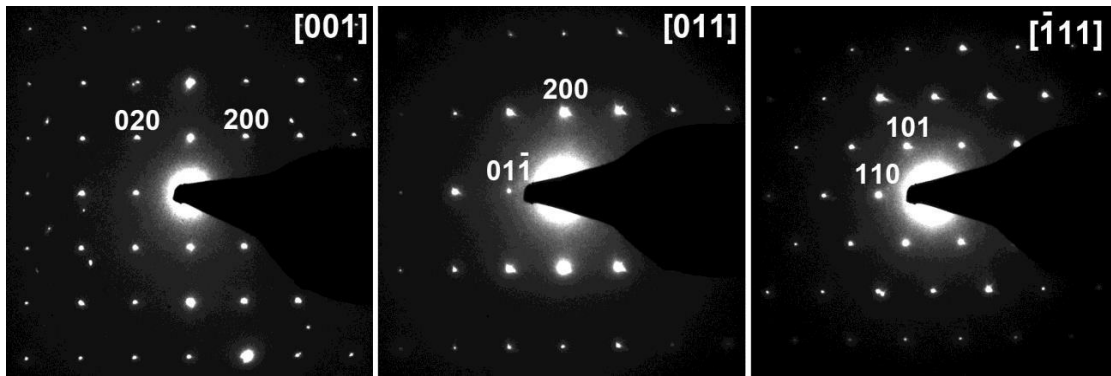


Figure IV.2: Electron diffraction patterns of $Li_2VO(SO_4)_2$ indexed with the I -centered ($a \approx 8.8$ Å) cubic unit cell.

Table IV.1: Structural parameters for $Li_2VO(SO_4)_2$, deduced from the combined Rietveld refinement of the neutron and synchrotron X-ray diffraction patterns at 300 K.

$Li_2VO(SO_4)_2$, Space Group: $I4cm$						
$a = 8.81158(4)$ Å, $c = 8.75256(6)$ Å, $V = 679.584(6)$ Å ³ , density = 2.668 g/cm ³ , $Z = 4$						
Atom	Wyckoff site	x	y	z	Occupancy	B(Å ²)
Li	8c	0.3865(6)	0.8865(6)	0.1681(8)	1	0.737(78)
V	4a	0	0	0	1	0.497(35)
S	8c	0.30544(13)	0.80544(13)	0.5250(4)	1	0.617(85)
O1	8c	0.3902(2)	0.8902(2)	0.6377(4)	1	1.303(12)
O2	16d	0.36268(17)	0.32610(18)	0.5522(3)	1	0.879 (73)
O3	8c	0.3454(2)	0.8454(2)	0.3704(4)	1	1.686(59)
O4	4a	0	0	0.8200(5)	1	1.267(74)

Reliability parameters: $\chi^2 = 3.02$;

Synchrotron: Bragg R-factor = 4.87%, Rf-factor = 3.17%;

Neutrons: Bragg R-factor = 4.59%, Rf-factor = 5.89%

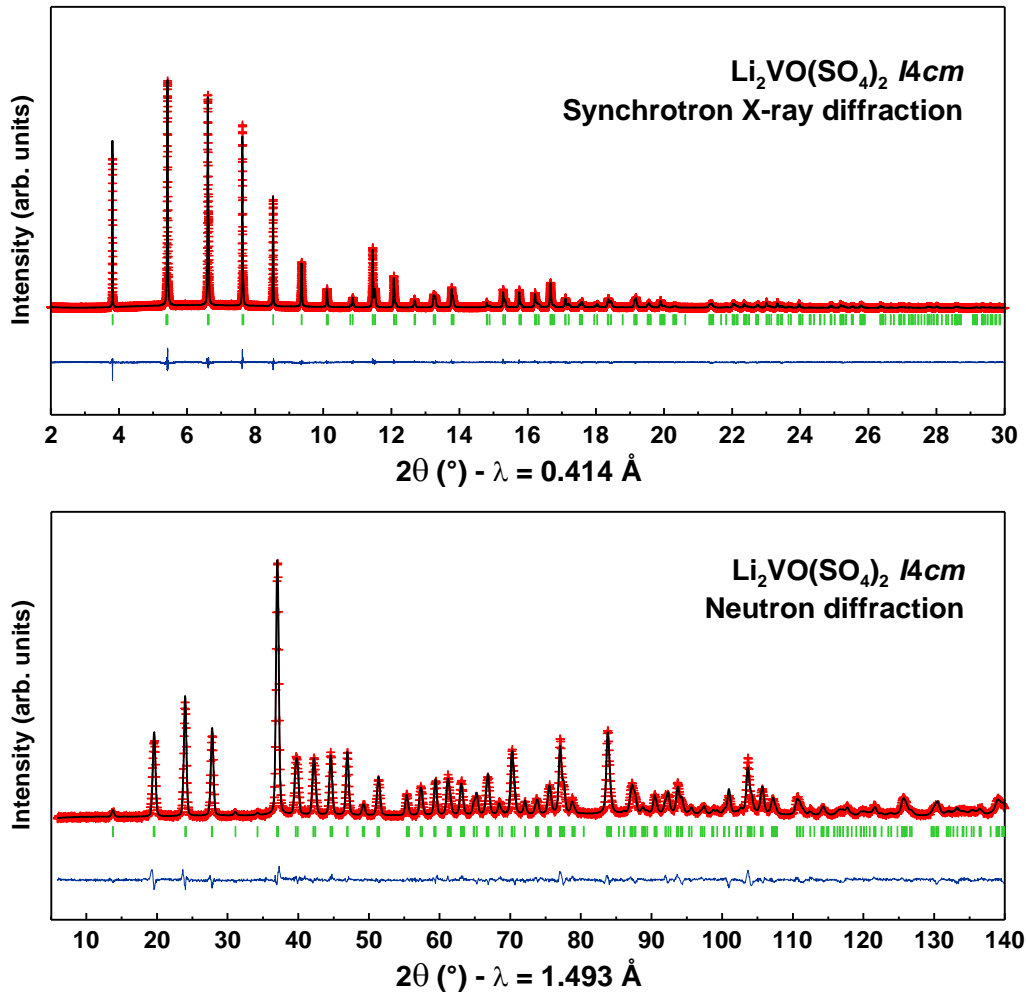


Figure IV.3: Combined Rietveld refinement of the synchrotron and neutron diffraction patterns of $Li_2VO(SO_4)_2$ ($T = 300$ K).

An overview of the structure of $Li_2VO(SO_4)_2$ is shown in **Figure IV.4**. Vanadium atoms are coordinated with one oxygen atom at a short distance of 1.58 \AA (vanadyl bond, shown a red line in **Figure IV.4 a**) and four equatorial oxygen atoms at 2.00 \AA , so as to form a square pyramidal environment commonly observed in V^{4+} containing compounds [321]. These VO_5 square-based pyramids are sharing vertices with SO_4 groups (**Figure IV.4 a, b**) to form layers perpendicular to $[001]$ (**Figure IV.4 b**). Along these chains, VO_4 squares are rotated by a minor angle along the $[001]$ direction (**Figure IV.4 d**). It is worth noting that if longer V-O distances are considered, the structure reveals alternated short (1.58 \AA) (red) and long (2.79 \AA) V-O bonds (blue) along $[001]$, which is considered to be particular for V^{4+} and V^{5+} instead of V^{3+} [321], similar to those observed in oxyphosphate, $LiVOPO_4$ and $Li_4VO(PO_4)_2$ (**Figure IV.5**). Please note the structure of our $Li_2VO(SO_4)_2$ resembles very well with the one of $Li_4VO(PO_4)_2$ (**Figure IV.6**). Both of them are layered 2D structure built on edge sharing SO_4 groups and VO_6 bipyramids, the most difference lies in there is only one Li site and one V site in $Li_2VO(SO_4)_2$ instead of three Li sites and two V sites in $Li_4VO(PO_4)_2$.

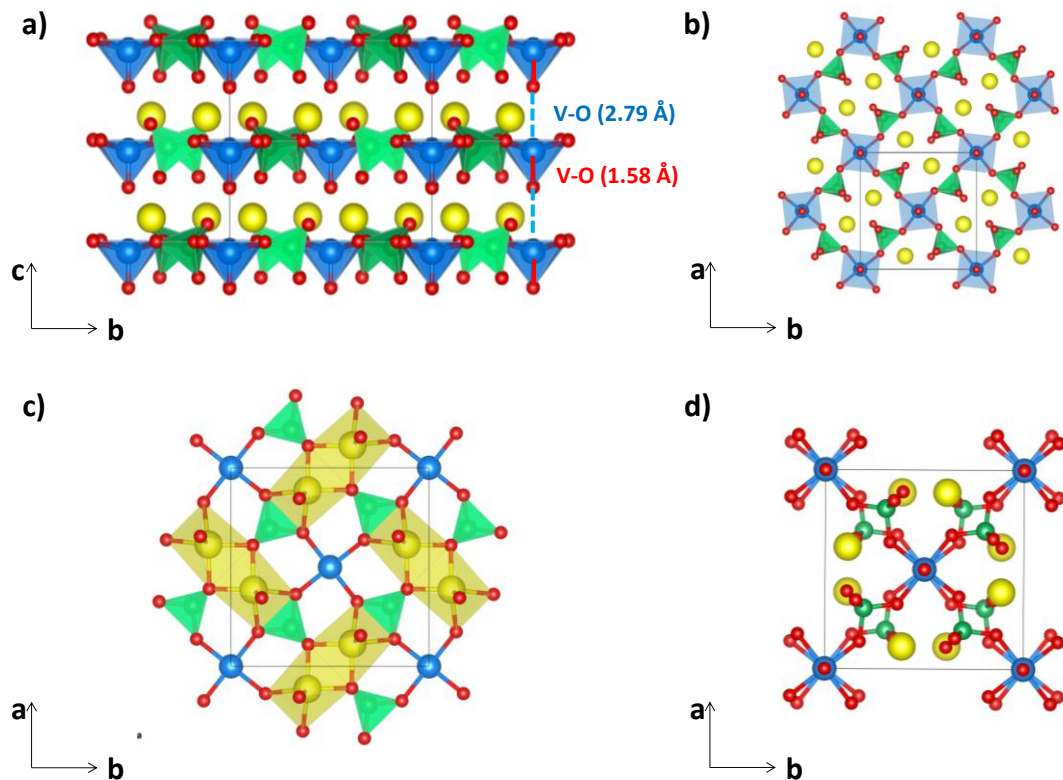


Figure IV.4: (a) Layered view of the structure of $Li_2VO(SO_4)_2$ perpendicular to $[100]$ direction. VO_5 square pyramids are colored in blue, SO_4 groups are green, and Li are shown as yellow balls. Alternated long and short bonds are shown in blue and red, respectively. (b) View of one layer along $[001]$, built on vertex-sharing VO_5 square pyramids and SO_4 tetrahedra. (c) Li coordination environment (LiO_5 square based pyramids sharing edges, colored in yellow). (d) Two layers perpendicular to $[001]$ which show VO_4 squares in different layers are rotated by a minor angle.

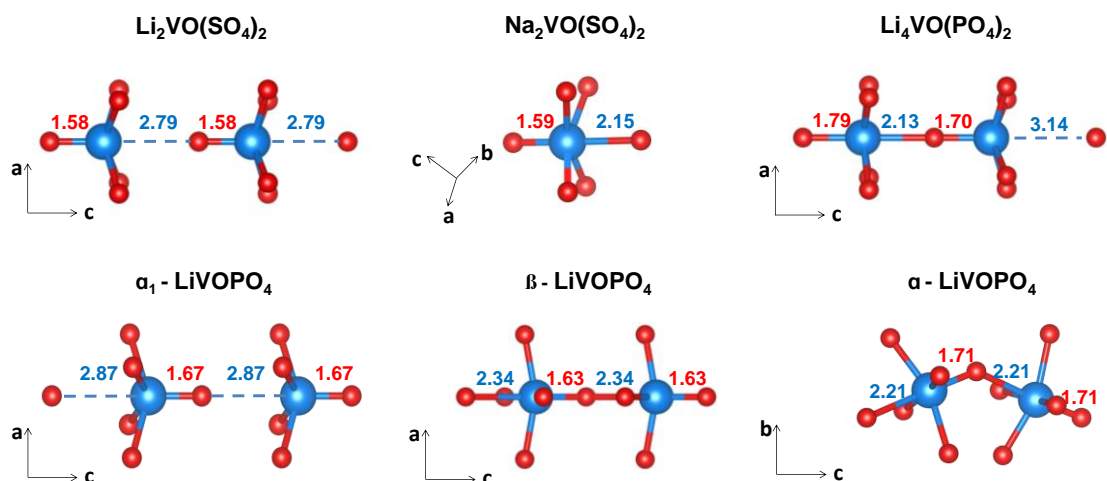


Figure IV.5: Alternated short (colored in red) and long V-O bonds (units: Å) among different vanadyl oxysulfate and oxyphosphate: $Li_2VO(SO_4)_2$, $Na_2VO(SO_4)_2$, $Li_4VO(PO_4)_2$ and three polymorphs of $LiVOPO_4$ (space groups for polymorph α, β, α_1 : $P\bar{1}, Pnma, P4/nmm$)

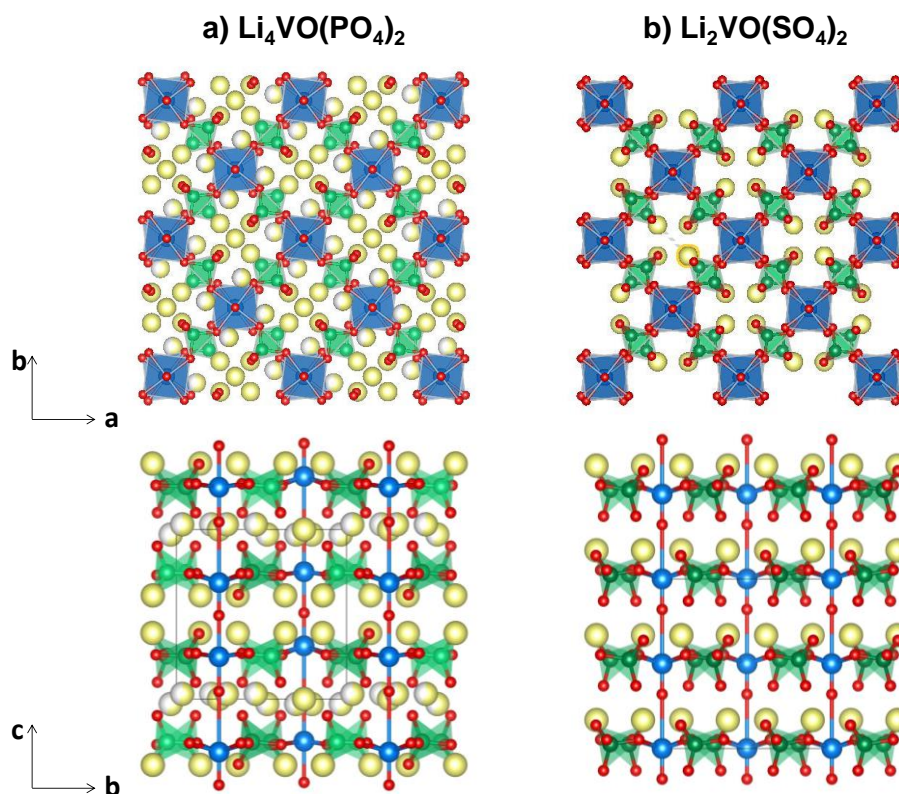


Figure IV.6: Similar structures of (a) $Li_2VO(SO_4)_2$ and (b) $Li_4VO(PO_4)_2$ as shown long [001] (top) and [100] direction (bottom).

IV.2.3. Electrochemical Performance

The electrochemical performance of $Li_2VO(SO_4)_2$ vs. Li was tested using Swagelok-type cells which were assembled in an argon dry glovebox and cycled with a VMP system (Biologic S.A., Claix, France) operating in galvanostatic mode.

Prior to be used as positive electrodes, the active materials were ball milled with 25% in mass of carbon SP for 15 minutes. The positive electrode was separated from the Li metal disc negative electrode by two Whatman GF/D borosilicate glass fiber sheets saturated with *LP100* electrolyte. The cells were started either on oxidation to investigate V^{5+}/V^{4+} redox activity or on reduction to detect the V^{4+}/V^{3+} redox activity. **Figure IV.7** shows the voltage-composition curve for a $Li_2VO(SO_4)_2||Li$ cell starting on the oxidation process. With the rate of C/25 (1 Li in 25 hours), the potential rapidly increases to 4 V and then progressively reaches a plateau located at 4.7 V whose amplitude corresponds to ~ 1.1 mol. of Lithium. Upon discharge, only ~ 0.5 out of the 1.1 Li can be reinserted on a 4.6 V plateau. This leads to an overall reversible capacity of ~ 50 mA·h/g for the first cycle, which gradually fades to ~ 25 mA·h/g after 20 cycles. There is a large irreversibility capacity between the first charge and discharge which is followed by a slippage of the cycling curves towards lower composition of x, suggesting

copious electrolyte decomposition together with the formation of an SEI (Solid State Electrolyte) layer.

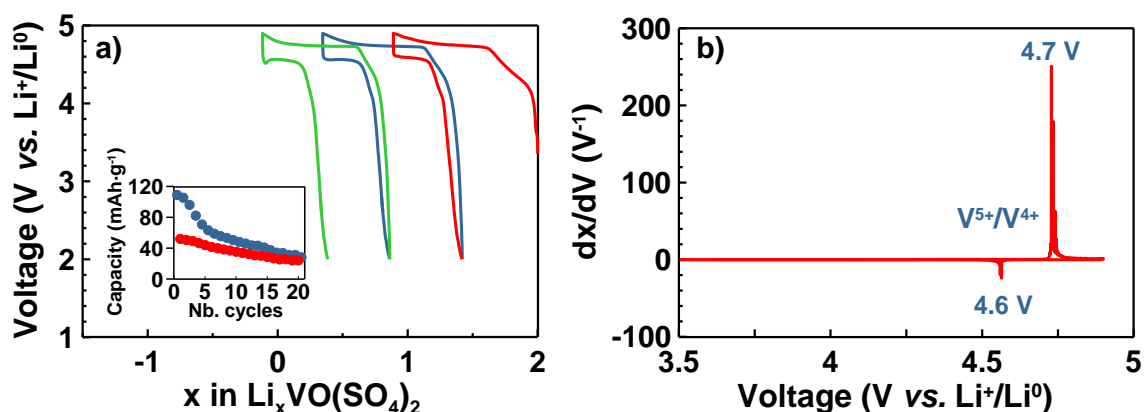


Figure IV.7: (a) Typical voltage–composition curve for the $Li_2VO(SO_4)_2||Li$ cell starting on charging process, with a rate of $C/25$. The capacity of cycles is shown as inset. (b) The derivative curve of the second cycle.

The decay of the capacity might be due to side reactions between the positive electrode and electrolyte, as the color of the separators recovered after cycling indeed changes. Furthermore, we performed the high temperature cycling measurement with the same experimental conditions but by increasing the temperature till 50 °C. For this experiment, the cell was placed in an oven of 50 °C and connected to the portable VMP system. Surprisingly, instead of improving the performance by increasing kinetics, the cell died on the first charge as shown on **Figure IV.8**, which suggests that the side reactions between the material and *LP100* electrolyte had been accelerated by the increasing temperature.

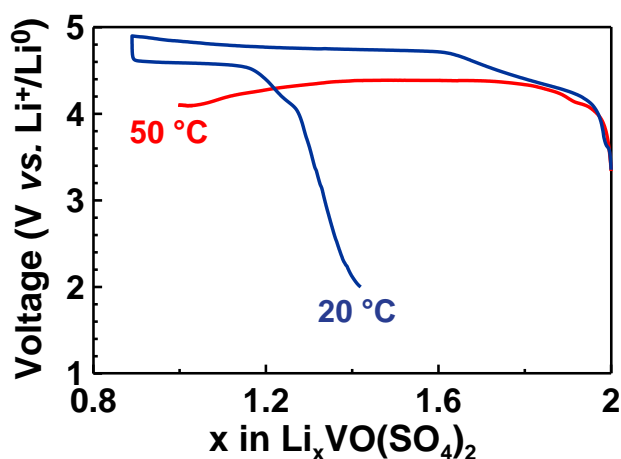


Figure IV.8: Comparison of the voltage–composition curves for the $Li_2VO(SO_4)_2||Li$ cells cycled at a rate of $C/25$ under room temperature (~ 20 °C) and high temperature (50 °C).

To examine the Li extraction-insertion mechanism during the oxidation process, *in situ* X-ray diffractions were recorded for a $Li_2VO(SO_4)_2/Li$ cell starting on charge at a rate of C/20 under Belgium window (**Figure IV.9 a**). During cell charging, no noticeable changes were observed in the X-ray powder pattern until the voltage reaches the plateau at 4.7 V. This suggests that the initial capacity in oxidation is mainly due to electrolyte decomposition. Once the plateau is reached, a new set of XRD peaks appear (noted as stars in **Figure IV.9**) and they grow upon further delithiation at the expense of the pristine phase. The peaks of the new phase can be indexed with the same tetragonal structural model as pristine $Li_2VO(SO_4)_2$ but with lattice parameters $a = 8.51 \text{ \AA}$, $c = 9.10 \text{ \AA}$, *i.e.* corresponding to a volume of 658 \AA^3 (*vs.* 679 \AA^3 for pristine, $\Delta V \approx -3.1 \%$), as shown in **Figure IV.9 b**. From refinement of the XRD pattern we estimate this new phase consists in a mixture of $Li_2VO(SO_4)_2$ and $LiVO(SO_4)_2$ with a $\sim 80\%/20\%$ ratio. Upon discharge, peaks from the $LiVO(SO_4)_2$ phase fully vanish to give a powder pattern analogue to that of the pristine $Li_2VO(SO_4)_2$ compound, hence revealing a reversible biphasic process.

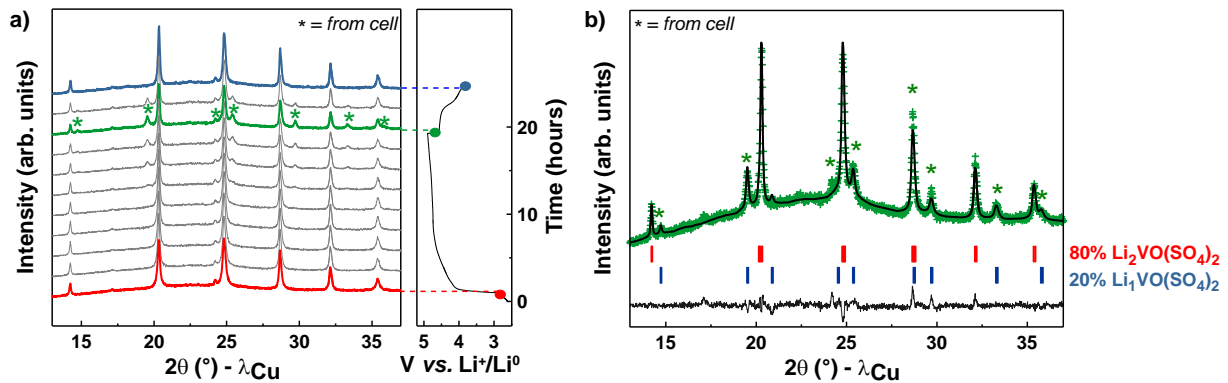


Figure IV.9: Behavior of a $Li_2VO(SO_4)_2||Li$ cell on charge. (a) *In situ* XRD patterns recorded while the cell is charged to 4.9 V, with the voltage-time curve on the right. The red, green, and blue patterns correspond to the pristine, fully oxidized, and the subsequent discharged phase, indicating the reversibility of this process. (b) Refinement of the XRD pattern of fully charged sample (4.9 V) with two phases: $Li_2VO(SO_4)_2$ (red vertical tick marks) and $Li_1VO(SO_4)_2$ (blue vertical tick marks) in a $\sim 80/20$ ratio.

To explore the possibility of multi electron transfer in $Li_2VO(SO_4)_2$, we assembled $Li_2VO(SO_4)_2/Li$ cells that were started upon reduction, as shown in **Figure IV.10 a**. Upon reduction, $Li_2VO(SO_4)_2$ can uptake 1 Li^+ at a potential of $\sim 2 \text{ V}$; upon the subsequent charge 1.85 Li^+ could be removed till 4.75 V with two pseudo plateaus located at $\sim 4.25 \text{ V}$ and $\sim 4.75 \text{ V}$ which correspond to the V^{4+}/V^{3+} and V^{5+}/V^{4+} redox couples, respectively. Pushing the charge cutoff potential to greater values (4.9 V) we could remove more Li^+ ($\sim 2 \text{ Li}^+$) (**Figure IV.10 b**). Through subsequent cycles, we note a charge capacity of $190 \text{ mA}\cdot\text{h/g}$ which is always exceeding the discharge one $140 \text{ mA}\cdot\text{h/g}$, hence leading to poor coulombic efficiency; the main reason being the copious decomposition of the electrolyte at such a high potential.

Moreover worth mentioning is the rapid capacity fading upon cycling so that the capacity has reached ~ 60 mA·h/g after 10 cycles.

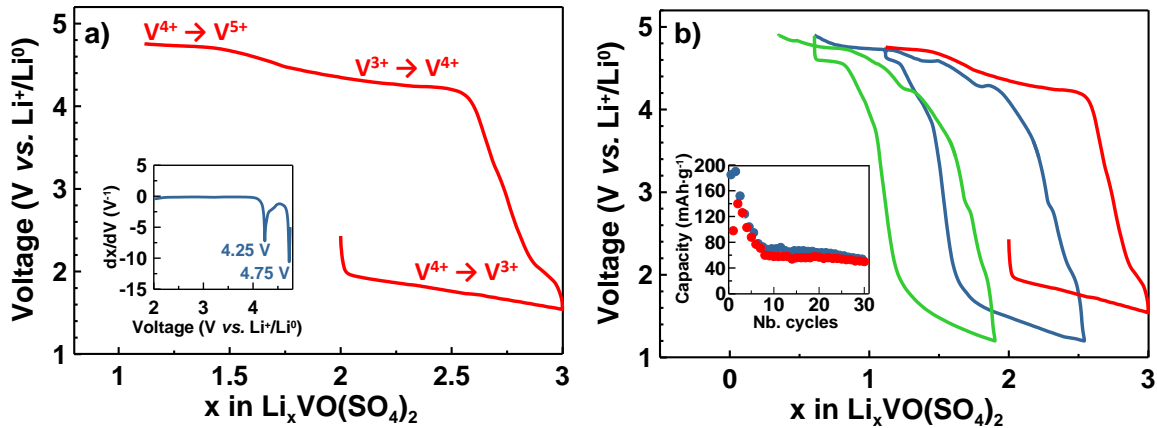


Figure IV.10: Typical voltage–composition curve for the $Li_2VO(SO_4)_2||Li$ cell starting on discharge process at C/20 rate, (a) First discharge and charge of the $Li_2VO(SO_4)_2/Li$ cell, upon discharge 1 Li^+ is fixed to be inserted, and the cutoff potential for charge is 4.75 V, with the derivative curve for discharge shown as inset. (b) The first three cycles are shown, and the capacity of 30 cycles is shown as inset.

To grasp further insights into the Li^+ insertion mechanism through the discharge process, *in situ* XRD measurement was operated by discharging a $Li_2VO(SO_4)_2/Li$ cell at the rate of C/30 with a fixed amount of 0.9 Li^+ (**Figure IV.11 a**). A set of new peaks gradually grow at the expense of the mother $Li_2VO(SO_4)_2$ phase, indicating the formation of $Li_3V^{3+}O(SO_4)_2$ phase as seen from the *ex situ* pattern (**Figure IV.12**).

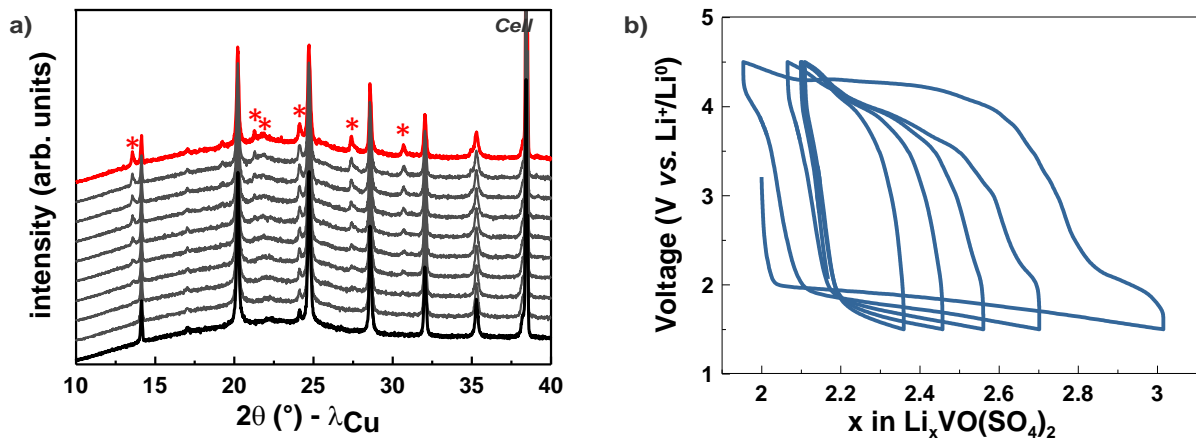


Figure IV.11: (a) *In situ* XRD patterns recorded during the first discharge to insert 1 Li^+ in $Li_2VO(SO_4)_2$. The black and red pattern refers pristine and ended discharged phase. The stars suggest new phase forming during this process. (b) Voltage – composition curve for a $Li_2VO(SO_4)_2||Li$ cell upon discharge with 1 Li^+ fixed to be inserted in the first cycle.

As one can notice on **Figure IV.10 b**, the plateau of the second discharge does not superimpose with the pristine one, suggesting that material is evolving through cycling with most likely the growth of a resistive phase which could explain the poor cycling performance of the cell. Whatever, the amphoteric nature of $Li_2V^{4+}O(SO_4)_2$ with $LiV^{5+}O(SO_4)_2 \rightarrow Li_2V^{4+}O(SO_4)_2 \rightarrow Li_3V^{3+}O(SO_4)_2$ is very similar to the one reported for $Li_5V^{3+}O(PO_4)_2 \rightarrow Li_4V^{4+}O(PO_4)_2 \rightarrow Li_3V^{5+}O(PO_4)_2$ [318]. A difference therefore resides in the redox potential values [4.75 V ($V^{4+} \rightarrow V^{5+}$) and 4.25 V ($V^{3+} \rightarrow V^{4+}$)] which are greater for the sulfates as compared to the corresponding phosphates due to the stronger inductive effect of $(SO_4)^{2-}$.

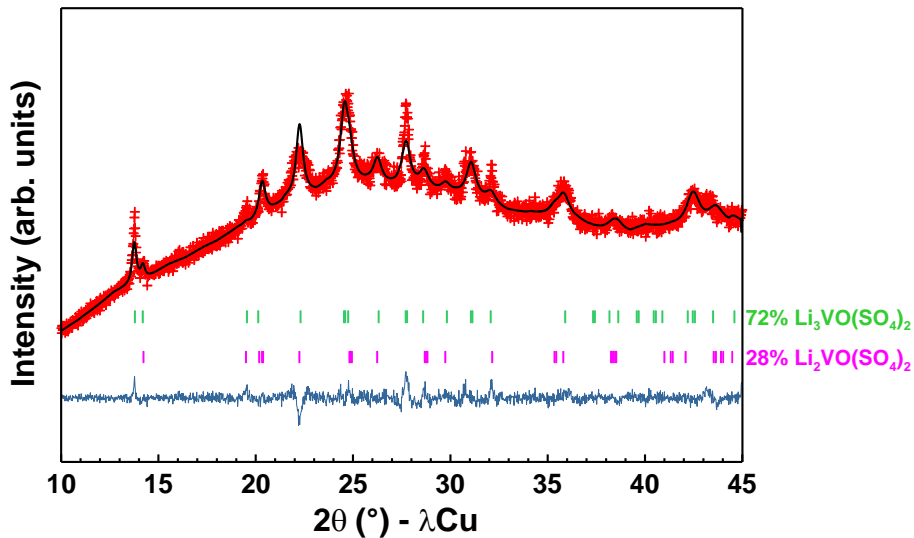


Figure IV.12: Refinement of the *ex situ* XRD pattern of a fully discharged sample (fixed to insert 1 Li^+ at the rate of C/25), suggesting the constitution of two phases: $Li_3VO(SO_4)_2$ (green vertical tick marks) and $Li_2VO(SO_4)_2$ (pink vertical tick marks) in a ~72/28 ratio.

IV.2.4. Magnetic Property

The temperature dependence of magnetization was measured using a SQUID (XL, Quantum Design), under both zero-field cooled (ZFC) and field cooled (FC) conditions under 1 kOe between 2 K and 400 K. The magnetic susceptibility curves $\chi(T)$ vs. temperature of $Li_2VO(SO_4)_2$ (**Figure IV. 13**) shows that above 10 K, it follows the Curie–Weiss law. This region was fitted to the Curie–Weiss equation $\chi_{cw} = C/(T - \theta) + \chi_0$. The effective magnetic moment of $\mu_{eff} = 1.70 \mu_B$ per V and $\theta = -3.7$ K are deduced, with the latter value in agreement with the calculated values for V^{4+} ($1.73 \mu_B$). The inset figure shows that the evolution of the magnetization of $Li_2VO(SO_4)_2$ with the applied field measured at 2 K which is nearly linear implying that the compound behaves as a classical paramagnet.

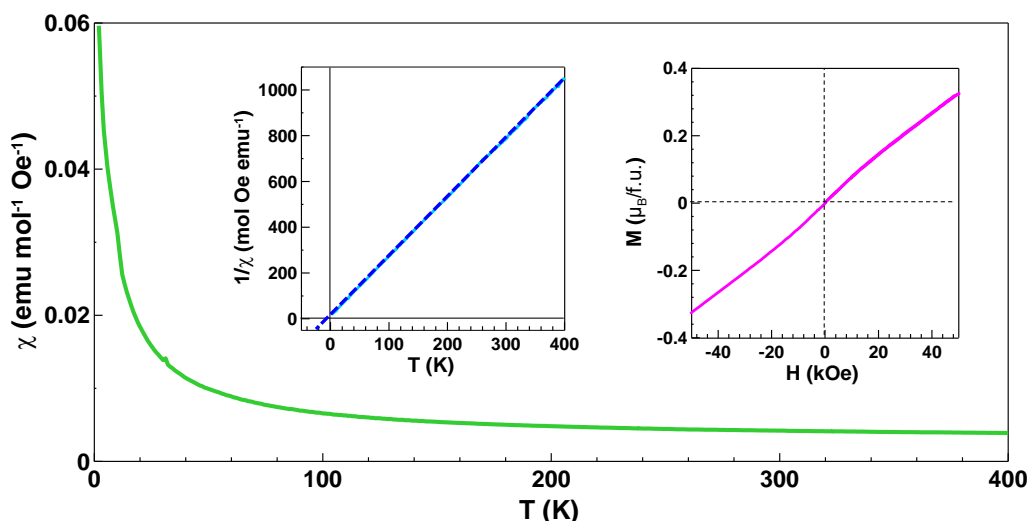


Figure IV.13: Temperature dependence of the magnetic susceptibility of $Li_2VO(SO_4)_2$, measured under field-cooling conditions with a field of 1 kOe between 400 K and 2 K (green line). The inverse magnetic susceptibility ($1/\chi$) as a function of temperature (light blue line) is shown as the left inset as well as the Curie–Weiss fit as indicated by the blue dotted line. The magnetization curve (pink) of $Li_2VO(SO_4)_2$ as a function of the applied field measured at 2 K is shown as the right inset.

IV.3. Exploration of Vanadium-Based Oxysulfate - $Na_2VO(SO_4)_2$ - as Electrode for Na-ion Batteries

IV.3.1. Synthesis

The synthesis of $Na_2VO(SO_4)_2$ was previously reported in the literature [319], which consists in the dissolution of V_2O_5 in molten $Na_2S_2O_7$ while bubbling a SO_2 - N_2 gas mixture through the solution. Here we used a rather simple solid state reaction route:



Na_2SO_4 (Alfa Aesar, 99%) and $VOSO_4$ (w:w = 1:1) were thoroughly ball milled, pressed into a pellet and annealed under argon for 10 hours at 415°C. The recovered powder displayed an XRD pattern identical to the reported pattern for $Na_2VO(SO_4)_2$ in reference [319].

IV.3.2. Structural Characterization

The structure of $Na_2VO(SO_4)_2$ was checked by Rietveld refinement (**Figure IV.14**) of the synchrotron X-ray diffraction based on the structure model previously published [319]. $Na_2VO(SO_4)_2$ synthesized as above crystallizes in an orthorhombic structure, with space group $P 2_1 2_1 2_1$ and lattice parameters $a = 6.310020(13) \text{ \AA}$, $b = 6.807419(13) \text{ \AA}$ and $c =$

16.69296(3) Å, all of which are similar to the literature. The other structural parameters including the atomic positions are listed in **Table IV.2**.

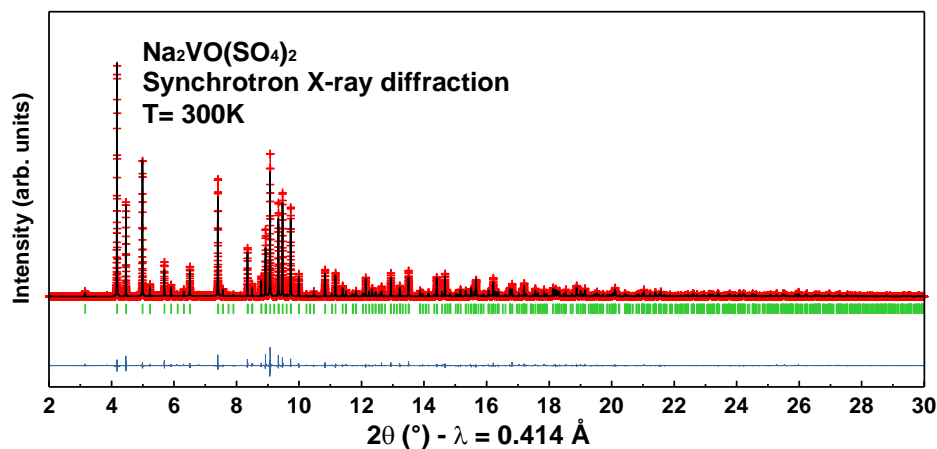


Figure IV.14: Rietveld refinement of the synchrotron powder diffraction pattern of $Na_2VO(SO_4)_2$.

Table IV.2 Structural parameters for $Na_2VO(SO_4)_2$ deduced from the Rietveld refinement of the synchrotron X-ray diffraction patterns at 300 K.

$Na_2VO(SO_4)_2$ Space Group: $P 2_1 2_1 2_1$						
$a = 6.310020(13)$ Å, $b = 6.807419(13)$ Å, $c = 16.69296(3)$ Å, $V = 717.045(3)$ Å ³ ,						
density = 2.826 g/cm ³ , $Z = 4$						
Atom	Wyckoff site	X	y	z	Occupancy	B(Å ²)
Na1	4a	0.6744(4)	0.1511(4)	0.59123(17)	1	3.12(6)
Na2	4a	0.3706(3)	0.1083(4)	0.23909(13)	1	1.54(5)
V	4a	0.53277(17)	0.14911(14)	0.91053(6)	1	0.71(2)
S1	4a	0.0340(2)	0.0853(2)	0.93224(9)	1	0.99(3)
S2	4a	0.8567(2)	0.1042(2)	0.25017(9)	1	0.88(3)
O1	4a	0.2166(5)	0.2001(4)	0.9056(2)	1	0.21(7)
O2	4a	0.5236(6)	0.4012(5)	0.97815(19)	1	1.01(7)
O3	4a	0.5104(6)	0.3592(5)	0.81536(20)	1	0.93(7)
O4	4a	0.8505(5)	0.1931(5)	0.8969(2)	1	0.92(7)
O5	4a	0.5157(5)	-0.0493(5)	0.8226(2)	1	0.94(7)
O6	4a	0.5374(5)	-0.0099(4)	0.9815(2)	1	1.19(8)
O7	4a	0.0478(5)	-0.1130(5)	0.9078(2)	1	1.46(8)
O8	4a	0.2722(6)	-0.2274(5)	0.2331(2)	1	0.84(8)
O9	4a	-0.2747(5)	-0.0647(5)	0.22501(19)	1	0.51(7)

Reliability parameters: $\chi^2 = 5.96$; Bragg R-factor = 5.64%

An overview of $Na_2VO(SO_4)_2$ structure is shown **Figure IV.15**. It presents a 3D interconnected framework built on corner-sharing VO_6 square-bipyramids and SO_4 tetrahedra. There is only one site for vanadium which nearly sits in the center of VO_6 square-bipyramids, which consists of O6 from $V=O$ and five oxygens from five different SO_4 tetrahedra. The $V=O_6$ bond is shorter (1.60 Å) while the trans $V-O_3$ bond is longer (2.14 Å). With a similar formulae but different structure, $3D Na_2VO(SO_4)_2$ shows two sites for Na instead of $Li_2VO(SO_4)_2$ presenting only one site for Li.

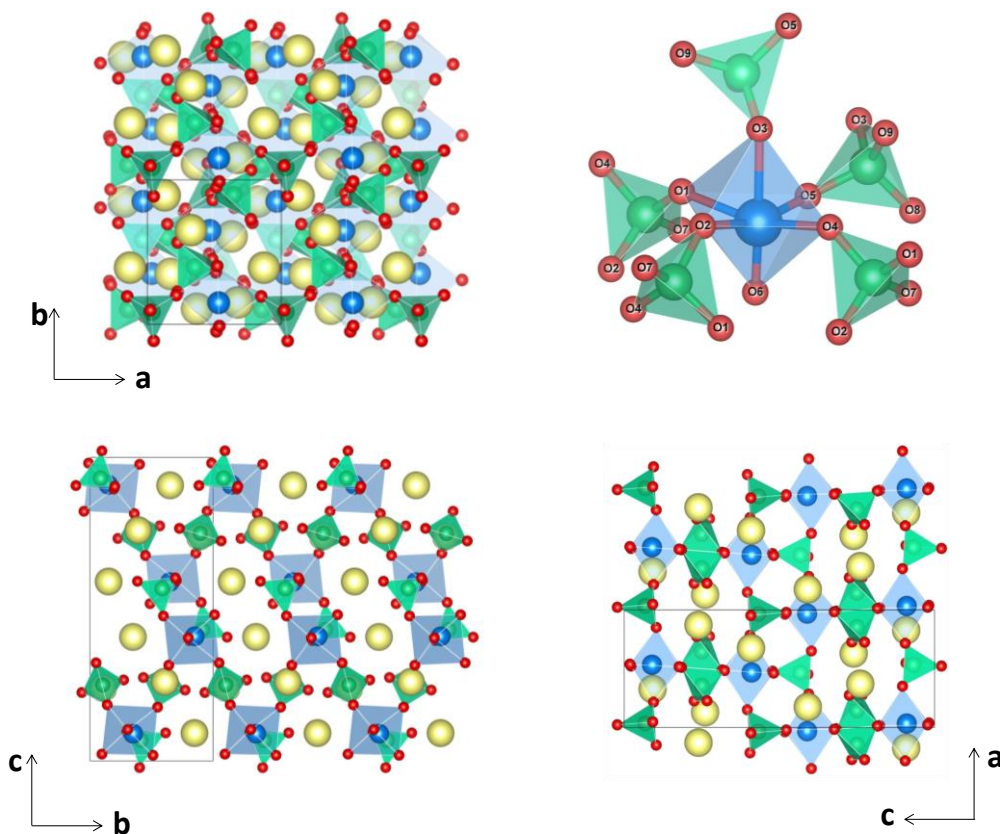


Figure IV.15: An overview of the structure of $Na_2VO(SO_4)_2$ along [100], [010], [001] direction. The VO_6 coordination is shown here. The square bipyramids are colored in blue, sulfate groups are green and Na atoms are yellow balls.

IV.3.3. Electrochemical Performance

The electrochemical activity of $Na_2VO(SO_4)_2$ electrodes vs. Na was tested in Swagelok cells using 1M $NaPF_6$ in EC-PC (3% FEC) as electrolyte. The positive electrode is prepared by ball milling $Na_2VO(SO_4)_2$ with 20% weight percentage of carbon. **Figure IV.16 a** shows the galvanostatic performance of $Na_2VO(SO_4)_2||Na$ cells cycled at a rate of C/30. Similar to $Li_2VO(SO_4)_2$, there is a large irreversibility capacity is observed between the first charge and

discharge due to electrolyte oxidation. However, from the second cycle and onwards the cell delivers a reversible capacity of 60 mA·h/g, which nearly corresponds to the delithiation and lithiation of 0.7 Na⁺. The derivative dx/dV curve for the 2nd cycle suggests two plateaus located at 4.5 V and 3.8 V (**Figure IV.16 a, bottom**). The presence of these 2 plateaus compared to a single one at 4.7 V as we observed for Li₂VO(SO₄)₂ could be due to the existence of two Na sites in Na₂VO(SO₄)₂. Note also that the profile of the charging curve through the second cycle and subsequent cycles differ from the first one with additionally the quasi disappearance of the irreversible capacity between charge and discharge at the opposite of what is observed during the first cycle.

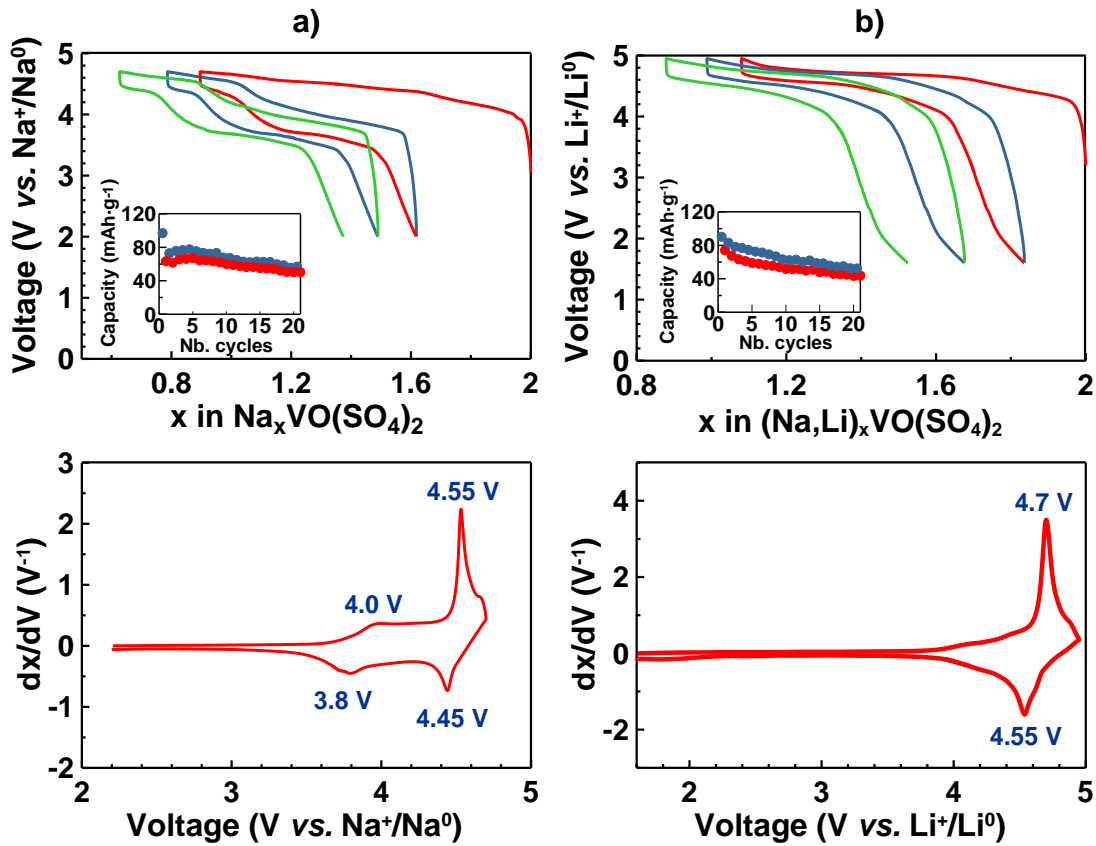


Figure IV.16: Typical voltage–composition curve for (a) the Na₂VO(SO₄)₂||Na cell and (b) the Na₂VO(SO₄)₂||Li cell. The capacity retention is shown as the inset and derivative curve of the second cycle is shown underneath for each cell respectively.

To gain further insights into this oxidation process, *in situ* X-ray diffraction measurement was performed for the first, second and the eleventh cycle (**Figure IV.17**). Upon the first charge, a set of new peaks appears with the most intense one being located at around 27° suggesting the growth of a new phase (noted as X phase). Upon the first discharge these peaks begin to change from the end of the first plateau with the huge peak at 27° diminishing, and result in another phase (noted as Y phase). Note that the XRD pattern of the Y phase does not

superimpose with the pristine one, suggesting an irreversible lithiation/delithiation process for the first cycle. From the second cycle, the X and Y phases undergo a reversible Li^+ extraction/insertion process, as indicated by their forming and disappearing till the 11th cycle recorded. However, neither of the X or Y phases could be analyzed further in terms of structure owing to the strong peak broadening of the collected XRD patterns.

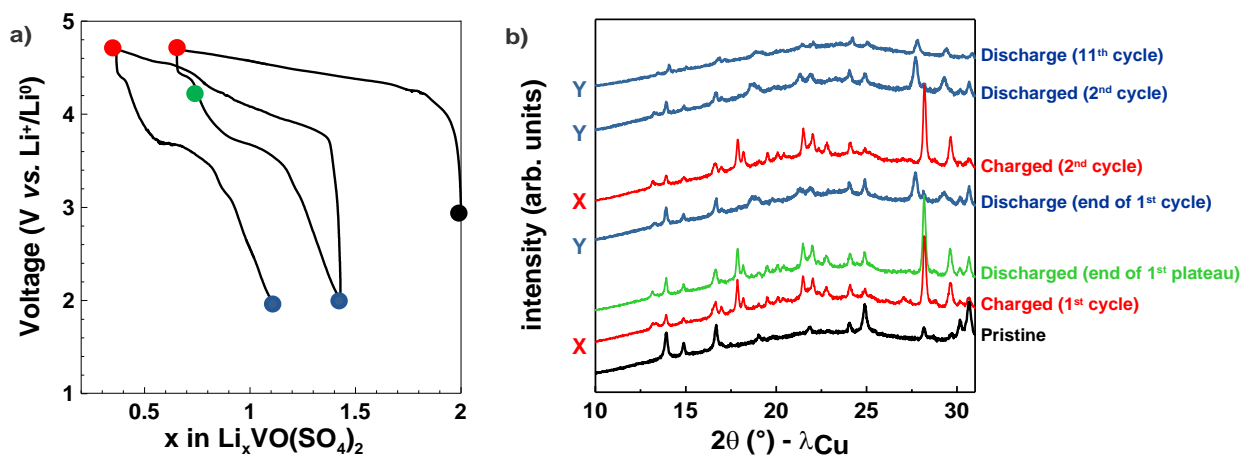


Figure IV.17: (a) Voltage–composition curve for the first two cycles of *in situ* $Na_2VO(SO_4)_2||Na$ cell. XRD were collected at the black, red, green and blue points. Which refers to the phases of pristine, fully charged, discharged ending at 1st plateau and fully discharged. (b) *In situ* XRD patterns while the cell charged to 4.7 V. The black pattern refers to the pristine phase, the red one refers to the fully oxidized sample (for both 1st and 2nd cycle), the green pattern refers to reduced sample at the end of 1st plateau, and the blue patterns were recorded at the subsequent discharge states (for all the 1st, 2nd, and 11th cycle). It indicates a reversible cycling of X and Y phase from the 2nd cycle of this process.

Lastly, although these two compounds are structurally different, it was tempting to check whether we could prepare $Li_2VO(SO_4)_2$ from $Na_2VO(SO_4)_2$ via ion exchange. All the attempts on the chemical ion exchange we have tried enlisting either solution ($LiCl$ in acetonitrile) or molten salt ($LiNO_3$) with temperatures ranging from 80°C to 250°C have failed, leading mainly to phase decomposition. To further pursue in this direction, we explored the possibility of electrochemical ion exchanging Na^+ for Li^+ . The electrochemical behavior of a $Na_2VO(SO_4)_2$ electrode vs. Li^+/Li^0 using *LP100* electrolyte is shown in **Figure IV.16 b**. Please note the feasibility to remove nearly 1 Na^+ during the first oxidation alike for $Na_2VO(SO_4)_2||Li$ cells. This removal occurs at a slightly lower potential (4.5 instead of 4.7 V) as expected due to the lower reducing potential (~300 mV) of Na compared to Li. The discharge curve is in contrast quite different between the two cells with a cascade voltage profile for $Na_2VO(SO_4)_2||Na$ cell as compared to a smooth voltage decrease for $Na_2VO(SO_4)_2||Li$ cell. Such a different profile is indicative of the reinsertion of Li^+ rather than Na^+ in the " $Na_{1.3}VO(SO_4)_2$ " phase. The Na content of ~1.3 was deduced by EDX analysis bearing in mind once again the difficulty to exploit coulometric titration. Upon subsequent

cycles, the cell can reversibly uptake ~ 0.7 (Li^+/Na^+) at an average voltage of 4.65 V leading to a reversible capacity of ~ 80 mA·h/g which progressively decays upon cycling. X-ray diffraction data of $Na_{1.3}Li_{0.5}VO(SO_4)_2$ nearly resembles that of the mother $Na_2VO(SO_4)_2$ phase with however contracted lattice parameters indicating that the $Na_2VO(SO_4)_2$ structural framework is preserved through the cycling process (**Figure IV.18**). Such a finding indicates the feasibility to partially substitute minute amounts of Na for Li in $Na_2VO(SO_4)_2$ while preserving the same structure.

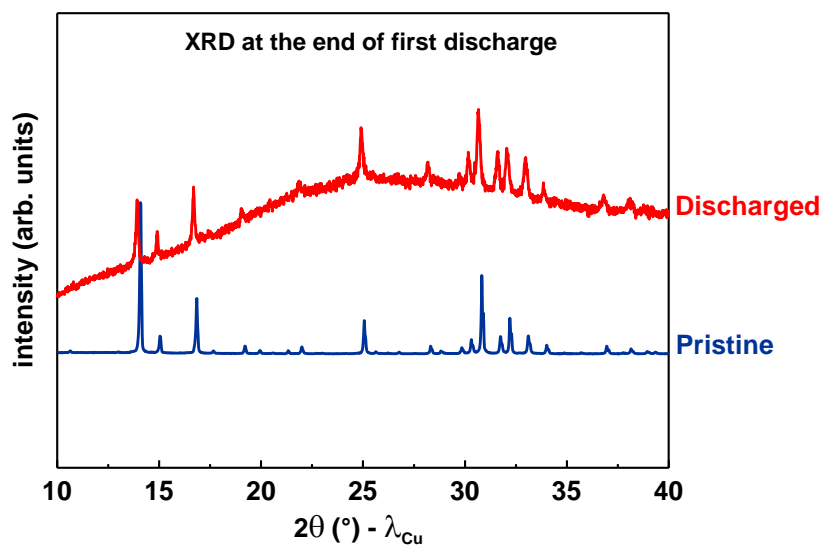


Figure IV.18: X-ray diffraction patterns collected at the end of first discharge of $Na_2VO(SO_4)_2||Li$ cell compared to the pristine phase of $Na_2VO(SO_4)_2$. Their similar profiles suggest that the $Na_2VO(SO_4)_2$ structural framework is preserved through the cycling process.

IV.4. DFT+U Calculations of $A_2VO(SO_4)_2$ ($V = Na, Li$)

Whatever the Li or Na phases explored herein, the study above reveals a redox activity at potentials greater than ~ 4.5 V that are particularly high for the V^{5+}/V^{4+} redox couple. To grasp some light on the origin of this the DFT calculations were undertaken. For both $Li_2VO(SO_4)_2$ and $Na_2VO(SO_4)_2$ the Density of States (DOS) combined with a Crystal Orbital Overlap Population (COOP) analysis show that the bonding electronic states of the vanadyl bond are far below the Fermi level and therefore are transparent to the oxidation process (**Figure IV.19**). In more details, the f^- Fukui functions (**Figures IV.19 d and e**) computed for $Li_2VO(SO_4)_2$ and $Na_2VO(SO_4)_2$ confirm that the electronic states involved in the oxidation process arise from a metallic orbital perpendicular to the V=O bond with mainly oxygen contributions from the SO_4 groups, hence stressing the efficacy of the inductive effect associated to the SO_4^{2-} polyanion. Moreover, the f^+ Fukui functions (**Figures IV.19 d**) show that the reduction process should now involve the V=O bonds as the main redox center, alike

the β - $VOSO_4$ phase [241] for which the strongly covalent V=O bond governs the V^{4+}/V^{3+} redox center (2.8 V). This Li^+ insertion occurs at a much lower reduction potential of ~ 2 V vs. Li^+/Li^0 for the V^{4+}/V^{3+} couple. At this stage, we should recall that the oxidation potential of $Li_2VO(SO_4)_2$ is about 0.6 V greater than for the $Li_4VO(PO_4)_2$ homologue. This voltage difference is due for a large part to the inductive effect associated to the replacement of PO_4^{3-} by SO_4^{2-} and to a lesser extent to the lower electrostatics of Li/Na cationic sites due to the higher Li/Na-stoichiometry in $(PO_4)^{3-}$ -based systems [247].

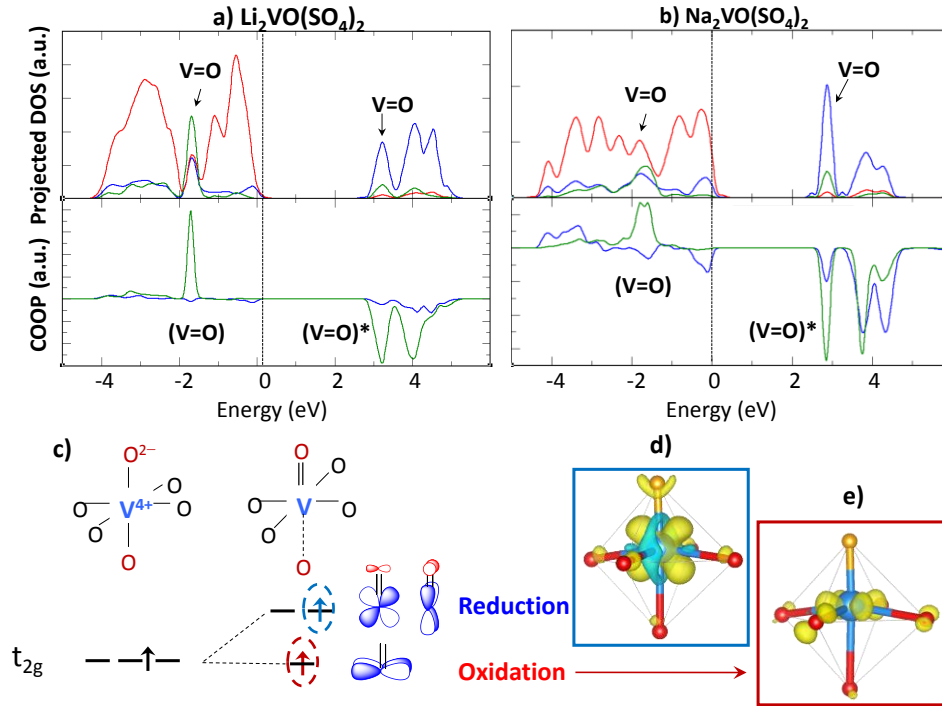


Figure IV.19: (top) Atom-projected density of states (DOS) and V=O and V-OSO₃ crystal orbital overlap population (COOP) computed for (a) $Li_2VO(SO_4)_2$ and (b) $Na_2VO(SO_4)_2$ with DFT+U ($U_{\text{eff}} = 4$ eV for V); (bottom) (c) T_{2g} -orbital splitting expected for the octahedral to pyramidal distortion showing the shape of the electronic levels involved in the oxidation and reduction processes of the $A_2VO(SO_4)_2$ phases ($A = Li, Na$). (d, e) The f^- and f^+ Fukui functions computed for these two processes confirm the expected orbital shape and indicate the redox centers in the two processes, *i.e.* the V-OSO₃ ionic bonds in oxidation and the V=O strongly covalent bond in reduction.

Regarding the possibility of partially exchanging Na^+ for Li^+ in the $Na_2VO(SO_4)_2$ polymorph, DFT calculations were also performed to investigate the stability of the $NaLiVO(SO_4)_2$ composition with respect to a proportional mixture of $Li_2VO(SO_4)_2$ (structure-type 1) and $Na_2VO(SO_4)_2$ (structure-type 2) (Figure IV.20). x in $Na_{2-x}Li_xVO(SO_4)_2$ refers to the hypothetical $Na_{2-x}Li_xVO(SO_4)_2$ phase that may adopt structure type 1 or 2, respectively. As expected, for $x = 0$ (*i.e.* $Na_2VO(SO_4)_2$), the polymorph of structural type 2 (Red) is found far more stable than the polymorph of structural type 1 (blue) where all Li were substituted by

Na. Vice versa, for $x = 2$ (*i.e.* $Li_2VO(SO_4)_2$) the polymorph of structural type 1 is found far more stable than the one of structural type 2 where all Na were substituted by Li. Then regarding the intermediate stoichiometry ($x = 1$) (*i.e.* $NaLiVO(SO_4)_2$), the 4 different configurations inequivalent by symmetry obtained by exchanging Na^+ for Li^+ in the structure type 2 were tested (since this was proved to be experimentally feasible). In all cases we obtain polymorphs with formation energy above the energy of the "phase segregation". Among the 4 polymorphs tested the one closes to stabilization are shown in **Figure IV.20** (the lowest one at $x = 1$). Overall this suggests that no solid solution is expected thermodynamically for this stoichiometry $NaLiVO(SO_4)_2$. The energy of zero reference being defined here in as $E = x/2$ (E_f of $Li_2VO(SO_4)_2$) + $(2-x)/2$ (E_f of $Na_2VO(SO_4)_2$). It reveals that this "mixed phase" in Li/Na is thermodynamically less stable than the end members, hence leading to phase segregation into $\frac{1}{2} Li_2VO(SO_4)_2 + \frac{1}{2} Na_2VO(SO_4)_2$ and explaining why this phase could not be observed experimentally. Electrochemically-driven insertion reactions, relying on topotactic mechanisms, are a nice way to overcome such limitations and to stabilize metastable phases as clearly indicated herein by our feasibility to prepare the $Na_{1.3}Li_{0.7}VO(SO_4)_2$ phase.

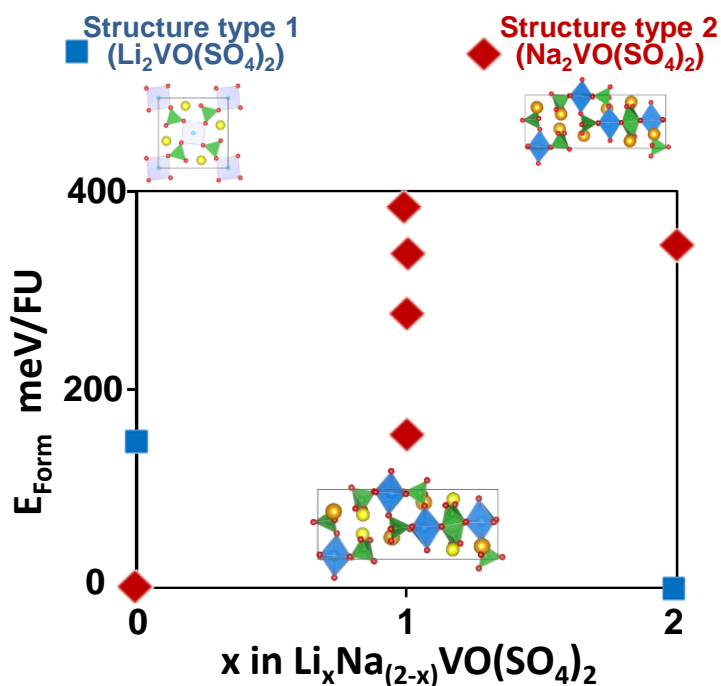


Figure IV.20: The thermodynamic stability of the Li/Na substitution in the two $A_2VO(SO_4)_2$ ($A = Li, Na$) structural type.

IV.5. Conductivity of $Na_2VO(SO_4)_2$ vs. $Li_2VO(SO_4)_2$

IV.5.1. Conductivity Measurement

Owing to the different crystal structures and electrochemical activities, we decided to measure the transport properties for $Li_2VO(SO_4)_2$ and $Na_2VO(SO_4)_2$. A.c. and d.c. impedance spectroscopies were performed to measure their conductivities. The a.c. conductivity was measured for temperatures ranging from 75 to 300°C, using a Bio-Logic MTZ-35 Impedance Analyzer in a frequency range of 35 MHz-0.01 Hz and an excitation voltage of 100 mV. The d.c. conductivity values were determined at the same temperatures by applying polarization voltages of 100 mV – 500 mV. The pellets were sintered at 400°C (\varnothing 10 mm, compactness 77% for both) were sputtered with gold and measured between platinum blocking electrodes under argon flow.

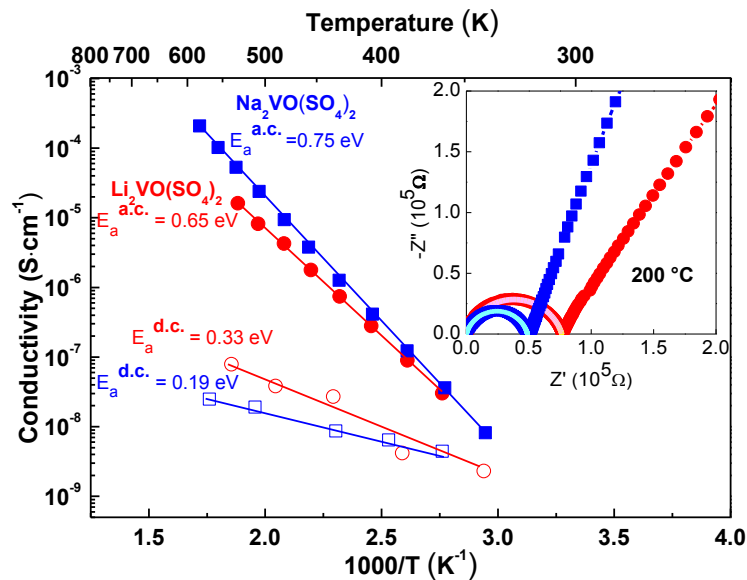


Figure IV.21: Transport properties of $Li_2VO(SO_4)_2$ (red circles) and $Na_2VO(SO_4)_2$ (blue squares), the filled and open circles/squares refer to a.c. and d.c. measurements, respectively; the inset shows impedance spectra (filled squares and circles) and the fit of each spectra (continuous line) of $Li_2VO(SO_4)_2$ (red) and $Na_2VO(SO_4)_2$ (blue) in argon at 200°C.

Values of activation energy E_a for cation migration were obtained by fitting the a.c. and d.c. data measured according to the Arrhenius equation $\sigma(T) = \sigma_0 \cdot \exp(-E_a/k_B T)$, in which σ is the conductivity at the temperature T , σ_0 is a pre-exponential factor, and k_B the Boltzmann constant. Activation energies of 0.75 and 0.65 eV were obtained for the $Na_2VO(SO_4)_2$ and $Li_2VO(SO_4)_2$ phases (**Figure IV.21**), and extrapolated ac conductivities at room temperature

are $2.6 \times 10^{-10} \text{ S}\cdot\text{cm}^{-1}$ and $4.2 \times 10^{-10} \text{ S}\cdot\text{cm}^{-1}$ for the Na and Li counterparts, respectively. For both samples, the low frequency tail of the impedance spectra suggests an ionic component to the overall conductivity. Dc activation energies of 0.33 and 0.19 eV were found for the Li and Na-based oxysulfates, respectively, with room temperature dc values nearly equal to or slightly greater than the ac ones. This indicates a predominant contribution of the electronic conductivity to the transport properties of these phases at room temperature as previously observed for other polyanionic compounds.

IV.5.2. Bond Valence Energy Landscape

To evaluate how A^+ ($A = Na, Li$) would diffuse in the two different structures of $Na_2VO(SO_4)_2$ and $Li_2VO(SO_4)_2$, we calculate Bond Valence Energy Landscapes (BVEL) [265] on these phases (**Figure IV.23**). Nearly equal “activation energy values” (defined as the minimum energy to obtain at least one infinitely connected path in a crystallographic direction) for Li^+ in $Li_2VO(SO_4)_2$ ($E_a = 1.28 \text{ eV}$) and Na^+ in $Na_2VO(SO_4)_2$ ($E_a = 1.00 \text{ eV}$) are obtained. Overall, although quite different from a structural point of view, these two compounds show transport properties quite similar to each other, which is consistent with the obtained electrochemical data.

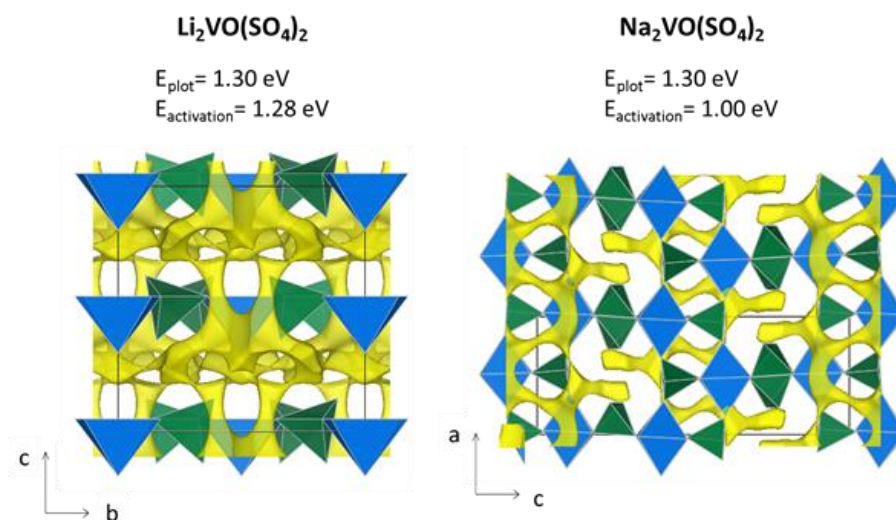


Figure IV.23: Bond Valence Energy Landscapes calculated for $A_2VO(SO_4)_2$ ($V = Na, Li$). SO_4 are coloured in green, VO_n polyhedra in blue, and the yellow domains correspond to the migration paths for Li/Na in the structures, both plotted using an iso-surface value of 1.30 eV over the minimum energy.

IV.6. Conclusion

Through this chapter, we reported the synthesis, structure and electrochemical activity of the novel $Li_2VO(SO_4)_2$ phase. We show that upon oxidation this compound displays a capacity of 50 mA·h/g at 4.7 V that is associated to the V^{4+}/V^{5+} redox couple. This leads to an energy density of 235 W·h/kg which is slightly lower than that previously obtained (280 W·h/kg) for $Li_4VO(PO_4)_2$ which has a lower voltage (~4 V) but larger capacity (70 mA·h/g).

Interestingly, while $Li_2VO(SO_4)_2$ is structurally related to $Li_4VO(PO_4)_2$, DFT calculations suggest that the electronic states involved in the oxidation process are mainly due to a metallic orbital with oxygen contributions of the SO_4 groups. This differs from our recently reported Cu-based oxysulfate, $Li_2Cu_2O(SO_4)_2$, which also displays a plateau at 4.7 V vs. Li^+/Li^0 ³¹. In that case we demonstrated that the band involved in the oxidation process is mainly attributed to O(2p) orbitals of the oxygen atoms bridging the CuO_4 square-planes.

Upon discharge, one Li^+ can be inserted at voltage lower than 2 V to form the $Li_3VO(SO_4)_2$ phase, which shows high charge and discharge capacity of 190 mA·h/g and 140 mA·h/g due to two redox couples ($V^{5+} \leftrightarrow V^{4+} \leftrightarrow V^{3+}$). The low potential to insert Li^+ enlists the V=O bonds as the main redox center suggested by DFT calculations.

Obvious direct extensions of this work range from finding ways to optimize and extract greater amounts of Li^+ or Na^+ at high voltage for enhancing their practical energy densities. This calls for innovative electrode wiring together with the development of electrolytes highly stable against oxidation. Efforts should also be paid to explore the possibility to stabilize and master the high capacity provided by making use to two electron transfer during the V^{5+}/V^{3+} process for $Li_2VO(SO_4)_2$, which is not studied deeply here due to time limitation. This could be the purpose of another PhD.

Conclusions and Perspectives

This thesis aimed towards the exploration of novel fluorine-free sulfate based polyanionic compounds for Li-ion batteries through environmental low cost and eco-friendly approaches. More specifically, the ultimate goal was to design compounds capable of competing with LiFePO_4 and LiFeSO_4F as electrode, in terms of energy density, cost, and sustainability. Bearing this in mind, oxysulfates offer a vast land of battery materials that were scarcely studied previously, hence our decision to explore them.

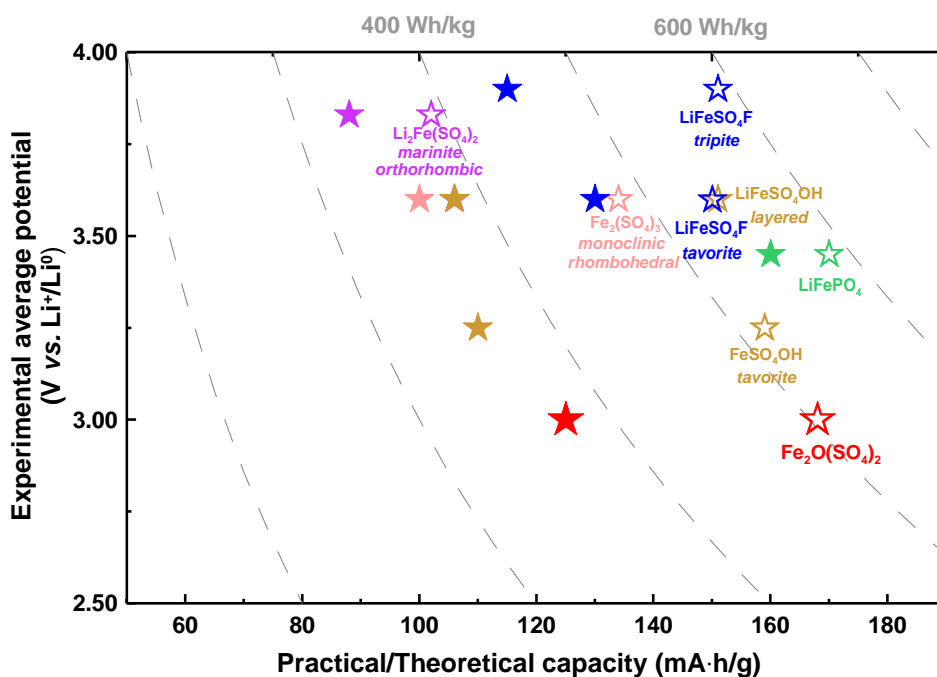
During this PhD, a new class of oxysulfate compounds, with formulae $\text{Fe}_2\text{O}(\text{SO}_4)_2$, $\text{Li}_2\text{Cu}_2\text{O}(\text{SO}_4)_2$, and $\text{Li}_2\text{VO}(\text{SO}_4)_2$, together with a new fluorosulfate LiCuSO_4F , were synthesized, their structures solved, and their electrochemical and some physical properties characterized for the first time.

These novel phases ($\text{Li}_2\text{Cu}_2\text{O}(\text{SO}_4)_2$, $\text{Li}_2\text{VO}(\text{SO}_4)_2$, and LiCuSO_4F) were mainly synthesized through classical solid state synthesis at low temperatures (≤ 400 °C) using a variety of well selected precursors taken in stoichiometric amounts. It is worth mentioning that we could succeed in preparing nearly pure $\text{Li}_2\text{Cu}_2\text{O}(\text{SO}_4)_2$ by thermal decomposition of LiCuSO_4F . However, neither of the above methods were successful in preparing the $\text{Li}_2M_2\text{O}(\text{SO}_4)_2$ with other 3d metals ($M = \text{Fe}, \text{Co}, \text{Mn}$) besides Cu. To alleviate this difficulty we took advantage of the Fe-based hydroxysulfate to prepare the Li-free iron oxysulfate, $\text{Fe}_2\text{O}(\text{SO}_4)_2$, which we electrochemically lithiate afterwards.

Electrochemically-wise, $\text{Fe}_2\text{O}(\text{SO}_4)_2$ can deliver a decent capacity of 125 mA·h/g at a voltage of 3.0 V vs. Li^+/Li^0 , offering an energy density of 375 W·h/kg which is lower than LiFeSO_4F (430 W·h/kg) and LiFePO_4 (550 W·h/kg), but higher than other sulfates, as shown in **Figure 1 a**. Due to the low cost and moisture non-sensitivity, this compound present attractive features that enable the compound to be used as electrode for Li-polymer batteries and not Li-ion because this positive electrode is Li-free.

Turning to $\text{Li}_2\text{VO}(\text{SO}_4)_2$, it shows an outstanding voltage of 4.7 V vs. Li^+/Li^0 upon oxidation, which is much higher than other V-based compounds (**Figure 1 b**), corresponding to $\text{V}^{5+}/\text{V}^{4+}$ redox activity. The increasing voltages observed in going from $\text{Li}_2\text{VOSiO}_4$ (3.65 V) to $\text{Li}_4\text{VO}(\text{PO}_4)_2/\text{LiVOAsO}_4$ (4.0 V), and further to $\text{Li}_2\text{VO}(\text{SO}_4)_2$ (4.7 V) phases (shown in gold, blue, green, and red stars, respectively in **Figure 1 b**) do not come as a surprise and can simply be rationalized by the inductive effect, bearing in mind that S is more electronegative than P

a) Iron base sulfate polyanionic electrode for Li-ion batteries



b) High voltage V-based polyanionic electrode for Li-ion batteries

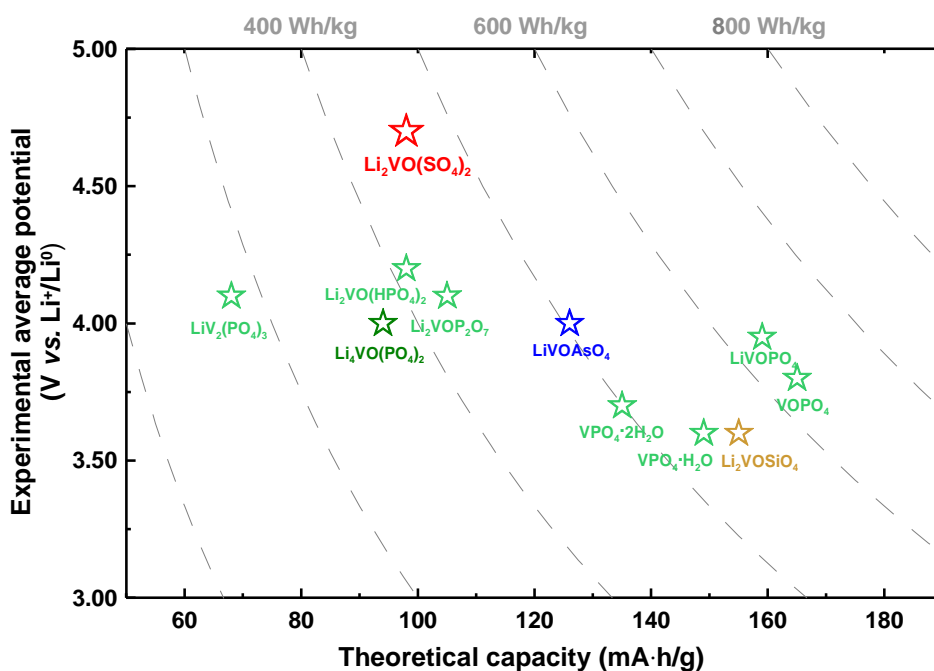


Figure 1: Electrochemical performances summarized for (a) Fe-based sulfates, **hollow** and **solid** stars refer to the **theoretical** and **experimental** specific capacity, respectively. The different sulfates are gathered in different red colours, while polymorphs are shown in the same colours, and marked in *italic*; for (b) V-based polyanionic compound with $\text{V}^{5+}/\text{V}^{4+}$ redox activity, in terms of the experimental potential and **theoretical** specific capacity. The different polyanionic families are gathered in different colours: red for sulfates, green for phosphates, blue for arsenates, gold for silicate.

and Si. However $\text{Li}_2\text{VO}(\text{SO}_4)_2$, as compared to the other V-based oxysulfates, shows a limited capacity (*i.e.* 50 mA·h/g) on its high voltage plateau due to Li-driven structural instabilities upon Li removal. Moreover, we show that upon reduction, $\text{Li}_2\text{VO}(\text{SO}_4)_2$ can uptake an extra Li^+ to form “ $\text{Li}_3\text{VO}(\text{SO}_4)_2$ ”, hence showing a high charge and discharge capacities of 190 mA·h/g and 140 mA·h/g, respectively, due to two electron transfer ($\text{V}^{5+} \leftrightarrow \text{V}^{4+} \leftrightarrow \text{V}^{3+}$). Unfortunately, such capacities rapidly decay upon cycling.

Regarding $\text{Li}_2\text{Cu}_2\text{O}(\text{SO}_4)_2$, it displays an amphoteric electrochemical behavior since it is electrochemically active upon oxidation as well as upon reduction. First, partial amount of Cu^{2+} (*i.e.* 0.3 per formula unit) can be oxidized to Cu^{3+} at a voltage of 4.7 V vs. Li^+/Li^0 , which is the highest voltage ever reported for any Cu-based inorganic compounds. DFT+U calculations have further shown that more capacity might be extracted for $\text{Li}_2\text{Cu}_2\text{O}(\text{SO}_4)_2$ at higher voltages (*i.e.* ≥ 4.9 V), but we have not succeeded so far. Conversely, we show that Cu^{2+} can be reduced to Cu^+ at 2.3 V with the triggering of a conversion reaction ($\text{Cu}^+ \rightarrow \text{Cu}^0$) for lower reducing potentials. Capacities of 200 mA·h/g can be achieved on reduction with however a large polarization and an increased capacity fade upon cycling.

Lastly, no electrochemical activity was observed for LiCuSO_4F up to the voltage of 5 V. Based on DFT calculations, we could deduce that this phase won't be electrochemically active till ~ 5.1 V, a voltage range over which most of the presently used electrolytes are copiously decomposing. If such an inactive electrochemical activity is an intrinsic property of LiCuSO_4F remains an open question. A possible answer lies in the use of solid state electrolytes which can sustain high potentials. Such type of experiments is being presently planned.

Overall, through our exploration we could not isolate new materials that show electrochemical performances competing with LiFePO_4 . Once again, this reminds us that searching for new electrode materials with excellent performances in terms of both operating voltage and capacities is not easy. Nevertheless, we believe that these four new sulfate compounds have enlarged our knowledge of the sulfate chemistry via their great diversity. Overall what we have learned or further confirmed are:

- i)* The presence of fluorine is not mandatory for designing high voltage positive electrode materials. Indeed, the oxysulfates, $\text{Li}_2\text{Cu}_2\text{O}(\text{SO}_4)_2$ and $\text{Li}_2\text{VO}(\text{SO}_4)_2$ exhibit redox centers locating at 4.7 V vs. Li^+/Li^0 , the highest voltages ever reported for Cu- and V- based positive electrode.
- ii)* The richness of the sulfate crystal-chemistry (**Figure 2**), as illustrated by the finding of the first the fully ordered *triplite* structure for LiCuSO_4F . Such a finding contributes

further in the understanding of technically important polyanionic electrodes, namely phosphates which also prone to crystalize in *triplite* structures.

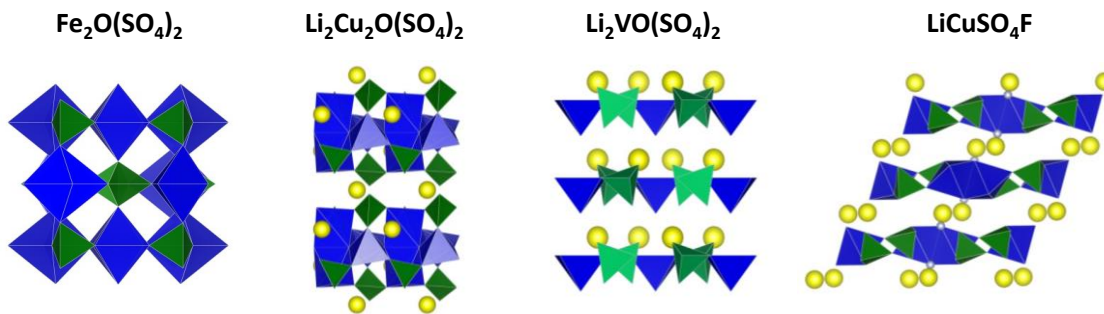


Figure 2: structures of the title compounds presented in this thesis: $\text{Fe}_2\text{O}(\text{SO}_4)_2$, $\text{Li}_2\text{Cu}_2\text{O}(\text{SO}_4)_2$, $\text{Li}_2\text{VO}(\text{SO}_4)_2$, and LiCuSO_4F .

- iii)* The feasibility to involve an oxygen anionic redox activity dominating in the $\text{Cu}^{2+} \rightarrow \text{Cu}^{3+}$ oxidation process in polyanionic compounds as determined by DFT calculations for $\text{Li}_2\text{Cu}_2\text{O}(\text{SO}_4)_2$, which have shown a strong hybridization of the metallic 3d-orbitals with the oxo-ligand's 2p-orbitals responsible for (Cu)(3d)/O(2p) overlap. This suggests that polyanionic type electrodes may also deliver anionic capacity, which broadens our scope in polyanionic materials design, a subject researchers neglected for long time that could bring access to achieve high energy density [110].
- iv)* Different chemical/physical properties were brought by oxysulfates, such as $\text{Fe}_2\text{O}(\text{SO}_4)_2$, which is the only sulfate based electrode that is not moisture sensitive. We believe the extra oxygen injected, not being part of a SO_4 group, can offer oxysulfates different physicochemical characteristics. $\text{Li}_2\text{Cu}_2\text{O}(\text{SO}_4)_2$ could be interesting in terms of the magnetic properties (which are under studied and will be reported later).

As most polyanionic compounds, the intrinsic electronic/ionic conductivities of oxysulfates are poor. Obvious optimization of these oxysulfates electrochemically-wise will call for innovative synthesis aiming to play with their morphology, a direction that we could not exploit because of lack of time. Whatever, we hope that this study will help for wiser design of polyanionic compounds which are essential for sustainability reasons.

Annexes

A.1. Samples Preparation

A Solid state synthesis process combining mechanical-milling (see § A.1.1), pelleting, and annealing in inert gases (see § A.1.2) was used for the title compounds named LiCuSO_4F , $\text{Li}_2\text{Cu}_2\text{O}(\text{SO}_4)_2$, $\text{Li}_2\text{VO}(\text{SO}_4)_2$ and $\text{Na}_2\text{VO}(\text{SO}_4)_2$ (Figure A.1).



Figure A.1: A solid state synthesis process in which precursors are thoroughly ball-milling, followed by being pressed into pellets and successive annealing in inert gases.

A.1.1 Mechanical-Milling

Mechanical-milling (or ball-milling) is highly energetic milling, which is used to thoroughly mix powder reactants for a synthesis, or a pristine material with carbon for electrode preparation. Note that ball-milling induces a reduction of the particle size as well.

Firstly, the powders to be mixed were filled into a stainless steel ball-mill cylindrical cell (inner volume of 40 cm^3 for reactant mixing or 10 cm^3 for electrode preparation) with stainless-steel balls (7 g/ball for synthesis, or 4 g/ball for electrode preparation) (Figure A.1 b). The mechanical-milling was carried out using a *SPEX 8000M miller*® (Figure A.1 a), which accommodates sample sizes ranging from 0.2 - 10 grams, for 15 to 60 minutes. During this process, the cell was moved with a complex movement in the three directions with a clamp speed of 1060 rpm. For samples which are prone to be oxidized, special care was taken in closing the ball-milling cell under argon, and separate the milling time into 30-min steps followed with 10-min pauses to prevent overheating generated locally in the cell.



Figure A.2: (a) *SPEX 8000 Mixer/Mill®* (b) stainless steel ball-mill cylindrical cell with stainless-steel balls to be launched on the mixer.

A.1.2 Heating Treatment

During the synthesis process of this thesis the heating treatments of samples were either done in the *CFW* laboratory chamber furnaces (Carbolite Gero, UK) or horizontal/vertical tube furnaces (Carbolite Gero, UK) (**Figure A.3**). The maximum heating limits of the furnaces are 1100 °C (chamber furnace) and 1200 °C (tube furnace). Tube furnaces were set up with protecting gases, such as Ar or Ar/H₂ flow for synthesis of air-sensitive compounds. Heating rates of 2-5 °C/min and intermediate gas flow were generally used in the synthesis.



Figure A.3: (a) *CFW* laboratory chamber furnace (b) *EHC* compact horizontal tube furnace (c) *VST / TVS* Vertical Split Tube Furnace

A.2. Structural Characterizations

A.2.1 Laboratory XRD Measurements

Laboratory X-ray diffraction (XRD) was used for this thesis work as a routine characterization method for exploring new phases and verifying the purity of the samples.

High-quality laboratory X-ray patterns of the best samples were required and chosen to perform Rietveld refinement of the structural models proposed in the literature.

A.2.1.1. Facilities

Laboratory XRD patterns presented in this thesis were recorded in Bragg-Brentano geometry with a Bruker D8 Advance diffractometer equipped with a copper source ($\lambda_{\text{Cu-K}\alpha 1} = 1.54056 \text{ \AA}$, $\lambda_{\text{Cu-K}\alpha 2} = 1.54439 \text{ \AA}$) and a LynxEye detector, operating at 40 kV and 40 mA, in reflection mode with a θ/θ Bragg-Brentano geometry.

A.2.1.2. Air Sensitive Samples

For air sensitive samples, XRD patterns of them were recorded using a special sample “dome” holder or below the X-ray transparent beryllium window of the electrochemical cell originally designed for *in operando* experiments and described below (see § A.3.2.2), which were prepared in the argon dry box.

A.2.1.3. In Situ XRD Experiments

For in operando XRD experiments, a special cell was designed (**Figure A.4**) in house by Jean-Bernard Leriche (Laboratoire de Réactivité et de Chimie des Solides – LRCS, UMR CNRS 6007, UPJV, France).

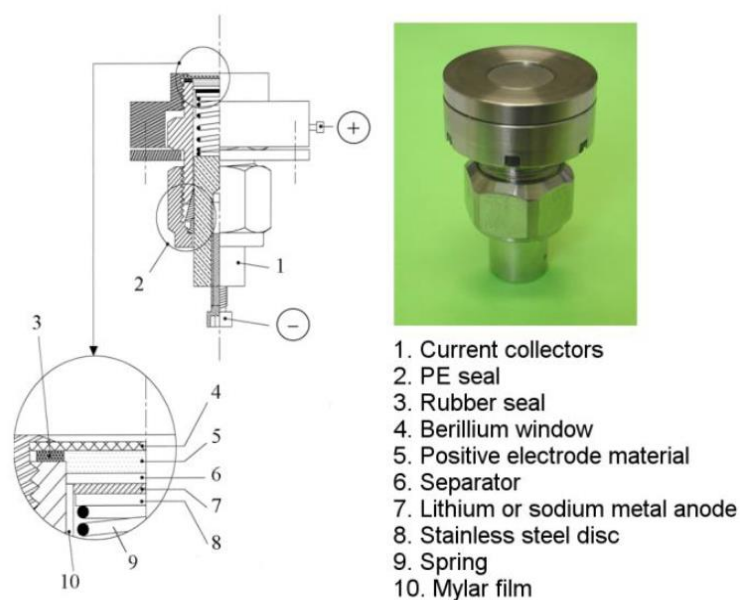


Figure A.4: Technical drawing and picture of the special cell designed at the LRCS for *in operando* XRD experiments.

The shape of cell adapts to the sample holder of the Bruker D8 diffractometers. The beryllium window equipped in the cell is almost transparent to X-ray beside acting as a current collector, on which the electrode material is deposited to be studied [322]. To prevent the oxidation of the beryllium at high cutoff voltage of cells, a thin sheet of aluminum foil (thickness: 3 μm , *Goodfellow*) was placed between the beryllium window and the positive electrode material. The rest of the cell was assembled as usual (cathode material // separator + electrolyte // anode material) in an argon-filled glove-box.

The cell was placed in the diffractometer (λ_{Cu}) in place of the standard sample holder, and connected to a portable VMP unit (Biologic S.A., Claix, France) to control the electrochemical experiment. XRD patterns were continuously recorded in the range $8 \leq 2\theta \leq 50^\circ$ (approximately two-hour scans) while performing a classical galvanostatic cycling of the cell at C/40-C/30 rates.

A.2.1.4. In Situ High Temperature XRD Measurement

Temperature-controlled XRD experiments were carried out on the *Bruker D8* diffractometer with the Cu source (see § A.2.1.1), which was equipped with an *Anton Paar HTK1200* furnace chamber (Figure A.5). For these experiments, the powder samples were placed on an alumina sample holder, and heated under air or under nitrogen flow, from room temperature to the target temperature with a ramp of $12^\circ\text{C}/\text{min}$. A delay of five minutes was observed before recording each pattern in the range $10 \leq 2\theta \leq 50^\circ$ for approximately one hour at constant temperature.

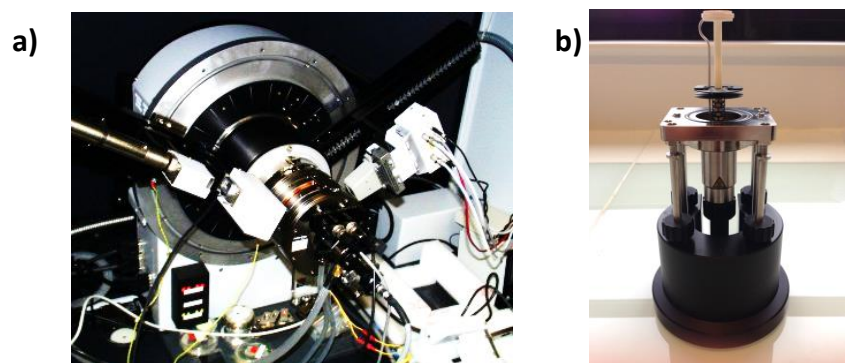


Figure A.5: (a) *Anton Paar HTK1200* furnace chamber mounted on the *Bruker D8* diffractometer. (b) Alumina sample holder for high-temperature XRD experiments.

A.2.2 Synchrotron XRD Measurements

High-resolution Synchrotron X-ray powder diffraction data were recorded for the purest samples in order to determine or confirm their structural models.

Samples were measured with Synchrotron X-ray radiation (wavelengths of $\lambda = 0.41374 \text{ \AA}$ or $\lambda = 0.41417 \text{ \AA}$) through the mail-in service of the 11-BM beamline of the Advanced Photon Source (APS) at Argonne National Laboratory (ANL, Argonne, USA). For these measurements, the samples were sealed under argon in 0.5/0.7-mm diameter quartz capillaries before being embedded in the kapton tubes of the sample bases (**Figure A.6**).

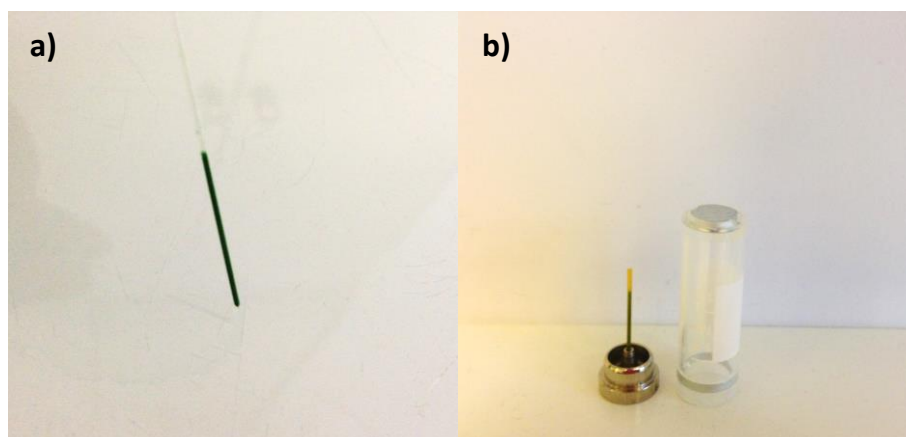


Figure A.6: An example of sample preparation for 11-BM mail-in service. (a) $\text{Li}_2\text{Cu}_2\text{O}(\text{SO}_4)_2$ being filled in a 0.7-mm diameter quartz capillary. (b) Sample ready for the 11-BM mail-in service.

A.2.3 Neutron Powder Diffraction (NPD)

Neutron diffraction is a complementary technique to X-ray diffraction, since the former enables to localize light elements (in our case the lithium atoms) which are barely visible with the latter. This is due to the fact that X-rays interfere with electrons, and are thus more scattered by heavier atoms. Conversely, neutrons interfere with nuclei.

Moreover when a compound presents antiferromagnetic interactions, neutron powder diffraction enables to determine the long range ordering of the magnetic moments. The spatial orientation and the magnitude of the magnetic moments carried by the transition metals can indeed be unambiguously determined.

In both cases, a large quantity of powder sample is necessary for NPD experiments as compared to XRD experiments (*i.e.* about one gram for the former *vs.* few milligrams for the latter).

For this thesis work, Neutron Powder Diffraction (NPD) has been performed on the two diffractometers the Paul Scherrer Institute (PSI, Switzerland) in with a wavelength of $\lambda = 1.493 \text{ \AA}$ and at the Institut Laue Langevin (ILL, Grenoble, France) with a wavelength of $\lambda = 1.495 \text{ \AA}$. Both diffractometers are in Debye-Scherrer geometry. Powder samples were filled into vanadium cylindrical sample holders (vanadium is transparent to neutrons).

A.2.4 TEM Investigation and EDX Analysis

High angle annular dark field (HAADF) imaging using scanning transmission electron microscopy (STEM) is a robust technique for identifying the position of atoms and atomic columns. The contrast in a HAADF image is approximately proportional to the square of the atomic number Z , which is an approximate method for identifying atomic species.

For the samples presented in this thesis, HAADF-STEM images, Selected Area Electron Diffraction (SAED) and Energy Dispersive X-ray (EDX) compositional maps were obtained with a *Tecnai Osiris* electron microscope equipped with a Super-X EDX detector and operated at 200 kV by Dr. Artem M. Abakumov and Dr. Gustaaf Van Tendeloo (Laboratory “Electron Microscopy for Materials Science”, University of Antwerp, Antwerp, Belgium). As sulfates are sensitive to the irradiation electron beam, we also tried ABF (Annular Bright Field) – STEM to visualize atomic repartition, which is insensitive to sample thickness and defocus amount.

Each sample was prepared in an Ar-filled glove box by crushing the grainy powder in a mortar in anhydrous hexane and depositing drops of suspension onto holey carbon grids and was transported to the microscope column completely excluding contact with air.

A.2.5 Diffraction Data Treatment

A.2.5.1. Refinement of the Structures from XRD and NPD Patterns

Crystal structure of each sample was refined against our experimental XRD and NPD patterns using the Rietveld method [262], as implemented in the FullProf suite of software [253, 323]. Results of these refinements are presented in different tables within this thesis. In most cases, a bond valence sum (BVS) analysis was also performed during the Rietveld refinement, using the b_0 parameters from Brown and Altermatt [263].

A.2.5.2. Crystal Structure Determination

To determine the structure of new compounds presented in this thesis, generally the XRD powder patterns were initially indexed using the Dicvol program [251], which is distributed with the FullProf suite software [253, 323]. From the angular positions of the main diffraction peaks observed in the XRD powder pattern, Dicvol program proposed one or several solutions of crystalline systems and unit cell parameters that could index the pattern. The XRD patterns were then refined using the Le Bail method (Profile Matching) with the FullProf program in order to determine more precisely the unit cell parameters. The TEM investigation could also

help to confirm the unit cell parameters and space group. The *Dicvol* program suggested. The formula of the compounds could be checked through EDX analysis and more precisely by atomic emission spectroscopy.

The structure determinations were then carried out with both the *EXPO* software, using the direct method [260, 324-325], or the *FOX* program [252], using global optimization (*ab initio* calculations). The as-determined crystal structures were then refined using the Rietveld method [262], as implemented in the FullProf suite of software [253, 323].

A.2.5.3. Visualization, Drawing and Analyses of the Structures

The structures were drawn and examined with the help of two programs: *i*) the *FullProf Studio* program of the *FullProf* suite [253, 323], *ii*) the *VESTA* visualization program [326].

Data of the structures that were not determined from our diffraction data were obtained from the ICSD database.

A.2.5.4. Bond Valence Energy Landscapes

BVEL are obtained from soft-BVS parameters by transforming them valence into energy units, using a Morse-type potential for the attractive part and a screened Coulomb potential for the repulsive part. [265] The probing ion, in our case the Li^+/Na^+ , is placed in all points of the unit cell and its interaction energy, using the above mentioned potential, is calculated up to a common distance of 8 Å with all ions of the structure. The previously existing Li-species are removed from the list of ions before the calculation. This approach has been successfully applied to energy materials and ionic conductors, [327-328] and was recently implemented in the program BondSTR of the FullProf Suite. [253, 323]

A.3. Electrochemical Characterizations

To characterize the electrochemical performance of our materials, all electrochemical tests were performed in half cells, which consist in using a single electrode material (the material to test) as the working electrode (WE) and pure lithium or sodium metal as the counter electrode (CE), which also functioned as the reference electrode (RE) since its potential does not change during the charge/discharge cycles (Li^+/Li^0 : -3.045 V vs. SHE and Na^+/Na^0 : -2.714 V vs. SHE).

A.3.1 Electrode Preparation

As discussed in Chapter I, polyanionic compounds present low electronic conductivities, which constitute an important limit factor for their electrochemical activity. To enhance the electronic conductivity of a material for preliminary evaluation of its electrochemical performances, the particles of the pristine compound can be reduced in size and mixed with a conductive additive using mechanical milling (cf. § A.1.1.1 Mechanical-milling). In general, we ball-milled the pristine materials with 20-25% carbon Super P (also named carbon SP) in mass for 15-20 minutes in a 10-cm³ ball-milling cell closed under argon.

A.3.2 Electrochemical Cells

A.3.2.1. Swagelok Cells

Most of the electrochemical tests versus lithium (or sodium) were carried out in Swagelok®-type cells (**Figure A.2**). The cells were assembled in an argon-filled glove box, using the as-prepared working electrode materials as the positive electrodes and lithium (or sodium) metal disc as the negative electrodes. These two electrodes were separated by one *Whatman® GF/D* borosilicate glass fiber sheet saturated with electrolyte. Usual cathode loading was 6-10 mg·cm⁻² per cell.

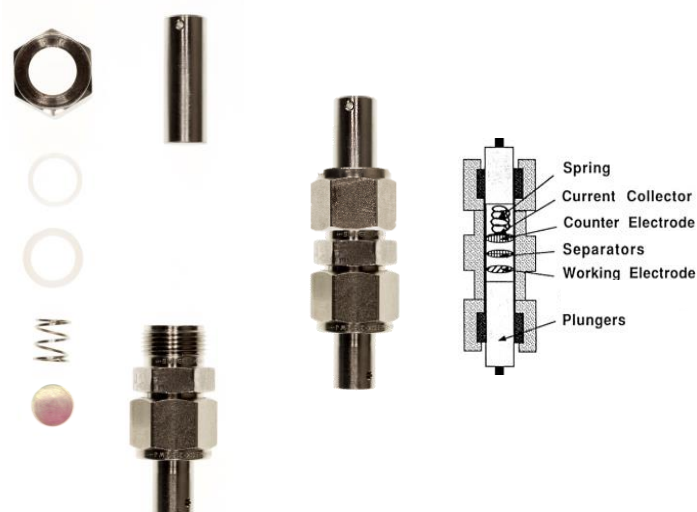


Figure A.7: A photo of a practical a Swagelok® - type electrochemical cell with its components (**left**) with a schematic description of the cell (**right**).

A.3.2.2. *In Situ* Electrochemical Experiments

A special cell was used for *in situ* electrochemical experiments (see § A.2.1.3). Due to the bigger size of this special cell compared to the Swagelok® - type cells, it was also used to prepare larger quantity of cycled electrode materials for ex situ experiments. In this case, the beryllium window was replaced by a stainless steel current collector, and the cathode loading was up to 40 mg per cell.

A.3.3 Electrochemical Cycling Tests

Electrochemical tests were conducted in a temperature controlled environment ($T = 25 \pm 0.5^\circ\text{C}$) at different rates via a VMP system (Biologic S.A., Claix, France) operating in galvanostatic mode. Unless otherwise specified, The positive electrode was separated from the Li metal disc negative electrode by the Whatman GF/D borosilicate glass fiber sheet saturated with either 1M LiPF_6 solution in a mixture of ethylene carbonate, propylene carbonate in 1:1 ratio by weight (*LP30* electrolyte) or 1M LiPF_6 solution in a mixture of ethylene carbonate, propylene carbonate and dimethyl carbonate in 1:1:3 ratio by weight (*LP100* electrolyte).

Most of the electrochemical tests presented in this thesis were operated in a galvanostatic mode, *i.e.* by imposing a constant current density to the cell and following the evolution of the cell voltage, which is recorded regularly. The charge (or discharge) rate is generally given using the nomenclature C/n , which means that the intensity of the current is imposed so that the complete charge (or discharge) is reached in n hours. Note that, in this thesis, a complete charge (or discharge) corresponds to the removal (or uptake) of 1 Li^+ or 1 Na^+ per transition metal.

These galvanostatic measurements enable to trace the voltage-composition curves $V = f(x)$ presented throughout the thesis. These curves provide first information on the charge/discharge mechanism, as they generally present either an S-shape for a single-phase (solid solution) process or a plateau (L-shape) for a two-phase mechanism. Moreover, calculating the derivative $-\delta x/\delta V$ of the voltage-composition traces and plotting the curves $-\delta x/\delta V = f(V)$ (*i.e.* ~simulation of a cyclic voltammetry) often enable to determine more precisely the average working potential of the electrode material.

A.4. Other Physical-Chemical Characterizations

A.4.1 ^{57}Fe Mössbauer Spectroscopy

For this thesis, the ^{57}Fe Mössbauer Spectroscopy of $\text{Fe}_2\text{O}(\text{SO}_4)_2$ sample were performed at the Institut Charles Gerhardt (UMR CNRS 5253, Université Montpellier 2, France) in collaboration with Dr. Moulay Tahar Sougrati. The spectra were recorded in transmission geometry in constant acceleration mode and with a ^{57}Co (Rh) source with normal activity of 925 MBq. The velocity scale ($\sim 4 \text{ mm}\cdot\text{s}^{-1}$) was calibrated at room temperature with α -Fe foil. The absorbers were typically prepared from 20 to 50 mg of powder samples. For *in operando* experiments, we used a special cell similar to the one designed for *in operando* experiments, but having two beryllium windows: one at the positive and one at the negative electrodes.

The ^{57}Fe Mössbauer Spectroscopy is a nuclear resonant technique, which permit to obtain information about the oxidation state of the iron, the symmetry of its environment and its magnetic properties, if any, in the material studied [329]. It implies transitions between the nuclear ground state of the ^{57}Fe and its first nuclear excited states, which are the consequences of the absorption of a photon.

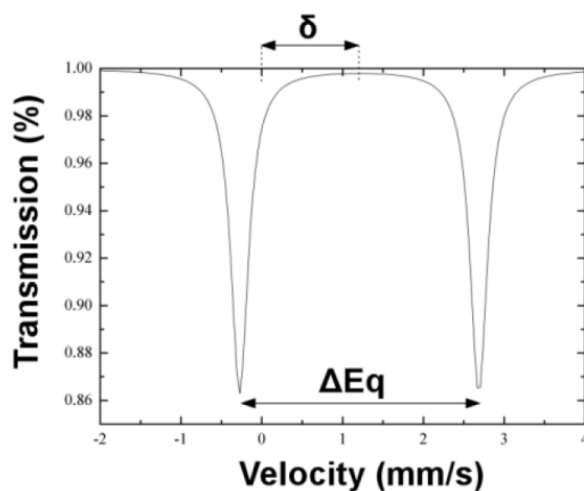


Figure A.8: Schematic Mössbauer spectra showing the isomer shift (δ) and the quadrupole splitting (ΔE_q) of a typical doublet of $\text{Fe}(2+)$.

If the material does not present magnetic interactions (which is the cases of the materials studied at room temperature in this thesis), the Mössbauer spectrum of a nucleus of ^{57}Fe is generally a doublet, as seen in **Figure A.8**. The difference between the two maxima of the doublet is named *quadrupole splitting* (noted ΔE_q), while their barycentre with respect to the origin of the velocities is named *isomeric shift* (noted δ). These two hyperfine parameters are

influenced by the electric field generated by the electrons of the iron atoms and the ones of the neighboring atoms. Thus the Mössbauer doublet of an iron in the oxidation state II⁺ typically presents an isomer shift around 1.0 mm·s⁻¹ and a quadrupole splitting ranging from 0.2 to 3.5 mm·s⁻¹, while the doublet of an iron III⁺ has an isomer shift close to 0.3-0.4 mm/s and a quadrupole splitting smaller than 2 mm·s⁻¹ [330].

A.4.2 Thermogravimetric Analysis

Thermal analyses enable to follow the physical and chemical changes of a material with the temperature. Thermogravimetric Analyses (TGA) detect mass variations (mass loss or mass gain) while heating the sample in a given atmosphere (*e.g.* inert gas, air, reducing conditions). They can be coupled to Mass Spectroscopy (MS), in order to analyze the gas associated with a mass loss. Differential Scanning Calorimetry (DSC) enable to observe changes of state, phase transitions and chemical reactions by measuring the difference in the amount of heat required to increase the temperature of the sample as compared to a reference.

In our case, these experiments were performed by Matthieu Courty (Laboratoire de Réactivité et de Chimie des Solides – LRCS, CNRS UMR 7314, UPJV, Amiens, France), TGA-MS analyses were carried out on ~20 mg of powder samples placed in an alumina or a platinum crucible, in the temperature range 20 – 800 °C (heating rate: 5°C/min) under argon flow (50 cm³/min) using a STA-449C Jupiter unit (Netzsch) coupled to a quadrupole mass spectrometer QMS 403 Aëlos equipped with a stainless-steel capillary and a secondary-electron multiplier detector (Channeltron). DSC measurements were performed under the same conditions using a 204F1 Netzsch unit, with the samples sealed in aluminum crucibles.

A.4.3 Conductivity Measurements

The a.c. and d.c. conductivities were measured on the pellets between ionically blocking gold electrodes using a Bio-Logic MTZ-35 Impedance Analyzer in a frequency range of 35 MHz to 0.01 Hz and an excitation voltage of 100 mV. The d.c. conductivity values were determined by applying polarization voltages of 100 mV – 500 mV. The pellets were sintered at 250-415°C (Ø 10 mm, compactness ~80-90%) (depending on thermal stability of each sample) and sputtered with gold before measured under argon flow at various stabilized temperatures ranging from 75 to 300°C. During heating the compounds were equilibrated at a constant temperature automatically prior to the impedance measurement. Values of activation energy E_a for cation migration were obtained by fitting the a.c. and d.c. data measured according to the Arrhenius equation $\sigma(T) = \sigma_0 \cdot \exp(-E_a/k_B T)$, in which σ is the conductivity at the temperature T , σ_0 is a pre-exponential factor, and k_B the Boltzmann constant.

A.4.4 DFT Calculations

In this thesis DFT calculations were performed in cooperation with M. Saubanère and M. L. Doublet (Institut Charles Gerhardt and University of Montpellier). All calculations were performed using the plane-wave density functional theory (DFT) code from the Vienna Ab initio Simulation Package (VASP) [331-332]. Spin-dependent calculations were performed using the generalized gradient approximation of Perdew, Burke, and Ernzerhof (PBE) [333] including Hubbard-U corrections following the rotationally invariant formalism of Dudarev [8]. The Hubbard-U parameter is added to recover part of the self-interaction error made by using classical LDA or GGA XC-functional in narrow bands. The U value used in a transition metal (TM) based material depends on the TM oxidation degree and the TM environment. Then the U value is generally fitted in order that theoretical and experimental properties match (*e.g.* cell parameters, band gap, *etc.*). In the calculations performed in the context of this thesis, several U values have been tested, and optimal results have been obtained at $U = 4\text{eV}$ for Cu, V and Fe atoms, in agreement with values generally found in the literature. The electron wave-functions were described in the projected augmented wave formalism (PAW) [334-335]. In all calculations the plane wave energy cutoff was set to 600 eV and the Brillouin zone integration was done in a converged k-point grid distributed as uniformly as possible, using Monkhorst-Pack meshes. All atom coordinates and lattice parameters were fully relaxed using conjugate gradient energy minimization until the forces acting on each atom were less than $1.10 \cdot 10^{-3} \text{eV}/\text{\AA}^2$.

A.4.5 Magnetic Measurements

Macroscopic magnetic properties of the samples were probed on about 20 mg of the powder samples filled into gel caps, using a *SQUID 5S* or a *SQUID XL* magnetometers (Quantum design). Susceptibility measurements ($\chi = f(T)$) were carried out in zero-field-cooled (ZFC) and field-cooled (FC) conditions, in the temperature range 2 K - 400 K, under applied magnetic fields (H) of 1 kOe. Magnetization curves ($M = f(H)$) were recorded at 2 K by varying the applied field between -50 kOe and 50 kOe.

Reference

1. New Energy Outlook 2016; Bloomberg New Energy Finance: 2016.
2. D. Larcher, J. M. Tarascon, Towards Greener and More Sustainable Batteries for Electrical Energy Storage. *Nature. Chem.* **2015**, 7, 19-29.
3. M. Winter, R. J. Brodd, What Are Batteries, Fuel Cells, and Supercapacitors? *Chem. Rev.* **2004**, 104, 4245-4270.
4. K. M. Abraham, K. Amine, C. Arbizzani, *Lithium Batteries: Advanced Technologies and Applications*. John Wiley & Sons, Inc.: Hoboken, New Jersey, **2013**.
5. M. R. Palacin, Recent Advances in Rechargeable Battery Materials: a Chemist's Perspective. *Chem. Soc. Rev.* **2009**, 38, 2565-2575.
6. M. Reynaud. Design of New Sulfate-Based Positive Electrode Materials for Li- and Na-Ion Batteries. University of Picardie Jules Verne, Amiens, France, **2013**.
7. M. Armand, J. M. Tarascon, Building Better Batteries. *Nature* **2008**, 451, 652-657.
8. J. M. Tarascon, M. Armand, Issues and Challenges Facing Rechargeable Lithium Batteries. *Nature* **2001**, 414, 359-367.
9. G. Planté, Nouvelle Pile Secondaire D'une Grande Puissance. *C. r. hebd. séances Acad. sci.* **1860**, 50, 640-642.
10. A. Volta, On the Electricity Excited by the Mere Contact of Conducting Substances of Different Kinds. In a Letter from Mr. Alexander Volta, F. R. S. Professor of Natural Philosophy in the University of Pavia, to the Rt. Hon. Sir Joseph Banks, Bart. K. B. P. R. S. *Philosophical Transactions of the Royal Society of London* **1800**, 90, 403-431.
11. S. Bergstrom, Nickel–Cadmium Batteries – Pocket Type. *J. Electrochem. Soc.* **1952**, 99, 248C-250C.
12. E. W. Jungner, Method of Producing Electrodes for Electric Accumulators. US Patent 731308 A, **1903**.
13. G. L. Holleck, J. R. Driscoll, B. E. Paul, The Use of LaNi₅H_x-Type Hydrides in Ni-H₂ batteries: Benefits and Problems. *J. Less-Common Met* **1980**, 74, 379-384.
14. K. Bullis, Old Battery Type Gets an Energy Boost. *Technology Review* **2015**.
15. H. Ikeda, T. Saito, H. Tamura, *Proc. Manganese Dioxide Symp.* IC Sample Office, Cleveland: OH, **1975**; Vol. 1.
16. M. S. Whittingham, Chalcogenide Battery. US Patent 4009052A, **1977**.
17. J. Broadhead, F. J. Disalvo, F. A. Trumbore, Non-Aqueous Battery Using Chalcogenide Electrode. US Patent 3864167, **1975**.
18. J. Broahead, A. D. Butherus, Rechargeable Non-Aqueous Battery. US Patent 3791867, **1974**.

19. D. W. Murphy, P. A. Christian, Solid State Electrodes for High Energy Batteries. *Science* **1979**, *205*, 651-656.
20. K. Mizushima, P. C. Jones, P. J. Wiseman, J. B. Goodenough, Li_xCoO_2 ($0 < x \leq 1$): a New Cathode Material for batteries of High Energy Density. *Mat. Res. Bull* **1980**, *15*, 783-789.
21. M. M. Thackeray, W. I. F. David, P. G. Bruce, J. B. Goodenough, Lithium Insertion into Manganese Spinels. *Mater. Res. Bull.* **1983**, *18*, 461-472.
22. D. W. Murphy, F. J. Di Salvo, J. N. Carides, J. V. Waszczak, Topochemical Reactions of Rutile Related Structures with Lithium. *Mater. Res. Bull.* **1978**, *13*, 1395-1402.
23. M. Lazzari, B. Scrosati, A Cyclable Lithium Organic Electrolyte Cell Based on Two Intercalation Electrodes. *J. Electrochem. Soc.* **1980**, *127*, 773-774.
24. K. Mizushima, P. C. Jones, P. J. Wiseman, J. B. Goodenough, Li_xCoO_2 ($0 < x < 1$): A New Cathode Material for Batteries of High Energy Density. *Mater. Res. Bull.* **1980**, *15*, 783-789.
25. M. Mohri, N. Yanagisawa, Y. Tajima, H. Tanaka, T. Mitate, S. Nakajima, M. Yoshida, Y. Yoshimoto, T. Suzuki, H. Wada, 4th International Meetings on Lithium Batteries Rechargeable lithium battery based on pyrolytic carbon as a negative electrode. *J. Power Sources* **1989**, *26*, 545-551.
26. S. Basu, Ambient Temperature Rechargeable Battery. US Patent 4423125A, **1983**.
27. D. Guérard, A. Hérol, New Method for the Preparation of Lithium Insertion Compounds in Graphite. *C.R. Acad. Sci. C* **1972**, *275*, 571-572.
28. Y. Nishi, H. Azuma, A. Omaru., Non Aqueous Electrolyte Cell. US Patent 4959281.
29. T. Nagaura, K. Tozawa., Lithium Ion Rechargeable Battery. *Prog. Batteries Solar Cells* **1990**, *9*, 209-217.
30. K. Ozawa, Lithium-ion rechargeable batteries with LiCoO_2 and carbon electrodes: the LiCoO_2/C system. *Solid State Ionics* **1994**, *69*, 212-221.
31. Y. Nishi, The Development of Lithium Ion Secondary Batteries. *Chem. Rec.* **2001**, *1*, 406-413.
32. B. Dunn, H. Kamath, J.-M. Tarascon, Electrical Energy Storage for the Grid: A Battery of Choices. *Science* **2011**, *334*, 928-935.
33. M. Armand, J. M. Chabagno, M. J. Duclot, Fast Ion Transport in Solids: Electrodes and Electrolytes. In *Proceedings of the International Conference on Fast ion Transport in Solids*, Vashishta, P.; Mundy, J. N.; Shenoy, G. K., Eds. Lake Geneva: Wisconsin, U.S.A., **1979**; pp 131-136.
34. M. Armand, M. Duclot, Nouveaux Matériaux Eastomères à Conduction Ionique. FR Patent 2442512, **1980**.
35. M. Armand, M. Duclot, Electrochemical Generators for Producing Current and New Materials for Their Manufacture. US Patent 4303748A. & CA Patent 1165814A1, **1981**.

36. G. Feuillede, P. Perche, Ion-Conductive Macromolecular Gels and Membranes for Solid Lithium Cells. *J. Appl. Electrochem.* **1975**, *5*, 63-69.
37. I. Kelly, J. R. Owen, B. C. H. Steele, Mixed Polyether Lithium-Ion Conductors. *J. Electroanal. Chem. Interfacial Electrochem.* **1984**, *168*, 467-478.
38. I. E. Kelly, J. R. Owen, B. C. H. Steele, Poly(ethylene oxide) Electrolytes for Operation at near Room Temperature. *J. Power Sources* **1985**, *14*, 13-21.
39. A. S. Gozdz, C. Schmutz, J.-M. Tarascon, P. C. Warren, Method of making an electrolyte activatable lithium-ion rechargeable battery cell. US Patent 5456000, **1995**.
40. A. S. Gozdz, C. Schmutz, J.-M. Tarascon, Rechargeable Lithium Intercalation Battery with Hybrid Polymeric Electrolyte. US Patent 5296318, **1994**.
41. A. S. Gozdz, C. Schmutz, J.-M. Tarascon, P. C. Warren, Polymeric electrolytic cell separator membrane. US Patent 5418091, **1995**.
42. J. M. Tarascon, A. S. Gozdz, C. Schmutz, F. Shokoohi, P. C. Warren, Performance of Bellcore's Plastic Rechargeable Li-ion Batteries. *Solid State Ionics* **1996**, *86*, 49-54.
43. M. M. Thackeray, P. J. Johnson, L. A. de Picciotto, P. G. Bruce, J. B. Goodenough, Electrochemical Extraction of Lithium from LiMn_2O_4 . *Mater. Res. Bull.* **1984**, *19*, 179-187.
44. A. K. Padhi, K. S. Nanjundaswamy, J. B. Goodenough, Phospho-Olivines as Positive-Electrode Materials for Rechargeable Lithium Batteries. *J. Electrochem. Soc.* **1997**, *144*, 1188-1194.
45. N. Recham, J. N. Chotard, L. Dupont, C. Delacourt, W. Walker, M. Armand, J. M. Tarascon, A 3.6 V Lithium-Based Fluorosulphate Insertion Positive Electrode for Lithium-Ion Batteries. *Nat Mater* **2010**, *9*, 68-74.
46. J. B. Goodenough, Design Considerations. *Solid State Ionics* **1994**, *69*, 184-198.
47. M. S. Whittingham, Lithium Batteries and Cathode Materials. *Chem. Rev.* **2004**, *104*, 4271-4302.
48. J. B. Goodenough, Y. Kim, Challenges for Rechargeable Li Batteries. *Chem. Mater.* **2010**, *22*, 587-603.
49. C. Masquelier, L. Croguennec, Polyanionic (Phosphates, Silicates, Sulfates) Frameworks as Electrode Materials for Rechargeable Li (or Na) Batteries. *Chem. Rev.* **2013**, *113*, 6552-6591.
50. G. Rouse, J. M. Tarascon, Sulfate-Based Polyanionic Compounds for Li-Ion Batteries: Synthesis, Crystal Chemistry, and Electrochemistry Aspects. *Chem. Mater.* **2014**, *26*, 394-406.
51. N. Nitta, F. Wu, J. T. Lee, G. Yushin, Li-ion Battery Materials: Present and Future. *Mater. Today* **2015**, *18*, 252-264.
52. T. Ohzuku, A. Ueda, Solid-State Redox Reactions of LiCoO_2 ($R\bar{3}m$) for 4 Volt Secondary Lithium Cells. *J. Electrochem. Soc.* **1994**, *141*, 2972-2977.

53. X. Q. Yang, X. Sun, J. McBreen, New Phases and Phase Transitions Observed in $\text{Li}_{1-x}\text{CoO}_2$ during Charge: In Situ Synchrotron X-ray Diffraction Studies. *Electrochem. Commun.* **2000**, *2*, 100-103.
54. A. Van der Ven, M. K. Aydinol, G. Ceder, First-Principles Evidence for Stage Ordering in Li_xCoO_2 . *J. Electrochem. Soc.* **1998**, *145*, 2149-2155.
55. Z. Chen, Z. Lu, J. R. Dahn, Staging Phase Transitions in Li_xCoO_2 . *J. Electrochem. Soc.* **2002**, *149*, A1604-A1609.
56. G. G. Amatucci, J. M. Tarascon, L. C. Klein, CoO_2 , The End Member of the Li_xCoO_2 Solid Solution. *J. Electrochem. Soc.* **1996**, *143*, 1114-1123.
57. J. M. Tarascon, C. Delacourt, A. S. Prakash, M. Morcrette, M. S. Hegde, C. Wurm, C. Masquelier, Various Strategies to Tune the Ionic/Electronic Properties of Electrode Materials. *Dalton Trans.* **2004**, 2988-2994.
58. A. Manthiram, J. Choi, W. Choi, Factors Limiting the Electrochemical Performance of Oxide Cathodes. *Solid State Ionics* **2006**, *177*, 2629-2634.
59. O. Masashige, S. Asami, Stacking Faults and Metallic Properties of Triangular Lattice CoO_2 with a Three-Layer Structure. *J. Phys.: Condens. Matter* **2008**, *20*, 175207.
60. H. Wang, Y. I. Jang, B. Huang, D. R. Sadoway, Y. M. Chiang, TEM Study of Electrochemical Cycling-Induced Damage and Disorder in LiCoO_2 Cathodes for Rechargeable Lithium Batteries. *J. Electrochem. Soc.* **1999**, *146*, 473-480.
61. E. Endo, T. Yasuda, A. Kita, K. Yamaura, K. Sekai, A LiCoO_2 Cathode Modified by Plasma Chemical Vapor Deposition for Higher Voltage Performance. *J. Electrochem. Soc.* **2000**, *147*, 1291-1294.
62. K. Y. Chung, W.-S. Yoon, J. McBreen, X.-Q. Yang, S. H. Oh, H. C. Shin, W. I. Cho, B. W. Cho, Structural Studies on the Effects of ZrO_2 Coating on LiCoO_2 during Cycling Using In Situ X-Ray Diffraction Technique. *J. Electrochem. Soc.* **2006**, *153*, A2152-A2157.
63. G. G. Amatucci, J. M. Tarascon, L. C. Klein, Cobalt Dissolution in LiCoO_2 -Based Non-Aqueous Rechargeable Batteries. *Solid State Ionics* **1996**, *83*, 167-173.
64. M. G. S. R. Thomas, W. I. F. David, J. B. Goodenough, P. Groves, Synthesis and Structural Characterization of the Normal Spinel $\text{Li}[\text{Ni}_2]\text{O}_4$. *Mater. Res. Bull.* **1985**, *20*, 1137-1146.
65. J. R. Dahn, U. von Sacken, C. A. Michal, Structure and Electrochemistry of $\text{Li}_{1\pm y}\text{NiO}_2$ and a New Li_2NiO_2 Phase with the $\text{Ni}(\text{OH})_2$ Structure. *Solid State Ionics* **1990**, *44*, 87-97.
66. J. R. Dahn, U. von Sacken, M. W. Juzkow, H. Al-Janaby, Rechargeable LiNiO_2 /Carbon Cells. *J. Electrochem. Soc.* **1991**, *138*, 2207-2211.
67. J. Morales, C. Pérez-Vicente, J. L. Tirado, Cation Distribution and Chemical Deintercalation of $\text{Li}_{1-x}\text{Ni}_{1+x}\text{O}_2$. *Mater. Res. Bull.* **1990**, *25*, 623-630.

68. R. J. Gummow, M. M. Thackeray, Lithium-Cobalt-Nickel-Oxide Cathode Materials Prepared at 400°C for Rechargeable Lithium Batteries. *Solid State Ionics* **1992**, *53*, 681-687.
69. I. J. Pickering, J. T. Lewandowski, A. J. Jacobson, J. A. Goldstone, A Neutron Powder Diffraction Study of the Ordering in $\text{Li}_x\text{Ni}_{1-x}\text{O}$. *Solid State Ionics* **1992**, *53*, 405-412.
70. R. Kanno, H. Kubo, Y. Kawamoto, T. Kamiyama, F. Izumi, Y. Takeda, M. Takano, Phase Relationship and Lithium Deintercalation in Lithium Nickel Oxides. *J. Solid State Chem.* **1994**, *110*, 216-225.
71. A. Rougier, P. Gravereau, C. Delmas, Optimization of the Composition of the $\text{Li}_{1-z}\text{Ni}_{1+z}\text{O}_2$ Electrode Materials: Structural, Magnetic, and Electrochemical Studies. *J. Electrochem. Soc.* **1996**, *143*, 1168-1175.
72. H. Arai, S. Okada, Y. Sakurai, J.-i. Yamaki, Thermal Behavior of $\text{Li}_{1-y}\text{NiO}_2$ and the Decomposition Mechanism. *Solid State Ionics* **1998**, *109*, 295-302.
73. NIOSH Pocket Guide to Chemical Hazards. Centers for Disease Control and Prevention (CDC) - U.S. National Institute for Occupational Safety and Health (NIOSH). <http://www.cdc.gov/niosh/npg/pgintrod.html>.
74. A. R. Armstrong, P. G. Bruce, Synthesis of Layered LiMnO_2 as an Electrode for Rechargeable Lithium Batteries. *Nature* **1996**, *381*, 499-500.
75. F. Capitaine, P. Gravereau, C. Delmas, A new Variety of LiMnO_2 with a Layered Structure. *Solid State Ionics* **1996**, *89*, 197-202.
76. M. Gu, I. Belharouak, J. Zheng, H. Wu, J. Xiao, A. Genc, K. Amine, S. Thevuthasan, D. R. Baer, J.-G. Zhang, N. D. Browning, J. Liu, C. Wang, Formation of the Spinel Phase in the Layered Composite Cathode Used in Li-Ion Batteries. *ACS Nano* **2013**, *7*, 760-767.
77. J. Tu, X. B. Zhao, G. S. Cao, D. G. Zhuang, T. J. Zhu, J. P. Tu, Enhanced Cycling Stability of LiMn_2O_4 by Surface Modification with Melting Impregnation Method. *Electrochim. Acta* **2006**, *51*, 6456-6462.
78. E. Rossen, C. D. W. Jones, J. R. Dahn, Structure and Electrochemistry of $\text{Li}_x\text{Mn}_y\text{Ni}_{1-y}\text{O}_2$. *Solid State Ionics* **1992**, *57*, 311-318.
79. Z. Lu, D. D. MacNeil, J. R. Dahn, Layered Cathode Materials $\text{Li}[\text{Ni}_x\text{Li}_{(1/3-2x/3)}\text{Mn}_{(2/3-x/3)}]\text{O}_2$ for Lithium-ion Batteries. *Electrochem. Solid-State Lett.* **2001**, *4*, A191-A194.
80. T. Ohzuku, Y. Makimura, Layered Lithium Insertion Material of $\text{LiNi}_{1/2}\text{Mn}_{1/2}\text{O}_2$: A Possible Alternative to LiCoO_2 for Advanced Lithium-ion Batteries. *Chem. Lett.* **2001**, 744-745.
81. J. Reed, G. Ceder, Charge, Potential, and Phase Stability of Layered $\text{Li}(\text{Ni}_{0.5}\text{Mn}_{0.5})\text{O}_2$. *Electrochem. Solid-State Lett.* **2002**, *5*, A145-A148.
82. X.-Q. Yang, J. McBreen, W.-S. Yoon, C. P. Grey, Crystal Structure Changes of $\text{LiMn}_{0.5}\text{Ni}_{0.5}\text{O}_2$ Cathode Materials during Charge and Discharge Studied by Synchrotron Based In Situ XRD. *Electrochem. Commun.* **2002**, *4*, 649-654.

83. Y. Arachi, H. Kobayashi, S. Emura, Y. Nakata, M. Tanaka, T. Asai, Structural Change of $\text{Li}_{1-x}\text{Ni}_{0.5}\text{Mn}_{0.5}\text{O}_2$ Cathode Materials for Lithium-ion Batteries by Synchrotron Radiation. *Chem. Lett.* **2003**, *32*, 60-61.
84. M. S. Islam, R. A. Davies, J. D. Gale, Structural and Electronic Properties of the Layered $\text{LiNi}_{0.5}\text{Mn}_{0.5}\text{O}_2$ Lithium Battery Material. *Chem. Mater.* **2003**, *15*, 4280-4286.
85. Y. Makimura, T. Ohzuku, Lithium Insertion Material of $\text{LiNi}_{1/2}\text{Mn}_{1/2}\text{O}_2$ for Advanced Lithium-ion Batteries. *J. Power Sources* **2003**, *119–121*, 156-160.
86. Y. Arachi, H. Kobayashi, S. Emura, Y. Nakata, M. Tanaka, T. Asai, H. Sakaebe, K. Tatsumi, H. Kageyama, Li De-intercalation Mechanism in $\text{LiNi}_{0.5}\text{Mn}_{0.5}\text{O}_2$ Cathode Material for Li-ion Batteries. *Solid State Ionics* **2005**, *176*, 895-903.
87. J. Bréger, Y. S. Meng, Y. Hinuma, S. Kumar, K. Kang, Y. Shao-Horn, G. Ceder, C. P. Grey, Effect of High Voltage on the Structure and Electrochemistry of $\text{LiNi}_{0.5}\text{Mn}_{0.5}\text{O}_2$: a Joint Experimental and Theoretical Study. *Chem. Mater.* **2006**, *18*, 4768-4781.
88. S. B. Schougaard, J. Bréger, M. Jiang, C. P. Grey, J. B. Goodenough, $\text{LiNi}_{0.5+\delta}\text{Mn}_{0.5-\delta}\text{O}_2$ - a High-Rate, High-Capacity Cathode for Lithium Rechargeable Batteries. *Adv. Mater.* **2006**, *18*, 905-909.
89. Y. Hinuma, Y. S. Meng, K. Kang, G. Ceder, Phase Transitions in the $\text{LiNi}_{0.5}\text{Mn}_{0.5}\text{O}_2$ System with Temperature. *Chem. Mater.* **2007**, *19*, 1790-1800.
90. F. Zhou, X. Zhao, Z. Lu, J. Jiang, J. R. Dahn, The Effect of Al Substitution on the Reactivity of Delithiated $\text{LiNi}_{(0.5-z)}\text{Mn}_{(0.5-z)}\text{Al}_{2z}\text{O}_2$ with Nonaqueous Electrolyte. *Electrochem. Solid-State Lett.* **2008**, *11*, A155-A157.
91. Z. Lu, D. D. MacNeil, J. R. Dahn, Layered $\text{Li}[\text{Ni}_x\text{Co}_{1-2x}\text{Mn}_x]\text{O}_2$ Cathode Materials for Lithium-Ion Batteries. *Electrochem. Solid-State Lett.* **2001**, *4*, A200-A203.
92. T. Ohzuku, Y. Makimura, Layered Lithium Insertion Material of $\text{LiCo}_{1/3}\text{Ni}_{1/3}\text{Mn}_{1/3}\text{O}_2$ for Lithium-Ion Batteries. *Chem. Lett.* **2001**, *30*, 642-643.
93. B. J. Hwang, Y. W. Tsai, D. Carlier, G. Ceder, A Combined Computational/Experimental Study on $\text{LiNi}_{1/3}\text{Co}_{1/3}\text{Mn}_{1/3}\text{O}_2$. *Chem. Mater.* **2003**, *15*, 3676-3682.
94. N. Yabuuchi, T. Ohzuku, Novel Lithium Insertion Material of $\text{LiCo}_{1/3}\text{Ni}_{1/3}\text{Mn}_{1/3}\text{O}_2$ for Advanced Lithium-ion Batteries. *J. Power Sources* **2003**, *119–121*, 171-174.
95. J.-M. Kim, H.-T. Chung, Role of Transition Metals in Layered $\text{Li}[\text{Ni},\text{Co},\text{Mn}]\text{O}_2$ under Electrochemical Operation. *Electrochim. Acta* **2004**, *49*, 3573-3580.
96. N. Yabuuchi, T. Ohzuku, Electrochemical Behaviors of $\text{LiCo}_{1/3}\text{Ni}_{1/3}\text{Mn}_{1/3}\text{O}_2$ in Lithium Batteries at Elevated Temperatures. *J. Power Sources* **2005**, *146*, 636-639.
97. K. K. Lee, W. S. Yoon, K. B. Kim, K. Y. Lee, S. T. Hong, Characterization of $\text{LiNi}_{0.85}\text{Co}_{0.10}\text{M}_{0.05}\text{O}_2$ ($\text{M} = \text{Al}, \text{Fe}$) as a Cathode Material for Lithium Secondary Batteries. *J. Power Sources* **2001**, *97–98*, 308-312.

98. J. S. Weaving, F. Coowar, D. A. Teagle, J. Cullen, V. Dass, P. Bindin, R. Green, W. J. Macklin, Development of High Energy Density Li-ion Batteries Based on $\text{LiNi}_{1-x-y}\text{Co}_x\text{Al}_y\text{O}_2$. *J. Power Sources* **2001**, 97–98, 733-735.
99. J. Shim, R. Kostecki, T. Richardson, X. Song, K. A. Striebel, Electrochemical Analysis for Cycle Performance and Capacity Fading of a Lithium-ion Battery Cycled at Elevated Temperature. *J. Power Sources* **2002**, 112, 222-230.
100. M. Guilmard, C. Pouillier, L. Croguennec, C. Delmas, Structural and Electrochemical Properties of $\text{LiNi}_{0.70}\text{Co}_{0.15}\text{Al}_{0.15}\text{O}_2$. *Solid State Ionics* **2003**, 160, 39-50.
101. R. Robert, C. Bünzli, E. J. Berg, P. Novák, Activation Mechanism of $\text{LiNi}_{0.80}\text{Co}_{0.15}\text{Al}_{0.05}\text{O}_2$: Surface and Bulk Operando Electrochemical, Differential Electrochemical Mass Spectrometry, and X-ray Diffraction Analyses. *Chem. Mater.* **2015**, 27, 526-536.
102. J. S. Kim, C. S. Johnson, M. M. Thackeray, Layered $x\text{LiMO}_2 \cdot (1-x)\text{Li}_2\text{M}'\text{O}_3$ Electrodes for Lithium Batteries: A Study of $0.95\text{LiMn}_{0.5}\text{Ni}_{0.5}\text{O}_2 \cdot 0.05\text{Li}_2\text{TiO}_3$. *Electrochem. Commun.* **2002**, 4, 205-209.
103. C. S. Johnson, J. S. Kim, C. Lefief, N. Li, J. T. Vaughey, M. M. Thackeray, The Significance of the Li_2MnO_3 Component in 'Composite' $x\text{Li}_2\text{MnO}_3 \cdot (1-x)\text{LiMn}_{0.5}\text{Ni}_{0.5}\text{O}_2$ electrodes. *Electrochem. Commun.* **2004**, 6, 1085-1091.
104. J.-S. Kim, C. S. Johnson, J. T. Vaughey, M. M. Thackeray, S. A. Hackney, W. Yoon, C. P. Grey, Electrochemical and Structural Properties of $x\text{Li}_2\text{M}'\text{O}_3 \cdot (1-x)\text{LiMn}_{0.5}\text{Ni}_{0.5}\text{O}_2$ Electrodes for Lithium Batteries ($\text{M}' = \text{Ti, Mn, Zr}$; $0 \leq x \leq 0.3$). *Chem. Mater.* **2004**, 16, 1996-2006.
105. M. M. Thackeray, C. S. Johnson, J. T. Vaughey, N. Li, S. A. Hackney, Advances in Manganese-Oxide 'Composite' Electrodes for Lithium-ion Batteries. *J. Mater. Chem.* **2005**, 15, 2257-2267.
106. R.-M. Gu, S.-Y. Yan, S. Sun, C.-Y. Wang, M.-W. Li, Electrochemical Behavior of Lithium-rich Layered Oxide $\text{Li}[\text{Li}_{0.23}\text{Ni}_{0.15}\text{Mn}_{0.62}]\text{O}_2$ Cathode Material for Lithium-Ion Battery. *J. Solid State Electrochem.* **2015**, 19, 1659-1669.
107. M. M. Thackeray, S. H. Kang, C. S. Johnson, J. T. Vaughey, S. A. Hackney, Comments on the Structural Complexity of Lithium-Rich $\text{Li}_{1+x}\text{M}_{1-x}\text{O}_2$ Electrodes ($\text{M} = \text{Mn, Ni, Co}$) for Lithium Batteries. *Electrochem. Commun.* **2006**, 8, 1531-1538.
108. C. S. Johnson, N. Li, C. Lefief, J. T. Vaughey, M. M. Thackeray, Synthesis, Characterization and Electrochemistry of Lithium Battery Electrodes: $x\text{Li}_2\text{MnO}_3 \cdot (1-x)\text{LiMn}_{0.333}\text{Ni}_{0.333}\text{Co}_{0.333}\text{O}_2$ ($0 \leq x \leq 0.7$). *Chem. Mater.* **2008**, 20, 6095-6106.
109. P. Rozier, J. M. Tarascon, Review—Li-Rich Layered Oxide Cathodes for Next-Generation Li-Ion Batteries: Chances and Challenges. *J. Electrochem. Soc.* **2015**, 162, A2490-A2499.
110. M. Sathiya, G. Rouse, K. Ramesha, C. P. Laisa, H. Vezin, M. T. Sougrati, M.-L. Doublet, D. Foix, D. Gonbeau, W. Walker, A. S. Prakash, M. Ben Hassine, L. Dupont, J.-M. Tarascon, Reversible Anionic Redox Chemistry in High-Capacity Layered-Oxide Electrodes. *Nat Mater.* **2013**, 12, 827-835.

111. R. Xiao, H. Li, L. Chen, Density Functional Investigation on Li_2MnO_3 . *Chem. Mater.* **2012**, *24*, 4242-4251.
112. H. Koga, L. Croguennec, M. Ménétrier, K. Douhil, S. Belin, L. Bourgeois, E. Suard, F. Weill, C. Delmas, Reversible Oxygen Participation to the Redox Processes Revealed for $\text{Li}_{1.20}\text{Mn}_{0.54}\text{Co}_{0.13}\text{Ni}_{0.13}\text{O}_2$. *J. Electrochem. Soc.* **2013**, *160*, A786-A792.
113. H. Koga, L. Croguennec, M. Ménétrier, P. Manessiez, F. Weill, C. Delmas, Different oxygen redox participation for bulk and surface: A possible global explanation for the cycling mechanism of $\text{Li}_{1.20}\text{Mn}_{0.54}\text{Co}_{0.13}\text{Ni}_{0.13}\text{O}_2$. *J. Power Sources* **2013**, *236*, 250-258.
114. M. Sathiya, K. Ramesha, G. Rouse, D. Foix, D. Gonbeau, A. S. Prakash, M. L. Doublet, K. Hemalatha, J. M. Tarascon, High Performance $\text{Li}_2\text{Ru}_{1-y}\text{Mn}_y\text{O}_3$ ($0.2 \leq y \leq 0.8$) Cathode Materials for Rechargeable Lithium-Ion Batteries: Their Understanding. *Chem. Mater.* **2013**, *25*, 1121-1131.
115. M. Sathiya, A. M. Abakumov, D. Foix, G. Rouse, K. Ramesha, M. Saubanère, M. L. Doublet, H. Vezin, C. P. Laisa, A. S. Prakash, D. Gonbeau, G. VanTendeloo, J. M. Tarascon, Origin of Voltage Decay in High-Capacity Layered Oxide Electrodes. *Nat Mater.* **2015**, *14*, 230-238.
116. J. M. Tarascon, E. Wang, F. K. Shokoohi, W. R. McKinnon, S. Colson, The Spinel Phase of LiMn_2O_4 as a Cathode in Secondary Lithium Cells. *J. Electrochem. Soc.* **1991**, *138*, 2859-2864.
117. J. M. Tarascon, D. Guyomard, Li Metal-Free Rechargeable Batteries Based on $\text{Li}_{1+x}\text{Mn}_2\text{O}_4$ Cathodes ($0 \leq x \leq 1$) and Carbon Anodes. *J. Electrochem. Soc.* **1991**, *138*, 2864-2868.
118. D. H. Jang, Y. J. Shin, S. M. Oh, Dissolution of Spinel Oxides and Capacity Losses in 4 V $\text{Li}/\text{Li}_x\text{Mn}_2\text{O}_4$ Cells. *J. Electrochem. Soc.* **1996**, *143*, 2204-2211.
119. H. Huang, C. A. Vincent, P. G. Bruce, Correlating Capacity Loss of Stoichiometric and Nonstoichiometric Lithium Manganese Oxide Spinel Electrodes with Their Structural Integrity. *J. Electrochem. Soc.* **1999**, *146*, 3649-3654.
120. Y. Shin, A. Manthiram, Factors Influencing the Capacity Fade of Spinel Lithium Manganese Oxides. *J. Electrochem. Soc.* **2004**, *151*, A204-A208.
121. M. M. Thackeray, Y. Shao-Horn, A. J. Kahaian, K. D. Kepler, E. Skinner, J. T. Vaughey, S. A. Hackney, Structural Fatigue in Spinel Electrodes in High Voltage (4 V) $\text{Li}/\text{Li}_x\text{Mn}_2\text{O}_4$ Cells. *Electrochem. Solid-State Lett.* **1998**, *1*, 7-9.
122. D. K. Kim, P. Muralidharan, H.-W. Lee, R. Ruffo, Y. Yang, C. K. Chan, H. Peng, R. A. Huggins, Y. Cui, Spinel LiMn_2O_4 Nanorods as Lithium Ion Battery Cathodes. *Nano Lett.* **2008**, *8*, 3948-3952.
123. E. Hosono, T. Kudo, I. Honma, H. Matsuda, H. Zhou, Synthesis of Single Crystalline Spinel LiMn_2O_4 Nanowires for a Lithium Ion Battery with High Power Density. *Nano Lett.* **2009**, *9*, 1045-1051.

124. H.-W. Lee, P. Muralidharan, R. Ruffo, C. M. Mari, Y. Cui, D. K. Kim, Ultrathin Spinel LiMn₂O₄ Nanowires as High Power Cathode Materials for Li-Ion Batteries. *Nano Lett.* **2010**, *10*, 3852-3856.
125. Y.-L. Ding, J. Xie, G.-S. Cao, T.-J. Zhu, H.-M. Yu, X.-B. Zhao, Single-Crystalline LiMn₂O₄ Nanotubes Synthesized via Template-Engaged Reaction as Cathodes for High-Power Lithium Ion Batteries. *Adv. Funct. Mater.* **2011**, *21*, 348-355.
126. B. L. Ellis, K. T. Lee, L. F. Nazar, Positive Electrode Materials for Li-Ion and Li-Batteries. *Chem. Mater.* **2010**, *22*, 691-714.
127. Z. Gong, Y. Yang, Recent Advances in the Research of Polyanion-Type Cathode Materials for Li-ion Batteries. *Energy Environ. Sci.* **2011**, *4*, 3223-3242.
128. J. Ni, L. Zhang, S. Fu, S. V. Savilov, S. M. Aldoshin, L. Lu, A Review on Integrating Nano-Carbons into Polyanion Phosphates and Silicates for Rechargeable Lithium Batteries. *Carbon* **2015**, *92*, 15-25.
129. J. B. Goodenough, H. Y. P. Hong, J. A. Kafalas, Fast Na⁺-ion Transport in Skeleton Structure. *Mater. Res. Bull.* **1976**, *11*, 203-220.
130. H. Y. P. Hong, Crystal Structures and Crystal Chemistry in the System Na_{1+x}Zr₂SixP_{3-x}O₁₂. *Mater. Res. Bull.* **1976**, *11*, 173-182.
131. N. Anantharamulu, K. Koteswara Rao, G. Rambabu, B. Vijaya Kumar, V. Radha, M. Vithal, A Wide-Ranging Review on Nasicon Type Materials. *J. Mater. Sci.* **2011**, *46*, 2821-2837.
132. N. Weber, J. T. Kummer, Proc. Annu. Power Sources Conf. **1967**, *21*, 37-39.
133. M. S. Whittingham, R. A. Huggins, Measurement of Sodium Ion Transport in Beta Alumina Using Reversible Solid Electrodes. *J. Chem. Phys.* **1971**, *54*, 414-416.
134. A. Nadiri, C. Delmas, R. Salmon, P. Hagenmuller., Chemical and electrochemical Alkali Metal Intercalation in the 3D-Framework of Fe₂(MoO₄)₃. *Rev. Chim. Miner.* **1984**, *21*.
135. W. M. Reiff, J. H. Zhang, C. C. Torardi, Topochemical Lithium Insertion into Fe₂(MoO₄)₃: Structure and Magnetism of Li₂Fe₂(MoO₄)₃. *J. Solid State Chem.* **1986**, *62*, 231-240.
136. C. Delmas, F. Cherkaoui, A. Nadiri, P. Hagenmuller, A Nasicon-Type Phase as Intercalation Electrode: NaTi₂(PO₄)₃. *Mater. Res. Bull.* **1987**, *22*, 631-639.
137. W. Weppner, H. Schulz, C. Delmas, A. Nadiri, J. L. Soubeyroux, Proceedings of the 6th International Conference on Solid State Ionics The Nasicon-type Titanium Phosphates Ati₂(PO₄)₃ (A = Li, Na) as Electrode Materials. *Solid State Ionics* **1988**, *28*, 419-423.
138. A. Manthiram, J. B. Goodenough, Lithium Insertion into Fe₂(MO₄)₃ Frameworks: Comparison of M = W with M = Mo. *J. Solid State Chem.* **1987**, *71*, 349-360.
139. A. Manthiram, J. B. Goodenough, Lithium insertion into Fe₂(SO₄)₃ frameworks. *J. Power Sources* **1989**, *26*, 403-408.

140. K. S. Nanjundaswamy, A. K. Padhi, J. B. Goodenough, S. Okada, H. Ohtsuka, H. Arai, J. Yamaki, Synthesis, Redox Potential Evaluation and Electrochemical Characteristics of NASICON-related-3D Framework Compounds. *Solid State Ion.* **1996**, *92*, 1-10.
141. A. K. Padhi, K. S. Nanjundaswamy, C. Masquelier, J. B. Goodenough, Mapping of Transition Metal Redox Energies in Phosphates with NASICON Structure by Lithium Intercalation. *J. Electrochem. Soc.* **1997**, *144*, 2581-2586.
142. A. K. Padhi, V. Manivannan, J. B. Goodenough, Tuning the Position of the Redox Couples in Materials with NASICON Structure by Anionic Substitution. *J. Electrochem. Soc.* **1998**, *145*, 1518-1520.
143. H. Huang, S. C. Yin, T. Kerr, N. Taylor, L. F. Nazar, Nanostructured Composites: A High Capacity, Fast Rate $\text{Li}_3\text{V}_2(\text{PO}_4)_3$ /Carbon Cathode for Rechargeable Lithium Batteries. *Adv. Mater.* **2002**, *14*, 1525-1528.
144. S. Patoux, C. Wurm, M. Morcrette, G. Rousse, C. Masquelier, A Comparative Structural and Electrochemical Study of Monoclinic $\text{Li}_3\text{Fe}_2(\text{PO}_4)_3$ and $\text{Li}_3\text{V}_2(\text{PO}_4)_3$. *J. Power Sources* **2003**, *119–121*, 278-284.
145. A. Castets, D. Carlier, K. Trad, C. Delmas, M. Ménétrier, Analysis of the ^7Li NMR signals in the Monoclinic $\text{Li}_3\text{Fe}_2(\text{PO}_4)_3$ and $\text{Li}_3\text{V}_2(\text{PO}_4)_3$ Phases. *J. Phys. Chem. C* **2010**, *114*, 19141-19150.
146. L. J. M. Davis, I. Heinmaa, G. R. Goward, Study of Lithium Dynamics in Monoclinic $\text{Li}_3\text{Fe}_2(\text{PO}_4)_3$ using ^6Li VT and 2D Exchange MAS NMR Spectroscopy. *Chem. Mater.* **2010**, *22*, 769-775.
147. M. Sato, H. Ohkawa, K. Yoshida, M. Saito, K. Uematsu, K. Toda, Enhancement of Discharge Capacity of $\text{Li}_3\text{V}_2(\text{PO}_4)_3$ by stabilizing the orthorhombic phase at room temperature. *Solid State Ionics* **2000**, *135*, 137-142.
148. J. Barker, M. Y. Saïdi, Lithium-containing Phosphates, Method of Preparation, and Uses Thereof. US Patent 6203946, **2001**.
149. D. Morgan, G. Ceder, Saïdi, J. Barker, J. Swoyer, H. Huang, G. Adamson, Experimental and Computational Study of the Structure and Electrochemical Properties of $\text{Li}_x\text{M}_2(\text{PO}_4)_3$ Compounds with the Monoclinic and Rhombohedral Structure. *Chem. Mater.* **2002**, *14*, 4684-4693.
150. M. Y. Saïdi, J. Barker, H. Huang, J. L. Swoyer, G. Adamson, Electrochemical Properties of Lithium Vanadium Phosphate as a Cathode Material for Lithium-Ion Batteries. *Electrochem. Solid-State Lett.* **2002**, *5*, A149-A151.
151. M. Morcrette, J.-B. Leriche, S. Patoux, C. Wurm, C. Masquelier, In Situ X-Ray Diffraction during Lithium Extraction from Rhombohedral and Monoclinic $\text{Li}_3\text{V}_2(\text{PO}_4)_3$. *Electrochem. Solid-State Lett.* **2003**, *6*, A80-A84.
152. M. Y. Saïdi, J. Barker, H. Huang, J. L. Swoyer, G. Adamson, Performance Characteristics of Lithium Vanadium Phosphate as a Cathode Material for Lithium-ion Batteries. *J. Power Sources* **2003**, *119–121*, 266-272.

153. S. C. Yin, H. Grondey, P. Strobel, M. Anne, L. F. Nazar, Electrochemical Property: Structure Relationships in Monoclinic $\text{Li}_{3-y}\text{V}_2(\text{PO}_4)_3$. *J. Am. Chem. Soc.* **2003**, *125*, 10402-10411.
154. S. C. Yin, P. S. Strobel, H. Grondey, L. F. Nazar, $\text{Li}_{2.5}\text{V}_2(\text{PO}_4)_3$: A Room-Temperature Analogue to the Fast-Ion Conducting High-Temperature γ -Phase of $\text{Li}_3\text{V}_2(\text{PO}_4)_3$. *Chem. Mater.* **2004**, *16*, 1456-1465.
155. P. Fu, Y. Zhao, Y. Dong, X. An, G. Shen, Synthesis of $\text{Li}_3\text{V}_2(\text{PO}_4)_3$ with High Performance by Optimized Solid-State Synthesis Routine. *J. Power Sources* **2006**, *162*, 651-657.
156. J. Barker, R. K. B. Gover, P. Burns, A. Bryan, The Effect of Al Substitution on the Electrochemical Insertion Properties of the Lithium Vanadium Phosphate, $\text{Li}_3\text{V}_2(\text{PO}_4)_3$. *J. Electrochem. Soc.* **2007**, *154*, A307-A313.
157. H. Huang, T. Faulkner, J. Barker, M. Y. Saidi, Lithium Metal Phosphates, Power and Automotive Applications. *J. Power Sources* **2009**, *189*, 748-751.
158. C. Masquelier, A. K. Padhi, K. S. Nanjundaswamy, J. B. Goodenough, New Cathode Materials for Rechargeable Lithium Batteries: The 3-D Framework Structures $\text{Li}_3\text{Fe}_2(\text{XO}_4)_3$ (X = P, As). *J. Solid State Chem.* **1998**, *135*, 228-234.
159. M. Morcrette, C. Wurm, C. Masquelier, On the Way to the Optimization of $\text{Li}_3\text{Fe}_2(\text{PO}_4)_3$ Positive Electrode Materials. *Solid State Sci.* **2002**, *4*, 239-246.
160. A. K. Padhi, K. S. Nanjundaswamy, C. Masquelier, S. Okada, J. B. Goodenough, Effect of Structure on the $\text{Fe}^{3+}/\text{Fe}^{2+}$ Redox Couple in Iron Phosphates. *J. Electrochem. Soc.* **1997**, *144*, 1609-1613.
161. G. Rouse, J. Rodriguez-Carvajal, S. Patoux, C. Masquelier, Magnetic Structures of the Triphylite LiFePO_4 and of Its Delithiated Form FePO_4 . *Chem. Mater.* **2003**, *15*, 4082-4090.
162. D. Morgan, A. Van der Ven, G. Ceder, Li Conductivity in Li_xMPO_4 (M = Mn, Fe, Co, Ni) Olivine Materials. *Electrochem. Solid-State Lett.* **2004**, *7*, A30-A32.
163. N. Ravet, J. B. Goodenough, S. Besner, M. Simoneau, P. Hovington, M. Armand 196th Meeting of the Electrochemical Society, **1999**.
164. N. Ravet, Y. Chouinard, J. F. Magnan, S. Besner, M. Gauthier, M. Armand, Electroactivity of Natural and Synthetic Triphylite. *J. Power Sources* **2001**, *97-98*, 503-507.
165. H. Huang, S.-C. Yin, L. F. Nazar, Approaching Theoretical Capacity of LiFePO_4 at Room Temperature at High Rates. *Electrochem. Solid-State Lett.* **2001**, *4*, A170-A172.
166. A. Yamada, S. C. Chung, K. Hinokuma Optimized LiFePO_4 for Lithium Battery Cathodes. *J. Electrochem. Soc.* **2001**, *148*, A224-A229.
167. G. T.-K. Fey, T.-L. Lu, Morphological Characterization of LiFePO_4/C Composite Cathode Materials Synthesized via a Carboxylic Acid Route. *J. Power Sources* **2008**, *178*, 807-814.

168. N. Iltchev, Y. K. Chen, S. Okada, J. Yamaki, LiFePO₄ Storage at Room and Elevated Temperatures. *J. Power Sources* **2003**, *119-121*, 749-754.
169. K.-F. Hsu, S.-Y. Tsay, B.-J. Hwang, Synthesis and Characterization of Nano-sized LiFePO₄ Cathode Materials Prepared by a Citric Acid-Based Sol-gel Route. *J. Mater. Chem.* **2004**, *14*, 2690-2695.
170. G. Arnold, J. Garche, R. Hemmer, S. Ströbele, C. Vogler, M. Wohlfahrt-Mehrens, Fine-particle Lithium Iron Phosphate LiFePO₄ Synthesized by a New Low-cost Aqueous Precipitation Technique. *J. Power Sources* **2003**, *119-121*, 247-251.
171. K. S. Park, J. T. Son, H. T. Chung, S. J. Kim, C. H. Lee, H. G. Kim, Synthesis of LiFePO₄ by Co-precipitation and Microwave Heating. *Electrochem. Commun.* **2003**, *5*, 839-842.
172. S. Yang, P. Y. Zavalij, M. Stanley Whittingham, Hydrothermal Synthesis of Lithium Iron Phosphate Cathodes. *Electrochem. Commun.* **2001**, *3*, 505-508.
173. S. Yang, Y. Song, P. Y. Zavalij, M. Stanley Whittingham, Reactivity, Stability and Electrochemical Behavior of Lithium Iron Phosphates. *Electrochem. Commun.* **2002**, *4*, 239-244.
174. S. Ferrari, R. L. Lavall, D. Capsoni, E. Quartarone, A. Magistris, P. Mustarelli, P. Canton, Influence of Particle Size and Crystal Orientation on the Electrochemical Behavior of Carbon-Coated LiFePO₄. *J. Phys. Chem. C* **2010**, *114*, 12598-12603.
175. A. V. Murugan, T. Muraliganth, A. Manthiram, Comparison of Microwave Assisted Solvothermal and Hydrothermal Syntheses of LiFePO₄/C Nanocomposite Cathodes for Lithium Ion Batteries. *J. Phys. Chem. C* **2008**, *112*, 14665-14671.
176. A. Vadivel Murugan, T. Muraliganth, A. Manthiram, Rapid Microwave-Solvothermal Synthesis of Phospho-Olivine Nanorods and Their Coating with a Mixed Conducting Polymer for Lithium Ion Batteries. *Electrochem. Commun.* **2008**, *10*, 903-906.
177. A. V. Murugan, T. Muraliganth, P. J. Ferreira, A. Manthiram, Dimensionally Modulated, Single-Crystalline LiMPO₄ (M = Mn, Fe, Co, and Ni) with Nano-Thumblike Shapes for High-Power Energy Storage. *Inorg. Chem.* **2009**, *48*, 946-952.
178. S. Yang, X. Zhou, J. Zhang, Z. Liu, Morphology-Controlled Solvothermal Synthesis of LiFePO₄ as a Cathode Material for Lithium-Ion Batteries. *J. Mater. Chem.* **2010**, *20*, 8086-8091.
179. C. M. Doherty, R. A. Caruso, B. M. Smarsly, C. Drummond, Colloidal Crystal Templating to Produce Hierarchically Porous LiFePO₄ Electrode Materials for High Power Lithium Ion Batteries. *Chem. Mater.* **2009**, *21*, 2895-2903.
180. G. Hasegawa, Y. Ishihara, K. Kanamori, K. Miyazaki, Y. Yamada, K. Nakanishi, T. Abe, Facile Preparation of Monolithic LiFePO₄/Carbon Composites with Well-Defined Macropores for a Lithium-Ion Battery. *Chem. Mater.* **2011**, *23*, 5208-5216.
181. A. Vu, A. Stein, Multiconstituent Synthesis of LiFePO₄/C Composites with Hierarchical Porosity as Cathode Materials for Lithium Ion Batteries. *Chem. Mater.* **2011**, *23*, 3237-3245.

182. N. Recham, M. Armand, L. Laffont, J.-M. Tarascon, Eco-Efficient Synthesis of LiFePO_4 with Different Morphologies for Li-Ion Batteries. *Electrochem. Solid-State Lett.* **2009**, *12*, A39-A44.
183. N. Recham, L. Dupont, M. Courty, K. Djellab, D. Larcher, M. Armand, J. M. Tarascon, Ionothermal Synthesis of Tailor-Made LiFePO_4 Powders for Li-Ion Battery Applications. *Chem. Mater.* **2009**, *21*, 1096-1107.
184. J.-M. Tarascon, N. Recham, M. Armand, J.-N. Chotard, P. Barpanda, W. Walker, L. Dupont, Hunting for Better Li-Based Electrode Materials via Low Temperature Inorganic Synthesis. *Chem. Mater.* **2010**, *22*, 724-739.
185. S. Yang, Y. Song, K. Ngala, P. Y. Zavalij, M. Stanley Whittingham, Performance of LiFePO_4 as Lithium Battery Cathode and Comparison with Manganese and Vanadium Oxides. *J. Power Sources* **2003**, *119–121*, 239-246.
186. M. S. Islam, D. J. Driscoll, C. A. J. Fisher, P. R. Slater, Atomic-Scale Investigation of Defects, Dopants, and Lithium Transport in the LiFePO_4 Olivine-Type Battery Material. *Chem. Mater.* **2005**, *17*, 5085-5092.
187. P. Gibot, M. Casas-Cabanas, L. Laffont, S. Levasseur, P. Carlach, S. Hamelet, J.-M. Tarascon, C. Masquelier, Room-Temperature Single-Phase Li Insertion/Extraction in Nanoscale Li_xFePO_4 . *Nat Mater* **2008**, *7*, 741-747.
188. S. Hamelet, P. Gibot, M. Casas-Cabanas, D. Bonnin, C. P. Grey, J. Cabana, J.-B. Leriche, J. Rodriguez-Carvajal, M. Courty, S. Levasseur, P. Carlach, M. Van Thournout, J.-M. Tarascon, C. Masquelier, The Effects of Moderate Thermal Treatments Under Air on LiFePO_4 -based Nano Powders. *J. Mater. Chem.* **2009**, *19*, 3979-3991.
189. R. Malik, D. Burch, M. Bazant, G. Ceder, Particle Size Dependence of the Ionic Diffusivity. *Nano Lett.* **2010**, *10*, 4123-4127.
190. S.-P. Badi, M. Wagemaker, B. L. Ellis, D. P. Singh, W. J. H. Borghols, W. H. Kan, D. H. Ryan, F. M. Mulder, L. F. Nazar, Direct Synthesis of Nanocrystalline $\text{Li}_{0.90}\text{FePO}_4$: Observation of Phase Segregation of Anti-site Defects on Delithiation. *J. Mater. Chem.* **2011**, *21*, 10085-10093.
191. Z. Chen, J. R. Dahn, Reducing Carbon in LiFePO_4/C Composite Electrodes to Maximize Specific Energy, Volumetric Energy, and Tap Density. *J. Electrochem. Soc.* **2002**, *149*, A1184-A1189.
192. K. Amine, H. Yasuda, M. Yamachi, Olivine LiCoPO_4 as 4.8 V Electrode Material for Lithium Batteries. *Electrochem. Solid-State Lett.* **2000**, *3*, 178-179.
193. S. Okada, S. Sawa, M. Egashira, J.-i. Yamaki, M. Tabuchi, H. Kageyama, T. Konishi, A. Yoshino, Cathode Properties of Phospho-olivine LiMPO_4 for Lithium Secondary Batteries. *J. Power Sources* **2001**, *97–98*, 430-432.
194. A. Yamada, S.-C. Chung Crystal Chemistry of the Olivine-Type $\text{Li}(\text{Mn}_y\text{Fe}_{1-y})\text{PO}_4$ and $(\text{Mn}_y\text{Fe}_{1-y})\text{PO}_4$ as Possible 4 V Cathode Materials for Lithium Batteries. *J. Electrochem. Soc.* **2001**, *148*, A960-A967.

195. F. Zhou, M. Cococcioni, K. Kang, G. Ceder, The Li Intercalation Potential of LiMPO_4 and LiMSiO_4 Olivines with $M = \text{Fe, Mn, Co, Ni}$. *Electrochem. Commun.* **2004**, *6*, 1144-1148.
196. C. Delacourt, P. Poizot, M. Morcrette, J. M. Tarascon, C. Masquelier, One-Step Low-Temperature Route for the Preparation of Electrochemically Active LiMnPO_4 Powders. *Chem. Mater.* **2004**, *16*, 93-99.
197. R. Dominko, M. Bele, M. Gaberscek, M. Remskar, D. Hanzel, J. M. Goupil, S. Pejovnik, J. Jamnik, Porous Olivine Composites Synthesized by Sol-gel Technique. *J. Power Sources* **2006**, *153*, 274-280.
198. J. Yang, J. J. Xu, Synthesis and Characterization of Carbon-Coated Lithium Transition Metal Phosphates LiMPO_4 ($M = \text{Fe, Mn, Co, Ni}$) Prepared via a Nonaqueous Sol-Gel Route. *J. Electrochem. Soc.* **2006**, *153*, A716-A723.
199. J. Barker, M. Y. Saidi, J. L. Swoyer., Lithium Metal Fluorophosphate Materials and Preparation Thereof. Patent WO 2001/084655, **2001**.
200. J. Barker, M. Y. Saidi, J. L. Swoyer, Electrochemical Insertion Properties of the Novel Lithium Vanadium Fluorophosphate, LiVPO_4F . *J. Electrochem. Soc.* **2003**, *150*, A1394-A1398.
201. J. Barker, M. Y. Saidi, J. L. Swoyer, A Comparative Investigation of the Li Insertion Properties of the Novel Fluorophosphate Phases, NaVPO_4F and LiVPO_4F . *J. Electrochem. Soc.* **2004**, *151*, A1670-A1677.
202. J. Barker, R. K. B. Gover, P. Burns, A. Bryan, M. Y. Saidi, J. L. Swoyer, Structural and Electrochemical Properties of Lithium Vanadium Fluorophosphate, LiVPO_4F . *J. Power Sources* **2005**, *146*, 516-520.
203. J. Barker, R. K. B. Gover, P. Burns, A. Bryan, M. Y. Saidi, J. L. Swoyer, Performance Evaluation of Lithium Vanadium Fluorophosphate in Lithium Metal and Lithium-Ion Cells. *J. Electrochem. Soc.* **2005**, *152*, A1776-A1779.
204. J.-M. Ateba Mba, C. Masquelier, E. Suard, L. Croguennec, Synthesis and Crystallographic Study of Homeotypic LiVPO_4F and LiVPO_4O . *Chem. Mater.* **2012**, *24*, 1223-1234.
205. J. L. Pizarro-Sanz, J. M. Dance, G. Villeneuve, M. I. Arriortua-Marcaida., The natural and synthetic tavorite minerals : crystal chemistry and magnetic properties. *Mater. Lett.* **1994**, *18*, 327-330.
206. L. A. Groat, M. Raudsepp, F. C. Hawthorne, T. S. Ercit, B. L. Sherriff, J. S. Hartman., The Amblygonite-Montebasite series: Characterization by Single-Crystal Structure Refinement Infrared Spectroscopy, and Multinuclear MAS-NMR Spectroscopy. *Am. Mineral.* **1990**, *75*, 992-1008.
207. N. Recham, J. N. Chotard, J. C. Jumas, L. Laffont, M. Armand, J. M. Tarascon, Ionothermal Synthesis of Li-Based Fluorophosphates Electrodes. *Chem. Mater.* **2010**, *22*, 1142-1148.
208. J.-M. Tarascon, N. Recham, M. Armand, Method for Producing Inorganic Compounds. Patent WO 2010046608, **2010**.

209. T. N. Ramesh, K. T. Lee, B. L. Ellis, L. F. Nazar, Tavorite Lithium Iron Fluorophosphate Cathode Materials: Phase Transition and Electrochemistry of $\text{LiFePO}_4\text{F} - \text{Li}_2\text{FePO}_4\text{F}$. *Electrochem. Solid-State Lett.* **2010**, *13*, A43-A47.
210. B. L. Ellis, T. N. Ramesh, W. N. Rowan-Weetaluktuk, D. H. Ryan, L. F. Nazar, Solvothermal Synthesis of Electroactive Lithium Iron Tavorites and Structure of $\text{Li}_2\text{FePO}_4\text{F}$. *J. Mater. Chem.* **2012**, *22*, 4759-4766.
211. B. L. Ellis, W. R. M. Makahnouk, Y. Makimura, K. Toghill, L. F. Nazar, A Multifunctional 3.5 V Iron- Based Phosphate Cathode for Rechargeable Batteries. *Nat Mater* **2007**, *6*, 749-753.
212. N. R. Khasanova, O. A. Drozhzhin, D. A. Storozhilova, C. Delmas, E. V. Antipov, New Form of $\text{Li}_2\text{FePO}_4\text{F}$ as Cathode Material for Li-Ion Batteries. *Chem. Mater.* **2012**, *24*, 4271-4273.
213. M. E. A. y. de Dompablo, U. Amador, J. M. Tarascon, A Computational Investigation on Fluorinated-Polyanionic Compounds as Positive Electrode for Lithium Batteries. *J. Power Sources* **2007**, *174*, 1251-1257.
214. M. Ati, M. Sathiya, S. Boulineau, M. Reynaud, A. Abakumov, G. Rousse, B. Melot, G. Van Tendeloo, J.-M. Tarascon, Understanding and Promoting the Rapid Preparation of the Triplite-Phase of LiFeSO_4F for Use as a Large-Potential Fe Cathode. *J. Am. Chem. Soc.* **2012**, *134*, 18380-18387.
215. B. C. Melot, G. Rousse, J. N. Chotard, M. Ati, J. Rodríguez-Carvajal, M. C. Kemei, J. M. Tarascon, Magnetic Structure and Properties of the Li-Ion Battery Materials FeSO_4F and LiFeSO_4F . *Chem. Mater.* **2011**, *23*, 2922-2930.
216. J.-M. Tarascon, N. Recham, M. Armand, Fluorosulphates Useful as Electrode Materials. Patent WO 2010046610.
217. L. Sebastian, J. Gopalakrishnan, Y. Piffard, Synthesis, Crystal Structure and Lithium Ion Conductivity of LiMgFSO_4 . *J. Mater. Chem.* **2002**, *12*, 374-377.
218. P. Barpanda, J.-N. Chotard, N. Recham, C. Delacourt, M. Ati, L. Dupont, M. Armand, J.-M. Tarascon, Structural, Transport, and Electrochemical Investigation of Novel AMSO_4F (A = Na, Li; M = Fe, Co, Ni, Mn) Metal Fluorosulphates Prepared Using Low Temperature Synthesis Routes. *Inorg. Chem.* **2010**, *49*, 7401-7413.
219. P. Barpanda, M. Ati, B. C. Melot, G. Rousse, J. N. Chotard, M. L. Doublet, M. T. Sougrati, S. A. Corr, J. C. Jumas, J. M. Tarascon, A 3.90 V Iron-Based Fluorosulphate Material for Lithium-Ion Batteries Crystallizing in the Rriplite Structure. *Nat Mater.* **2011**, *10*, 772-779.
220. M. Ati, B. C. Melot, G. Rousse, J.-N. Chotard, P. Barpanda, J.-M. Tarascon, Structural and Electrochemical Diversity in $\text{LiFe}_{1-\delta}\text{Zn}_\delta\text{SO}_4\text{F}$ Solid Solution: A Fe-Based 3.9 V Positive-Electrode Material. *Angew. Chem. Int. Ed.* **2011**, *50*, 10574-10577.
221. R. Tripathi, G. Popov, B. L. Ellis, A. Huq, L. F. Nazar, Lithium Metal Fluorosulfate Polymorphs as Positive Electrodes for Li-ion Batteries: Synthetic Strategies and Effect of Cation Ordering. *Energy Environ. Sci.* **2012**, *5*, 6238-6246.

222. M. Ati, W. T. Walker, K. Djellab, M. Armand, N. Recham, J.-M. Tarascon, Fluorosulfate Positive Electrode Materials Made with Polymers as Reacting Media. *Electrochem. Solid-State Lett.* **2010**, *13*, A150-A153.
223. R. Tripathi, T. N. Ramesh, B. L. Ellis, L. F. Nazar, Scalable Synthesis of Favorite LiFeSO₄F and NaFeSO₄F Cathode Materials. *Angew. Chem. Int. Ed.* **2010**, *49*, 8738-8742.
224. M. Ati, M. T. Sougrati, N. Recham, P. Barpanda, J.-B. Leriche, M. Courty, M. Armand, J.-C. Jumas, J.-M. Tarascon, Fluorosulfate Positive Electrodes for Li-Ion Batteries Made via a Solid-State Dry Process. *J. Electrochem. Soc.* **2010**, *157*, A1007-A1015.
225. M. Ben Yahia, F. Lemoigno, G. Rousse, F. Boucher, J.-M. Tarascon, M.-L. Doublet, Origin of the 3.6 V to 3.9 V Voltage Increase in the LiFeSO₄F Cathodes for Li-ion Batteries. *Energy Environ. Sci.* **2012**, *5*, 9584-9594.
226. M. Ati, B. C. Melot, J. N. Chotard, G. Rousse, M. Reynaud, J. M. Tarascon, Synthesis and Electrochemical Properties of Pure LiFeSO₄F in the Triplite Structure. *Electrochem. Commun.* **2011**, *13*, 1280-1283.
227. L. Liu, B. Zhang, X.-J. Huang, A 3.9 V Polyanion-Type Cathode Material for Li-ion Batteries. *Progress in Natural Science: Materials International* **2011**, *21*, 211-215.
228. R. Tripathi, G. Popov, X. Sun, D. H. Ryan, L. F. Nazar, Ultra-Rapid Microwave Synthesis of Triplite LiFeSO₄F. *J. Mater. Chem. A.* **2013**, *1*, 2990-2994.
229. L. Zhang, J.-M. Tarascon, M. T. Sougrati, G. Rousse, G. Chen, Influence of Relative Humidity on the Structure and Electrochemical Performance of Sustainable LiFeSO₄F Electrodes for Li-ion Batteries. *J. Mater. Chem. A.* **2015**, *3*, 16988-16997.
230. D. Aurbach, Review of Selected Electrode–solution Interactions Which Determine the Performance of Li and Li ion Batteries. *J. Power Sources* **2000**, *89*, 206-218.
231. S. F. Lux, I. T. Lucas, E. Pollak, S. Passerini, M. Winter, R. Kostecki, The Mechanism of HF Formation in LiPF₆ Based Organic Carbonate Electrolytes. *Electrochem. Commun.* **2012**, *14*, 47-50.
232. S.-W. Kim, K.-W. Nam, D.-H. Seo, J. Hong, H. Kim, H. Gwon, K. Kang, Energy Storage in Composites of a Redox Couple Host and a Lithium Ion Host. *Nano Today* **2012**, *7*, 168-173.
233. X.-M. Liu, S.-L. Zhang, M. Yang, X.-Z. Liao, H. Yang, X.-D. Shen, Z.-F. Ma, Synthesis and Electrochemical Evolution of Mesoporous LiFeSO₄F_{0.56}(OH)_{0.44} with High Power and Long Cyclability. *Chem. Commun.* **2014**, *50*, 15247-15250.
234. M. Ati, M. T. Sougrati, G. Rousse, N. Recham, M. L. Doublet, J. C. Jumas, J. M. Tarascon, Single-Step Synthesis of FeSO₄F_{1-y}OH_y (0 ≤ y ≤ 1) Positive Electrodes for Li-Based Batteries. *Chem. Mater.* **2012**, *24*, 1472-1485.
235. C. V. Subban, M. Ati, G. Rousse, A. M. Abakumov, G. Van Tendeloo, R. Janot, J.-M. Tarascon, Preparation, Structure, and Electrochemistry of Layered Polyanionic Hydroxysulfates: LiMSO₄OH (M = Fe, Co, Mn) Electrodes for Li-Ion Batteries. *J. Am. Chem. Soc.* **2013**, *135*, 3653-3661.

236. N. Marx, L. Croguennec, D. Carlier, A. Wattiaux, F. L. Cras, E. Suard, C. Delmas, The Structure of Tavorite $\text{LiFePO}_4(\text{OH})$ from Diffraction and GGA + U Studies and Its Preliminary Electrochemical Characterization. *Dalton Trans.* **2010**, 39, 5108-5116.
237. M. Anji Reddy, V. Pralong, V. Caignaert, U. V. Varadaraju, B. Raveau, Monoclinic Iron Hydroxy Sulphate: a New Route to Electrode Materials. *Electrochem. Commun.* **2009**, 11, 1807-1810.
238. K. Saravanan, H. S. Lee, M. Kuezma, J. J. Vittal, P. Balaya, Hollow $\alpha\text{-LiVOPO}_4$ Sphere Cathodes for High Energy Li-ion Battery Application. *J. Mater. Chem.* **2011**, 21, 10042-10050.
239. M. Bianchini, J. M. Ateba-Mba, P. Dagault, E. Bogdan, D. Carlier, E. Suard, C. Masquelier, L. Croguennec, Multiple Phases in the $\varepsilon\text{-VPO}_4\text{O-LiVPO}_4\text{O-Li}_2\text{VPO}_4\text{O}$ System: a Combined Solid State Electrochemistry and Diffraction Structural Study. *J. Mater. Chem. A.* **2014**, 2, 10182-10192.
240. A. S. Prakash, P. Rozier, L. Dupont, H. Vezin, F. Sauvage, J. M. Tarascon, Electrochemical Reactivity of $\text{Li}_2\text{VOSiO}_4$ toward Li. *Chem. Mater.* **2006**, 18, 407-412.
241. J. Gaubicher, Y. Chabre, J. Angenault, A. Lautié, M. Quarton, Lithium Electrochemical Intercalation in $\beta\text{-VOSO}_4$. *J. Alloys Compd.* **1997**, 262, 34-38.
242. P. Kierkegaard, J. M. Longo, B. O. Marinder, *Acta Chem. Scand.* **1965**, 19, 763-764.
243. J. M. Longo, R. J. Arnett, Structure and Magnetic Properties of VOSO_4 . *J. Solid State Chem.* **1970**, 1, 394-398.
244. S. Boghosian, K. M. Eriksen, R. Fehrmann, K. Nielsen, Synthesis, Crystal Structure Redetermination and Vibrational Spectra of Beta- VOSO_4 . *Acta Chem. Scand.* **1995**, 49, 703-708.
245. E. Fluegel-Kahler, Die Kristallstruktur von Dolerophanit, Cu_2OSO_4 . *Acta Crystallographica* **1963**, 16, 1009-1014.
246. H. Effenberger, $\text{Cu}_2\text{O}(\text{SO}_4)$, Dolerophanite: Refinement of the Crystal Structure with a Comparison of $[\text{OCu}(\text{II})_4]$ Tetrahedra in Inorganic Compounds. *Monatsh. Chem.* **1985**, 116, 927-931.
247. M. Saubanère, M. B. Yahia, S. Lebègue, M. L. Doublet, An Intuitive And Efficient Method for Cell Voltage Prediction of Lithium And Sodium-Ion Batteries. *Nat Commun* **2014**, 5.
248. T. Mueller, G. Hautier, A. Jain, G. Ceder, Evaluation of Tavorite-Structured Cathode Materials for Lithium-Ion Batteries Using High-Throughput Computing. *Chem. Mater.* **2011**, 23, 3854-3862.
249. M. Reynaud, P. Barpanda, G. Rousse, J.-N. Chotard, B. C. Melot, N. Recham, J.-M. Tarascon, Synthesis and Crystal Chemistry of the NaMSO_4F Family (M = Mg, Fe, Co, Cu, Zn). *Solid State Sci.* **2012**, 14, 15-20.
250. M. Sun, G. Rousse, A. M. Abakumov, M. Saubanère, M.-L. Doublet, J. Rodríguez-Carvajal, G. Van Tendeloo, J.-M. Tarascon, $\text{Li}_2\text{Cu}_2\text{O}(\text{SO}_4)_2$: a Possible Electrode for

- Sustainable Li-Based Batteries Showing a 4.7 V Redox Activity vs Li^+/Li^0 . *Chem. Mater.* **2015**, *27*, 3077-3087.
251. A. Boultif, D. Louër, Indexing of Powder Diffraction Patterns for Low-symmetry Lattices by the Successive Dichotomy Method. *J. Appl. Crystallogr.* **1991**, *24*, 987-993.
252. V. Favre-Nicolin, R. Cerny, FOX, 'Free Objects for Crystallography': a Modular Approach to Ab Initio Structure Determination from Powder Diffraction. *J. Appl. Crystallogr.* **2002**, *35*, 734-743.
253. J. Rodriguez-Carvajal, Recent Advances in Magnetic-Structure Determination by Neutron Powder Diffraction. *Physica B* **1993**, *192*, 55-69.
254. L. Waldrop, The Crystal Structure of Triplite, $(\text{Mn,Fe})_2\text{FPO}_4$. *Z. Kristallogr.* **1969**, *130*, 1-14.
255. J. R. Rea, E. Kostiner, The Crystal Structure of Manganese Fluorophosphate, $\text{Mn}_2(\text{PO}_4)\text{F}$. *Acta Crystallographica Section B* **1972**, *28*, 2525-2529.
256. A. R. Oganov, M. Valle, How to Quantify Energy Landscapes of Solids. *J. Chem. Phys.* **2009**, *130*, 104504.
257. T. Maxisch, F. Zhou, G. Ceder, Ab Initio Study of the Migration of Small Polarons in Olivine Li_xFePO_4 and Their Association with Lithium Ions And Vacancies. *Physical Review B* **2006**, *73*, 104301.
258. N. A. Spaldin, *Magnetic Materials: Fundamentals and Applications*. Cambridge University Press: **2010**.
259. H. Effenberger, $\text{Cu}_2\text{O}(\text{SO}_4)$, Dolerophanite: Refinement of the Crystal Structure, with a Comparison of $[\text{O Cu(II)}_4]$ Tetrahedra in Inorganic Compounds. *Monatsh. Chem.* **1985**, *116*, 927-931.
260. A. Altomare, M. C. Burla, M. Camalli, B. Carrozzini, G. L. Cascarano, C. Giacovazzo, A. Guagliardi, A. G. G. Moliterni, G. Polidori, R. Rizzi, EXPO: A Program for Full Powder Pattern Decomposition and Crystal Structure Solution. *J. Appl. Crystallogr.* **1999**, *32*, 339-340.
261. P. Fischer, G. Frey, M. Koch, M. Könecke, V. Pomjakushin, J. Schefer, R. Thut, N. Schlumpf, R. Bürge, U. Greuter, S. Bondt, E. Berruyer, *Phys. B: Condens. Matter* **2000**, 276-278, 146.
262. H. M. Rietveld, A Profile Refinement Method for Nuclear and Magnetic Structures. *J. Appl. Crystallogr.* **1969**, *2*, 65.
263. I. D. Brown, D. Altermatt, Bond-Valence Parameters Obtained from a Systematic Analysis of the Inorganic Crystal Structure Database. *Acta Crystallographica Section B* **1985**, *41*, 244-247.
264. S. Adams, From Bond Valence Maps to Energy Landscapes for Mobile Ions in Ion-Conducting Solids. *Solid State Ionics* **2006**, *177*, 1625-1630.

265. S. Adams, R. P. Rao, I. D. Brown, K. R. Poeppelmeier, Bond Valences. In *Struct. Bond.*, Brown, I. D.; Poeppelmeier, K. R., Eds. Springer Berlin Heidelberg: **2014**; pp 129-159.
266. M. Morcrette, P. Rozier, L. Dupont, E. Mugnier, L. Sannier, J. Galy, J. M. Tarascon, A Reversible Copper Extrusion – Insertion Electrode for Rechargeable Li Batteries. *Nat. Mater.* **2003**, *2*, 755-761.
267. P. Poizot, S. Laruelle, S. Grugeon, L. Dupont, J. M. Tarascon, Nano-Sized Transition-Metal Oxides as Negative-Electrode Materials for Lithium-Ion Batteries. *Nature* **2000**, *407*, 496-499.
268. J. Cabana, L. Monconduit, D. Larcher, M. R. Palacín, *Adv. Mater.* **2010**, *22*, E170.
269. A. Kirfel, K. Eichhorn, Accurate Structure Analysis with Synchrotron Radiation. The Electron Density in Al₂O₃ and Cu₂O. *Acta Crystallogr., Sect. A* **1990**, *46*, 271.
270. M. Okeeffe, J. Bovin, The Crystal Structure of Paramelaconite, Cu₄O₃. *Am. Mineral.* **1978**, *63*, 180.
271. M. Reynaud, M. Ati, B. C. Melot, M. T. Sougrati, G. Rouse, J.-N. Chotard, J.-M. Tarascon, Li₂Fe(SO₄)₂ as a 3.83 V Positive Electrode Material. *J. Electrochem. Commun.* **2012**, *21*, 77-80.
272. M. Reynaud, G. Rouse, J. N. Chotard, J. Rodríguez-Carvajal, J. M. Tarascon, Marinite Li₂M(SO₄)₂ (M = Co, Fe, Mn) and Li₁Fe(SO₄)₂: Model Compounds for Super-Super-Exchange Magnetic Interactions. *Inorg. Chem.* **2013**, *52*, 10456.
273. L. Lander, M. Reynaud, G. Rouse, M. T. Sougrati, C. Laberty-Robert, R. J. Messinger, M. Deschamps, J.-M. Tarascon, Synthesis and Electrochemical Performance of the Orthorhombic Li₂Fe(SO₄)₂ Polymorph for Li-Ion Batteries. *Chem. Mater.* **2014**, *26*, 4178-4189.
274. M. Reynaud, J. Rodríguez-Carvajal, J.-N. Chotard, J.-M. Tarascon, G. Rouse, Magnetic Structure and Properties of Orthorhombic Li₂Ni(SO₄)₂: A Possible Magnetoelectric Material. *Physical Review B* **2014**, *89*, 104419.
275. J.-M. Tarascon, N. Recham, M. Armand, J.-N. Chotard, P. Barpanda, W. Waker, L. Dupont, Tailoring a Fluorophosphate as a Novel 4 V Cathode for Lithium-Ion Batteries. *Chem. Mater.* **2010**, *22*, 724-739.
276. A. S. Prakash, P. Rozier, L. Dupont, H. Vezin, F. Sauvage, J. M. Tarascon, Electrochemical Reactivity of Li₂VOSiO₄ toward Li. *Chem. Mater.* **2005**, *18*, 407-412.
277. A. Bristoti, J. I. Kunrath, P. J. Viccaro, L. Bergter, Mössbauer and Thermogravimetric Analysis of the Oxidation Pathway in the Thermal Decomposition of FeSO₄·7H₂O. *J. Inorg. Nucl. Chem.* **1975**, *37*, 1149.
278. K. S. Neto, V. K. Garg, Mössbauer thermal decomposition studies of Fe(II) sulphate. *J. Inorg. Nucl. Chem.* **1975**, *37*, 2287-2290.
279. M. S. R. Swamy, T. P. Prasad, B. R. Sant, Thermal Analysis of Ferrous Sulphate Heptahydrate in Air - Part I. Some General Remarks and Methods *J. Thermal Anal.* **1979**, *15*, 307-314.

280. M. S. R. Swamy, T. P. Prasad, Thermal Analysis of Iron(II) Sulphate Heptahydrate in Air - V. Thermal Decomposition of Hydroxy and Oxysulphates *J. Thermal Anal.* **1981**, *20*, 107-114.
281. Y. Pelovski, V. Petkova, S. Nikolov, Study of the Mechanism of the Thermochemical Decomposition of Ferrous Sulphate Monohydrate. *Thermochim. Acta* **1996**, *274*, 273.
282. V. Petkova, Y. Pelovski, Investigation on The Thermal Properties of Fe₂O(SO₄)₂. Part I. *J. Therm. Anal. Calorim.* **2001**, *64*, 1025-1035.
283. V. Petkova, Y. Pelovski, D. Paneva, I. Mitov, Influence of Gas Media on the Thermal Decomposition of Second Valence Iron Sulphates. *J. Therm. Anal. Calorim.* **2011**, *105*, 793-803.
284. A. Boultif, D. Louer, Indexing of Powder Diffraction Patterns for Low-Symmetry Lattices by the Successive Dichotomy Method. *Journal of Applied Crystallography* **1991**, *24*, 987-993.
285. P.-E. Werner, L. Eriksson, M. Westdahl, TREOR, a semi-exhaustive trial-and-error powder indexing program for all symmetries. *Journal of Applied Crystallography* **1985**, *18*, 367-370.
286. A. Altomare, M. C. Burla, M. Camalli, B. Carrozzini, G. L. Casciarano, C. Giacovazzo, A. Guagliardi, A. G. G. Moliterni, G. Polidori, R. Rizzi, EXPO: a program for full powder pattern decomposition and crystal structure solution. *Journal of Applied Crystallography* **1999**, *32*, 339-340.
287. H. M. Rietveld, A Profile Refinement Method for Nuclear and Magnetic Structures. *Journal of Applied Crystallography* **1969**, *2*, 65-71.
288. J. Rodriguez-Carvajal, Recent Advances in Magnetic-Structure Determination by Neutron Powder Diffraction. *Physica B* **1993**, *192*, 55-69.
289. P. W. Stephens, Phenomenological Model of Anisotropic Peak Broadening in Powder Diffraction. *J. Appl. Cryst.* **1999**, *32*, 281-289.
290. I. D. Brown, D. Altermatt, Bond-valence parameters obtained from a systematic analysis of the Inorganic Crystal Structure Database. *Acta Cryst.* **1985**, *B41*, 244-247.
291. L. K. Elbouaanani, B. Malaman, R. Gérardin, M. Ijjaali, Crystal Structure Refinement and Magnetic Properties of Fe₄(P₂O₇)₃ Studied by Neutron Diffraction and Mössbauer Techniques. *J. Solid State Chem.* **2002**, *163*, 412-420.
292. M. Bouchdoug, A. Courtois, R. Gerardin, J. Steinmetz, C. Gleitzer, Preparation et Etude d'un Oxyphosphate Fe₄(PO₄)₂O. *J. Solid State Chem.* **1982**, *42*, 149-157.
293. A. M. Abakumov, D. Batuk, J. Hadermann, M. G. Rozova, D. V. Sheptyakov, A. A. Tsirlin, D. Niermann, F. Waschkowski, J. Hemberger, G. Van Tendeloo, E. V. Antipov, Antiferroelectric (Pb,Bi)_{1-x}Fe_{1+x}O_{3-y} Perovskites Modulated by Crystallographic Shear Planes. *Chem. Mater.* **2010**, *23*, 255-265.
294. D. Batuk, M. Batuk, A. M. Abakumov, A. A. Tsirlin, C. McCammon, L. Dubrovinsky, J. Hadermann, Effect of Lone-Electron-Pair Cations on the Orientation of

- Crystallographic Shear Planes in Anion-Deficient Perovskites. *J. Inorg. Chem.* **2013**, *52*, 10009-10020.
295. F. Scordari, The Crystal Structure of Hohmannite, $\text{Fe}_2(\text{H}_2\text{O})_4[(\text{SO}_4)_2\text{O}] \cdot 4\text{H}_2\text{O}$ and its Relationship to Amarantite, $\text{Fe}_2(\text{H}_2\text{O})_4[(\text{SO}_4)_2\text{O}] \cdot 3\text{H}_2\text{O}$. *Mineral Mag.* **1978**, *42*, 144.
296. F. Scordari, G. Ventruti, A. F. Gualtieri, The Structure of Metahohmannite, $\text{Fe}^{3+2}[\text{O}(\text{SO}_4)_2] \cdot 4\text{H}_2\text{O}$, by In Situ Synchrotron Powder Diffraction. *Am. Mineral.* **2004**, *89*, 265-370.
297. P. Süsse, Crystal Structure of Amarantite. *Naturwissenschaften* **1967**, *54*, 642-643.
298. P. Kierkegaard, J. M. Longo, The Crystal Structure of Vanadium(IV) Oxide Sulphate, VO_2SO_4 . *Acta Chem. Scand.* **1965**, *19*, 1906-1914.
299. K.-L. Richter, R. Mattes, Darstellung, Ramanspektren und Kristallstrukturen von $\text{V}_2\text{O}_3(\text{SO}_4)_2$, $\text{K}[\text{VO}(\text{SO}_4)_2]$ und $\text{NH}_4[\text{VO}(\text{SO}_4)_2]$. *Z. Anorg. Allg. Chem.* **1992**, *611*, 158-164.
300. B. M. Gatehouse, S. N. Platts, T. B. Williams, Structure of Anhydrous Titanyl Sulfate, Titanyl Sulfate Monohydrate and Prediction of a New Structure. *Acta Cryst. B* **1993**, *49*, 428-435.
301. Z. Chen, Q. Chen, H. Wang, R. Zhang, H. Zhou, L. Chen, M. S. Whittingham, A β - $\text{VOPO}_4/\varepsilon$ - VOPO_4 composite Li-ion battery cathode. *Electrochem. Commun.* **2014**, *46*, 67-70.
302. S. V. Krivovichev, L. P. Vergasova, S. N. Britvin, S. K. Filatov, V. Kahlenberg, V. V. Ananiev, Pauflerite, β - $\text{VO}(\text{SO}_4)$, A New Mineral Species from the Tolbachik Volcano, Kamchatka Peninsula, Russia *The Canadian Mineralogist* **2007**, *45*, 921-927.
303. G. Hautier, A. Jain, S. P. Ong, B. Kang, C. Moore, R. Doe, G. Ceder, Phosphates as Lithium-Ion Battery Cathodes: An Evaluation Based on High-Throughput ab Initio Calculations. *Chem. Mater.* **2011**, *23*, 3495-3508.
304. J. Gaubicher, T. Le Mercier, Y. Chabre, J. Angenault, M. Quarton, Li / β - VOPO_4 : A New 4 V System for Lithium Batteries. *J. Electrochem. Soc.* **1999**, *146*, 4375-4379.
305. T. A. Kerr, J. Gaubicher, L. F. Nazar, Highly Reversible Li Insertion at 4 V in ε - VOPO_4/α - LiVOPO_4 Cathodes. *Electrochem. Solid-State Lett.* **2000**, *3*, 460-462.
306. N. Dupré, J. Gaubicher, J. Angenault, G. Wallez, M. Quarton, Electrochemical Performance of Different Li- VOPO_4 Systems. *J. Power Sources* **2001**, *97-98*, 532-534.
307. N. Dupré, J. Gaubicher, T. Le Mercier, G. Wallez, J. Angenault, M. Quarton, Positive Electrode Materials for Lithium Batteries Based on VOPO_4 . *Solid State Ionics* **2001**, *140*, 209-221.
308. B. M. Azmi, T. Ishihara, H. Nishiguchi, Y. Takita, Cathodic Performance of VOPO_4 with Various Crystal Phases for Li Ion Rechargeable Battery. *Electrochim. Acta* **2002**, *48*, 165-170.
309. B. M. Azmi, T. Ishihara, H. Nishiguchi, Y. Takita, Vanadyl Phosphates of VOPO_4 as a Cathode of Li-Ion Rechargeable Batteries. *J. Power Sources* **2003**, *119-121*, 273-277.

310. F. Girgsdies, W. S. Dong, J. K. Bartley, G. J. Hutchings, R. Schlögl, T. Ressler, The Crystal Structure of ϵ -VOPO₄. *Solid State Sci.* **2006**, *8*, 807-812.
311. Z. Chen, Q. Chen, L. Chen, R. Zhang, H. Zhou, N. A. Chernova, M. S. Whittingham, Electrochemical Behavior of Nanostructured ϵ -VOPO₄ over Two Redox Plateaus. *J. Electrochem. Soc.* **2013**, *160*, A1777-A1780.
312. J. Barker, M. Y. Saidi, J. L. Swoyer, Electrochemical Properties of Beta-LiVOPO₄ Prepared by Carbothermal Reduction. *J. Electrochem. Soc.* **2004**, *151*, A796-A800.
313. M. M. Ren, Z. Zhou, X. P. Gao, L. Liu, W. X. Peng, LiVOPO₄ Hollow Microspheres: One-Pot Hydrothermal Synthesis with Reactants as Self-Sacrifice Templates and Lithium Intercalation Performances. *J. Phys. Chem. C* **2008**, *112*, 13043-13046.
314. G. He, C. A. Bridges, A. Manthiram, Crystal Chemistry of Electrochemically and Chemically Lithiated Layered α_1 -LiVOPO₄. *Chem. Mater.* **2015**, *27*, 6699-6707.
315. K. L. Harrison, C. A. Bridges, C. U. Segre, C. D. Varnado, D. Applestone, C. W. Bielawski, M. P. Paranthaman, A. Manthiram, Chemical and Electrochemical Lithiation of LiVOPO₄ Cathodes for Lithium-Ion Batteries. *Chem. Mater.* **2014**, *26*, 3849-3861.
316. Y.-C. Lin, B. Wen, K. M. Wiaderek, S. Sallis, H. Liu, S. H. Lapidus, O. J. Borkiewicz, N. F. Quackenbush, N. A. Chernova, K. Karki, F. Omenya, P. J. Chupas, L. F. J. Piper, M. S. Whittingham, K. W. Chapman, S. P. Ong, Thermodynamics, Kinetics and Structural Evolution of ϵ -LiVOPO₄ over Multiple Lithium Intercalation. *Chem. Mater.* **2016**, *28*, 1794-1805.
317. M. S. Kishore, V. Pralong, V. Caignaert, U. V. Varadaraju, B. Raveau, Synthesis and Electrochemical Properties of a New Vanadyl Phosphate: Li₄VO(PO₄)₂. *Electrochem. Commun.* **2006**, *8*, 1558-1562.
318. M. Satya Kishore, V. Pralong, V. Caignaert, S. Malo, S. Hebert, U. V. Varadaraju, B. Raveau, Topotactic Insertion of Lithium in the Layered Structure Li₄VO(PO₄)₂: The Tunnel Structure Li₅VO(PO₄)₂. *J. Solid State Chem.* **2008**, *181*, 976-982.
319. R. Fehrmann, S. Boghosian, G. N. Papatheodorou, K. Nielsen, R. W. Berg, N. J. Bjerrum, Crystal Structure and Vibrational Spectra of Disodium Oxo(disulfato)vanadate. *Inorg. Chem.* **1990**, *29*, 3294-3298.
320. M. A. G. Aranda, J. P. Attfield, S. Bruque, M. Martinez-Lara, Order and Disorder of Vanadyl Chains: Crystal Structures of Vanadyl Dihydrogen Arsenate (VO(H₂AsO₄)₂) and the Lithium Derivative Li₄VO(AsO₄)₂. *Inorg. Chem.* **1992**, *31*, 1045-1049.
321. M. Schindler, F. C. Hawthorne, W. H. Baur, Crystal Chemical Aspects of Vanadium: Polyhedral Geometries, Characteristic Bond Valences, and Polymerization of (VO_n) Polyhedra. *Chem. Mater.* **2000**, *12*, 1248-1259.
322. M. Morcrette, Y. Chabre, G. Vaughan, G. Amatucci, J. B. Leriche, S. Patoux, C. Masquelier, J. M. Tarascon, In Situ X-ray Diffraction Techniques as a Powerful Tool to Study Battery Electrode Materials. *Electrochim. Acta* **2002**, *47*, 3137-3149.
323. J. Rodriguez-Carvajal Fullprof Suite. <http://www.ill.eu/sites/fullprof>.

324. A. Altomare, R. Caliandro, M. Camalli, C. Cuocci, C. Giacovazzo, A. G. G. Moliterni, R. Rizzi, Automatic Structure Determination from Powder Data with EXPO2004. *J. Appl. Crystallogr.* **2004**, *37*, 1025-1028.
325. A. Altomare, M. Camalli, C. Cuocci, C. Giacovazzo, A. Moliterni, R. Rizzi, EXPO2009: Structure Solution by Powder Data in Direct and Reciprocal Space. *J. Appl. Crystallogr.* **2009**, *42*, 1197-1202.
326. K. Momma, F. Izumi, VESTA 3 for Three-Dimensional Visualization of Crystal, Volumetric and Morphology Data. *J. Appl. Crystallogr.* **2011**, *44*, 1272-1276.
327. J. B. Leriche, S. Hamelet, J. Shu, M. Morcrette, C. Masquelier, G. Ouvrard, M. Zerrouki, P. Soudan, S. Belin, E. Elkaim, F. Baudelet, *J. Electrochem. Soc.* **2010**, *157*, A606.
328. M. Avdeev, M. Sale, S. Adams, R. P. Rao, *Solid State Ionics.* **2012**, *225*, 43.
329. C. Janot, Effet Mössbauer et Applications à la Physique du Solide. *Pure & Appl Chem* *48*, 53-64.
330. R. G. Burns, Mineral Mössbauer Spectroscopy: Correlations Between Chemical Shift and Quadrupole Splitting Parameters. *Hyperfine Interact.* **1994**, *91*, 739-745.
331. G. Kresse, J. Hafner, Ab Initio Molecular Dynamics for Liquid Metals. *Physical Review B* **1993**, *47*, 558-561.
332. G. Kresse, J. Furthmüller, Efficiency of Ab-Initio Total Energy Calculations for Metals and Semiconductors Using a Plane-Wave Basis Set. *Computational Materials Science* **1996**, *6*, 15-50.
333. J. P. Perdew, K. Burke, M. Ernzerhof, Generalized Gradient Approximation Made Simple. *Phys. Rev. Lett.* **1996**, *77*, 3865-3868.
334. P. E. Blöchl, Projector Augmented-Wave Method. *Physical Review B* **1994**, *50*, 17953-17979.
335. G. Kresse, D. Joubert, From Ultrasoft Pseudopotentials to the Projector Augmented-Wave Method. *Physical Review B* **1999**, *59*, 1758-1775.